

HETEROGENEOUS SODIUM FAST REACTOR DESIGNED FOR TRANSMUTING
MINOR ACTINIDE WASTE ISOTOPES INTO PLUTONIUM FUEL

By

SAMUEL EUGENE BAYS

A DISSERTATION PRESENTED TO THE GRADUATE SCHOOL
OF THE UNIVERSITY OF FLORIDA IN PARTIAL FULFILLMENT
OF THE REQUIREMENTS FOR THE DEGREE OF
DOCTOR OF PHILOSOPHY

UNIVERSITY OF FLORIDA

2008

© 2008 Samuel Eugene Bays

To Nikki.

ACKNOWLEDGMENTS

I would like to thank my faculty advisor, James Tulenko, for his constructive comments and guidance of this work. I would also like to thank the other members of my advisory panel, Edward Dugan, Samim Anghaie, Ronald Baney and Steve Herring for their sensible recommendations. I would like to especially thank and recognize Steve Herring for his technical guidance and support of this work. I greatly thank and appreciate Idaho National Laboratory for its financial support of this dissertation project. Thanks go to Douglas Crawford and David Nigg for their management of projects and activities in which this work supported. I thank Doug Porter, Mitch Meyer, Steve Hayes, Jon Carmack and Rory Kennedy for their technical feedback and discussions on transmutation and fast reactor fuels. Special thanks are given to Pavel Medvedev for his input on establishing the fuel performance criteria of the transmutation targets. Special thanks are given to Bevin Brush and Thomas Johnson for their technical insight of fuel handling and separations operations at the EBR-II fuel cycle facility. Special thanks are given to Steve Piet, Gretchen Matthern and David Shropshire for their technical insight into the system dynamics and economics of closing the domestic and international fuel cycles. Special thanks are given to Roald Wigeland, Giuseppe Palmiotti and Massimo Salvatores for their technical insight into reactor physics and design methodologies of sodium fast reactors. Many thanks are given to my friends and colleagues of the INL fuel cycle analysis team: Mehdi Asgari, Rodolfo Ferrer, Benoit Forget and Michael Pope for the excellent studies and results that we have produced over the last two years.

TABLE OF CONTENTS

	<u>page</u>
ACKNOWLEDGMENTS	4
LIST OF TABLES	9
LIST OF FIGURES	12
ABSTRACT	22
CHAPTER	
1 INTRODUCTION	24
Motivation and Objectives.....	26
Transmutation Physics.....	31
Neutron Spectrum Influence on Transmutation Behavior.....	32
Transmutation and Nuclear Stability.....	36
Isotopic Aspects of Repository Impacts.....	39
Background on Previously Proposed TRU Burning SFRs.....	41
The Advanced Burner Reactor Design Concept	43
Transmutation Target Designs: Radial Blankets and Moderated Targets.....	45
Transmutation Target Designs: Axial Blankets and Axial Targets.....	48
Transmutation Based Reactivity Control Concept.....	49
Design Rationale of an Axial Heterogeneous Fast Transmutation Reactor	52
Compensation for Inherent Positive Void Reactivity Feedback	53
Benefits of Axial Targets for a Dedicated MA Burner Core Design	54
Technology Compatibilities and Synergies.....	58
Actinide Partitioning: PUREX and UREX.....	59
Pyroprocessing and the Integral Fuel Cycle.....	61
Assumptions for Using Transmutation Targets in SFRs.....	63
2 COMPUTATIONAL METHODS AND FAST REACTOR PHYSICS.....	66
Calculations and Fuel Cycle Modeling.....	66
Fast Reactor Equilibrium Fuel Cycle Calculations Using the REBUS Code	68
Light Water Reactor Spent Fuel Calculations Using the TRITON Code	72
Scoping Calculations and Benchmarking Using the MCNP Code	73
Physics of the Reference Metal Fueled Advanced Burner Reactor.....	74
Conversion Ratio and High Leakage Cores	75
Conversion Ratio and High TRU Enriched Fuels	80
Physics of the Axially Heterogeneous Fast Transmutation Reactor	82
Axial Targets and Axial Leakage Recovery.....	82
Axial Targets and Minor Actinide Conversion	85
Combining Leakage and Capture Effects.....	90

3	AXIAL TARGET DESIGN ANALYSIS.....	93
	Waste Management Philosophies and Conversion Ratio Definition.....	93
	Transmutation Based Reactor Design	96
	Transmutation Targets and Accompanying Fuel Cycle	99
	Transmutation Target Physics	103
	Parametric Study.....	106
	Effects of Pin Diameter and Core Height.....	107
	Effects of Moderating Pins.....	111
	Tall and Flattened Axial Heterogeneous Core Designs.....	115
	Radial and Axial Power Profiles	116
	Reactivity Feedbacks.....	123
	Fuel Performance Indicators.....	125
	Final Down-Selection: The AHFTR Design	128
	Fuel Cycle Performance of the Final AHFTR Design	129
	Reactor Performance Characteristics of the Final AHFTR Design.....	132
	Transmutation Analysis of the Final AHFTR Design.....	135
4	REACTOR REACTIVITY CONTROL STRATEGY	139
	Tc-99 versus B-10 as a Control Rod Neutron Poison.....	139
	Control Assembly Design.....	143
	Traditional SFR Control Assembly Design: B ₄ C Ultimate Shutdown Assembly.....	143
	Technetium Based Primary Control Assembly Design.....	144
	Gas Expansion Module.....	148
	Control Rod Worth	150
	Reactivity Worth of Boron versus Technetium.....	155
	Top versus Bottom Inserted Shim Rods	156
	Axial Power Tilt and Shim Rod Insertion	157
	Other Reactivity Feedbacks.....	157
	Axial Fuel Expansion	160
	Radial Fuel Bowing.....	161
	Technetium Transmutation Rate.....	164
5	DIFFUSION VERSUS TRANSPORT BENCHMARKS	167
	Diffusion and Transport Methods.....	168
	Flux Spectrum Analysis	170
	Spatial Flux Analysis.....	172
	Differences between BOEC and EOEC Fluxes.....	175
	Depletion Test.....	176
	Spatial Self-Shielding Test	180
	Spatial Shadowing Test	182
	Calculation Validation Remarks.....	186
6	THE AHFTR FUEL DESIGN.....	188

Fuel Pin Design.....	189
Target Alloy Selection and Design Considerations.....	190
Target and Driver Fuel Burnup Criteria.....	194
Cladding Damage Criteria.....	195
Fuel Pin Thermal Performance Criterion.....	197
Fuel Temperature Criterion.....	198
Cladding Temperature Criterion.....	199
Thermal Analysis.....	200
Fuel Assembly Power Peaking.....	200
Peak Fuel Pin Hot Channel Analysis.....	206
Metallurgical Diffusion Effects.....	215
Inter-Diffusion Data.....	216
Penetration Distance.....	217
Transmutation Gas Generation and Plenum Sizing.....	218
Helium and Fission Product Gas Calculation.....	220
Transmutation and Fission Gas Analysis.....	223
Fuel Design Basis Summary.....	226
Fuel Processing Considerations.....	227
Higher Mass Actinide Considerations.....	230
Repository Considerations.....	234
7 ECONOMICS OF THE TWO-TIER AHFTR FUEL CYCLE.....	238
Economic Issues of Reprocessing.....	238
Capitol Costs.....	240
Fuel Costs.....	243
First-Core Reprocessing Cost.....	243
Subsequent Core Reprocessing Cost.....	244
High Level Waste Disposal Cost.....	247
Fuel Fabrication Cost.....	248
Front-End Uranium Costs.....	249
Back-End Uranium Costs.....	251
Discounting and Financing.....	252
Operations and Maintenance.....	253
Construction Capital.....	254
Fuel Investment.....	256
Fuel Cycle Base Cases.....	257
The MOX Fuel Cycle.....	258
The ABR Fuel Cycle.....	262
The Combined “Mixed-Fleet” AHFTR and ABR Fuel Cycle.....	265
Sensitivity Analysis.....	270
Breakeven Unit Costs for ABRs and AHFTRs.....	270
Cost Sensitivities for a Combined ABR and AHFTR Fleet.....	274
Converting Neutrons into Dollars.....	278
8 SUMMARY AND CONCLUSIONS.....	282

Method of Reactor Design.....	284
Reactor Control and Safety Features	286
Code Validation.....	288
Transmutation Target Fuel Design	289
Fuel Processing and Repository Considerations.....	290
Fuel Cycle Economic Analysis.....	291
Concluding Remarks	292

APPENDIX

A REBUS INPUT DECK.....	294
B PARAMETRIC DESIGN ANALYSIS	296
LIST OF REFERENCES	300
BIOGRAPHICAL SKETCH	309

LIST OF TABLES

<u>Table</u>	<u>page</u>
1-1 ABR fission and capture cross section data.....	35
1-2 IMF fission and capture cross section data.....	36
1-3 Fuel assembly and pin dimensions for the S-PRISM and ABR designs	46
1-4 Summary of relative studies on transmutation targets.....	48
1-5 Examples of real fast reactor plants that have incorporated axial blankets	49
1-6 Fuel assembly design of the AHFTR compared to ABR designs.....	58
1-7 Core design for the AHFTR compared to similar ABR designs	59
1-8 Waste stream partitioning afforded by various reprocessing technologies	60
1-9 Technology compatibility assumptions used for fuel cycle analysis.....	65
2-1 Isotopic composition for UOX SNF	73
2-2 Atom densities and one-group microscopic cross sections for Pu-239 and U-238	76
2-3 AHFTR fission and capture cross sections data	89
3-1 Reactor thermal power and core heights evaluated in parametric analysis	97
3-2 Reference fuel assembly design for varying height-to-diameter ratio.....	97
3-3 Transmutation utilization factor.....	105
3-4 Single group cross section ratio	105
3-5 Transmutation half-lives for a preliminary AHFTR design	108
3-6 Transmutation half-life of Am-241 for varying number of moderating rods	111
3-7 Core design summary for the reference ABR with tall and flat AHFTR	116
3-8 Fuel cycle comparison for the reference ABR with tall and flat AHFTR	122
3-9 Physics comparison for the reference ABR with tall and flat AHFTR.....	125
3-10 Fuel performance comparison for the reference ABR with tall and flat AHFTR	127
3-11 Mass flow analysis of the downselected AHFTR.....	130

3-12	Target and active core region fuel inventory of the downselected AHFTR	131
3-13	Initial reactor physics and fuel performance of the downselected AHFTR	134
3-14	Mass production and destruction rates per installed megawatt per year	135
3-15	Isotopic contribution of external supply versus contributing to fission.....	137
4-1	Atomic concentrations of absorber atoms in B ₄ C versus technetium.....	142
4-2	Control assembly types and dimensions	143
4-3	Core reactivity worth for independently separate reactivity feedback effects.....	160
4-4	Summary of Tc-99 consumption by the AHFTR	165
5-1	Select reactor parameters for the AHFTR given by DIF3D and VARIANT.	175
5-2	Comparison of mean-free-paths of different reaction types	185
6-1	Peak burnups for the driver fuel and targets	194
6-2	Average burnups for the driver fuel and targets	195
6-3	Average and peak fast fluence (E>0.1 MeV) and peak dpa	195
6-4	ABR fuel assembly peak-to-core average LHGR ratio taken at BOEC	204
6-5	Beginning of Equilibrium Cycle AHFTR fuel assembly peak-to-core average LHGR ..	204
6-6	End of Equilibrium Cycle AHFTR fuel assembly peak-to-core average LHGR	204
6-7	Ternary inter-diffusion coefficients	216
6-8	AHFTR fuel pin dimensions.....	224
7-1	Unit costs and fees for the open single-tier MOX fuel cycle.....	260
7-2	Uranium Oxide once through fuel cycle fuel costs.....	261
7-3	Mixed Oxide fuel cycle fuel costs	261
7-4	Unit costs and fees for the closed single-tier ABR fuel cycle	264
7-5	Advanced Burner Reactor fuel cycle fuel costs.....	264
7-6	Unit costs and fees for the closed double-tier AHFTR fuel cycle	268
7-7	Advanced Burner Reactor fuel costs in a mixed ABR and AHFTR fleet	268

7-8	Fuel costs for the AHFTR tier of the mixed ABR and AHFTR fleet.....	269
7-9	Advanced Burner Reactor two-tier fuel cycle breakeven unit costs.....	272
7-10	Axial Heterogeneous Fast Transmutation Reactor fuel cycle breakeven costs	272
7-11	Mixed fleet fuel cycle breakeven costs.....	274
7-12	Inter-comparison of aqueous reprocessing costs for various scenarios	280

LIST OF FIGURES

<u>Figure</u>	<u>page</u>
1-1 Synergy between GNEP and IFR fuel recycling strategies	30
1-2 Important transmutation reactions of americium and neptunium into plutonium	33
1-3 Periodic relationship between fissile and fertile transuranic isotopes.	38
1-4 Decay heat plot for pressurized water reactor SNF	40
1-5 Core layouts for the S-PRISM and ABR designs	44
1-6 Cross section plots of U-238 and Tc-99 total absorption cross sections	52
1-7 Core design of the Axial Heterogeneous Fast Transmutation Reactor.....	56
1-8 Modification to the ABR fuel cycle by the axial targets	57
1-9 Partitioning and transmutation scenario of an ABR and AHFTR mixed-fleet.....	63
2-1 Coupled DIF3D core physics and REBUS fuel cycle algorithm.....	69
2-2 Flow diagram of data transfer between the MC ² -2 and REBUS codes.....	71
2-3 Material buckling of a simple bare homogeneous SFR.....	77
2-4 Critical radius required to equate geometric buckling with material buckling.....	77
2-5 Generalized conversion ratio of simple bare homogeneous SFR.....	79
2-6 Mean-free-path of neutron travel between interactions.....	79
2-7 Leakage fraction of a simple bare homogeneous SFR.....	80
2-8 Conversion ratio and the corresponding TRU enrichment for a fixed core size	81
2-9 Axial current distribution of the AHFTR and ABR.....	84
2-10 Axial flux distribution of the AHFTR and ABR	85
2-11 Moderated target region binned “microscopic” reaction rate spectra.....	86
2-12 Active core region binned “microscopic” reaction rate spectra.....	87
2-13 Comparison of capture and fission cross sections between Am-241 and Pu-238	88
2-14 Comparison of flux spectrums between LWR IMF target region and active core	91

3-1	Preliminary AHFTR core design used in parametric analyses	98
3-2	Zirconium hydride phase diagram for varying hydrogen content	99
3-3	Representation of the axial target pin-lattice showing the orientation of targets	100
3-4	AHFTR fuel cycle scenario for the REBUS calculation	101
3-5	Americium and plutonium cross section plots versus a SFR neutron flux	104
3-6	Spectrum comparison between inner, middle, outer core and targets	106
3-7	Change in target isotope masses as a function irradiation time	107
3-8	Active core radial power density profile for a preliminary AHFTR	110
3-9	Inner core axial power density profile for a preliminary AHFTR	110
3-10	Lin.-Log Scale: Neutron flux in the target region for varying moderating rods.....	112
3-11	Log.-Log Scale: Neutron flux in the target region for varying moderating rods.....	112
3-12	Percent of the initial Am-241 mass remaining in the target rod	114
3-13	Percent of the initial Pu-238 mass created in the target rod	115
3-14	“Flat” preliminary AHFTR design with eight rows of fuel instead of seven	117
3-15	Radial power density profile for six axial slices through the core.....	118
3-16	Axial power density profile for each row of fuel.....	119
3-17	Target region buildup and depletion curve	131
3-18	Active core region buildup and depletion curve.....	132
4-1	Total neutron absorption cross section plots for select absorber materials	142
4-2	Ultimate shutdown control assembly configuration.	145
4-3	Primary control assembly configuration.....	147
4-4	Gas expansion module assembly configuration.....	149
4-5	Shim control rod bank reactivity worth at BOEC.....	150
4-6	Shim control rod bank reactivity worth at EOEC.....	151
4-7	Safety control rod bank reactivity worth at BOEC.....	152

4-8	Neutron spectrum in the targets as a function of safety rod insertion	152
4-9	Safety control rod bank reactivity worth at EOEC	153
4-10	Ultimate shutdown system worth at BOEC	154
4-11	Ultimate shutdown system worth at EOEC	154
4-12	Shim control rod bank reactivity worth for metallic Tc-99 compared to B ₄ C.....	156
4-13	Radial flux distributions for shim rods inserted from the top or the bottom	157
4-14	Axial power distribution for increasing shim rod insertion into the active core	158
4-15	Neutron spectrum for steady state operation versus a complete loss of sodium	159
5-1	Core midplane energy spectrum for code validation comparison	171
5-2	Target region energy spectrum for code validation comparison	171
5-3	Cod validation comparison of the flux axial profile	173
5-4	Cod validation comparison of the flux radial profile at the core mid-plane.....	173
5-5	Cod validation comparison of the flux radial profile at the axial target region.....	174
5-6	Comparison between the BOEC and EOEC neutron spectrums	175
5-7	Comparison between the BOEC and EOEC radial flux profiles	176
5-8	Comparison between BOEC and EOEC axial flux profiles	177
5-9	Reactivity curve comparison between REBUS and MONTEBURNS.....	178
5-10	Advanced Burner Test Reactor benchmark using “fresh core” composition	180
5-11	MCNP sub-lattice model.....	181
5-12	Neutron spectrum as a function of the zirconium hydride slug radius	183
5-13	Neutron spectrum as a function of the target slug radius.....	183
5-14	MCNP unit-cell model with homogenized fuel annulus.....	184
5-15	Neutron spectrum within the homogenized annulus.....	185
6-1	Conceptual AHFTR Fuel Pin Design	190
6-2	Optical microscopy for three of the AFC-1B samples.....	192

6-3	Fuel swelling performance for the AFC-1B samples	193
6-4	AHFTR power density profile as a function of fuel row and axial region	202
6-5	ABR reference power density profile as a function of fuel row and axial region	202
6-6	BOEC LHGR for the driver fuel mid-plane and target regions.....	205
6-7	EOEC LHGR for the driver fuel mid-plane and target regions	206
6-8	Peak pin axial BOL LHGR distribution.....	208
6-9	Axial node procession for Nusselt analysis	209
6-10	Assumed thermal properties of TRU-U-Zr metal alloy fuel.....	213
6-11	Axial temperature profiles for a “typical” fuel rod in the hottest fuel assembly	214
6-12	Percent contribution to helium production by alpha decay	219
6-13	Gas plenum pressures resulting from transmutation and fission gas production.....	225
6-14	Envisioned power block reactor plant model.....	229
6-15	Average neutron emission rate for processed initial TRU in fresh fuel	231
6-16	Average gamma decay energy rate for processed initial TRU in fresh fuel.....	233
6-17	Average alpha decay heat rate for processed initial TRU in fresh fuel	234
6-18	Decay heat plot for AHFTR fuel cycle losses in a repository	236
7-1	The open single-tier MOX fuel cycle	259
7-2	The closed single-tier ABR fuel cycle.....	263
7-3	The closed double-tier AHFTR fuel cycle.....	266
7-4	Fuel cycle costs for the ABR and AHFTR for varying aqueous unit costs	276
7-5	Fuel cycle costs for the ABR and AHFTR for varying pyroprocessing unit costs.....	276
7-6	Transuranic-free HLW disposal fee adjustment for breakeven	278
8-1	Cross section data for Am-241, Pu-238 and Pu-239.....	283
8-2	Radial power distribution for the ABR versus the AHFTR.....	285
A-1	REBUS input cards.....	294

B-1	Excess Reactivity of the core design in “tall” for varying core height and p/d	296
B-2	Excess Reactivity of the core design in “flat” for varying core height and p/d	297
B-3	TRU enrichment of the core given in “tall” for varying core height and p/d	297
B-4	TRU enrichment of the core design in “flat” for varying core height and p/d	298
B-5	Cycle length of the core given in “tall” for varying core height and p/d	298
B-6	Cycle length of the core design in “flat” for varying core height and p/d	299

LIST OF ABBREVIATIONS AND TERMINOLOGY

AAA	Advanced Accelerator Applications
ABR	Advanced Burner Reactor
ABTR	Advanced Burner Test Reactor
AFCI	Advanced Fuel Cycle Initiative
AHFTR	Axial Heterogeneous Fast Transmutation Reactor
ALMR	Advanced Liquid Metal Reactor
ANL	Argonne National Laboratory
ARR	Advanced Recycling Reactor
ATR	Advanced Test Reactor
ATW	Accelerator Transmutation of Waste
B ₄ C	Boron Carbide
BOC	Beginning of Cycle
BOEC	Beginning of Equilibrium Cycle
BOL	Beginning of Life
CAPRA	Consommation Améliorée du Plutonium dans les Réacteurs Avancés
CCCC	Committee on Computer Code Coordination
CDA	Core Disruptive Accident
CDF	Cumulative Damage Fraction
COMPX	CCCC format binary macroscopic cross section data file
Critical Radius	Effective core radius required to meet the reactivity criticality requirement by equating geometric buckling with material buckling
CRGT	Control Rod Guide Tube
D-9	Austenitic steel that can be used for SFR fuel cladding and structural components

DIF3D	Multigroup neutron diffusion code developed for modeling steady-state reactor physics and other critical systems developed by ANL
DOE	Department of Energy
dpa	Displacements per Atom
EBR-I	Experimental Breeder Reactor – I
EBR-II	Experimental Breeder Reactor – II
EFPD	Effective Full Power Day
EFR	European Fast Reactor
ENDF	Evaluated Nuclear Data File
Enrichment Zone	Same TRU enrichment/composition regions within a SFR
EOC	End of Cycle
EOEC	End of Equilibrium Cycle
EOL	End of Life
FCCI	Fuel-to-Cladding Chemical Interaction
FCF	Fuel Cycle Facility
FCMI	Fuel-to-Cladding Mechanical Interaction
FFTF	Fast Flux Test Facility
FOAK	First of a Kind
GEM	Gas Expansion Module
GNEP	Global Nuclear Energy Partnership
HLW	High Level Waste
HM	Heavy Metal
HT-9	Ferritic/Martensitic high chromium steel used for SFR fuel cladding and structural materials
IBA	Integral Burnable Absorber
IFBA	Integral Fuel Burnable Absorber

IFC	Integral Fuel Cycle
IFR	Integral Fast Reactor
iHM	Initial Heavy Metal or fresh fuel going into the reactor
IHX	Intermediate Heat Exchanger
ILW	Intermediate Level Waste
IMF	Inert Matrix Fuel
INL	Idaho National Laboratory
ISOTXS	CCCC format binary microscopic cross section data file
JSFR	Japanese Atomic Energy Agency SFR
KALIMER	Korean Advanced Liquid Metal Cooled Reactor
LANL	Los Alamos National Laboratory
LEU	Light Enriched Uranium
LHGR	Linear Heat Generation Rate
LLW	Low Level Waste
LOCA	Loss of Coolant Accident
LOHS	Unprotected Loss of Heat Sink
LWR	Light Water Reactor
MA	Minor Actinide
Matino Plane	Contact surface between two inter-diffusing compositions
MC ² -2	Multigroup cross section generation code by solution of the neutron slowing down equations developed by ANL
MCNP	Monte Carlo N-Particle general geometry, continuous energy and angle Monte Carlo transport code developed by LANL
mil	one-tenth of one cent
MIT	Massachusetts Institute of Technology
Mixed waste	Chemically and radiologically hazardous waste

MOEC	Middle of Equilibrium Cycle
MONTEBURNS	Coupling code for MCNP and ORIGEN developed by LANL
MOX	Mixed Oxide
MWD	Megawatt-day
MWY	Megawatt-year
NOAK	N th of a Kind
NRC	Nuclear Regulatory Commission
NUS	Nuclear Utility Service code of account
NWF	Nuclear Waste Fund
NWPA	Nuclear Waste Policy Act
OCRWM	Office of Civilian Radioactive Waste Management
ORIGEN	General use isotope buildup, depletion and decay code for solving the Bateman equations by the exponential matrix method developed by ORNL
ORNL	Oak Ridge National Laboratory
p/d	Pitch-to-diameter ratio
PHWR	Pressurized Heavy Water Reactor
PIE	Post Irradiation Examination
PUREX	Plutonium Uranium Redox Extraction
PWR	Pressurized Water Reactor
Pyroprocess	Metal fuel reprocessing whereby uranium and transuranics are separated by electro-deposition on cathodes immersed in a eutectic LiCl-KCl bath
REBUS	REactor BUrnup System – Fuel cycle analysis code developed by ANL
SCNES	Self-Consistent Nuclear Energy System
SFF	Spent Fast reactor Fuel
SFR	Sodium Fast Reactor
SHRT	Shutdown and Heat Removal Test

SNF	Spent “LWR” Nuclear Fuel
S-PRISM	Super – Power Reactor Innovative Small Module
Support Ratio	Mass balance ratio of installed thermal capacity for the mass consuming reactor per installed thermal capacity for the mass producing reactor
SWU	Separative Work Unit
THORP	Thermal Oxide Reprocessing Plant, Britain
TOP	Transient Overpower
TREAT	Transient Reactor Test facility
TRU	Transuranic
TRU Enrichment	Concentration by volume of TRU over HM in SFR or MOX-LWR fuels
ULOF	Unprotected Loss of forced circulation Flow
UOX	Uranium Oxide
UP1 & UP2	Reprocessing plants at LaHague, France
UREX	Uranium Extraction aqueous reprocessing technology
UREX+	Uranium Extraction Plus – Including waste stream partitioning
USEC	United States Enrichment Corporation
UxC	Uranium Exchange Consulting Company
VARIANT	Variational Anisotropic Nodal Transport Code developed by ANL
YM-EIS	Yucca Mountain – Environmental Impact Statement
ZrH _{1.6}	Zirconium Hydride

Abstract of Dissertation Presented to the Graduate School
of the University of Florida in Partial Fulfillment of the
Requirements for the Degree of Doctor of Philosophy

HETEROGENEOUS SODIUM FAST REACTOR DESIGNED FOR TRANSMUTING
MINOR ACTINIDE WASTE ISOTOPES INTO PLUTONIUM FUEL

By

Samuel Eugene Bays

May 2008

Chair: James Tulenko

Major: Nuclear Engineering Sciences

In the past several years there has been a renewed interest in sodium fast reactor (SFR) technology for the purpose of destroying transuranic waste (TRU) produced by light water reactors (LWR). The utility of SFRs as waste burners is due to the fact that higher neutron energies allow all of the actinides, including the minor actinides (MA), to contribute to fission. It is well understood that many of the design issues of LWR spent nuclear fuel (SNF) disposal in a geologic repository are linked to MAs. Because the probability of fission for essentially all the “non-fissile” MAs is nearly zero at low neutron energies, these isotopes act as a neutron capture sink in most thermal reactor systems. Furthermore, because most of the isotopes produced by these capture reactions are also non-fissile, they too are neutron sinks in most thermal reactor systems. Conversely, with high neutron energies, the MAs can produce neutrons by fast fission. Additionally, capture reactions transmute the MAs into mostly plutonium isotopes, which can fission more readily at any energy. The transmutation of non-fissile into fissile atoms is the premise of the plutonium breeder reactor. In a breeder reactor, not only does the non-fissile “fertile” U-238 atom contribute fast fission neutrons, but also transmutes into fissile Pu-239.

The fissile value of the plutonium produced by MA transmutation can only be realized in fast neutron spectra. This is due to the fact that the predominate isotope produced by MA

transmutation, Pu-238, is itself not fissile. However, the Pu-238 fission cross section is significantly larger than the original transmutation parent, predominately: Np-237 and Am-241, in the fast energy range. Also, Pu-238's fission cross section and fission-to-capture ratio is almost as high as that of fissile Pu-239 in the fast neutron spectrum. It is also important to note that a neutron absorption in Pu-238, that does not cause fission, will instead produce fissile Pu-239.

Given this fast fissile quality and also the fact that Pu-238 is transmuted from Np-237 and Am-241, these MAs are regarded as fertile material in the SFR design proposed by this dissertation. This dissertation demonstrates a SFR design which is dedicated to plutonium breeding by targeting Am-241 transmutation. This SFR design uses a moderated axial transmutation target that functions primarily as a pseudo-blanket fuel, which is reprocessed with the active driver fuel in an integrated recycling strategy. This work demonstrates the cost and feasibility advantages of plutonium breeding via MA transmutation by adopting reactor, reprocessing and fuel technologies previously demonstrated for traditional breeder reactors. The fuel cycle proposed seeks to find a harmony between the waste management advantages of transuranic burning SFRs and the resource sustainability of traditional plutonium breeder SFRs. As a result, the enhanced plutonium conversion from MAs decreases the burner SFR's fuel costs, by extracting more fissile value from the initial TRU purchased through SNF reprocessing.

CHAPTER 1 INTRODUCTION

Sodium Fast Reactors (SFRs) are currently being evaluated as a means of eliminating the long-lived transuranic (TRU) waste produced by Light Water Reactors (LWR). Historically, the inherent neutron surplus, necessary for overcoming neutron losses by leakage, has been used to breed fissile Pu-239 by transmuting U-238 in a blanket. In the context of a transuranic-burning SFR, these excess neutrons are applied to destroying, by fission, the transuranic atoms of Spent Nuclear Fuel (SNF) produced by LWRs.

However, not all transuranic isotopes can be destroyed by fission with the same efficiency. This is because many of the isotopes in SNF TRU can only fission above a given threshold neutron energy. Unfortunately, these isotopes, such as Np-237 and Am-241, present in SNF, pose the largest decay heat and radiotoxicity issues for permanent disposal of this waste in a geologic repository. The repository space benefit stems principally from the removal of Am-241 from the fuel cycle. This is because the repository's waste emplacement drift spacing is limited by the maximum rock temperature between drifts. The mid-drift temperature is principally a function of the decay heat produced by Am-241. Additionally, alpha decay of Am-241 is chiefly responsible for the buildup of Np-237 in the repository many years after it is closed.

The Am-241 cross section for fission is orders of magnitude less than its capture cross section at neutron energies less than one MeV. Because the average neutron flux for most nuclear reactors, including fast reactors, exists at energies below one MeV, fission can not be the primary mechanism for removing americium from the fuel cycle. In fact, this fission threshold property for both Np-237 and Am-241 is very pronounced when compared to most other heavy metal (HM) actinides. Therefore, it is useful to convert these isotopes, especially Am-241, into more fissionable plutonium isotopes, using specialized transmutation targets. Irradiating Am-

241 in an epithermal or thermal spectrum (below one MeV) maximizes its destruction by neutron capture. This neutron capture and its subsequent decay chain leads to the breeding of the even mass number plutonium isotope: Pu-238. This even-plutonium isotope, though not truly fissile, has a larger fission cross section below one MeV compared with the initial Am-241 atom. The fast reactor core design proposed in this dissertation uses the plutonium breeding “fertile” property of Am-241 to maximize the available fissile worth that can be derived from this otherwise non-fissile transuranic waste.

The relative increase in fissile worth contributed by the transmuted Pu-238 can only be realized in fast neutron spectra. This is because Pu-238 has a fission threshold of its own. However, the Pu-238 fission threshold is simply less sharply defined at one MeV than Am-241 (or Np-237). The fissile worth of Pu-238 is only comparable to that of odd mass number *fissile* Pu-239 and Pu-241 in the unresolved resonance range of its fission cross section. At thermal spectrum energies, the resolved capture resonances of Pu-238 render it effectively *non-fissile* with no reactivity benefit. Even though it is possible that a thermal spectrum reactor could be used to transmute Am-241 into Pu-238, a fast reactor would still be necessary to fully benefit from this conversion. This scenario would require that both thermal and fast reactors be collocated with all the necessary fuel recycling facilities at the same location. This concentration of large infrastructure facilities is considered unfeasible for this work. Instead, this dissertation will demonstrate a fast reactor design which is dedicated to plutonium breeding via americium transmutation. This fast reactor design uses a moderated axial transmutation target that functions as a pseudo-blanket fuel for breeding Pu-238. The transmuted Pu-238 is then co-reprocessed along with the SFR’s active driver fuel in an integrated recycling strategy.

Motivation and Objectives

The United States commercial nuclear power industry currently produces approximately 20% of the nation's electricity. LWRs have become the industry work horse for producing this power since the first fully commercial LWR was brought online in the United States at Shippingport Pennsylvania in 1957. Orders for new nuclear power plants grew steadily during the 1960's and continued through the 1970's. In 1979, a partial reactor meltdown accident at Three Mile Island, Pennsylvania caused investor confidence in nuclear reactor safety to essentially disappear. The accident prompted the Nuclear Regulatory Commission (NRC) to impose stricter safety standards for all existing and future commercial reactors. Though no new nuclear power plants were ordered after the Three Mile Island Accident, completion of existing construction projects since then continued to expand the industry's electrical capacity. By 1991, 22% of the nation's electricity was produced by 111 nuclear power plants [1]. Since then, several nuclear power plants have been decommissioned before the end of their licensed lifetimes. Despite the loss of these reactors, the current share of nuclear in the nation's electric resources has stabilized at 20%.

The sustainability of electric generation, even with increasing electricity demands, is due in part to an overall technological maturity afforded by years of safe operational experience since the Three Mile Island accident. Gradual improvements in the irradiation integrity of the uranium fuel have allowed more fission energy to be extracted per initial mass (i.e., burnup) than ever before. Enhancements in computer simulation have enabled an increased understanding of the nuclear, mechanical, hydraulic and materials physics within LWRs which allows them to be operated safely without sacrificing performance. Also, increased attention to human factors has enhanced operational safety, which in turn, has generally reciprocated public trust in nuclear energy.

These improvements have allowed nuclear power plant operators to minimize the time the reactor is shutdown for refueling and maintenance activities. Therefore, the capacity for LWRs to operate at full power has steadily increased from approximately 55% in the 1960's to over 90% in the 21st century [2]. This “capacity” is equivalent to saying that nuclear power plants produce 90% of the energy that could be generated if they were operated at full power all of the time. The remaining 10% roughly accounts for the time required to discharge old fuel and reload fresh fuel. Therefore, it is arguable that LWRs have achieved their practical limit in nuclear electricity generating capacity.

Further improvements in LWR fuel technology may allow slightly higher operating capacities without adding additional fuel costs. However, this is unlikely because the burnup of enriched fuel is generally linearly proportional to the level of uranium enrichment of the fissile isotope, U-235, in the fuel [3]. Currently, the NRC enforces a cap on enrichment at five percent to protect fuel fabrication workers from possible criticality accidents. Due to the criticality safety implications of exceeding this enrichment limit, it is assumed that additional safety measures will be required by enrichment and fabricators for achieving higher burnups in LWRs. These additional safety measures could increase LWR fuel costs. Unless technology becomes available that makes the process of enrichment significantly cheaper, the cost of additional criticality safety practices will cause the cost of LWR fuel to increase in order to achieve higher burnups.

These practical limitations extend essentially to the “front-end” of the nuclear fuel cycle. This part of the commercial industry is responsible for all processes from mining the uranium from the ground through its irradiation in the reactor. This is also the sector of the commercial industry in which the private sector has the most control over electricity costs.

The “back-end” of the fuel cycle, and its associated cost, is currently the responsibility of the federal government in accordance with the Nuclear Waste Policy Act (NWPA). As required by the NWPA, the nuclear industry pays 0.1 ¢ per every kW-h of electricity produced by this fuel to the federal government as payment towards its eventual permanent disposal in a geologic repository [4]. The LWR fleet currently produces approximately 2,000 metric tons of SNF each year [5]. Assuming that no additional reactors are built, the adequacy of this levee to pay for geologic SNF disposal has been assessed as adequate by the Office of Civilian Radioactive Waste Management (OCRWM) [6]. However if new LWRs are constructed to meet rising electricity demands, then it becomes possible that several repositories will be required. This could substantially change the economic compatibility of the NWPA levee with future nuclear forecasts.

However, if the number of repositories can be limited to one, the NWPA revenue collected from the existing LWR fleet for the remainder of the lifetime of those plants will be adequate to pay the full cost of the repository [7]. The utilization of the storage space within the repository design is critical in determining its effective capacity to store radioactive wastes. The NWPA stipulates that the repository be designed to not only dispose of SNF, but also for disposing of *separated* High Level Wastes (HLW). HLW is comprised of fission product and transuranic isotopes present in SNF. It is the HLW component of SNF that represents almost the entire radioactivity produced in the nuclear fuel cycle. In actuality, roughly 90% of the SNF mass is the original uranium that was mined from the ground. Therefore, substantial improvements in repository utilization can be achieved by storing only the volume of HLW within SNF.

The cost competitiveness of this option hinges upon the economic advantage gained by separating HLW versus storing unaltered SNF. Separating transuranic and fission product

isotopes from SNF imply that technologies such as that used for nuclear fuel reprocessing are required. Reprocessing is an integral step in nuclear fuel recycling which is the process of separating the TRU isotopes from SNF to create new reactor fuel.

TRU comprises only about 1% of SNF. Additionally, TRU can be further categorized into major actinides (i.e., plutonium) and minor actinides (MA) (i.e. neptunium, americium, curium, berkelium and californium) which represent only about 10% of TRU. Therefore, it is the approximate 0.1% of the total mass of the SNF that strongly controls repository utilization. Because most of TRU is “fissile” plutonium, it is arguable that it could be recycled in LWRs. Nevertheless, it is the MAs that create the difficulties for the repository. These isotopes are much more difficult to destroy in LWRs due to the fact that they have no fissile value in the LWR’s thermal neutron spectrum.

It is because of the improved fissile value of MAs in a fast neutron spectrum that the United States has renewed its interest in SFR technology. The current Global Nuclear Energy Partnership (GNEP) program is currently investigating a symbiosis between SFRs and the SNF generated by TRU (Figure 1-1). Unlike TRU recycling in LWRs, which only recycles TRU once (limited by fissile concentration in Pu), the GNEP scenario would continuously recycle TRU in SFRs in a closed fuel cycle after the initial separation from SNF. Because the GNEP scope of the SFR is tailored for TRU destruction, it is dubbed the Advanced Burner Reactor (ABR) by this program.

An important note should be made here that the exact GNEP nomenclature refers to the ABR as a demonstration prototype for proving the technology of building a fleet of TRU burner SFRs called Advanced Recycling Reactors (ARR) [7]. However, the term “advanced recycling reactor” is to general descriptor for this dissertation. The term ABR is used regularly in recent

SFR literature to mean specifically a transuranic burning SFR design with a homogenous core configuration that excludes the use of transmutation targets or uranium blankets [7]. This definition is adopted by this dissertation.

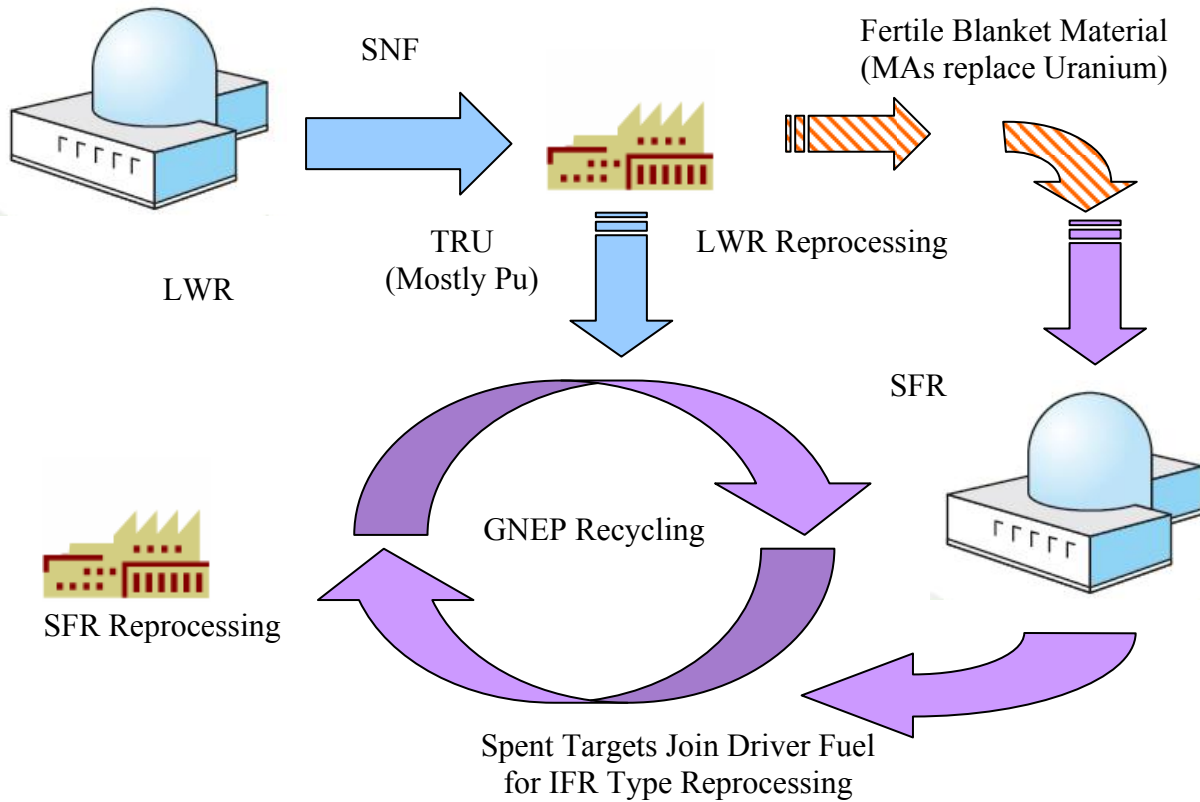


Figure 1-1. Synergy between GNEP and IFR fuel recycling strategies: .Purple represents the basic IFR closed fuel cycle scenario. Blue represents the LWR input into the IFR closed fuel cycle for the GNEP recycling scenario. The striped orange represents the replacement of fertile uranium blankets with MA transmutation targets.¹

Reprocessing, fuel fabrication and reactor irradiation in the GNEP closed fuel cycle, creates a role for the private industry to minimize the “back-end” costs by using LWR and SFR spent fuel in the “front-end”. The further extraction of fission energy from the recycled fuel

¹ The original IFR scenario would not require a constant supply of externally reprocessed SNF TRU because the SFR would create its own plutonium from the external supply of uranium. In the current GNEP scenario, the uranium blankets are removed and TRU is continuously recycled in the active core driver fuel without targets.

enhances the energy sustainability of nuclear power by making maximum use of the initial uranium mined. Currently, the GNEP fuel cycle (Figure 1-1) does not have a targeted solution for MAs. Research and development by the GNEP program has not currently revealed a conclusive decision to include MA within the closed fuel cycle because the americium in MAs is easily transmuted (even in the fast reactor) into the higher mass actinides of curium, berkelium and californium. These higher mass actinides, with relatively shorter half-lives, are highly radiotoxic and sometimes thermally hot. Additionally, these isotopes do not significantly contribute fissile worth to the SFR compared to plutonium.

If the MAs are not burned in SFRs then they must be discharged from the fuel cycle as transuranic HLW. The HLW disposal at the repository is one of the cost contributors of the closed fuel cycle that hinders economic competitiveness with the option to directly dispose of the SNF without reprocessing. However, as discussed above, it is possible to transmute plutonium isotopes from the neptunium and americium in the MAs. Approximately two-thirds of SNF MAs are Np-237 and Am-241. Therefore, it is necessary to design the SFR in such a way that is favorable to producing plutonium isotopes as opposed to the higher mass isotopes.

Closed SFR fuel cycles have been technologically demonstrated during the United States Integral Fast Reactor (IFR) program (~1984 - 1994). In the IFR scenario, the recycling of the SFR's uranium blanket and driver fuel was integrated into the same reprocessing step (Figure 1-1). It is proposed in this dissertation that the MA transmutation can be achieved by irradiating MA targets in lieu of blankets in an IFR amendment to the GNEP scenario.

Transmutation Physics

Transmutation means literally the conversion of one thing into another and is rooted in the Latin word “trans-mutare” which is “to change”. The modern definition was coined by 17th century alchemists to define the process of converting baser metals into gold. If the meaning of

transmutation is to transform one isotope into another, then transmutation is accomplished naturally by radioactive decay. It is the relatively *long* decay half-life of certain actinide and fission product isotopes that are the essence of the repository storage problem. This is because their decay heat, radiological and chemical toxicity are present for many hundreds to thousands of years. Transmutation can be accomplished artificially by adding neutrons to the long lived atomic nucleus until a less stable nucleus is created with a disproportionate neutron-to-proton ratio, which is less stable, thus having a *shortened* half-life.

There are two primary processes for converting long lived isotopes into shorter lived ones. These are successive neutron capture or fission. Neutron energy determines the extent that fission can play in the transmutation of certain actinide isotopes. This is because the fission-to-absorption ratio for MAs is dominated by the neutron flux available for absorption above the one MeV fission threshold. Generally, the reactor type and corresponding transmutation behavior can be categorized by the energy range dominated by the neutron energy spectrum. These are fast and thermal reactors.

Neutron Spectrum Influence on Transmutation Behavior

Because of the large MA neutron capture cross sections at thermal spectrum energies, thermal reactors have a high efficiency at transmuting MA isotopes by neutron capture. However, at the same time thermal reactors accumulate other actinides within the fuel cycle that are equally hazardous and long lived. A primary example of this is the transmutation of Am-241, which is the principle americium isotope in SNF (Figure 1-2). Am-241 is generated from the decay of the plutonium isotope, Pu-241, with a half-life of 14.35 years. Am-241 itself has a half-life of 432.2 years and decays by alpha particle emission. It is the kinetic energy deposition of this alpha particle in SNF, which dominates the heat generation in the repository for the first 1000 years. Am-241's well resolved thermal neutron capture cross section resonances, in the

thermal to epithermal energy range, expedites transmuting it into the shorter lived isotope Am-242. Am-242 in turn beta decays into Cm-242 with a yield fraction of 83%. Cm-242 alpha decays with a half-life of 163 days into Pu-238. Also, the other 17% of the transmuted Am-242 decays by electron capture into Pu-242 which through successive capture reactions followed by decay results in the production of Am-243 and eventually Cm-244.

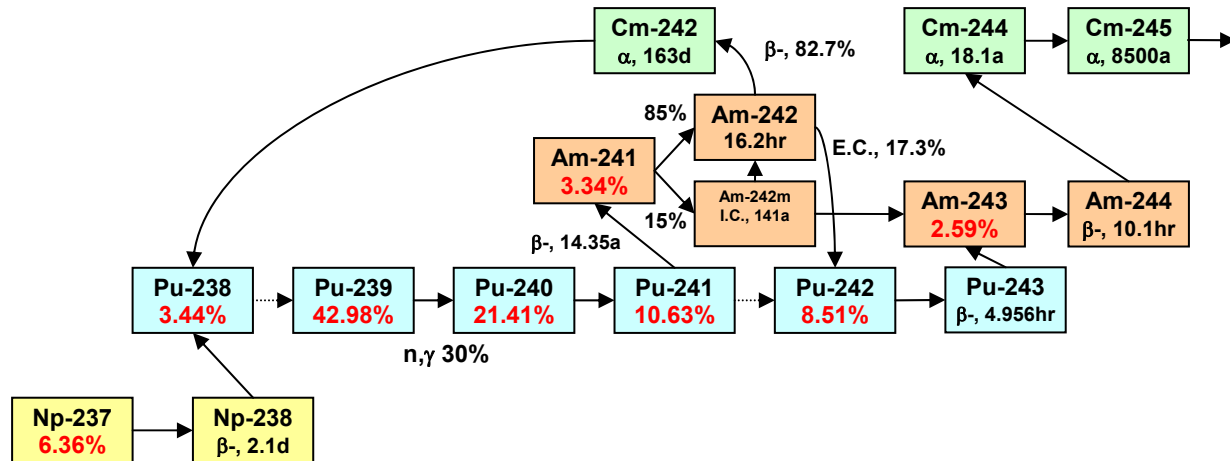


Figure 1-2. Important transmutation and subsequent decay of americium and neptunium into Pu-238, Pu-242 and curium and the higher mass actinides. The percentages shown in red are the starting concentrations of these isotopes in LWR SNF TRU.

Proposed thermal spectrum transmutation fuels such as LWR Inert Matrix Fuel (IMF) are very efficient at destroying americium isotopes by transmuting them into Pu-238 and Pu-242 but also generate Cm-244 to a large extent. Cm-244 has an 18 year alpha decay half-life that dominates the near term or first century heat generation for spent IMF. Successive neutron captures from Cm-244 causes the accumulation of higher mass curium, berkelium and californium isotopes. These isotopes have very little repository impact because their half-lives are short compared to the expected repository lifetime given in the hundreds-of-thousands of years. However, the gamma and neutron radiation fields associated with these isotopes dominate the near term radiological hazard that IMF fuel handlers would need protection from if spent IMF were recycled and re-irradiated in multiple reactor passes [8].

Alternatively, a SFR has a higher efficiency at destroying TRU isotopes by fission because a greater share of the neutron flux exists above the threshold fission energy. Essentially all of the transuranics are more fissionable in a fast rather than a thermal reactor. This means that all TRU atoms are supporting the chain reaction by contributing to fast fission. Conversely, in the thermal spectrum, the transmutation process in MAs acts as a capture sink for neutrons generated by the fissile isotopes.

The single group fission and capture cross sections for a metallic fueled SFR as well as for a representative IMF assembly are tabulated in Table 1-1 and Table 1-2 respectively. The neutron physics simulation code Monte Carlo N-Particle was used to generate the single group cross sections by tallying over all energies within the fuel region of the ABR. This code is used periodically throughout this dissertation for analysis and verification of results produced by other codes and is described in more detail in the next chapter. The SFR driver fuel is based on the ABR with a metallic alloy consisting of 30TRU/60DU/10Zr metallic alloy by weight percent. The IMF fuel is an 8 v/o weapons grade PuO₂ mixed with 2 v/o AmO₂ in a Nd₂Zr₂O₇ matrix [9].

Notice that the fission and capture cross sections are orders of magnitude less for the SFR than the IMF. It is also interesting to note that the fission-to-capture ratios for the SFR odd-Pu isotopes are only slightly greater than that for IMF. However, the fission-to-capture ratios for the SFR MAs are an order of magnitude greater than the IMF MAs. The fission-to-capture ratio is a strong indicator of whether fission or capture is the primary mode for removing an isotope from the fuel cycle.

This is especially true when the capture cross section for any given MA is comparable in magnitude to that of Pu-239. For example, the ratio of Am-241 capture to Pu-239 fission in the IMF fuel is 1.64 versus 0.83 for the SFR. This indicates that Am-241 capture is a stronger

competitor against Pu-239 fission for neutrons in the IMF case as opposed to the SFR case.

Furthermore, the ratio of total absorption in Am-241 over total absorption in Pu-239 is 1.1 for IMF versus 0.81 for the SFR.

Table 1-1. SFR fission and capture cross section data based on the Argonne National Laboratory Advanced Burner Reactor design with a conversion ratio of 0.5.

	Fission (barns)	Capture (barns)	Fission per Capture	Fission per Absorption	Capture per (Pu-239) Fission	Absorption per (Pu-239) Absorption
U-234	0.34	0.50	0.67	0.40	0.29	0.40
U-235	1.73	0.47	3.71	0.79	0.27	1.05
U-236	0.10	0.37	0.26	0.21	0.22	0.22
U-238	0.04	0.24	0.16	0.14	0.14	0.13
Np-237	0.32	1.31	0.25	0.20	0.77	0.78
Np-238	3.80	0.12	32.76	0.97	0.07	1.87
Pu-236	3.47	0.53	6.50	0.87	0.31	1.91
Pu-238	1.10	0.62	1.78	0.64	0.36	0.82
Pu-239	1.71	0.38	4.45	0.82	0.22	1.00
Pu-240	0.38	0.41	0.91	0.48	0.24	0.38
Pu-241	2.28	0.37	6.19	0.86	0.22	1.27
Pu-242	0.26	0.36	0.73	0.42	0.21	0.30
Am-241	0.27	1.42	0.19	0.16	0.83	0.81
Am-242 ^m	3.55	0.31	11.51	0.92	0.18	1.84
Am-243	0.20	1.27	0.15	0.13	0.74	0.70
Cm-242	0.16	0.25	0.63	0.39	0.15	0.19
Cm-243	2.37	0.20	12.14	0.92	0.11	1.23
Cm-244	0.42	0.72	0.58	0.37	0.42	0.55
Cm-245	2.14	0.27	7.87	0.89	0.16	1.15
Cm-246	0.26	0.19	1.36	0.58	0.11	0.22
Cm-247	1.93	0.27	7.12	0.88	0.16	1.05
Cm-248	0.30	0.20	1.52	0.60	0.12	0.24
Bk-249	0.16	1.09	0.15	0.13	0.64	0.60
Cf-249	2.43	0.58	4.16	0.81	0.34	1.44
Cf-250	1.15	0.33	3.52	0.78	0.19	0.71
Cf-251	2.21	0.27	8.22	0.89	0.16	1.19
Cf-252	0.63	0.25	2.49	0.71	0.15	0.42
Combined	0.05	0.06	0.85	0.46	0.03	0.05

Considering these two facts, americium is a stronger competitor against Pu-239 for neutrons in the IMF case as opposed to the SFR. Therefore, the thermal spectrum allows more neutrons to be absorbed into americium rather than plutonium because the thermal americium capture cross section is larger than the plutonium fission cross section. A higher absorption rate

facilitates greater removal from the fuel cycle and in the case of IMF is caused by neutron capture reactions rather than fission.

Table 1-2. IMF fission and capture cross section data based on a typical 17x17 ressurized Water Reactor fuel assembly design fueled with a TRU-O₂/Nd₂O₂ZrO₇ Matrix.

	Fission (barns)	Capture (barns)	Fission per Capture	Fission per Absorption	Capture per (Pu-239) Fission	Absorption per (Pu-239) Absorption
U-234	0.62	19.09	0.03	0.03	0.99	0.67
U-235	12.55	4.84	2.59	0.72	0.25	0.59
U-236	0.36	7.68	0.05	0.05	0.40	0.27
U-238	0.13	8.16	0.02	0.02	0.42	0.28
Np-237	0.64	19.99	0.03	0.03	1.04	0.70
Np-238	54.01	2.29	23.63	0.96	0.12	1.91
Pu-236	30.31	8.33	3.64	0.78	0.43	1.31
Pu-238	1.87	8.39	0.22	0.18	0.44	0.35
Pu-239	19.23	10.27	1.87	0.65	0.53	1.00
Pu-240	0.70	49.27	0.01	0.01	2.56	1.69
Pu-241	28.05	8.74	3.21	0.76	0.45	1.25
Pu-242	0.54	33.07	0.02	0.02	1.72	1.14
Am-241	0.82	31.54	0.03	0.03	1.64	1.10
Am-242 ^m	127.14	23.68	5.37	0.84	1.23	5.11
Am-243	0.54	40.02	0.01	0.01	2.08	1.37
Cm-242	0.48	3.57	0.13	0.12	0.19	0.14
Cm-243	55.59	6.85	8.12	0.89	0.36	2.12
Cm-244	1.04	13.16	0.08	0.07	0.68	0.48
Cm-245	36.23	4.89	7.41	0.88	0.25	1.39
Cm-246	0.71	2.17	0.33	0.25	0.11	0.10
Cm-247	16.50	10.29	1.60	0.62	0.54	0.91
Cm-248	0.90	7.36	0.12	0.11	0.38	0.28
Bk-249	0.85	71.05	0.01	0.01	3.69	2.44
Cf-249	60.43	15.13	3.99	0.80	0.79	2.56
Cf-250	1.12	208.03	0.01	0.01	10.82	7.09
Cf-251	140.51	54.98	2.56	0.72	2.86	6.63
Cf-252	4.59	1.66	2.77	0.73	0.09	0.21
Combined	0.44	0.58	0.76	0.43	0.03	0.03

Transmutation and Nuclear Stability

The actinide cross sections in the SFR neutron energy spectrum are almost completely in the *unresolved* resonance range. Therefore, the *resolved* resonance cross section of one isotope self-shielding the reaction rate of another does not play a significant role. Hence, the ratio of plutonium versus americium fission is more related to the number density of each isotope and the percent of neutrons above the threshold energy. In fact, the magnitude of the fission-to-

absorption ratio in the epithermal to fast energy range is strongly tied to the relative magnitudes of the unresolved capture cross section below and the fission cross section above the one MeV threshold. For example, the capture cross section for Am-241, Am-243 and Cm-244 are at least two orders of magnitudes greater than fission at energies between one keV and one MeV (Figure 1-3). In addition, the magnitude of the capture cross sections is roughly the same as that for the Pu-239 fission cross section. If the neutron spectrum for the target is made epithermal, a greater americium destruction rate can be achieved by the neutron capture mechanism below the one MeV threshold. A softer spectrum would enhance the neutron capture importance relative to fission in the competition for neutrons in this energy range. The general increase in the total absorption probability shifts the competition in favor of the fertile MA isotopes.

As discussed in the previous section, removing MAs by neutron capture transmutes them into higher mass actinides. However, similar to IMF, the transmutation of Am-241 into Am-242 is followed by a decay path into curium and eventually plutonium. A similar transmutation behavior is exhibited by Am-243. Am-243 is transmuted by neutron capture into Am-244 which in turn beta decays into Cm-244 with a half-life of 10.1 hours. Cm-244 decays by alpha particle emission with an 18.1 year half-life into the even plutonium isotope Pu-240.

As identified earlier, Am-241 has a long half-life and has a fission threshold of one MeV. Transmuting Am-241 produces the fissile Am-242,242^m atom. By fissile, it is meant that virtually zero kinetic energy is required to overcome the energy barrier for fission to occur. This fissile characteristic is exhibited by essentially all actinides with an odd neutron number.

Eighty-five percent of this transmuted Am-242 is the ground state which is not long lived enough to be used as fuel in the reactor [10,11]. Am-242's primary daughter by beta emission is Cm-242 whose short lived alpha decay results in Pu-238 (Figure 1-3). This Pu-238 has a larger

fission-to-capture ratio in the fast spectrum than the starting Am-241. However, Pu-238 is not truly fissile because some kinetic energy is required to cause it to fission. But, the amount of added kinetic energy needed for Pu-238 to fission is much less than that needed for Am-241. This explains why the Pu-238 fission cross section is so much higher than Am-241 at energies below one MeV. In addition to being more fissionable than the starting Am-241, Pu-238 is only one neutron capture away from becoming the long lived Pu-239 atom which is fissile.

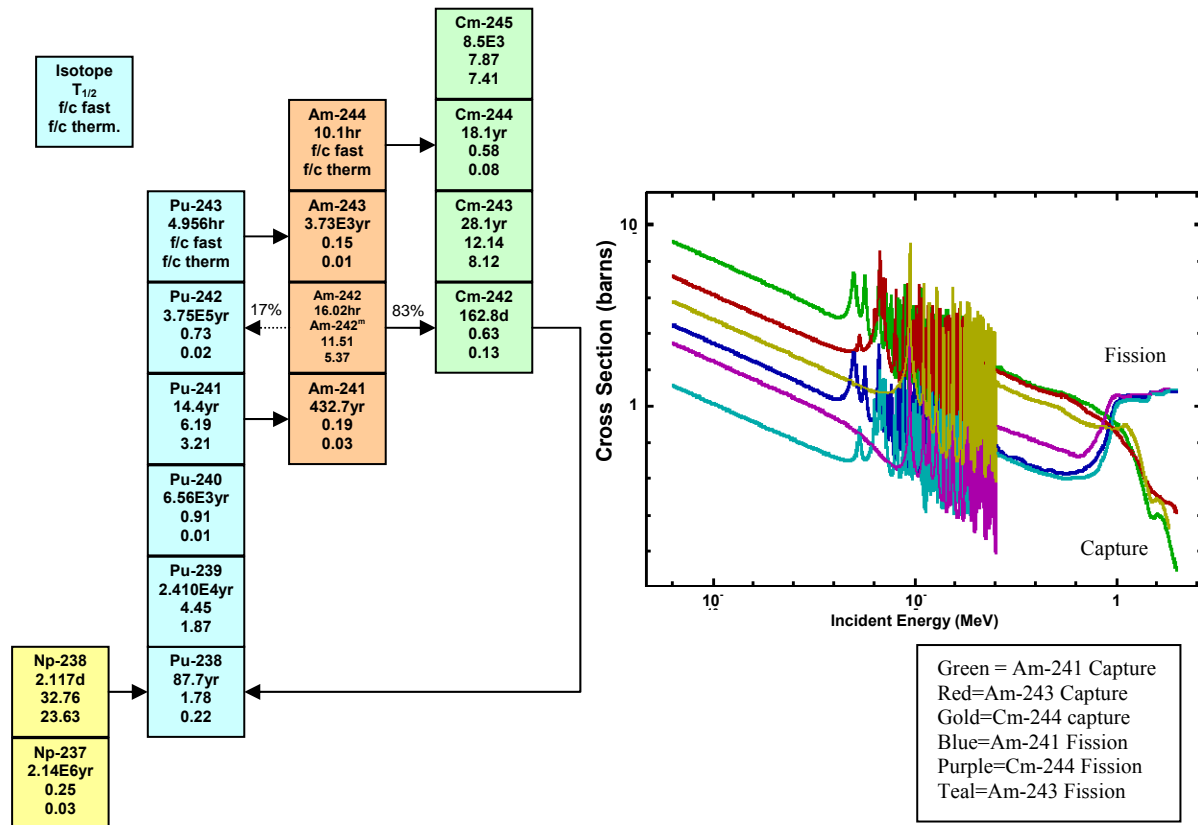


Figure 1-3. Periodic relationship between fissile and fertile transuranic isotopes

This circular behavior is also exhibited by Am-243 (Figure 1-3). The long-lived Am-243 nucleus is transmuted into Am-244 (fissile) which decays by beta emission into Cm-244. This Cm-244 has a short half-life compared to the starting Am-243. Its 18.1 year half-life alpha decay produces Pu-240 which is more fissionable (but not truly fissile) than the starting Am-243 and is only one neutron capture away from the fissile Pu-241 which is fissile.

Isotopic Aspects of Repository Impacts

For this dissertation work the motivation behind transmutation of Am-241 (and Np-237) is rooted in the site selection and design constraints of the proposed repository site at Yucca Mountain in Nevada. Yucca Mountain is a ridge line located in the desert region of Amargosa Valley approximately 90 miles from the city of Las Vegas. The mountain ridge is formed by layers of volcanic rock called “tuff”. This rock was deposited by falling ash from successive eruptions of nearby super-volcanoes many millions of years ago. These volcanoes are now extinct.

The heat generation rate produced by the alpha decay by Am-241 is the main governing parameter that determines the separation distance between drifts. The drift spacing is determined by the thermal heat rate produced by the SNF waste packages. The spacing between drifts is the minimum separation needed to keep the mid-drift rock temperature beneath the boiling point of water (96°C) at the elevation of the Yucca Mountain repository site [12]. The reason for the prevention of complete “dry-out” between drifts is to ensure that rain water, which is transported via fractures in the tuff layers, is allowed to flow freely through the repository to the water table below it.

The second heat generation limit is the drift tunnel wall surface temperature. The drift wall surface temperature limit is established to be below 200°C to prevent crystalline alteration of the rock. Wigeland et al indicated that this limit is not strongly influenced by the presence of Am-241 but rather from the barium and yttrium decay products of the cesium and strontium fission products [13]. Cs-137 ($T_{1/2}=30.07$) and Sr-90 ($T_{1/2}=28.78$) both have half-lives less than 100 years. Therefore, similar to Wigeland, it is assumed for this work that these isotopes could be separated and diverted from repository storage during the fuel cycle [13]. Figure 1-4 shows the decay heat contribution for the principal heat generating SNF isotopes.

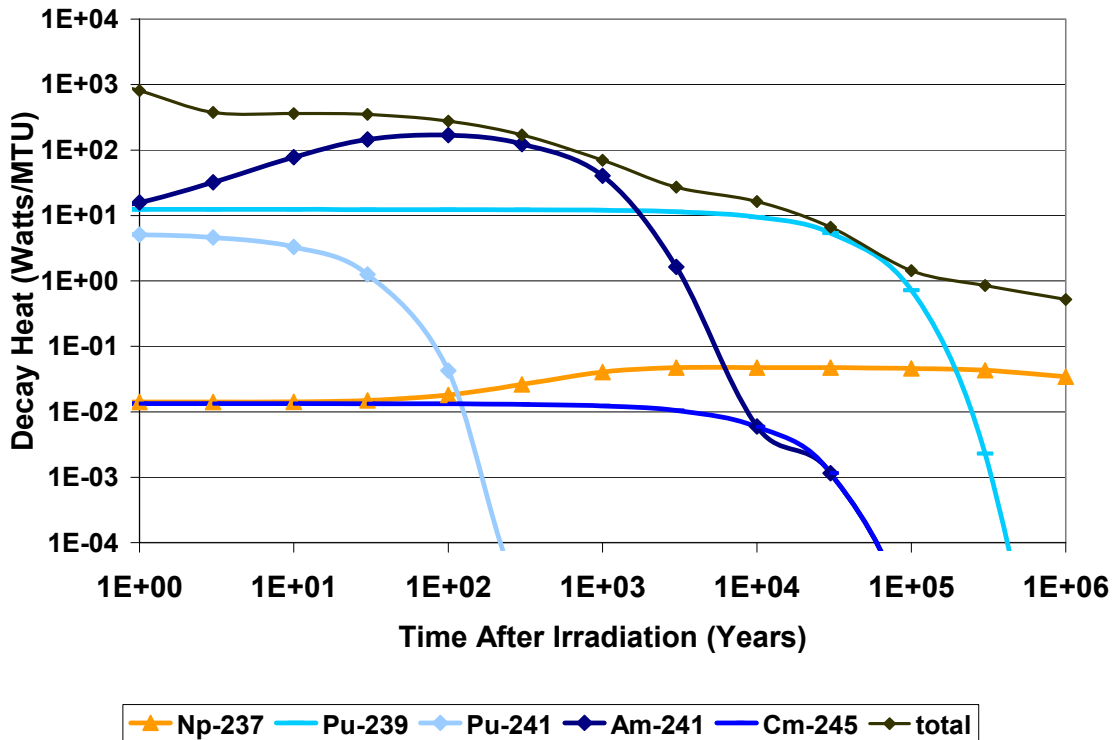


Figure 1-4. Decay heat plot for pressurized water reactor SNF (5 w/o starting enrichment and 45 MWD/kg discharge burnup)

There is a third repository design consideration. Because of its long half-life, radiotoxicity, high solubility and low sorption in Yucca Mountain tuffs, Np-237 is the principle environmental concern to the biosphere if water does come into contact with the SNF [12]. The natural and engineered waste package barriers are designed to minimize the likelihood that water may contact Np-237 for at least 10,000 years. The other soluble SNF isotopes of interest are: Tc-99, I-129 and U-234. However, the radiation doses from these isotopes are not expected to be as significant as from Np-237. This is principally due to the fact that Np-237 is the alpha decay product of Am-241. Therefore, Am-241 destruction in the SFR is not only important to the emplacement drift spacing but also important for controlling the Np-237 accumulation in the repository.

Three repository design benefits are sought for SNF isotope transmutation within the heterogeneous SFR design evaluated in this dissertation. The first is the removal of Am-241 by

neutron capture in a heterogeneous target. The second is the removal of Np-237 by neutron capture and fission within the driver fuel. Also, Tc-99 is evaluated as a control rod neutron poison for reactor performance purposes with the added benefit that this isotope is not sent to the repository.

Background on Previously Proposed TRU Burning SFRs

The net TRU destruction of the SFR increases for decreasing conversion ratio. The conversion ratio is commonly defined in fuel cycle terms as the ratio of the TRU production rate divided by the TRU destruction rate averaged over the reactor and irradiation cycle. The most straight forward way to decrease the conversion is by decreasing the parasitic capture of neutrons in U-238. This prevents the breeding of Pu-239 by transmutation from U-238. Decreasing parasitic capture can be done by simply removing uranium from the fuel. It can also be achieved by shifting the neutron balance between parasitic capture and neutron losses by leakage.

Generally, for low conversion ratio SFRs with high MA loaded fuels, there is a tradeoff between the optimal Doppler and void coefficients and the attainable TRU destruction efficiency. The two most basic SFR reactivity feedback mechanisms are the Doppler feedback provided by U-238 in the fuel and blankets; and the increase in axial and radial neutron streaming that occurs during coolant voiding. The tradeoff stems from the fact that the mechanisms commonly used to remove neutrons from the reactor during transients also remove them in steady state operation. For example, enhancing axial streaming with a pancake geometry or a reduced fuel pin diameter (large sodium fraction) makes the void coefficient more negative. But, the increased overall leakage reduces the available excess reactivity. Alternatively, increasing U-238 increases resonance capture and makes the Doppler coefficient more negative. However, this produces further TRU from captures in the same resonances that provide the beneficial feedback. In both cases, more fissile plutonium is required to compensate for

reactivity lost by the modifying strategy. The added plutonium and lack of fertile material increases the rate that the reactor loses reactivity as a function of the burnup of the TRU.

During coolant voiding, the lack of neutron down scattering in sodium causes the neutron spectrum to harden. This hardening causes an increase in the fission-to-capture ratios and hence an increase in multiplication [14]. SFR designs typically do *not* have a passive sodium void negative reactivity feedback. In case of a sodium density reduction, passive negative reactivity feedback is normally achieved by thermal expansion of the fuel. Engineered and inherent negative leakage reactivity feedback mechanisms will be explained in a later discussion on SFR reactor control.

Most SFR designs are fairly insensitive to changes in the sodium density. However, the spectrum hardening effect, caused by a complete void of sodium coolant, is more pronounced for higher MA loadings. The increase in void worth is because more neutrons are absorbed at energies greater than the threshold fission energy which causes an increased multiplication feedback. Past parametric studies in the literature showed that the void coefficient increased too much when the MA content exceeded roughly 10% (MA per mass of HM) [15]. This is because the multiplication increase given by Np-237 and Am-241 creates more neutrons than the Doppler broadening feedback from U-238 can absorb. In some instances the constraint on MA density is as low as 5% or 2.5% such as the Consommation Améliorée du Plutonium dans les Réacteurs Avancés (CAPRA) type core [16,17].

Because the MA loading (in the fuel) is limited by a void coefficient constraint, the attainable MA destruction rate for that design suffers. Several pathways to optimize total TRU destruction, and hence MA destruction, while maintaining acceptable reactivity coefficients and reactivity swing have been considered. First and most importantly, the rate of total TRU

destruction by fission is fixed by the fission reaction rate of the core. This occurs because the rate at which the overall mass is destroyed by fission is fixed by the power rating of the reactor. On average, the amount of energy produced by one megawatt of power produced in one day “Megawatt-day” (MWD) requires approximately one gram of HM to undergo fission.

Therefore, reducing the TRU generation is the only possibility for maximizing the *net* TRU destruction, which can only be reduced by eliminating Pu-239 creation from U-238. Enhanced leakage is accomplished by altering the geometric buckling. Axial buckling can be increased by reducing the core height with respect to its diameter giving a configuration known as a “pancake” core. Parasitic neutron capture is increased by the addition of an alternate resonance absorber. This raises the unique possibility of using fission products such as Tc-99 as an alternate epithermal absorber for replacing U-238, thus reducing the conversion ratio.

In any case, the reduced “poorer” neutron population in the core caused by these modifying strategies ultimately results, in most cases, a higher fissile loading to compensate for neutron losses. Therefore, the burnup reactivity swing increases as a result or the refueling cycle length being reduced. The first option has the drawback of requiring an unrealistic control rod worth to manage the excess reactivity. The second option has the drawback of limiting the irradiation time allotted for burning MAs. This second option is important because the probability for absorption in the MA is much less than that for plutonium (Table 1-1), even in the fast spectrum, meaning that more neutrons are being consumed to fission plutonium in the fuel instead of transmuting MA in the fuel.

The Advanced Burner Reactor Design Concept

The ABR fuel, core internals, and power plant are essentially identical to the Advanced Liquid Metal Reactor (ALMR) and Super Power Reactor Innovative Small Module (S-PRISM) designs that were produced during the IFR program [7,18,19]. In order to achieve a low

conversion ratio, the ABR draws upon several of the modifications discussed above. First, to reduce parasitic capture in U-238, the internal rows of uranium blankets were removed from the S-PRISM design (Figure 1-5).

These blankets were an integral component to the plutonium self-sustainability of the IFR fuel cycle but are now contradictory to the TRU burning philosophy of the ABR. Second, the ABR core height-to-diameter ratio is only 0.5 to enhance axial buckling. Typically, in the absence of internal rows of blankets, the active core (driver fuel only) of a SFR breeder would need a height-to-diameter ratio closer to unity [14].

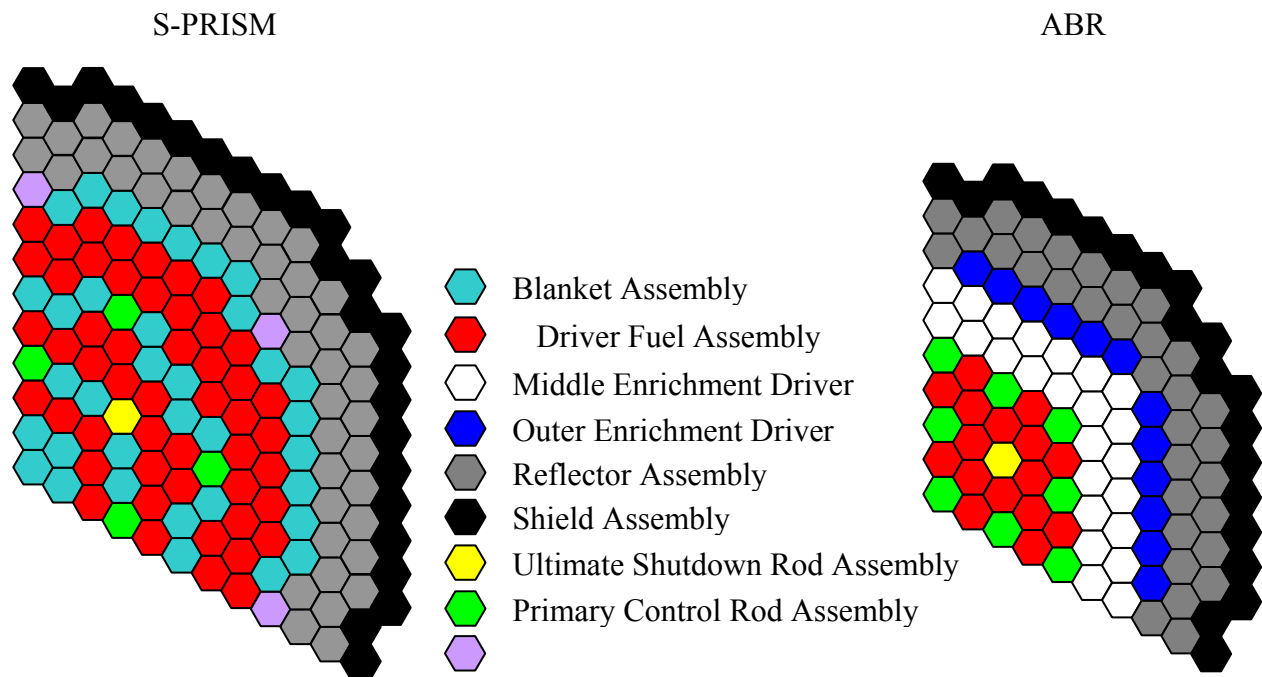


Figure 1-5. Core layouts for the S-PRISM and ABR designs²

² The ABR uses the same driver fuel assembly design throughout the core but with different TRU enrichments for Inner, Middle and Outer core regions. The three different “enrichment zones” are necessary for radial power profile flattening. The reflector and shield are both dummy assemblies filled with steel rods to reflect some of the neutrons back into the core and also to protect the reactor vessel from neutron damage by fast neutrons. Some variations of the shield include neutron absorbing material. The Gas Expansion Module is a special reflector assembly designed to provide negative reactivity feedback by increasing leakage in the event of loss of coolant flow

Parametric studies performed by Morris et al showed that further reductions in height (from one meter) do not yield significant reductions in conversion ratio [20]. Therefore, the ABR core height is the same as the one meter height of the S-PRISM. However, the removal of the blankets allowed the radius to be reduced from 2.7 to 2.2 meters. Finally, the ABR fuel pin pitch-to-diameter ratio was reduced from that of the S-PRISM. This had the attribute of adding more sodium volume to the core which also allows for more neutrons to stream out of the core. The volume of uranium in the pin was reduced in step with the reduction in fuel pin volume. Hence, the loading of TRU is roughly kept constant across the S-PRISM and ABR designs but the volume of uranium is decreased. This had the effect of increasing the fuel concentration of TRU per total HM in the core, also known as the *TRU enrichment*. The increase in TRU enrichment dictates a significantly different fuel assembly design in terms of fuel pin diameter, pin spacers, etc. than the S-PRISM. The fuel assembly and pin dimensions of the S-PRISM and the ABR reference core design used for comparisons in this dissertation are given in Table 1-3.

As stated by Hoffman et al, the reduction in pin diameter and the corresponding increase in TRU enrichment cause the fuel excess reactivity to increase and the irradiation cycle length to decrease [7]. Because, of cycle length reduction, large excess reactivity and large enrichment, the ABR has a correspondingly different refueling interval, control rod worth requirement and fuel composition from the current experience database based on past SFR experience.

Transmutation Target Designs: Radial Blankets and Moderated Targets

The principal drawback of having an enhanced leakage SFR core design, such as the ABR, is that the reactor purposely wastes neutrons through leakage instead of re-investing them in the fuel. This is contrary to previous plutonium breeders, which used uranium blankets to recover the neutrons leaked from the active driver core.

Table 1-3. Fuel assembly and pin dimensions for the S-PRISM and ABR designs

Fuel Type	S-PRISM Driver	S-PRISM Blanket	Ref. ABR (CR=0.5)*
Approximate core conversion ratio		1.00	0.50
Fuel type	Metal	Metal	Metal
Fuel alloy composition	Pu/U/10-Zr	U/10-Zr	TRU/U/20-Zr
TRU Enrichment (%)	20	0	35
Assembly pitch, cm	16.142	16.142	16.142
Inter-assembly gap, cm	0.432	0.432	0.432
Duct outside flat-to-flat, cm	15.710	15.710	15.710
Duct material	HT-9 Steel	HT-9 Steel	HT-9 Steel
Duct thickness, cm	0.394	0.394	0.394
Pins per assembly	271	127	324 (7 support)
Fuel pin spacer mechanism	Helical wire wrap	Helical wire wrap	Grid
Spacer wire wrap diameter, cm	0.142	0.094	n/a
Bond material in cladding gap	Na	Na	Na
Overall fuel pin length, cm	407.040	407.040	407.040
Top - fission gas plenum height, cm	191.140	191.140	191.140
Middle - Active fuel “core” height, cm	101.600	101.600	101.600
Bottom - Axial reflector height, cm	114.300	114.300	114.300
Fuel smeared/ fabrication density, % TD	75/100	85/100	75/100
Pin outer diameter, cm	0.744	1.201	0.6230
Cladding thickness, cm	0.0559	0.0559	0.0559
Pin pitch-to-diameter ratio	1.191	1.078	1.293

*The ABR reference design is currently not yet a finalized point design in the SFR community. The pin diameter, spacer type, fuel composition, etc. vary depending on the desired conversion ratio of the reactor design [7].

In general, the long mean-free-path of fast neutrons causes SFRs to have a high neutron escape probability. In fact, the active driver fueled region of most plutonium breeders purposely had a high leakage. However, the high leakage was created only to maximize the amount of neutrons invested in the uranium blankets. Therefore, the overall leakage, including the blankets, would be less than the active core by itself. The use of the blankets increases the overall utilization of neutrons to produce new fuel in the SFR fuel cycle.

Remembering back to Table 1-1 and Table 1-2, though the fission-to-absorption ratio of the even neutron number MAs (i.e., Am-241, Am-243, Cm-244) are greater in the fast spectrum than in the thermal spectrum, they are still much less than that of the plutonium isotopes. In fact, the fast spectrum fission-to-absorption ratio of most of these MAs is actually closer to that of U-

238. Considering that the transmutation path of most of the MAs leads directly to much more fissionable material (i.e., Pu-238, Pu-242 and Cm-245) within one to two-neutron captures, it is possible that they could be a suitable fertile material for replacing the uranium in the blankets.

This heterogeneous approach has been proposed by previous authors studying fuel cycles similar to that of the ABR. Buiron et al studied wrapping a radial external blanket of *un-moderated* target assemblies around the active core region of the European Fast Reactor (EFR) [21]. Similarly, Fujimura et al and Sanda et al proposed a SFR core where *moderated* target assemblies containing neptunium and americium were scattered throughout the active core and also in a radial blanket surrounding the active core of the Self-Consistent Nuclear Energy System (SCNES) [22,23,24].

The moderation was provided by a U/MA/Zr/H dispersion matrix. These target assemblies were first heterogeneously scattered throughout the center core region and eventually shuffled to the first row of the radial reflector. The shuffling was done to ensure that the plutonium atoms generated from neptunium and americium transmutation did not create an unacceptable power peak at the end of the one year irradiation. This study demonstrated that the overall destruction efficiency is enhanced by including moderation to the target design. It also demonstrated a fuel cycle scenario where the transmuted plutonium from the targets was recycled into the driver assemblies. Similar results were observed separately by Eliseev et al and Rome et al. Eliseev et al proposed a target assembly having the outer two rows of the assembly comprised of neptunium and americium target pins with all inside rows being moderator rods filled with zirconium hydride [25]. Rome et al also proposed a heterogeneous target assembly where the moderating rods and transmutation target rods were equally distributed throughout the assembly [26,27].

A table of most relevant transmutation target design studies is offered in Table 1-4. The transmutation target design proposed in this work is a hybrid compilation of:

- Transmutation targets located on the top axial top core periphery to have a close proximity of the target and active core regions for flux sharing
- A heterogeneous lattice of MA pins and zirconium hydride moderating pins to take advantage of existing metal fuel technology for the target transmutation matrix
- A slight uranium content in the MA axial blanket/target region of the core (i.e., in the MA loaded pins) for minimizing power swing in the targets during irradiation

In all of the radial heterogeneous core designs with target assemblies, the moderating effect of neutrons leaving the target and entering the driver fuel assembly caused localized power peaking in the neighboring fuel pins. To compensate, all the moderated target assembly designs, found in the literature, used a thermal neutron filter that encompassed the target assembly to ensure that thermal neutrons did not leave the target. The filter used by Fujimura et al replaced the peripheral ring of rods within the target assembly with Tc-99 bearing rods. Eliseev et al used a cadmium laced fuel assembly shroud as the thermal filter.

Table 1-4. Summary of relative studies on transmutation target assembly: matrix compositions and moderating strategies

Author	Reactor Type	Target Location	Target Composition	Moderator	Reference
Buiron et al	EFR	Outer radial blanket	MA-O2/UOX	n/a	21
Fujimura et al	SCNES	Both active core and radial blanket	U/MA/Zr/H	Hydride Matrix	22,23,24
Sanda et al	SCNES	Both active core and radial blanket	U/MA/Zr/H	Hydride Matrix	28
Eliseev et al	BN-800	Outer core	MA-O2 “rock-like”	ZrH ₂ Pins	25
Rome et al	EFR	Internal and outer radial blankets	MA-O2	CaH ₂ or ZrH ₂ Pins	26,27

Transmutation Target Designs: Axial Blankets and Axial Targets

The issue of localized power peaking may be avoided altogether by taking advantage of the large spatial gradient typical of most SFR radial and axial power profiles. A large flux and power profile gradient is typical of most SFR core designs because of the large geometric

buckling caused by high leakage. Given that the power on the periphery is significantly less than the peak power at the core's axial and radial center, localized power peaking from moderation can actually be favorable as a means to flatten the power profile across the core. In fact, Rome et al found that the issue of power peaking was minimized when the moderated targets were placed exclusively on the core periphery and not in the core center. In this work a moderated axial target/blanket is proposed for capturing the neutrons leaked from the active core. As it will be shown in Chapter 3, the affect of this moderation actually decreases the axial power gradient in the target region.

Axial blankets are actually not a new concept in SFR design. Table 1-5 gives a list of examples of past reactor cores that incorporated axial blankets into their designs [29]. Axial target designs are also not a completely foreign concept for transmutation purposes. Kuraishi et al and Arie et al proposed replacing radial and axial blankets with fission product targets [30,31].

Table 1-5. Examples of real fast reactor plants where axial blankets have been incorporated into the SFR core design

Reactor	Location
EBR-I (United States)	Above and Below
EBR-II (United States)	Above
FERMI (United States)	Above and Below
Clinch River (United States)	Above and Below
JOYO (Japan)	Above and Below
MONJU (Japan)	Above and Below
Dounrey (Great Britain)	Above and Below
Rapsodie (France)	Below
Phenix (France)	Above and Below
Super-Phenix (France)	Above and Below
BN-350/600/800 (Russia)	Above and Below

Transmutation Based Reactivity Control Concept

Due to the fast neutron's long mean-free-path, spatial heterogeneities on the dimensional level of a fuel pin virtually have zero impact on the local neutron flux. Therefore, the major geometry features of SFR are on the dimensional level of the fuel assembly. The fuel

enrichment zoning in the ABR is possible due to this “smearing” effect. This smearing effect over the fuel assembly is also why the SFR has whole “primary control” and “ultimate shutdown control” assemblies as shown in Figure 1-5. This smearing principle of neutron absorbers in a SFR makes introduction of burnable poison materials problematic unless they can be implemented in standalone fuel assembly structures.

Kim et al explored the homogeneous pin distribution and heterogeneous assembly distribution of burnable poisons in the Korean Advanced Liquid Metal Cooled Reactor (KALIMER) [32]. The burnable poison used was boron carbide (B_4C) which was enriched to 90 w/o in the highly absorbing B-10 isotope. The purpose of the KALIMER study was not only to determine the B_4C 's potential excess reactivity suppression benefit, but also to determine the affect that the neutron poison would have on the void and Doppler feedback.

The first case studied by Kim was a homogeneous loading where 30 of the 271 fuel pins were replaced with burnable poison rods. The second case was a parametric study to determine the optimal location for burnable poison assemblies instead of homogeneously placed rods. Homogeneous and heterogeneous burnable poison options were compared to a non-poisoned base case. It was found that the homogeneous case actually made the sodium void worth more positive than the base case. This is because the U-238 fast fission contribution increases in the harder spectrum attained during voiding. The sodium void worth increases because the thermal (resonance) absorption cross sections of B-10 (and also the actinides) are significantly greater than U-238. Therefore, the neutron spectrum becomes harder during voiding. Thus, undesirable fast fission neutron multiplication surpasses the desirable neutron consumption by parasitic capture. The heterogeneous loadings had the opposite effect because the burnable poison assembly is closer in physical dimensions to the fast neutron mean-free-path. Since the burnable

poison becomes more visible to fast neutrons, the achievement of lower sodium void worth is primarily owing to the parasitic capture in the burnable poison assembly. However, just as in most “typical” SFR designs the void coefficient was still positive.

This concept of burnable control assemblies is applied to the primary control assembly design discussed in Chapter 4. However, the fission product technetium (Tc-99) is used instead of B₄C. Metallic Tc-99 is chosen as for reactivity control shim because:

- The atom density of Tc-99 is higher than that of B-10 in enriched-B₄C.
- Tc-99 has an unresolved cross section structure in the fast neutron energy range similar to U-238 making it suitable for a *gray* absorber rod in a SFR.
- The combination of long fast neutron mean-free-path with the gray absorbing Tc-99 in *discrete* primary control assemblies is ideal for reactivity shim control.
- The magnitude of the Tc-99 unresolved cross section resonances falls off sharply at energies above one MeV which could promote the *above-threshold* fission of MAs.
- Transmuting Tc-99 reduces the amount of this radiotoxic and long lived SNF (or HLW) isotope that would otherwise be destined for the Yucca Mountain repository.

Messaoudi et al investigated burning Tc-99 as a potential replacement for all of the U-238 in the CAPRA core design [33]. The CAPRA design achieved a low conversion ratio by replacing fuel pins from the driver fuel assemblies with dummy “dilution” pins of stainless steel (or Tc-99 as proposed by Messaoudi et al). Without changing the loading of TRU in the CAPRA core, the dilution rods displaced uranium from the core. This strategy was similar to what was done for the ABR but without changing the fuel pin diameters.

However, in the Messaoudi et al CAPRA design all U-238 was displaced from the core and was replaced by Tc-99 as a potential resolved capture resonance surrogate. It is important to note that Tc-99 has some resolved and unresolved resonances similar to U-238 (Figure 1-6). Messaoudi et al first loaded Tc-99 homogeneously in all fuel pins. It was found that this homogeneous loading increased the void coefficient compared to the base case with U-238

present. Similar to the results achieved by Kim et al, the increase was explained by the fast fission multiplication feedback becoming greater than the compensation of the Doppler broadening feedback. Unlike Kim et al, Messaoudi et al chose not to concentrate the Tc-99 in specialized standalone assemblies. Instead, a calcium hydride moderator was placed in dilution pins of discrete fuel assembly locations throughout the core. For the CAPRA design these dilution assemblies comprised every third row of fuel assemblies in the core. The moderation allowed more neutrons to be down-scattered to lower energies where the Tc-99 resolved resonances could have more effect which reduced the magnitude of the positive void coefficient.

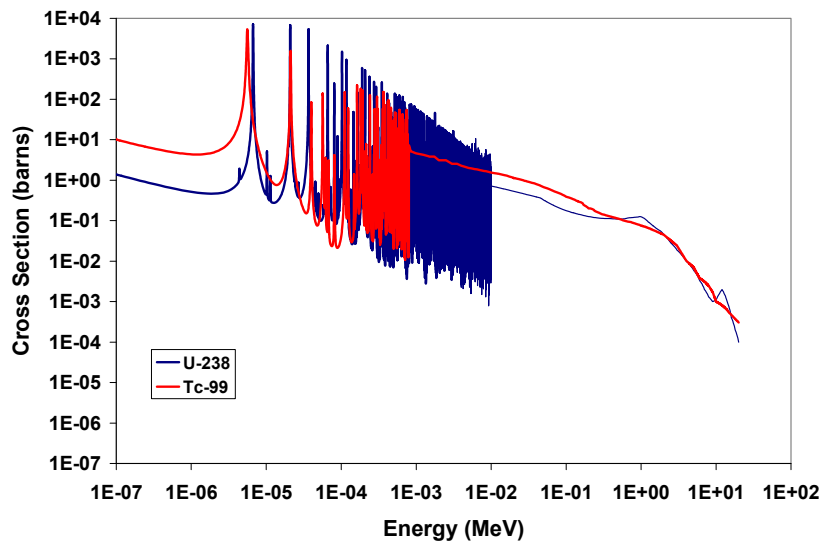


Figure 1-6. ENDF-VI plot of U-238 (blue) and Tc-99 (red) total absorption cross sections

Design Rationale of an Axial Heterogeneous Fast Transmutation Reactor

Because the SFR's resonance feedback is highly dependent on the presence of sodium, it is important to have a design that can compensate with alternative neutron sinks during the event of a loss-of-coolant-accident (LOCA). The large mean-free-path of fast neutrons allows feedback by neutron streaming as a common solution to this problem in many SFR designs.

However, designing core geometry for high streaming neutron losses during LOCA's also requires a high neutron leakage during steady-state operation. Therefore, implementing axial

targets will have a dual role: (1) MA conversion into more fissionable plutonium isotopes, and (2) recovering the axial leakage lost by the active core during steady-state operation.

Compensation for Inherent Positive Void Reactivity Feedback

It was discovered in the operational experience of the Experimental Breeder Reactor – I (EBR-I) that the SFR core's reactivity was highly sensitive to core geometry. During overpower tests, the EBR-I exhibited oscillatory power characteristics and periods of prompt positive (increasing with increasing power) reactivity feedback. Operating the reactor in order to quantify these prompt reactivity feedbacks caused a partial meltdown of the EBR-I Core-II fuel. It was later found that the positive power coefficient was due to thermal-mechanical bowing of the fuel pins towards the core center. The bowing was caused by axial and lateral temperature differentials across the fuel tubes. The inward bowing made the reactor more compact thus causing the reactivity increase [34]. The positive power feedback was resolved in the Experimental Breeder Reactor – II (EBR-II) by removal of the upper grid plate [35]. The lack of a lateral constraint at the top of the core allowed the fuel to bow outwards, instead of inwards, under thermal gradients. The increase in outward bowing with increasing temperature thus enhanced neutron streaming. Hence, the bowing and subsequent enhancement in neutron losses during a LOCA provided an inherent negative reactivity feedback which was demonstrated in tests performed at EBR-II.

The inclusion or concentration of MAs in the central region of the core can actually increase the positive void feedback. Compared to U-238, most MAs do not possess resolved resonances at energies high enough in the SFR fast flux spectrum to provide useful amounts of negative reactivity feedback. Also, because the fast flux energy spectrum becomes harder during a LOCA, the above-threshold multiplication contribution from MAs further complicates and increases the positive reactivity void feedback by the fuel.

The positive reactivity feedback by the MAs creates a need to further enhance the negative streaming feedback of the core design. Finding a core geometry that possesses an enhanced leakage property during a LOCA without removing too much reactivity from the core during steady-state operation is essentially the Holy Grail of SFR design. Traditionally, flattening the core height-to-diameter ratio into a “pancake” geometry has been the most straightforward route for achieving this higher leakage. Remember back to the previous discussion on core geometry modifications for attaining a TRU burner, a pancake geometry has also been proposed for achieving a “very low” conversion ratio. However, as discussed earlier, the high leakage necessitates a high TRU enrichment and a shortened cycle length [36]. Therefore, there is a practical limit on how flat the pancake core can be made.

In this work, a hybrid pancake core design is sought that *slightly* reduces the height of the ABR design while preserving the volume of its active core. The flatter core design:

- Enhances neutron losses during a LOCA compared to a taller core
- Reduces the conversion ratio of the active core compared to the ABR
- Invests the neutron leakage from the active core during steady-state operation into transmutation of new plutonium in the axial targets

Benefits of Axial Targets for a Dedicated MA Burner Core Design

Earlier studies indicate that a low conversion ratio, attained by a high leakage core design, is necessary to destroy the undesired transuranics waste isotopes found in SNF. From a physics standpoint, a low conversion ratio is ideal for reducing the production of plutonium and MAs by reducing parasitic capture. This work makes a fundamental change in philosophy regarding MA waste management in the SFR. Previous repository studies establish the limitation that the Am-241 isotope puts on the quantity of SNF that can be stored in Yucca Mountain [13]. Because this isotope is not fissile, its removal from the fuel cycle can best be achieved by increasing its

transmutation rate by neutron capture. Because this neutron capture in americium leads to a transmutation path ending in Pu-238 (and the other plutonium isotopes to a lesser extent), it can be used as a fertile blanket material.

The reactor design proposed and analyzed in this dissertation uses both a moderated epithermal transmutation target fuel and an un-moderated fast spectrum driver fuel to achieve the maximum MA transmutation rate. Therefore, the design has a heterogeneous fuel configuration where excess neutrons from the fast driver zone are used to transmute fertile MA in the epithermal target zone. For the remainder of this dissertation, this hybrid MA-to-plutonium converter reactor is given the name: Axially Heterogeneous Fast Transmutation Reactor (AHFTR)

This breeding of transmuted isotopes can be accomplished with a MA fast flux trap at the axial top periphery of the active core. The goal of such a flux trap is to recover the fast flux leakage from the active core and moderate it to a softer spectrum which enhances neutron capture in the MA rich target. The relationship of this flux trap (target) to the active core (driver) is shown in Figure 1-7. This symbiotic arrangement allows the driver fuel to have a low MA content while the MA concentration in the targets is significantly higher. The moderation in the targets increases the capture cross section magnitude (especially in Am-241) relative to fission (especially in Pu-239). Thus, the active core neutron flux entering the axial targets is invested into capture reactions leading to transmutation as opposed to being lost to leakage.

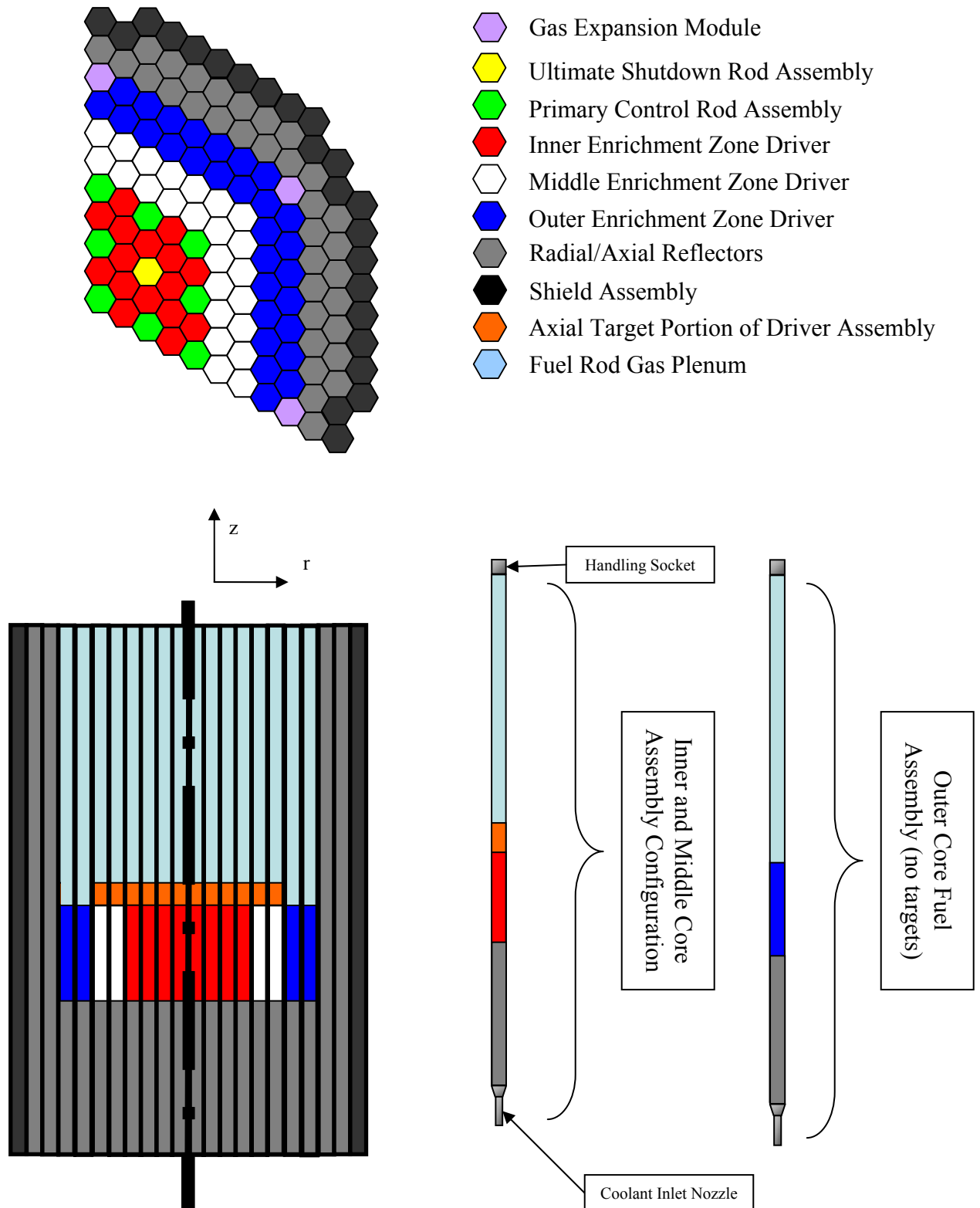


Figure 1-7. Core design of the Axial Heterogeneous Fast Transmutation Reactor

When the transmuted product from the targets is recycled and used later as driver fuel, the Pu-238 (and other transmuted fissile material such as Pu-238 and Cm-245) will be exposed to the fully fast flux of the active core. There, the transmuted Pu-238 will have higher “fast spectrum” fissile worth than the initially loaded MAs (Table 1-1). To take advantage of this fast fissile improvement, the spent axial targets are co-processed with the spent driver fuel and included in the fresh driver fuel fabrication for the next reactor pass (Figure 1-1 and Figure 1-8).

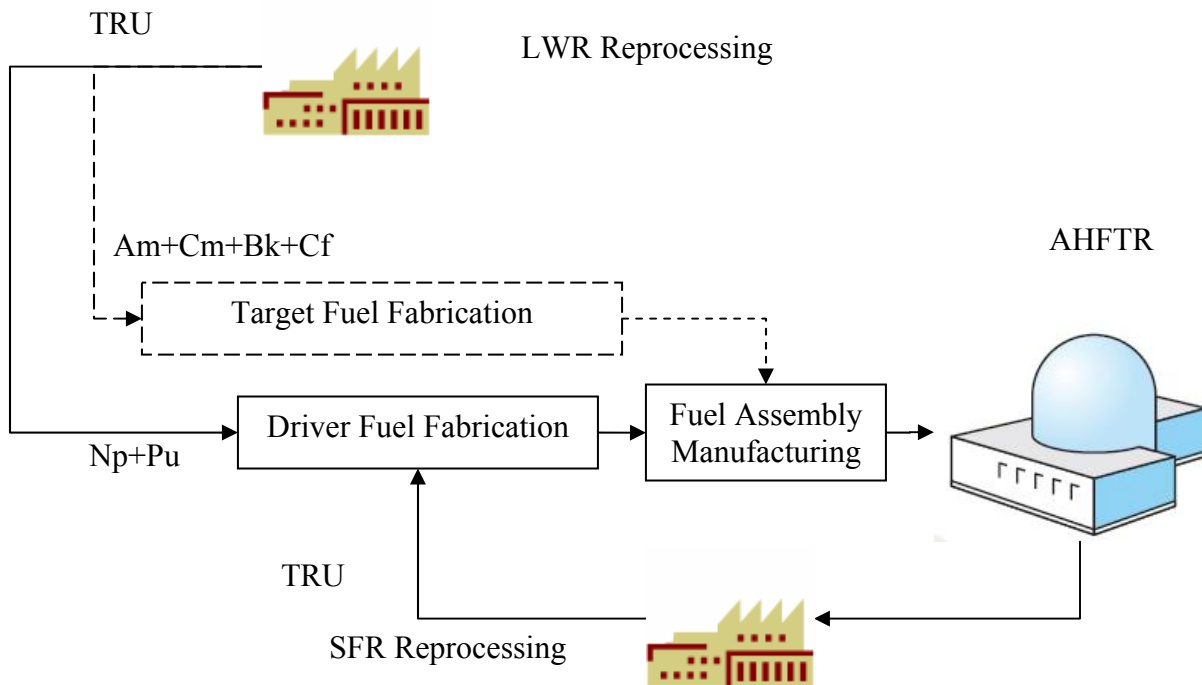


Figure 1-8. Modification to the ABR fuel cycle by the axial targets: Solid lines represent the reference ABR fuel cycle. Dashed line represents modifications to include axial targets.

The key technical attribute of converting MAs into plutonium isotopes is the relaxation of the requirement to have a low conversion ratio. As will be discussed in the next chapter, homogenous core designs, such as pancake designs or the ABR, require a high TRU enrichment in order to achieve a low conversion ratio. The AHFTR axial blanket converts MAs into plutonium. Because, one type of TRU is being traded for another, the targets have a negligible impact on the overall core conversion ratio. However because the MAs are preconditioned into

plutonium before being applied to the active core, the fissile worth of TRU used by the driver fuel is increased. This effect allows the AHFTR fuel composition to be more comparable to IFR fuel testing experience than ABR designs of equal conversion ratio. The fuel assembly and pin dimensions of the AHFTR and two ABR core designs are given in Table 1-6.

Table 1-6. Fuel assembly design of the AHFTR compared to similar ABR designs

Fuel Type	AHFTR	ABR (CR=0.75)	Ref. ABR (CR=0.5)
Approximate core conversion ratio	0.70	0.75	0.50
Fuel type	Metal	Metal	Metal
Driver fuel alloy composition	TRU/U/10-Zr	TRU/U/10-Zr	TRU/U/20-Zr
Axial target alloy composition	MA/Pu/U/40-Zr	n/a	n/a
TRU Enrichment (%)	20	25	35
Assembly pitch, cm	16.142	16.142	16.142
Inter-assembly gap, cm	0.432	0.432	0.432
Duct outside flat-to-flat, cm	15.710	15.710	15.710
Duct material	HT-9 Steel	HT-9 Steel	HT-9 Steel
Duct thickness, cm	0.394	0.394	0.394
Pins per assembly	271	271	324 (7 support)
Fuel pin spacer mechanism	Helical wire wrap	Helical wire wrap	Grid
Spacer wire wrap diameter, cm	0.1329	0.1329	n/a
Bond material in cladding gap	Na	Na	Na
Overall fuel pin length, cm	407.040	407.040	407.040
Top - fission gas plenum height, cm	191.140	191.140	191.140
Middle - Active fuel "core" height, cm	91.600	101.600	101.600
Bottom - Axial reflector height, cm	114.300	114.300	114.300
Fuel smeared/ fabrication density, % TD	75/100	75/100	75/100
Pin outer diameter, cm*	0.755	0.755	0.623
Cladding thickness, cm	0.0559	0.0559	0.0559
Pin pitch-to-diameter ratio	1.176	1.176	1.293

*The pin diameter varies depending on the desired conversion ratio

A more practical driver fuel composition allows the fuel assembly design to be more similar to what was proposed for the S-PRISM. Table 1-7 compares the main differences between the AHFTR core design and the ABR designs.

Technology Compatibilities and Synergies

One of the technology goals of the GNEP program is to establish a higher level of accountability for HLW mass streams than previous fuel cycles. Aqueous reprocessing (using

liquid organic solvents) of SNF has been performed in Europe, Russia and Japan on a commercial scale using the Plutonium-Uranium Redox Extraction (PUREX) process.

Table 1-7. Core design for the AHFTR compared to similar ABR designs

Fuel Type	AHFTR	ABR (CR=0.75)	ABR (CR=0.5)
Driver Assemblies	192	144	144
Inner (Lowest Enrichment)	42	30	42
Middle (Medium Enrichment)	66	42	66
Outer (Highest Enrichment)	84	72	36
Primary Control Assemblies	16	16	16
Ultimate Shutdown Assemblies	3	3	3
Gas Expansion Modules	6	0	0
Reflector Assemblies	96	90	90
Shield Assemblies	66	60	60
Core Diameter (m)	2.6	2.3	2.3
Reactor Diameter (m)	3.2	3.0	3.0
Active Core Height (m)	71.6	101.6	101.6
Total Core Height (m)	91.6	101.6	101.6

However, this technology extracts relatively pure uranium and plutonium products and leaves behind a highly radioactive “mixed waste” of fission products and MAs which are also considered HLW. From the discussion on the isotopic aspects of the repository design, it is evident that not all of these isotopes carry the same importance for needing disposal in the repository. Therefore, the GNEP program and its predecessors have developed a suite of additional separations steps to aqueous reprocessing, called Uranium Extraction Plus (UREX+) [37]. The UREX+ reprocessing technology, and its associated sub-steps, divides the HLW stream into individualized mass streams. Uranium Extraction (UREX) by itself is an aqueous partitioning technology designed only for creating a highly pure uranium stream from SNF. UREX is expanded into UREX+ by adding additional extraction steps for partitioning: technetium, iodine and Cesium/Strontium.

Actinide Partitioning: PUREX and UREX

An additional advantage of the UREX or UREX+ suite is the ability to control the level of elemental actinide partitioning. The only partitioning possible by the PUREX process is the

creation of a plutonium and uranium product. The production of pure plutonium raises some debate over the nuclear weapons proliferation resistance of this technology. The UREX+ suite was designed to provide elemental partitioning such that plutonium is always diluted in another actinide. For example, the UREX+1a process separates all the TRU together as one product so that plutonium is diluted over all the transuranics. As seen in Table 1-8, additional separations steps to the UREX+1a process creates an increasing number of product streams.

Table 1-8. Waste stream partitioning afforded by various reprocessing technologies*

Process	Prod. 1	Prod. 2	Prod. 3	Prod. 4	Prod. 5	Prod. 6	Prod. 7
PUREX	U	Pu	MA+all FP				
UREX+1	U	Tc	Cs/Sr	TRU+Ln	FP		
UREX+1a	U	Tc	Cs/Sr	TRU	FP+Ln		
UREX+2	U	Tc	Cs/Sr	Pu+Np	Am+Cm +Ln	FP	
UREX+3	U	Tc	Cs/Sr	Pu+Np	Am+Cm	FP+Lanth	
UREX+4	U	Tc	Cs/Sr	Pu+Np	Am	Cm	Cm+Ln
Pyroproc.	U	TRU	All FP				

*Prod. is product. Tc is technetium. Cs is cesium. Sr is strontium. Ln is lanthanides. FP is fission products

Of these options, the UREX+1a process has the most resemblance to PUREX. The primary difference is that plutonium is diluted by all of the MAs found with it in SNF. As mentioned in the motivations and objections section, inclusion of these MAs in the SFR driver fuel can lead to an accumulation of curium, berkelium and californium [38]. The associated gamma and neutron radioactivity, as well as thermal heat, associated with decay of these actinides may significantly complicate fuel handling and fabrication of recycled fast reactor fuel. These high radiation fields raise the possibility that expensive hot-cell facilities would be necessary for all fuel handling operations. Hot-cells are large monolithic shielded facilities where radioactive material is handled remotely using mechanical master-slave manipulator arms. Because of their large size and relative complexity, it is expected that hot-cell facilities are significantly more expensive than glove-box facilities. The PUREX fuel cycle allows fabrication in glove-box environments because the MAs and higher mass actinides are removed during

reprocessing. Also, as a general rule, the commercial PUREX fuel cycles to date have not dealt with the multi-recycling scenario. Hence, the accumulation of highly radioactive curium, berkelium and californium has not been dealt with on a commercial level.

To avoid the fuel handling penalty, it has been proposed by Pillon et al that the complexities of MA management in hot-cells could be limited to a small fraction of the fuel cycle infrastructure [39]. Because the MAs constitute only a small fraction of TRU, the associated hot-cell infrastructure (MA) can be made significantly smaller than the glove-box (Pu) infrastructure. By constantly partitioning the MAs from the plutonium driver fuel, after each reloading cycle, and continuously recycling them in targets the driver fuel fabrication process could be performed with less difficulty.

To achieve the MA partitioning, the UREX+3 process from Table 1-8 is selected. This option provides that plutonium is not separated by itself but diluted by neptunium. Also the MAs, of highest importance to repository and hot-cell criteria (Am+Cm+Bk+Cf), are partitioned and sent to target fabrication in Figure 1-8. The fuel cycle in Figure 1-8 is slightly different than that proposed by Pillon et al. Instead of continuously separating MAs from the driver fuel and sending them to targets, it is assumed that the transmutation conversion efficiency of americium into plutonium is sufficient enough to not require that the MAs be multi-recycled in the targets. Therefore, the MAs separated from SNF are irradiated only once in the targets before this mass is co-reprocessed with the driver fuel into the next batch of driver fuel. Special attention is given to the sizing of the target region in the AHFTR to ensure that the concentration of MAs in the driver fuel is small.

Pyroprocessing and the Integral Fuel Cycle

The small concentration of MAs in the driver fuel and the single-pass target irradiation makes feasible the choice of metallic fuel and metallic fuel reprocessing. Metal alloys of

uranium, plutonium and zirconium were successfully used as reactor fuel at both EBR-I and EBR-II for over 40 years. Metal fuel reprocessing was demonstrated at EBRR-II during the IFR program using the pyrometallurgical process involving metal alkaline salts (Table 1-8) [40]. The benefits of applying pyroprocessing to any SFR fuel cycle are:

- Pyroprocessing does not require water, avoiding many criticality safety issues.
- Pyroprocessing is performed at high temperatures and does not use organic solvents. From the PUREX experience, organic solvents decompose when exposed to the radiation fields of SNF/HLW.
- The reprocessing machinery of pyroprocessing is considerably more compact than aqueous reprocessing which makes it more suitable for deployment in hot-cells.
- Similar to UREX+1a, pyroprocessing does not allow for actinide partitioning which increases its general proliferation resistance.

Because of these attributes, pyroprocessing sufficiently meets the requirements for reducing the infrastructure dealing with MAs. The primary difference from the approach taken by Pillon et al, is that the entire AHFTR and its associated IFR style co-reprocessing (targets plus driver) perform the task of dedicated MA burning. Hence, the AHFTR and its associated reprocessing machinery constitute a small fraction of the overall fuel cycle and ABR/AHFTR mixed-fleet. In this fuel cycle, the AHFTRs and ABRs would work in parallel to accomplish the overall directive to burn SNF TRU. The relationship between ABRs and AHFTRs in this hybrid partitioning and transmutation strategy is given in Figure 1-9.

In Figure 1-9, the AHFTRs are the only reactors committed to destroying the MAs separated from SNF. For the purpose of this dissertation, the ABRs in the mixed-fleet are also assumed to use pyroprocessing technology which may or may not require hot-cell facilities due to an eventual buildup of higher mass actinides (Cm+Bk+Cf). The rate of this buildup for various partitioning strategies is currently the topic of ongoing studies in the transmutation analysis field. Given the suitability of metal fuel with pyroprocessing, it is assumed that if these

technologies are adopted for the AHFTR they will reach economical maturity and would ultimately be adopted for the ABRs as well.

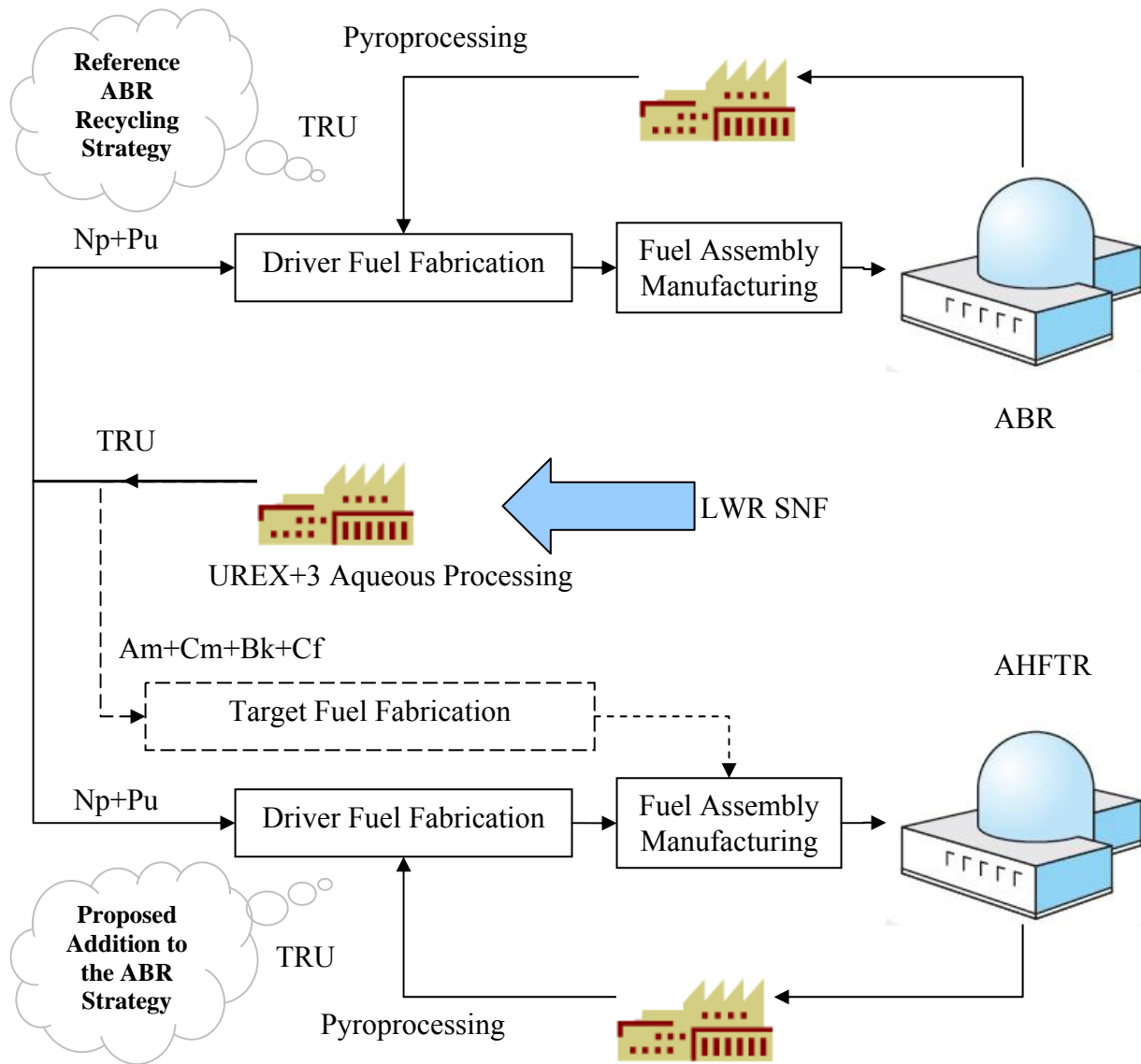


Figure 1-9. Partitioning and transmutation scenario of a combined ABR and AHFTR mixed-fleet

Assumptions for Using Transmutation Targets in SFRs

It is important to mention that the choice to use pyroprocessing in hot-cells which are collocated with the ABR or AHFTR is based on the fact that the need to transport spent SFR fuel to a centralized reprocessing plant is eliminated. Avoiding the need for a large centralized

reprocessing plant may have a significant economic advantage because the cost of transportation is eliminated. Also, it can be argued that the fast reactor fuel cycle services will require collocation with the reactor in order to simplify the handling issues associated with “hot” fuel. Though centralized reprocessing and fuel fabrication facilities benefit from economy of scale, they have not been demonstrated on a large scale with the high fissile concentrations and possible radiation fields inherent with fast reactor fuels. LWR SNF is stored for a period no less than approximately five years in order to minimize the radiation fields from fission products (and Cm+Bk+Cf). When spent fuel (LWR or SFR) comes out of the reactor it is thermally hot due to the decay energy of these fission products. To cool the SNF during the decay time, LWR operators store the spent fuel assemblies in large pools of water before transportation them offsite. Fast reactor operators will not have the luxury of using water to cool the fuel because of the high fissile content in the driver assemblies. Therefore, the cost to cool spent fast reactor fuel could be a foreseeable additional non-trivial cost if an interim decay period is required before it can be reprocessed. These assumptions are stated in Table 1-9.

Using Table 1-9 as a guide, fast reactors with heterogeneous targets are chosen because similar core configurations have been used in the past explicitly for the purpose of transmutation. Historically, the main transmutation process in SFRs was the conversion of U-238 into fissile Pu-239 atoms. However, regardless of whether or not the transmutation product is fissile, the inherent neutron economy of fast reactors enables bombardment of heterogeneous targets using excess neutrons. Furthermore, fast-fission by all actinides, including MAs and their transmutation products, contributes to reactivity which gives them a neutronic advantage over LWRs where transmutation is concerned. As discussed earlier, moderating pins in the target region is adopted to provide a spectrum benefit that can enhance transmutation. Finally,

pyroprocessing of metallic fuel at a hot-cell facility which is co-located with the SFR is chosen.

These technologies have been demonstrated during the IFR program to have an industrial synergy when implemented together.

Table 1-9. Technology compatibility assumptions with Pros and Cons (Technology options indicated by † represent technologies adopted for this dissertation)*

	Pro	Con
MA targets in LWRs	Using existing reactors utilizes existing technology. Thermal capture cross sections are high for most SNF MAs	MAs and most of their transmutation daughters are neutron sinks. Conventional LWRs do not possess the surplus of neutrons required to continuously irradiate MAs (<u>and transmuted products</u>) once the initial fissile material has been exhausted.
MA targets in SFRs †	Fast reactors derive all of its reactivity from fast-fission enabling <u>all</u> actinides to be a neutron source (as opposed to a sink)	Implementation of SFRs requires reprocessing technology in order to fully utilize the reactivity investment made by transmuting fertile isotopes including the MAs.
Moderated targets †	Utilization of neutron capture enhances conversion into even-plutonium isotopes	Moderated targets require placement on the core periphery to minimize adverse power peaking and kinetics feedbacks. Less flux on periphery.
Un-moderated targets	Simplifies materials science and reactor physics issues	No spectrum benefits that could potentially enhance transmutation.
Once-Through Deep Burn of Targets	Eliminates recycling/handling of higher mass actinides	Achieving a net-zero MA mass balance with “deep-burn” is difficult in any real reactor system. Material science does not currently exist to withstand ultra-long irradiations.
Multi-Recycling of Targets †	Ultra-long irradiations are not necessary. Closed fuel cycle allows a net-zero MA mass balance	Shielding requirements of higher mass actinides essentially requires a hot-cell infrastructure for MA recycling.
Aqueous reprocessing with SFRs	Economic advantages due to the economy of scale	Spent fast reactor cooling will be considerably more expensive than in LWRs because cooling methods other than spent fuel pools “water” will be required for criticality safety.
Pyroprocessing with SFRs †	Pyroprocessing has been demonstrated with SFRs and is more adaptable to handling thermally “hot” spent fast reactor fuels	Pyroprocessing does not allow for elemental transuranic partitioning which requires that the targets and driver fuel be reprocessed together thus preventing complete segregation of MA and plutonium mass streams within the fuel cycle
Co-location of reprocessing with SFRs †	Transportation of spent fast reactor fuel is eliminated	Fuel reprocessing and fabrication facilities for every reactor site adds extra capital cost
Centralized Reprocessing Oxide fuel and targets	Economic advantage due to the economy of scale Oxide fuels are well recognized in LWR commercial experience	Transportation of fuel is required which also necessitates a spent fast reactor fuel cooling facility The higher burnup and temperatures of SFRs mutes many advantages such as fission gas retention and pellet integrity
Metal fuel and targets †	Metal fuels have been demonstrated as compatible with SFRs but not demonstrated on a commercial scale	Metal fuels are not widely recognized by the commercial nuclear industry

*Further advances in any of these technologies may change the validity of the assumptions made.

CHAPTER 2 COMPUTATIONAL METHODS AND FAST REACTOR PHYSICS

Many of the methods for cross section preparation and flux calculations used to study LWR core physics today, have their origins in the analysis of fast reactors. This is partly because fast reactors were essentially one of the first nuclear energy systems. It is also due to the fact that the spatial smearing approximations made to simplify lattice and pin-cell calculations for these early methods were usually sufficient to achieve acceptable accuracy in fast reactor applications. Due to the lack of SFR commercialization, the demand to update fast reactor simulation and computational methods has been low. Furthermore, due to the general adequacy of smearing fuel pin and assembly heterogeneities over large core regions, fast reactor analysis methods have not evolved to the extent of those used for LWR analysis over the past two decades. Several calculation codes are used throughout this dissertation. Figures and Tables will be labeled according to the calculation method used. Sometimes the results produced by one code are used as the input data for a secondary code. If this is the case, special mention of the coupling process is given in notes below the graphic or within the nearby text.

Calculations and Fuel Cycle Modeling

The Argonne National Laboratory (ANL) fast reactor codes MC²-2, DIF3D and REBUS are used for the reactor physics and fuel cycle calculations [41,42,43]. These codes have been developed together by ANL for SFR design since the mid-1970's and are well benchmarked against SFR operational data [44]. The MC²-2 code was used to generate region dependent, 33 energy-group cross sections at hot fuel, cladding and coolant temperatures based on an ultra-fine group cross section library. The MC²-2 ultra-fine libraries were pre-processed at ANL from evaluated nuclear data files (ENDF) and using a standard fast spectrum distribution for appropriately weighting the fine group generation. Starting with the ultra-fine group libraries,

MC²-2 creates a collapsed coarse group cross section set by performing a zero dimensional infinite dilution critical buckling search using the extended P1 method [41]. The MC²-2 code also performs a resolved resonance broadening treatment, to account for energy shielding only, at user defined material and fuel temperatures. A continuous slowing down calculation is performed at lower energies to handle elastic scattering [45]. A direct multigroup spectrum calculation accounting for inelastic and anisotropic scattering and upscattering is performed at higher energies.

It should be noted that the calculations performed by the publically available release of this code are limited to using an older ENDF/B-V.2 release of cross section data because the publicly available release of MC²-2 does not come standard with the preprocessed ultra-fine group libraries generated from newer ENDF/B-VII data. Also, it should be noted that there are two additional code packages (SDX and DB2), which are typically used by ANL in concert with MC²-2 and REBUS, but are not publicly available, and thus were not used in the calculations performed by this work, which was performed at the Idaho National Laboratory (INL). The first of these codes, SDX, accounts for the spatial effect of heterogeneity introduced by pins in an assembly, which is modeled initially in MC²-2 as a homogenized region. The second, DB2, takes the fission energy spectrum from areas on the periphery of the core and collapses the cross sections for the neighboring control rod, reflector, and shield regions based on the leakage spectrum.

The approach taken by this dissertation (and parallel ABR core physics studies performed by INL) was to disregard the spatial heterogeneity introduced by pins in the assembly. This zero-dimensional approach in the cross section collapsing does not account for spatial *resonance* shielding effects between the various core regions. However, for fast reactor calculations this is

generally sufficient due to the long neutron mean-free-path. The fast flux is almost entirely in the unresolved resonance range, thus making *unresolved* energy shielding the dominating effects in the group collapsing. This assumption is supported by the good agreement between the INL benchmarking effort (INL-EXT-12466) of the ABR and the ANL scoping calculations for the ABR (ANL-AFCI-177) [7,38]. Also for this work and the INL benchmark, the reflector and shield region cross sections were collapsed, without DB2, using a generic Pu-239 fission energy spectrum in MC²-2.

These 33-group cross section sets produced by MC²-2 are then used by the DIF3D code to perform the actual core physics and criticality calculation. The DIF3D diffusion code was used to solve the multigroup steady state neutron diffusion equation using a hexagonal-z nodal coordinate system [42]. In the nodal discretization, each hexagonal node in the lateral direction represents a fuel assembly. Because the mean-free-path is on the dimensional level of the fuel assembly, the individual fuel rods are homogenized across this hexagon.

Fast Reactor Equilibrium Fuel Cycle Calculations Using the REBUS Code

The actual fuel depletion and fuel cycle modeling, including the mass balance between reactors and reprocessing plants, is performed by the REactor BUrnup System (REBUS) code [43,46]. REBUS uses DIF3D to generate reaction rate and flux information at each time step “burn step” in its fuel depletion algorithm. Once the reactor physics calculation is completed, the fluxes from DIF3D are fed to a depletion solver routine. This solver uses the exponential matrix method to solve the Bateman equations for isotopic buildup and decay within the discretized burn step. REBUS also performs the in-core fuel management and out-of-core cooling, reprocessing and re-fabricating for each reactor cycle. The REBUS depletion and fuel management algorithm is given in Figure 2-1.

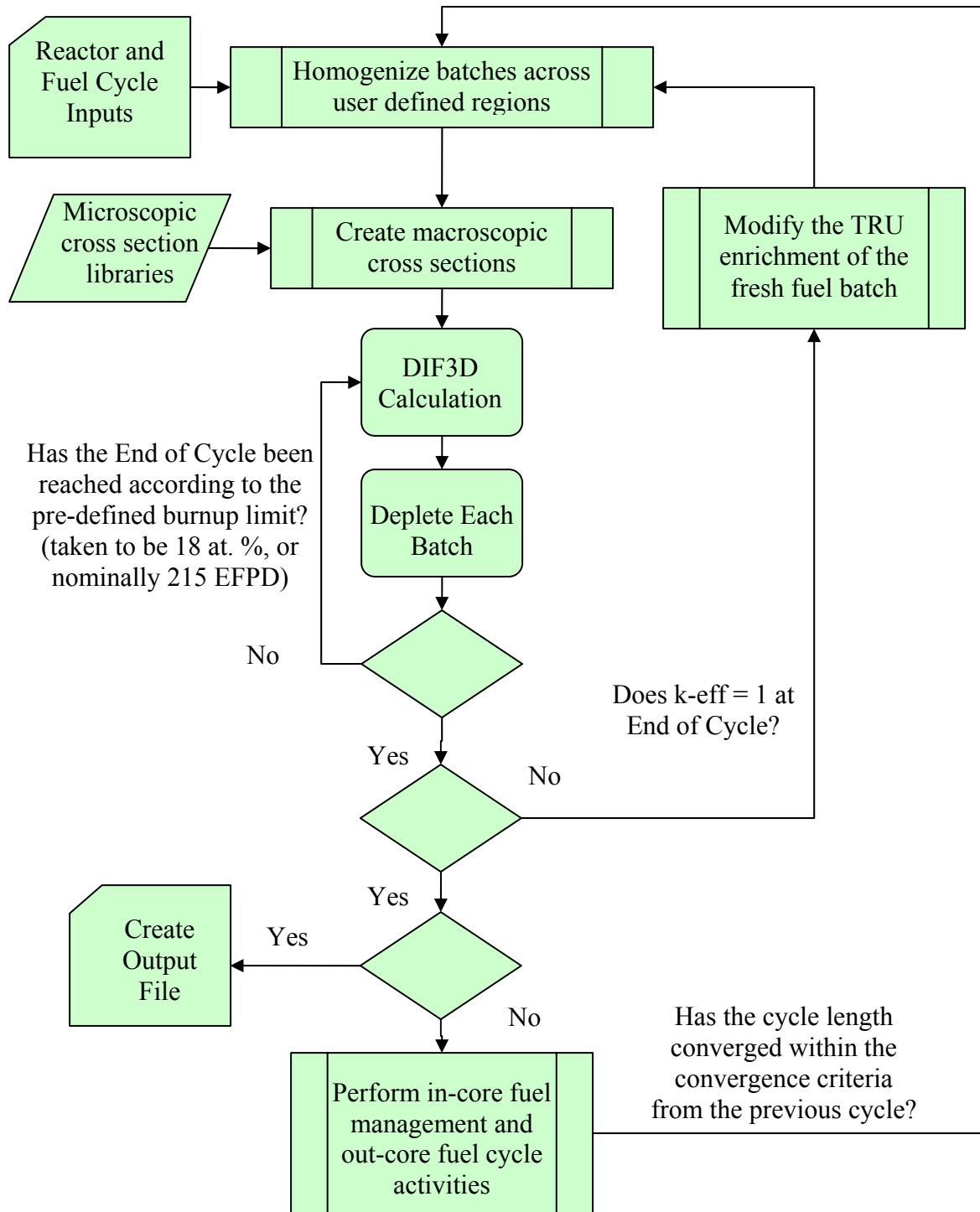


Figure 2-1. Coupled DIF3D core physics and REBUS fuel cycle algorithm

In the REBUS fuel cycle model, individual fuel assemblies are homogenized into “like neutron spectrum” representative regions. Therefore, independent batches of fuel are tracked

within the external fuel cycle but not explicitly spatially represented in the physics calculation. These regions may represent all of the batches of fuel having common transuranic enrichment, defined as an enrichment zone. However, it is not essential to divide the same-spectrum regions according to the enrichment zoning. The AHFTR fuel management model assumes that each row in the core is a same-spectrum region. Because fuel is typically not shuffled in SFRs, the assumption is made that each row in the AHFTR core is filled with fuel assemblies of the exact same fresh fuel specifications but having different levels of depletion. Therefore, the average fuel composition within each row (or more generally region) is the volumetric average of the same fuel assembly at the different stages of its depletion.

The in-core fuel management and out-of-core fuel cycle activities are carried out until the *equilibrium* cycle was achieved. The equilibrium cycle is defined as the equilibrium or “steady-state” condition of the fuel cycle when the reactor performance properties (i.e., k-eff, enrichment, cycle length, etc.) become invariant from cycle to cycle. This equilibrium mode calculation was performed for both the ABR and the AHFTR. In a typical REBUS equilibrium fuel cycle calculation, the fuel management operations are carried out until the excess reactivity and equilibrium cycle length are found. A maximum fuel burnup of 18 a/o after 6 reactor cycles (seven cycles for the outer core of the ABR) was used to constrain the search procedure to determine the equilibrium cycle length. This burnup constraint nominally gives an equilibrium cycle length of approximately 215 Effective Full Power Days (EFPD) for both the ABR reference and the AHFTR. This burnup closely correlates to the maximum exposure limitations of SFR metallic fuel and cladding integrity. These limitations will be discussed in Chapter 6.

To account for the spectral changes during fuel depletion, the 33-group cross section library was updated using a coupled corrector-predictor loop between MC²-2 and REBUS. This

loop is initialized by a first guess of the region and depletion averaged fuel composition in the core. This guess is made by using a SNF TRU composition, depleted uranium composition and approximating the fresh fuel TRU enrichment. This composition data is used by MC²-2 to generate a guessed cross section set. Then REBUS uses the guessed cross section set to perform a guessed fuel cycle calculation. Finally, the region and depletion averaged fuel composition is extracted from the REBUS output and imported into a new MC²-2 calculation. An automated scripting system is used to continuously re-calculate the cross sections for each enrichment zone based on that zone's fuel inventory at equilibrium. Figure 2-2 shows the flow of cross section and isotopic composition data between MC²-2 and REBUS.

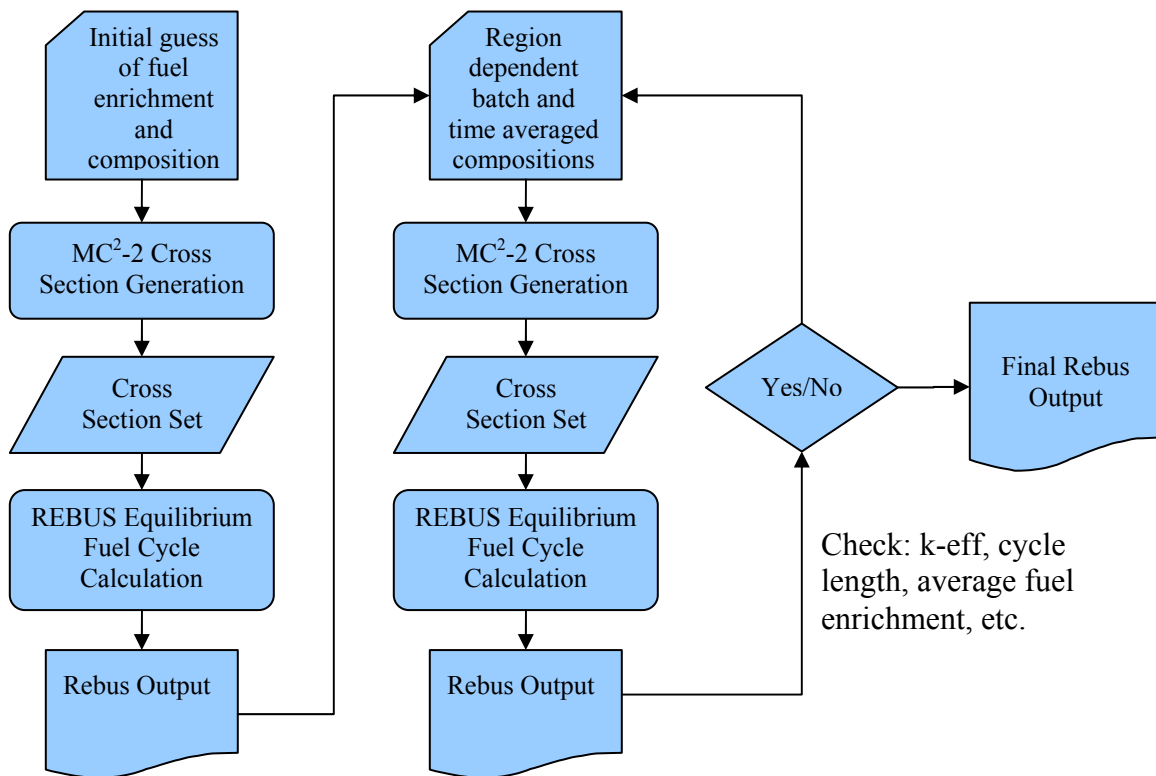


Figure 2-2. Flow diagram of data transfer between the MC²-2 and REBUS codes

Once this equilibrium fuel cycle was attained, the Beginning-of-Equilibrium-Cycle (BOEC) and End-of –Equilibrium-Cycle (EOEC) total core void and Doppler coefficients were calculated. The total core void worth was attained by taking the BOEC number densities from

each isotope in each axial and radial region from the REBUS output file into a new DIF3D (no depletion) input file. The number density for sodium for each region was reduced by the coolant volume fraction leaving only the bond sodium in the fuel rod gap with the coolant sodium voided. The sodium fraction was also reduced for the corresponding MC²-2 calculation. The Doppler coefficient was calculated in a similar procedure without the change in sodium number density. Instead, a new MC²-2 calculation was performed with all cross sections broadened at a temperature 100 K greater than that for the REBUS calculation. Then a new DIF3D calculation was performed with the BOEC number densities unchanged from the REBUS output file.

Light Water Reactor Spent Fuel Calculations Using the TRITON Code

Since REBUS only deals with the closed portion of the fuel cycle involving fast reactors, the external supply of TRU to this closed fuel cycle must be generated externally. To perform this task, the Oak Ridge National Laboratory (ORNL) code package, Scale 5.1, was used to generate the composition of SNF by performing a single fuel assembly depletion and decay calculation [47]. Using the geometry of a (Pressurized Water Reactor) PWR 17x17 pin bundle design, a two-dimensional lattice calculation was performed to represent the in-core irradiation. The SCALE5.1 depletion code, TRITON, was used to perform the physics and depletion calculations for this single assembly model. TRITON uses several other scale codes within SCALE5.1 to perform the cross section generation and depletion of the fuel in this single assembly calculation.

- BONAMI was used to apply Bonderenko factors to correct for energy shielding between un-resolved resonances
- NITAWL was used to apply the Nordheim integral treatment for spatial shielding between resolved resonances
- NEWT is a two-dimensional discrete-ordinance code used to solve the neutron transport equation and create reaction rate and flux data.

- ORIGEN-S is a fuel depletion solver used to carry out the isotope buildup and decay process by solving the Bateman equations for each burn step and also for the post-irradiation decay period

Using TRITON simulation, a uranium oxide (UOX) fuel composition, enriched to 4.5%, was irradiated to a burnup of 50 MWD/kg. After this irradiation, the fuel was allowed to decay for five years to represent the spent fuel pool cooling time. It is assumed that the fuel will be partitioned into the Np+Pu and Am+Cm+Bk+Cf streams after this cooling off period. After partitioning, an additional decay time of two years was assumed for the time after separation which includes: reprocessing, fuel fabrication and transportation to the AHFTR. The isotopic composition of the SNF that is used as the external feed to the SFR is given in Table 2-1.

Table 2-1. Isotopic composition in weight percent for UOX SNF

	Spent Fuel Pool and Transportation to Reprocessing Center		UREX+3 Reprocessing	
	Discharged from LWR	After Five Year Decay	Np+Pu	Am+Cm
Np-237	5.46%	5.54%	5.88%	
Pu-238	2.47%	2.55%	2.66%	
Pu-239	45.79%	46.16%	49.01%	
Pu-240	22.61%	22.58%	24.01%	
Pu-241	13.18%	10.28%	9.94%	
Pu-242	7.05%	7.01%	7.44%	
Am-241	0.50%	3.28%	1.01%	55.75%
Am-242 ^m	0.01%	0.01%		0.17%
Am-243	1.92%	1.91%		32.37%
Cm-242	0.18%	0.00%		0.00%
Cm-243	0.01%	0.01%		0.09%
Cm-244	0.78%	0.64%		10.89%
Cm-245	0.04%	0.04%		0.65%
Cm-246	0.00%	0.00%		0.08%

Scoping Calculations and Benchmarking Using the MCNP Code

Given the dissimilarities between the core physics of LWRs and SFRs, it is prudent to test the computational methods available for fast reactor analysis using state-of-the-art tools that can simulate both reactor types. The Los Alamos National Laboratory (LANL) code Monte Carlo N-Particle (MCNP) is a general purpose physics simulation tool that uses the Monte Carlo method to recreate the exact particle physics of neutrons (and photons and electrons) in any arbitrary

three-dimensional geometry over a continuous energy range [48]. All scoping calculations and benchmarking analysis in this dissertation are performed with the MCNP code. MCNP allows the user to tally the neutron flux, and energy spectrum, as well as fission and capture reaction rates, in any region of the core. This neutron tally feature is used to indicate certain core physics parameters such as leakage and transmutation performance in the axial targets.

The MCNP code is also used to benchmark the accuracy of the deterministic diffusion method used by DIF3D to model the heterogeneity between the active core (fast spectrum) and the axial targets (epithermal spectrum). To model the accuracy of the coupled reactor physics and depletion algorithm of the MC²-2/DIF3D/REBUS scripting system, the LANL depletion code package MONTEBURNS was used in conjunction with MCNP [49]. MONTEBURNS uses MCNP tally data to produce single group fission, capture and n,2n cross sections and fluxes. These cross sections are used for neutron flux determination at a particular time step. These fluxes and cross sections are then fed into the ORNL fuel depletion code ORIGEN2 for burnup and decay calculations to the next time step [50, 51]. Then MONTEBURNS feeds the updated isotopic composition back to MCNP and the process begins anew.

Physics of the Reference Metal Fueled Advanced Burner Reactor

In the introduction, it was established by references to literature that a SFR conversion ratio is essentially a function of parasitic capture by uranium and neutron escape by leakage.

- A SFR's conversion ratio can be decreased by increasing axial leakage, as in a pancake design.
- The conversion ratio can also be decreased by decreasing the ratio of TRU to uranium loaded in the core (i.e., TRU enrichment) as was done by the ABR.

In order to establish the motivation for using a heterogeneous design, such as axial targets, it is important to first qualify these statements. The computational tools described in this chapter are used to explore these heterogeneous qualities and their affect on axial leakage. However, the

ABR, unlike the S-PRISM or the axial target design proposed here, exploits very little heterogeneity (no blankets or transmutation targets). Because the homogeneous ABR design does not take advantage of blankets or transmutation targets, decreases in conversion ratio are made by changes in the neutron economy (balance between neutron losses and neutrons contributing to fission or fissile production).

Conversion Ratio and High Leakage Cores

Consider the criticality condition that the geometric and material buckling must be equated in order for a reactor core to be critical [45].

$$B_g^2 = B_m^2 \quad (2-1)$$

Where: B_g^2 is the flux curvature's geometric buckling and B_m^2 is the material buckling.

For a *bare* right circular cylinder, the geometric buckling (without reflection) is defined by

Equation 2-2:

$$B_g^2 = B_r^2 + B_z^2 = \left(\frac{2.405}{R + z_o} \right)^2 + \left(\frac{\pi}{H + z_o} \right)^2 \quad (2-2)$$

Where: B_r^2 and B_z^2 are the radial and axial component of the geometric buckling, respectively. R and H are the critical radius and height of the core respectively taking into account the extrapolation distance:

$$z_o = 0.71\lambda_{tr} = 0.71 \times \frac{1}{\Sigma_{tr}} = 0.71 \times \frac{1}{\Sigma_t + \bar{\mu}_o \Sigma_s} = 0.71 \times \frac{1}{N_{tot} \sigma_t + \bar{\mu}_o N_{tot} \sigma_s} \quad (2-3)$$

Where: z_o is the extrapolation distance. λ_{tr} is the transport mean-free-path. Σ_{tr} , Σ_t and Σ_s are the macroscopic cross sections for transport, total interaction and scattering, respectively. N_{tot} is the total number of atoms in the homogenized composition. μ_o is the average cosine of the neutron scattering angle assuming elastic isotropic scatter in the lab system. The material buckling of a homogeneous mixture is defined as:

$$B_m^2 = \frac{\nu \Sigma_f + \Sigma_a}{D} = \frac{\nu \Sigma_f + \Sigma_a}{\frac{1}{3(\Sigma_{tr})}} = \frac{\nu \Sigma_f + \Sigma_a}{\frac{1}{3(\Sigma_t - \bar{\mu}_o \Sigma_s)}} \quad (2-4)$$

Where: ν is the average number of neutrons produced per fission. D is the diffusion coefficient. Σ_f and Σ_a are the macroscopic fission and absorption cross sections, respectively.

For the purpose of this discussion, consider only the Pu-239 and U-238 isotopes.

Therefore, the macroscopic cross sections in Equation 2-4 can be represented in terms of the enrichment and the total HM atom content by:

$$B_m^2 = \frac{\nu \times (r_{TRU} N_{tot} \sigma_{f,239} + (1 - r_{TRU}) N_{tot} \sigma_{f,238}) + (r_{TRU} N_{tot} \sigma_{a,239} + (1 - r_{TRU}) N_{tot} \sigma_{a,238})}{1 / (3((r_{TRU} N_{tot} \sigma_{t,239} + (1 - r_{TRU}) N_{tot} \sigma_{t,238}) - \bar{\mu}_o (r_{TRU} N_{tot} \sigma_{s,239} + (1 - r_{TRU}) N_{tot} \sigma_{s,238})))} \quad (2-5)$$

Where: r_{TRU} is the TRU enrichment which for this sample calculation is equal to Pu-239 divided by the sum of Pu-239 and U-238 atoms. $\sigma_{f,239}$, $\sigma_{f,238}$, $\sigma_{a,239}$, $\sigma_{a,238}$, $\sigma_{t,239}$, $\sigma_{t,238}$, $\sigma_{s,239}$ and $\sigma_{s,238}$ are the fission, absorption, total interaction and scattering microscopic cross sections for Pu-239 and Pu-238, respectively.

The microscopic cross sections for Equation 2-5 were generated by tallying the ABR neutron flux and capture and fission reaction rates over all energies and collapsing using MCNP. These tallies were used to create representative one-group cross sections for U-238 and Pu-239. These cross sections and the combined number density N_{tot} of U-238 and Pu-239 are given in Table 2-2. For a constant total HM atom density, increasing the TRU enrichment also increases the material buckling, as shown in Figure 2-3.

Table 2-2. Reference ABR atom densities and one-group microscopic cross sections for: Pu-239 and U-238

	N (atom/b*cm) of ref. ABR	One-group Microscopic Cross Sections (barns)			
		Fission	Scatter	Absorption	Fission
Total	0.0062				
Pu-239	0.0007	11.27	8.28	2.09	1.71
U-238	0.0054	10.88	9.53	0.28	0.04

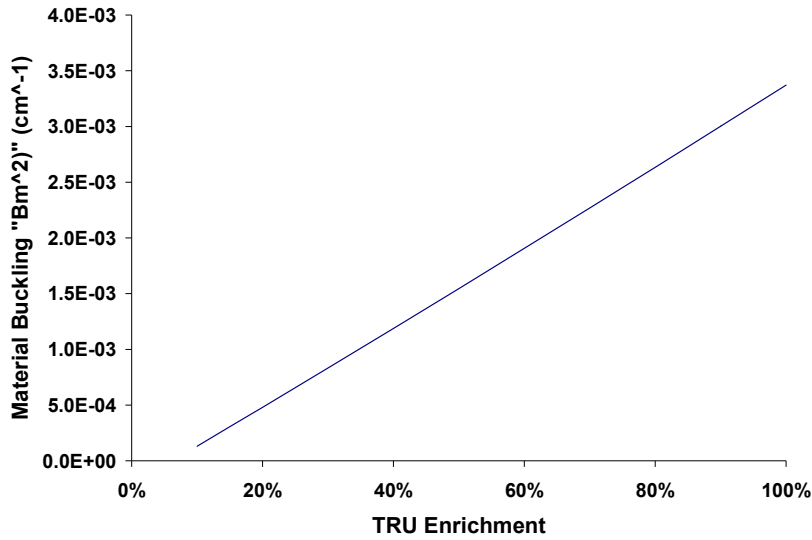


Figure 2-3. Material buckling of simple bare homogeneous SFR as a function of TRU enrichment (Hand Calculation)

Therefore, for increasing TRU enrichment, the geometric buckling required for criticality must also increase. Thus, for a given height “H” the axial buckling can be increased by decreasing the core’s *critical radius* “R”. The critical radius required to equate geometric and material buckling will vary depending on core height. The critical radius for different core heights and varying enrichment is given in Figure 2-4.

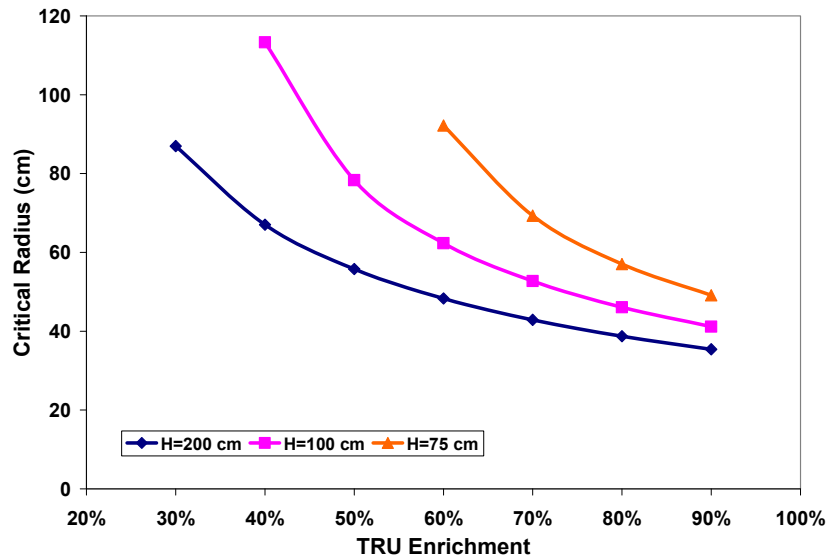


Figure 2-4. Critical radius required to equate geometric buckling with material buckling for increasing TRU enrichment (Hand Calculation)

The converse of the above statement is also true. If the geometric buckling is increased (either by reducing height or radius) the TRU enrichment that is necessary for criticality must increase. Note that this is the reason for flattening the SFR's height-to-diameter ratio to make a pancaked design. The flattened design increases buckling and decreases neutron economy. Hence, in order to achieve criticality, the TRU enrichment must be high.

Increasing TRU concentration and decreasing uranium concentration equates into a reduction in conversion ratio. For the purpose of this example, consider that the only source of TRU breeding results from neutron capture in U-238. Also assume that any neutron absorption in Pu-239 for this simplified model results in TRU destruction. This is not entirely the case in reality because some neutron absorptions in Pu-239 result in Pu-240 and the rest of TRU.

Therefore, the conversion ratio as a function of enrichment is given by:

$$CR_{generalized} = \frac{TRU \text{ production}}{TRU \text{ destruction}} \cong \frac{\Sigma_{a,238} - \Sigma_{f,238}}{\Sigma_{a,239}} = \frac{(1 - r_{TRU})(\sigma_{a,238} - \sigma_{f,238})}{r_{TRU} \sigma_{a,239}} \quad (2-6)$$

Where: $CR_{generalized}$ is the generalized conversion ratio definition for the two isotopes considered in this sample calculation. This equation is plotted using the values from Table 2-2 for varying TRU enrichment in Figure 2-5.

Therefore, an enrichment of 30% yields approximately a CR of 0.25 in this bare (un-reflected) sample problem. From Figure 2-4, this corresponds to a critical radius of over 120 cm for a core height of one meter. This generalized bare reactor conversion ratio is significantly less than the actual reference ABR (CR=0.5) due to the absence of reflectors. This draws attention to the importance of reflection in a SFR design. The mean-free-path between interactions of HM atoms is significantly high in a SFR (Figure 2-6). Therefore it is probable that a neutron can travel great distances in the reactor core without interacting with another fuel atom which

increases the likelihood of escape by leakage. The axial and radial reflectors in SFR designs are necessary to maintain some base level of neutron economy.

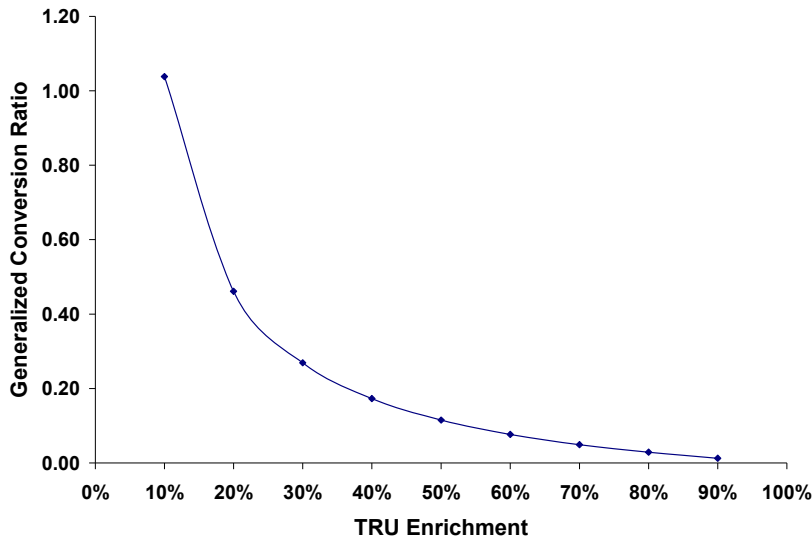


Figure 2-5. Generalized conversion ratio of a simple bare homogeneous SFR as a function of TRU enrichment (Hand Calculation)

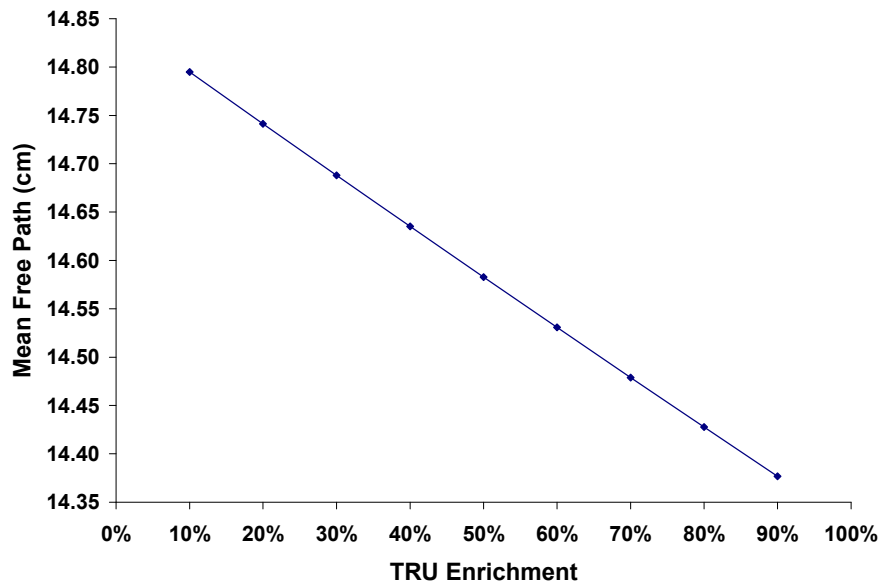


Figure 2-6. Mean-free-path of neutron travel between interactions (of any reaction type) between HM atoms (Hand Calculation)

The correlation between leakages, TRU enrichment and CR can be observed by plotting the leakage fraction which is given by:

$$LF = 1 - P_{\text{non-leakage}} = 1 - \frac{1}{1 + L^2 B_g^2} = 1 - \frac{1}{1 + (D/\Sigma_a) B_g^2} \quad (2-7)$$

Where: $P_{\text{non-leakage}}$ is the probability of non-leakage and L is the diffusion length. The leakage fraction is plotted in Figure 2-7.

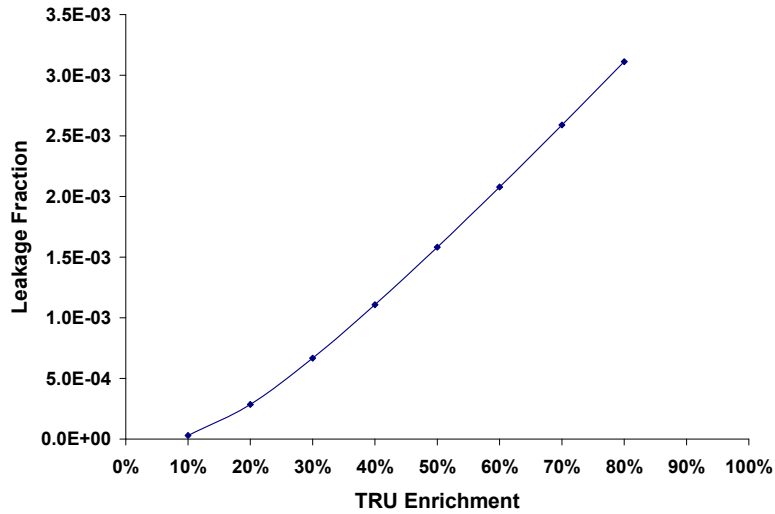


Figure 2-7. Leakage fraction of a simple bare homogeneous SFR as a function of TRU enrichment (Hand Calculation)

Conversion Ratio and High TRU Enriched Fuels

Assume that a very low CR is desired. But the prospect of core flattening and a pancake design may be unattractive for other reasons such as the expense of a large core barrel. Therefore, it would be necessary to fix the geometric buckling with a fixed set of core dimensions: $H=100$ cm, $R=113$ cm. Because the geometric buckling has been fixed, the material buckling is also a fixed quantity. As previously stated, in order to achieve a low CR, a very high TRU enrichment is necessary (e.g., $f_{\text{TRU}} > 90\%$). Because the geometric/material buckling and TRU enrichment is fixed by Equation 2-5, the density of HM atoms (N_{tot}) in the core must decrease to meet the criticality condition. The decrease in HM atom density is caused by the fact that as the TRU enrichment increases, the fuel becomes mostly fissile. Therefore,

less fuel (i.e., heavy metal) is needed to be critical. Figure 2-8 shows this relationship between the CR, TRU enrichment and the HM core loading.

This is the approach taken to achieve decreasing low conversion ratios by a homogeneous ABR design. The ABR height is 101.6 cm and its active core radius is 109 cm. A final decision on the design conversion ratio of the ABR has not been made in the GNEP program. Currently, there are several variations of the ABR design that range from having a CR of 0.25 to 0.75.

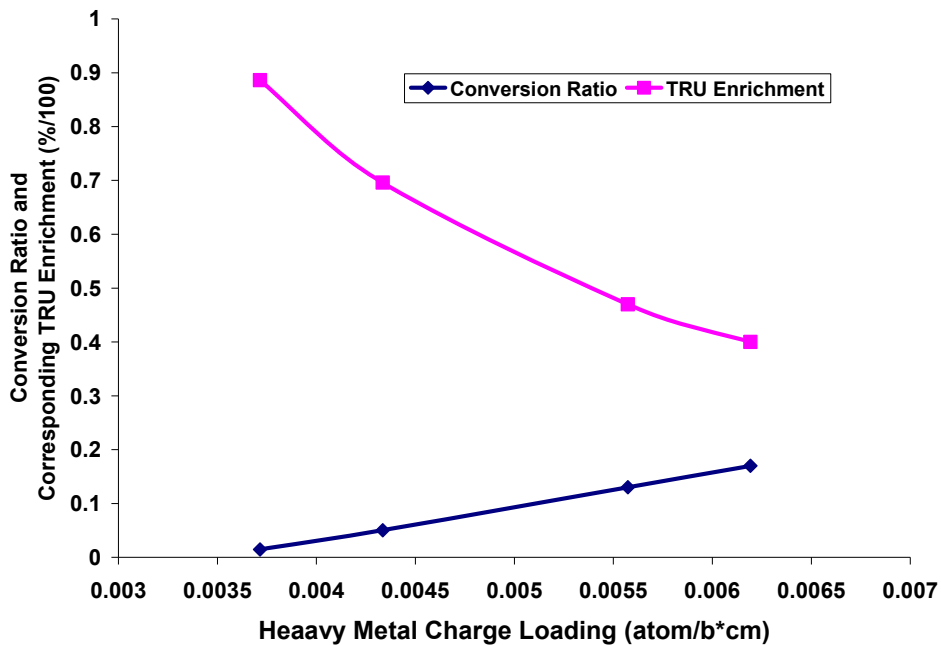


Figure 2-8. Conversion ratio and the corresponding TRU enrichment as a function of HM atom charge density for a bare homogeneous SFR of fixed size (Hand Calculation)

The decision on conversion ratio is primarily dictated by the feasibility of fabricating and irradiating high TRU with low uranium concentration in the SFR driver fuel. In the homogeneous burner reactors proposed for the ABR, reductions in CR are achieved by removing from the fuel pin, the volume corresponding to uranium [7,52,53,54]. This decrease in volume for constant fissile inventory increases the TRU enrichment which reduces the CR. Since the volume reduction is done such that the fuel pin radius is decreased, the fabrication feasibility of very small diameter fuel pins becomes a design factor. There is also a separate feasibility issues

related to reactor kinetics and safety of a low conversion ratio SFR with virtually zero uranium content.

Physics of the Axially Heterogeneous Fast Transmutation Reactor

The AHFTR design concept seeks to increase the neutron economy of the overall SFR design by using axial targets to recover the axial leakage produced by the active core. This enables the active core to maintain some level of high leakage which is important for establishing a baseline conversion ratio. Establishing a “reasonably” low conversion ratio without the targets is important because, as will be shown, the axial target region operates in a converter mode (i.e., MA converted into Pu with little decrease in total TRU). This is an important point to make because the design rationale of the targets is to convert MAs into plutonium which is a different philosophy from a purely MA burning target or a plutonium breeding blanket.

The enhanced neutron economy without significantly sacrificing conversion ratio allows the AHFTR to have a TRU enrichment that is more akin to past SFR fuel experience than the lower conversion ratio forms of the homogeneous ABR. The more feasible TRU enrichment also solves the problem of fabricating small pin diameters. This is because the higher uranium loading in the fuel also adds volume and hence diameter to the fuel pin. Also, increasing the uranium content of the driver fuel generally enhances the resonance feedback attributes of the reactor design.

Axial Targets and Axial Leakage Recovery

To highlight the potential for neutron economy improvements, the ability of the axial targets to “trap” axial leakage is tested. A series of parametric studies on core and pin geometry are performed in the next chapter using the REBUS code. These analyses ultimately culminated in the AHFTR design described in the Introduction. For the purpose of showing the axial target

effectiveness in this chapter, the region homogenized atom density data was imported to an MCNP calculation to recreate the BOEC DIF3D calculation from the REBUS fuel cycle simulation. No attempt was made to unfold the actual batch or exact fuel assembly compositions from this region-by-region data. The MCNP calculation was performed for both the AHFTR and ABR reference design.

Within the MCNP model, neutron current tallies were made for increasing heights in the core geometry. In MCNP, the current is tallied by simply totaling the number of particles, crossing a given surface within a specified angular range. This range corresponds to the limits of integration of the summation over $d\Omega$ about Ω in the equation:

$$J = \int_E dE \int_t dt \int_{\hat{\Omega}} d\hat{\Omega} \int_A dA \left| \hat{\Omega} \cdot \hat{n} \right| \phi(\hat{r}, E, \hat{\Omega}, t) \quad (2-8)$$

Where: J is the net leakage. E is neutron energy, t is time, A is the area of the tally surface, Ω is the solid angle over which the tally is taken. \hat{n} is the unit normal vector to the tally surface and ϕ is the region, energy and time dependent angular flux.

Integration of Equation 2-8 gives the net current with a positive sense in the direction of the normal vector. For the following calculation, this normal direction was chosen to be positive upward in the direction towards the top of the core. For neutrons leaving through the bottom of the core, the absolute value of the current is taken so that the current appears positive at all locations. The current and flux distribution for the AHFTR is given in Figure 2-9 and Figure 2-10.

The change in current per change in height is, for all practical purposes, the average axial leakage. It can be observed from Figure 2-9 that the net number of neutrons moving out of the core is less at the top of the targets (90 cm) than it is at the top of the active core (70 cm). This represents the combined effect of reflection and absorption by the targets. To quantify reflection

at the top of the core, the targets were replaced by: (1) a region of sodium, (2) axial reflector or (3) driver fuel. When compared with a sodium or steel reflector, the targets have less net current at the top of the target region than either of the two reflector compositions. This indicates the added effect of absorption in the targets. When the axial target region is replaced by fuel, the shape of the axial current profile flattens out as the neutrons enter the gas plenum above the core. Therefore, it is apparent that even though the target region contains some TRU, its neutron production is less than that produced by the active core region.

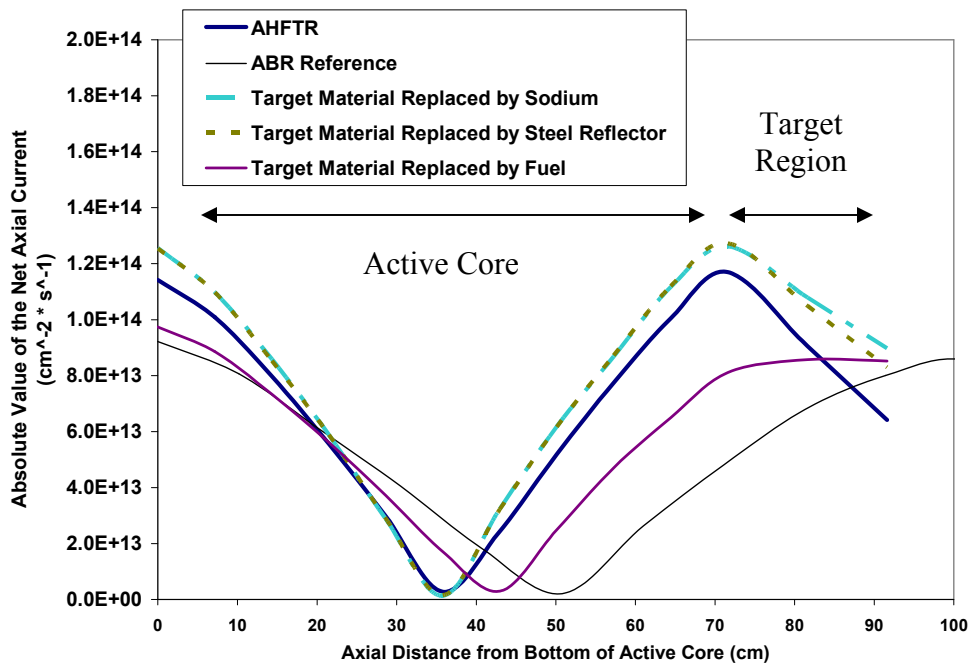


Figure 2-9. Axial current distribution of the AHFTR and ABR (MCNP)

Thus, it can be inferred from this comparison that the decrease in current in the axial targets is caused by a combination of axial reflection as well as capture reactions by the MAs. The reduction in the net current from the top of the active core to the top of the target region equates into a reduction in leakage by the target region. This reduction in leakage can also be seen by comparing the curvature of the scalar flux in the target region compared to that of the active core (Figure 2-10).

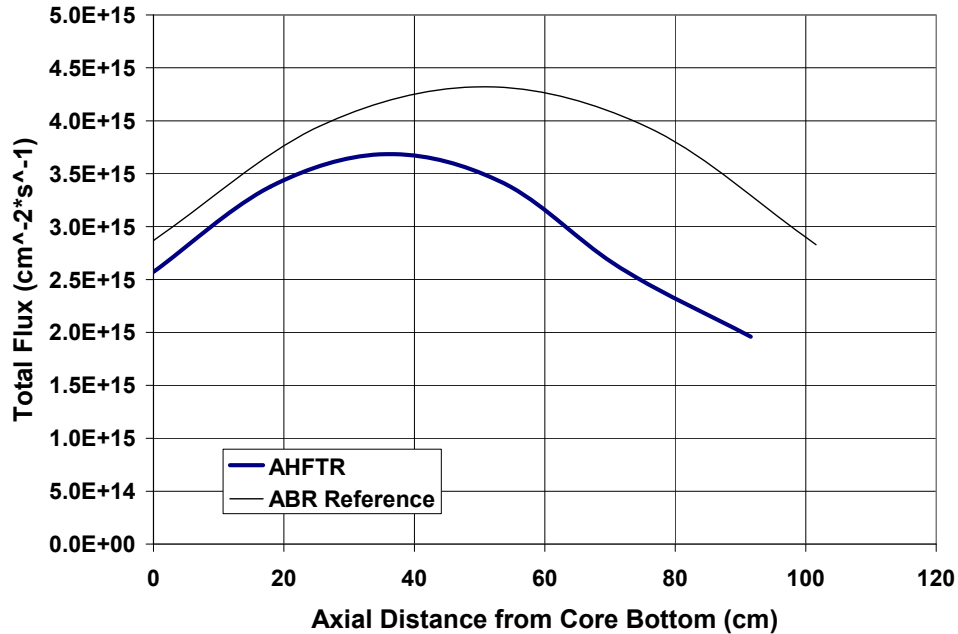


Figure 2-10. Axial flux distribution of the AHFTR and ABR (DIF3D)

Axial Targets and Minor Actinide Conversion

The capture effect of the MAs in the moderated target region can best be qualified by examining the energy dependence of the capture and fission reaction rate of Am-241. To do this, the MCNP model used for the above neutron current calculation was modified to tally the neutron flux in the target region and in the active core region. This flux tally was discretized into 33 equal lethargy sized bins (same as that used by MC²-2) in order to create a point-wise neutron energy spectrum for both regions. This binned flux tally was weighted with a cross section multiplier corresponding to the isotopes and reaction rates of interest. Using the Monte Carlo method, this multiplier effectively integrates the reaction rate in each bin from an energy continuous flux and cross section. To calculate a volume averaged flux, MCNP sums the length of all neutron track-lengths crossing the tally region and then divides this summation over the region's volume. The flux multiplier is used in a similar way except the track-length of each

tally is multiplied by the continuous energy microscopic cross section of the desired reaction and isotope type.

$$R(E_{i+1/2}) = \int_{E_i}^{E_i+\Delta E} \phi(\tilde{E})\sigma(\tilde{E})d\tilde{E} = \frac{\sum_E L_{\text{track-length}}(E) \times \sigma_i(E)}{V} \quad (2-9)$$

Where: $L_{\text{track-length}}$ is the total length of travel of a neutron as it passes through the tally region. V is the volume of the tally region. $\sigma_i(E)$ is the microscopic cross section for the reaction and isotope of interest for the tally multiplier.

Using the 33 energy bins, the binned reaction rates give an approximately smooth distribution of the reaction rates as a function of energy. The binned capture and fission reaction rate spectra for Am-241, Pu-238 and Pu-239 are plotted in Figure 2-11 and Figure 2-12. It is important to mention that these plots give the *microscopic* reaction rate which is normalized per atom and not the *macroscopic* reaction rate which would be weighted by the atom density of each isotope.

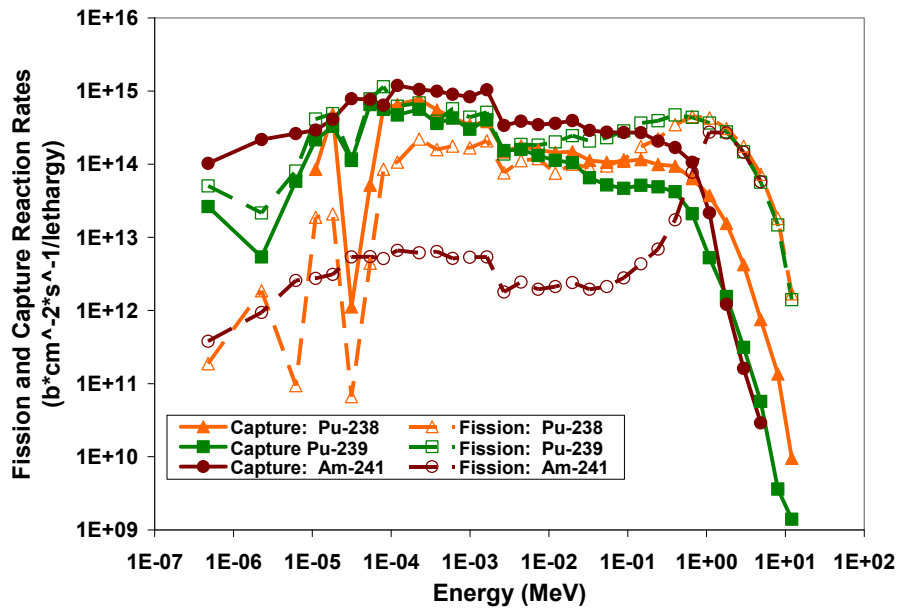


Figure 2-11. Binned “microscopic” reaction rate spectra of select isotopes as a function of incident neutron energy on an atom in the moderated target region (MCNP)

As can be seen in Figure 2-11, the fission reaction rate of Am-241 is several orders of magnitude less below one MeV than for any of the plutonium atoms. However, the Am-241 capture reaction rate is of the same order of magnitude as any of the plutonium fission reactions in plutonium. Therefore it is evident that transmutation of an Am-241 atom into a plutonium (i.e., Pu-238) atom will increase its fissile worth. It is useful to note that the Pu-238 fission rate falls off sharply at energies below 100 eV (Figure 2-13). This is due to the fact that the Pu-238 fission cross section falls off sharply below 100 eV.

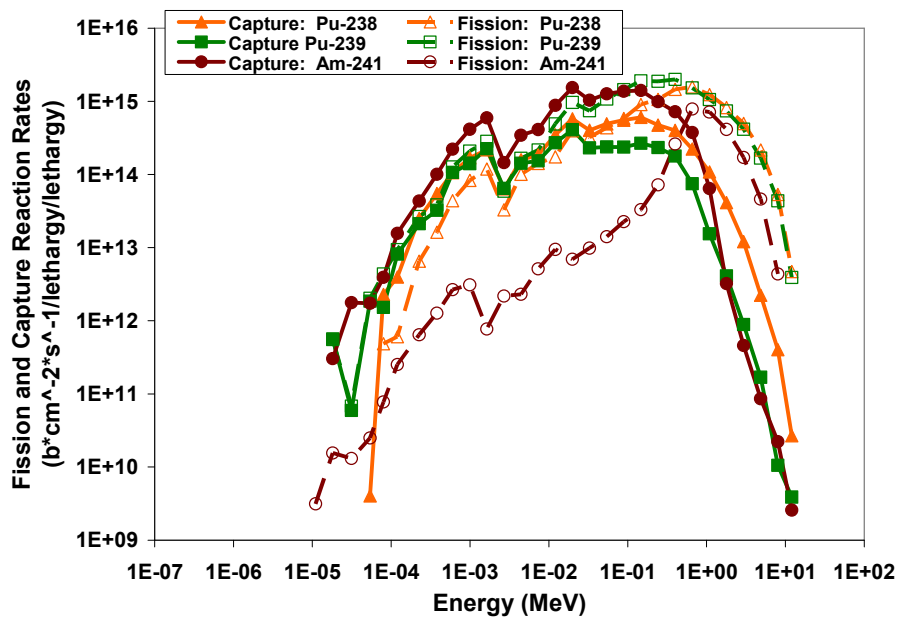


Figure 2-12. Binned “microscopic” reaction rate spectra of select isotopes as a function of incident neutron energy on an atom in the active core (MCNP)

It is also noteworthy to point out that neutron absorptions in Pu-238, that do not result in fast fission transmutes into fissile Pu-239, which has a high fission cross section at all energies. Unlike the purely fast spectrum (Figure 2-12), isotopes in the axial target are equally exposed to neutron fluxes in both energy ranges. Because the practical energy range for fission reactions increases with each successive neutron capture (Figure 2-11), the target is essentially breeding fissile worth, even though fissile atoms are not a direct result of the first neutron capture.

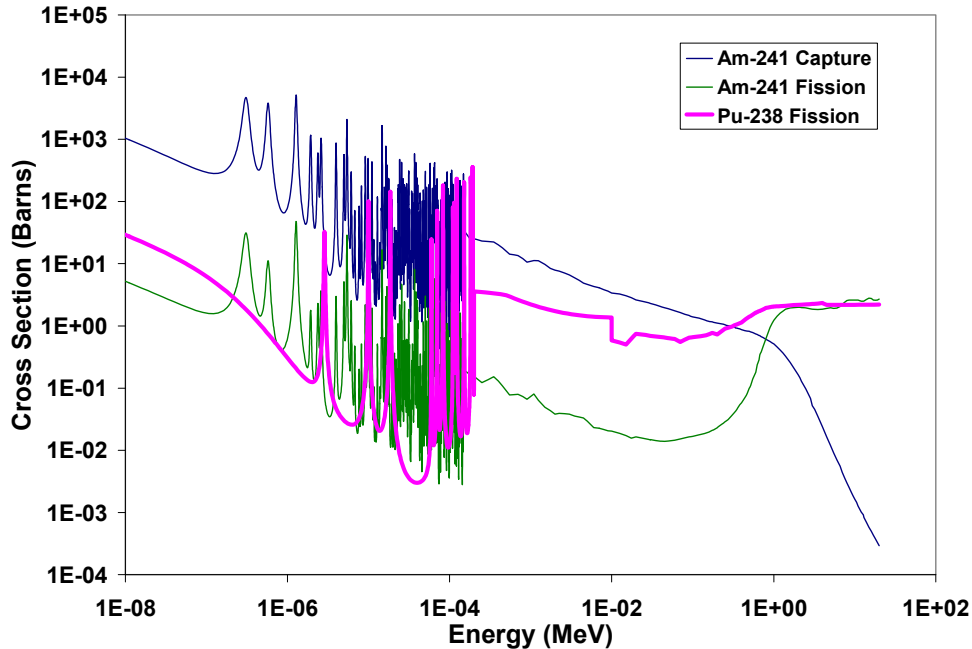


Figure 2-13. Comparison of capture and fission cross sections between Am-241 and Pu-238 (ENDF-VI)

If the MA atom concentration in the targets is sufficiently high, the Am-241 capture reactions will energy shield the fission reaction of both Pu-238 and Pu-239. Because neutrons are being absorbed in Am-241 instead of plutonium, this energy shielding effect is roughly analogous to the spatial resonance shielding provided by a burnable poison in an LWR fuel pin. Because of this energy shielding, the fissile worth created via transmutation in the target region can not be truly realized until the transmuted plutonium atoms are reprocessed and placed in the fast spectrum as driver fuel.

The flux in the active core is entirely fast (Figure 2-12). Therefore, the corresponding reaction rate spectra are also in the fast energy range. Hence, the energy shielding ability of Am-241 over Pu-238 or Pu-239 is not available. The capture cross section of Am-241 falls off sharply after one MeV, whereas the fission cross sections of Pu-238 and Pu-239 are much higher in this energy range. Also, the concentration of Am-241 is significantly less in the driver fuel than it was in the targets because of the much smaller Am-241 concentration in the driver fuel

than in the targets. Hence, without the energy shielding by Am-241, the fissile worth of Pu-238 and Pu-239 is higher in the active core than in the target region. The change in fissile worth can be seen by observing the differences in fission-to-absorption ratio between the target region and the active core region (Table 2-3).

Table 2-3. Fission and capture one-group cross sections and fission-to-absorption ratios for the AHFTR axial target and active core regions (MCNP)

	Axial Targets			Driver Fuel/Active Core		
	Fission (barns)	Capture (barns)	Fission per Absorption	Fission (barns)	Capture (barns)	Fission per Absorption
U-234	0.32	3.00	0.10	0.35	0.46	0.44
U-235	3.93	1.69	0.70	1.64	0.42	0.80
U-236	0.12	1.73	0.06	0.10	0.33	0.23
U-238	0.04	0.63	0.06	0.04	0.22	0.15
Np-237	0.31	4.83	0.06	0.34	1.19	0.22
Np-238	10.16	0.36	0.97	3.52	0.11	0.97
Pu-236	8.54	1.66	0.84	3.30	0.50	0.87
Pu-238	1.36	2.02	0.40	1.10	0.56	0.66
Pu-239	3.58	1.91	0.65	1.67	0.33	0.83
Pu-240	0.37	2.19	0.15	0.39	0.38	0.51
Pu-241	5.74	1.45	0.80	2.18	0.33	0.87
Pu-242	0.26	1.78	0.13	0.27	0.33	0.46
Am-241	0.28	4.75	0.06	0.28	1.29	0.18
Am-242 ^m	11.54	1.71	0.87	3.31	0.26	0.93
Am-243	0.20	4.68	0.04	0.20	1.15	0.15
Cm-242	0.15	1.57	0.09	0.16	0.21	0.44
Cm-243	8.58	1.20	0.88	2.24	0.17	0.93
Cm-244	0.45	2.24	0.17	0.44	0.66	0.40
Cm-245	6.31	0.83	0.88	2.00	0.25	0.89
Cm-246	0.28	0.93	0.23	0.27	0.17	0.61
Cm-247	2.59	0.98	0.73	1.94	0.25	0.88
Cm-248	0.35	1.96	0.15	0.31	0.18	0.64
Bk-249	0.18	5.14	0.03	0.17	0.97	0.15
Cf-249	6.03	1.45	0.81	2.33	0.56	0.81
Cf-250	0.95	5.78	0.14	1.19	0.29	0.81
Cf-251	6.09	1.66	0.79	2.16	0.25	0.90
Cf-252	1.94	0.80	0.71	0.62	0.23	0.73
Combined	0.05	0.12	0.27	0.06	0.06	0.47

Based on fission-to-capture ratio data from Table 2-3, one Pu-238 atom is produced for every 1.38 neutron captures in Am-241 in the target region. This newly formed Pu-238 atom than fissions for every 2.49 neutron absorptions. This is a smaller neutron investment compared to LWR IMF; which is 5.47 absorptions per fission (Table 1-2). An additional capture in Pu-238

produces Pu-239 which has a fission-to-absorption ratio in the targets of 0.65. In the fast active core region, 1.586 neutrons are required to convert an Am-241 atom into a Pu-238 atom. This newly formed Pu-238 atom then fissions for every 1.51 neutron absorptions. The much higher fission-to-absorption rate of Pu-238 in the active core (i.e., $1/1.51=0.66$) than the axial targets (i.e., $1/2.49=0.40$) shows the utility of the spectrum shift from the thermalized to the fast spectrum. An additional capture in Pu-238 produces Pu-239 which has a fission-to-absorption ratio in the active core of 0.83.

Combining Leakage and Capture Effects

As can be seen from Figure 2-14, even though the target region contains moderating pins, the moderating effect places most of the flux in the epithermal to fast energy range. In this energy range, most of the resolved resonances are very close to each other and not sufficiently wide to create local flux depressions in the core or pin geometry. This is different from thermal spectrums where neutron slowing down places most of the neutrons in the thermal energy range where the resonances are much wider and well separated. Therefore, spatial self-shielding effects between well resolved and well separated resonances have less importance in the axial target region than for completely thermal spectrums such as for LWRs. Hence, the “same-spectrum” region-wide homogenization assumptions used in cross section and flux calculations by the MC²-2 and DIF3D/REBUS codes are adequate for approximating the lattice physics in the active core and target regions.

Also, it was demonstrated in this chapter that SFRs inherently have a high TRU enrichment for criticality reasons because of their inherent high rate of neutron leakage. Therefore, the relative change in concentration of fissile atoms (i.e., TRU enrichment) as a function of burnup can be small, even for high burnups. Hence, it should be expected that the neutron spectrum in the core is fairly insensitive to the effect of fissile atom depletion.

Therefore, the need for spectrum updated cross section sets (i.e., *micro-depletion*) in analyzing the ABR and AHFTR is not as strong as it is for LWR spectrums. In LWR fuels, the enrichment is small compared to SFRs. Therefore as the LWR fissile atoms are depleted, the percent change in the fissile concentration is significantly more than it is for SFRs. The burnout of isotopes with resonances that are well resolved and well separated changes the magnitudes of flux depressions that are caused by those resonances. Therefore, for LWR fuels it is important to create several cross section libraries corresponding to different stages in depletion. Because, SFRs such as the ABR and AHFTR do not have significant changes in the neutron spectrum with burnup, this spectrum updating or micro-depletion is not necessary.

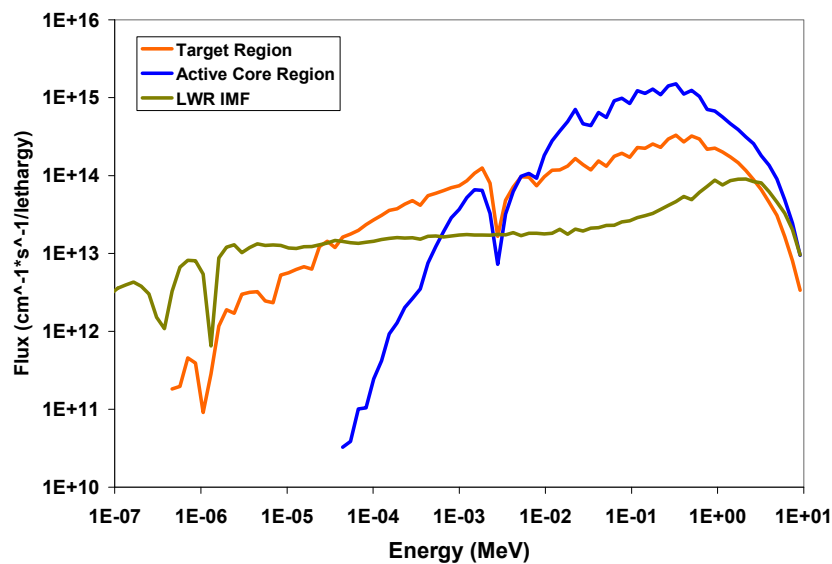


Figure 2-14. Comparison of flux spectrums between LWR IMF (thermal), AHFTR target region (epithermal-fast) and AHFTR active core region (fast) (MCNP)

In fact, the ability of the AHFTR to breed plutonium through Am-241 transmutation is made possible because the target region's spectrum does not change significantly with burnup. The moderation effect causes the energy shielding of plutonium unresolved and poorly resolved resonances by Am-241. This energy shielding minimizes the in situ burnup of plutonium isotopes in the target region. Therefore, transmuted plutonium isotopes are allowed to

accumulate with irradiation. The fissile usefulness of this transmuted plutonium is only fully realized when these isotopes are placed in the active core where the spectrum is much harder.

The negligible spectrum change in the target region is mostly due to the fact that the target region's epithermal spectrum is not strongly affected by the well resolved and well separated resonances occurring at thermal energies. The epithermal flux can be explained by the fact that the target volume (despite the presence of moderating rods) is still mostly filled with sodium, steel and HM atoms. In addition, the curvature of the flux (i.e., buckling) in the targets is not completely flat and is similar to the active core. Therefore, the axial leakage through the targets is still fairly significant. This fact suggests that the target region is not a black absorber and that a significant number of neutrons are lost through leakage before they can be moderated and absorbed. Hence, the axial target region behaves more as an integral component of the core than a neutron sponge outside of the core.

The target composition contains a starting amount of plutonium and uranium that makes the total plutonium content and corresponding spectrum roughly constant throughout the irradiation. This constant level of plutonium (regardless of isotopic composition) helps minimize spectrum shifts in the target region. A detailed explanation of the target composition of MAs, some plutonium and some uranium is given in the next chapter.

CHAPTER 3 AXIAL TARGET DESIGN ANALYSIS

As discussed in the previous chapter, in order to give a high net TRU destruction rate it is necessary to greatly reduce the SFR's conversion ratio. This has the advantage from a waste management point of view of decreasing the amount of net TRU production from neutron capture in U-238. The first necessary requirement for reducing the amount of U-238 capture reactions is to decrease the amount of U-238 in the SFR. This decision leads to an ABR design with no U-238 radial blankets. Furthermore, the removal of blanket assemblies reduces the overall reactor size from an S-PRISM design which has nine rows of driver and blankets to the current 1000 MWth ABR design with seven driver rows [7,19,55,56].

Waste Management Philosophies and Conversion Ratio Definition

Traditionally, the fissile CR (f CR) has been defined as the fissile atom production rate divided by the fissile atom destruction rate [14]. The fissile production rate is defined as the sum of neutron capture reactions (including reactions of fissile atoms) that lead to production of a fissile atom. The fissile destruction rate is the sum of neutron capture and fission reactions which remove fissile atoms. Therefore, the f CR is simply the ratio "or balance" between the mass production rate (source) divided by the rate of mass destruction (sink). This more traditional CR definition is the one calculated and reported by the REBUS code [57].

$$f \text{ CR} = \frac{\text{Fissile Atom Production}}{\text{Fissile Atom Destruction}} = \frac{\sum_p N^p \sigma_c^p \phi}{\sum_d N^d (\sigma_c^d + \sigma_f^d) \phi} \quad (3-1)$$

Where: (d) is the daughter product resulting from the neutron capture and subsequent decay (transmutation) from the (p) parent isotope. N is atom density and σ_c and σ_f are the single group neutron capture and fission cross sections respectively.

This definition has been altered slightly by authors in recent years to mean the net TRU produced from uranium divided by the net TRU destroyed by fission giving a transuranic burning CR (τ CR) [58]. The difference between the τ CR and ι CR is that the ι CR does not give credit to capture reactions in the denominator because these reactions only transmute existing TRU into other TRU. From a waste management standpoint only fission removes transuranic waste from the fuel cycle. Additionally, only capture reaction of uranium (specifically U-236 and U-238) that lead to TRU atoms are allowed in the denominator of the τ CR because these isotopes directly transmute into Np-237 and Pu-239.

$$\tau \text{CR} = \frac{\text{TRU Production}}{\text{TRU Fission}} \cong \frac{N^{U-236} \sigma_c^{U-236} \phi + N^{U-238} \sigma_c^{U-238} \phi}{\sum_d N^{TRU} (\sigma_f^{TRU}) \phi} \quad (3-2)$$

The change in the definition of CR is made to reflect the ABR's principle design objective, which is to destroy TRU. The only real discrepancy between these two definitions is the accounting of MA transmutation. The τ CR does not consider fissile plutonium generation from MAs as a source term in the numerator. The ι CR gives an indication of the balance between transmutations over total absorption reactions in the fuel but does not give an indication of the actual TRU burning performance of the core. In both cases, MA transmutation is simply treated as existing TRU isotopes being converted into other TRU. For example, if only plutonium and no uranium are supplied to the SFR, then the τ CR is zero. This is because the net TRU production in the numerator of the τ CR is zero. The ι CR would also be near zero because the transmutation parent of Pu-239 is U-238. The τ CR and ι CR would be in good agreement because the contribution of U-238, which is the dominating parent isotope in the numerator of the τ CR, would be near zero.

However, if neptunium and americium is the only fertile species and the only fissile species is their transmutation daughter Pu-238 (and ultimately other TRU through successive neutron capture), then the ρ_{CR} is still zero. Yet, the ρ_{CR} would be near unity. In this hypothetical situation, there is no net production of TRU. However, this hypothetical core would generate its own fissile worth, in the form of transmuted plutonium, in order to meet the excess reactivity and cycle length requirements. Therefore, the core would be self sufficient from a reactivity standpoint and thus require no external supply of *fissile* isotopes. Similar to a breeder reactor, only an external supply of *fertile* MA isotopes would be required.

It is important to remember that transmuted plutonium (Pu-238) is not fissile in the classical sense because in order for it to fission, additional kinetic energy must be added to overcome the critical energy for fission. This is why the fission cross section of Pu-238 is so much higher in the fast spectrum than in the thermal spectrum (Table 1-1). Pu-239 is fissile by definition because fission can occur simply by contact with a neutron of virtually zero kinetic energy.

The AHFTR design concept uses the fertile nature of SNF MAs to reduce the amount of externally supplied SNF Pu-239 needed to supplement the plutonium bred internally. This has the overall effect of reducing the ρ_{CR} while increasing the ρ_{CR} . Meeting the reactivity demands of the fuel cycle using MAs reduces the demand for externally supplied fissile material from SNF. The resulting surplus of SNF plutonium could be better used to fuel other SFRs such as the ABR or perhaps be used to make plutonium based Mixed Oxide (MOX) fuel for LWRs.

Odd mass number plutonium isotopes (Pu-239,241) are fissile in any spectrum which makes them a viable fuel for thermal reactors. In effect, SNF plutonium in a MOX fuel form can have a ρ_{CR} between 0.6 and 0.7 when irradiated in a PWR [14]. Given that several of the newer

classes of LWR's (Generation III and III+) are designed with the capability to be fueled with full MOX cores, these reactors are a possibility for burning the plutonium component of SNF.

However, for the purpose of bounding the scope of this work, only the ABR and AHFTR are considered as the final destination for SNF Pu and MAs in the closed fuel cycle analyses. For the closed fuel cycle analyses to follow, the emphasis of the AHFTR is on MA consumption, whereas the ABR focus is to destroy the plutonium component of SNF TRU.

This chapter will show that the AHFTR is well suited for the task of burning the MAs from TRU. Therefore, a combination of ABRs and AHFTRs can be used to burn the TRU produced by LWRs. In this scenario, most of the TRU mass, which is plutonium, would be burned by ABRs. A fraction of the mixed-fleet (ABR and AHFTR) would be reserved for AHFTRs which are dedicated to MA burning (Figure 1-9). An economic evaluation that compares this hybrid ABR and AHFTR fuel cycle with the single reactor ABR fuel cycle will be evaluated in Chapter 7.

Transmutation Based Reactor Design

In this chapter, a parametric design study is conducted on the effects of core flattening, moderation and heavy metal fuel content upon the transmutation performance of the axial targets. The plutonium generation in the axial targets is also a function of reactor and fuel geometry. Therefore, the primary purpose of the parametric study is to evaluate the tradeoff between core performance factors and the maximum MA destruction rate. Also evaluated is the: cycle length, excess reactivity, and "total core" Doppler coefficient and sodium void worth. All these factors are related by core geometry and fuel composition.

In this parametric study, the target's height and composition are held constant. The targets comprise a 20 cm tall axial blanket placed between the plenum and active core. In this parametric study, the lateral core layout is assumed to be identical to the ABR case, reported by

Hoffman, with a τ CR of 0.5 [7]. The lateral core layout for the ABR with the axial target modification is shown in Figure 3-1. Starting with the ABR reference height of 101.6 cm, the active driver core height was varied to 51.6 cm in 10 cm increments. For each core height, the total core power was reduced by the fraction of volume removed from the active core by the height reduction. The reduction in power with height was done in the parametric study to give an equally comparable power density, depletion rate and cycle length for each height. Table 3-1 gives the reactor power of the core shown in Figure 3-1 for each increment in active core height.

Table 3-1. Reactor thermal power and core heights evaluated in parametric analysis

Total core height (cm)	121.6	111.6	101.6	91.6	81.6	71.6
Active core height (cm)	101.6	91.6	81.6	71.6	61.6	51.6
Reactor Thermal Power (MW)	1000	900	800	700	600	500

For each one of these active core heights, a range of pin pitch-to-diameter ratios, which correspond to variable CR, is evaluated. For comparison purposes, the ABR reference (Figure 1-5) was evaluated for each increment in pin pitch-to-diameter ratio. These ABR reference cases provide a benchmark for comparison of reactor parameters for down-selecting to a practical AHFTR core height and pin diameter.

The pin pitch-to-diameter ratios and the corresponding fuel assembly volume fractions are shown in Table 3-2. These values represent the fuel pin dimensions, used by Hoffman, to vary the ABR τ CR from 1.0 to 0.25.

Table 3-2. Reference fuel assembly design for varying pitch-to-diameter ratio.

	p/d=1.1	p/d=1.176	p/d=1.293	p/d=1.357
τ CR of the reference ABR	1.00	0.750	0.500	0.250
Fuel pin diameter (cm)	0.808	0.755	0.623	0.464
Fuel pin pitch (cm)	0.888	0.888	0.806	0.630
Pins per assembly	271	271	324	540
	Fuel Assembly Volume Fraction			
Fuel	34.27%	29.30%	22.08%	17.40%
Bond	11.42%	9.77%	7.36%	5.81%
Structure	25.73%	25.68%	26.41%	29.15%
Coolant	28.79%	35.25%	44.15%	47.60%

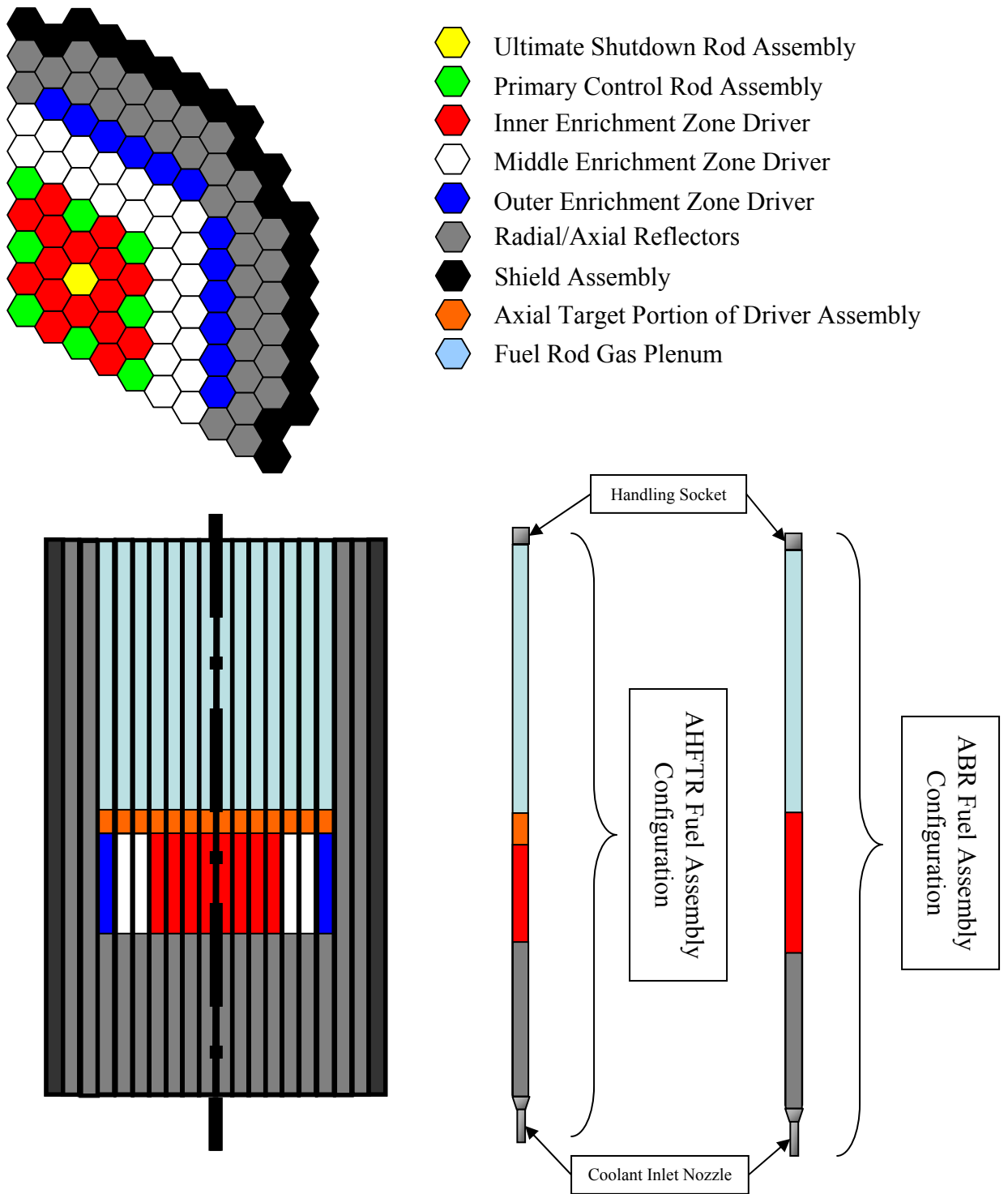


Figure 3-1. Preliminary AHFTR core design used in parametric analyses

Finally, a core height and pin diameter that gives the highest transmutation efficiency while at the same time ensuring reactivity coefficients within the boundaries of the homogeneous

reference was selected. Using this core height and pin diameter combination, additional driver assemblies were added to the AHFTR core radius to bring the thermal power rating back to 1000 MWth as it is for the ABR design. This gives the AHFTR a commercial scale by roughly equating the overall active core volume and power to that of the ABR.

Transmutation Targets and Accompanying Fuel Cycle

Target rods are placed adjacent to zirconium hydride ($ZrH_{1.6}$) “dilution” rods in an axial blanket configuration above the driver fuel. The term “dilution” was adopted to describe blank fuel pins within the CAPRA core design that were filled with steel instead of fuel. A zirconium metallic fuel alloy is assumed for both driver and target rods. Zirconium hydride was selected as the moderator for its high thermal conductivity and melting temperature. A hydrogen-to-zirconium stoichiometric ratio of 1.6 was selected for zirconium hydride’s delta phase which retains composition for temperatures up to 1000°C (Figure 3-2) [59].

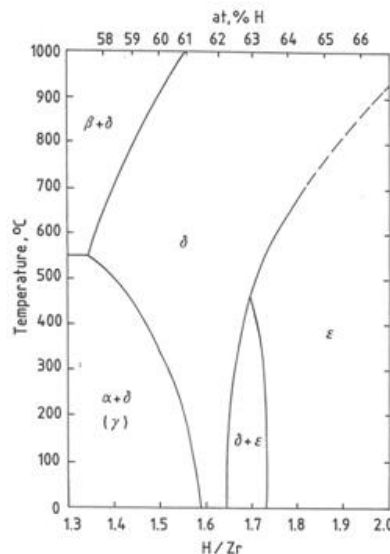


Figure 3-2. Zirconium hydride phase diagram for varying hydrogen content [59].

These driver fuel and axial target rodlets, “slugs”, are collocated within the same fuel pin and share the same plenum space. The term “slug” is common in metal alloy fuel literature which indicates the injection casting process used in fabrication. Therefore, the fuel rod contains

a stack of metal slugs as opposed to the ceramic oxide pellets typical of LWRs. The ratio of target to $ZrH_{1.6}$ containing fuel pins is approximately five to one (Figure 3-3). Therefore, for a typical hexagonal fuel assembly, 226 of the 271 pins contain target and 45 contain $ZrH_{1.6}$ slugs.

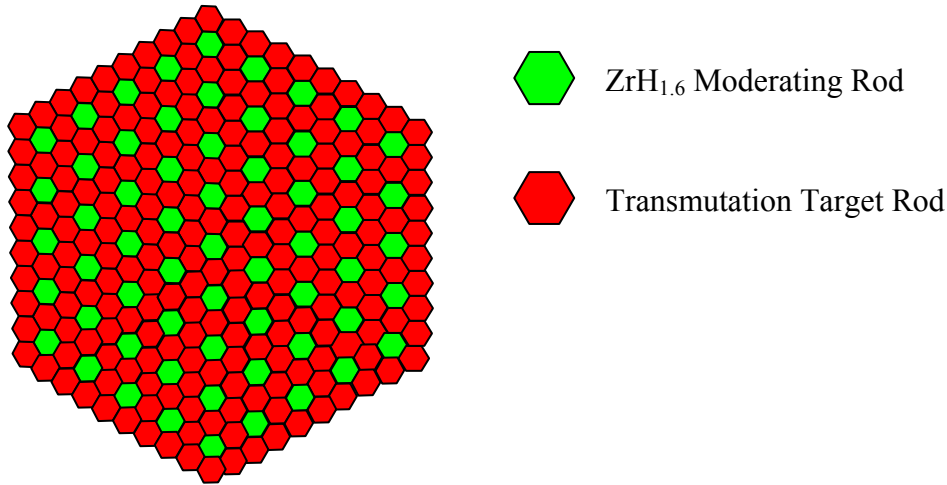


Figure 3-3. Representation of the axial target pin-lattice showing the orientation of targets (red) and zirconium hydride pins (green)¹

The accompanying fuel management strategy allows the targets and driver fuel to be discharged and recycled together in the same pyroprocessor batch. After pyroprocessing, the mixed target and driver mass streams supplies the fabrication of fresh driver fuel. Fresh targets are fabricated from the americium and curium component of SNF. This americium and curium stream is provided by the UREX+3 separations process (Table 1-8) for LWR fuel. The UREX+3 neptunium and plutonium stream provides the external fissile feed to the driver fuel as well as the targets. The neptunium is kept with the plutonium by the UREX+3 process for the purpose of enhancing proliferation resistance. Some plutonium is supplied to the targets to minimize the power swing as a result of Pu-238 and Pu-239 generation during the irradiation. The reasons and effectiveness of this approach are discussed in Chapter 6.

¹ The color pattern indicates the five-to-one relationship between targets and moderating rods. However, the actual number of pins in the picture is 210 targets and 61 zirconium hydride rods which is 77% and 23% of the total 271 pins respectively.

As depicted in Figure 3-4, the SNF americium and curium is irradiated only once in targets before it rejoins the neptunium and plutonium in the driver fuel. The fuel cycle scenario in Figure 3-4 (and also in Figure 1-8) is used as the model for the out-of-core fuel management operations performed by the REBUS code (Figure 2-1). The combined fuel cycle represented in Figure 1-9 is performed by two separate REBUS calculations: one for the ABR and one for the AHFTR.

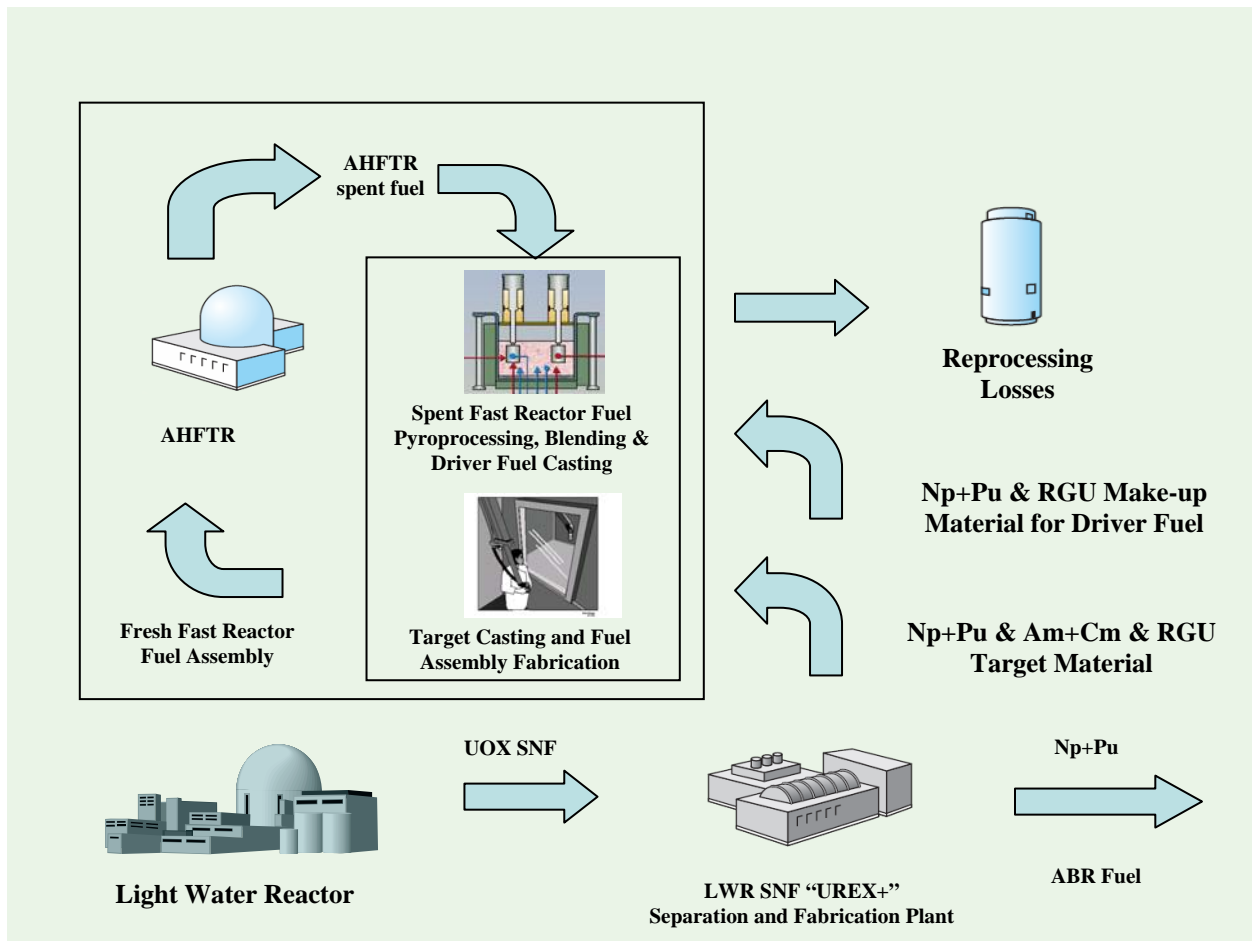


Figure 3-4. AHFTR fuel cycle scenario showing connections between partitioning and transmutation technology²

² Fuel cycle calculations performed for the LWR-through-UREX+ portion of the fuel cycle were performed by TRITON. Equilibrium fuel cycle calculations performed for the boxed portion of the flow chart were performed by REBUS. A separate REBUS calculation is performed to model the equilibrium cycle of the ABR. (See Figure 1-1 and Figure 1-9).

Therefore, sufficient americium must be destroyed in the targets such that the unburned americium is less than 5 w/o of the HM in the driver. The 5 w/o limit for MA driver fuel concentrations is selected as a guideline for ensuring acceptable reactivity kinetics features of the fast reactor. This limiting MA concentration also ensures that the expected irradiation performance of the driver fuel does not significantly deviate from the current experience base on metallic SFR fuels. The decision to use 5 w/o of MA per total HM is based on results obtained by the CAPRA program conducted in Europe to evaluate the EFR [16,17].

Similar to the ABR, the AHFTR has no radial blankets and uses three enrichment zones to flatten the radial power profile across the core [7]. For the purpose of simplification of nomenclature, the term “enrichment zone” is dropped and only the terms: inner core, middle core and outer core are used instead. The driver fuel composition is a TRU/U/10Zr (by weight) alloy. The ratio of middle and outer core enrichments to that of the inner core is: 1.25 and 1.50 respectively. The driver fuel composition definition is the same as the homogeneous ABR reference with the exception of the external feed being UREX+3 Np+Pu. The external feed for the reference metallic fueled ABR design groups all of TRU elements together using the UREX+1a process at the SNF aqueous reprocessing facility.

The target fuel fixed composition is $10\text{Np}+10\text{Pu}/10\text{Am}+10\text{Cm}+10\text{Bk}+10\text{Cf}/40\text{U}/40\text{Zr}$ by weight. Some of the UREX+3 separated Np+Pu stream (i.e. external feed) is diverted from the active driver fuel supply to the targets. None of the pyroprocessed plutonium is used to refuel the targets. This is mainly because the current pyroprocessing technology does not readily allow for elemental separation. The choice to use pyroprocessing allows the higher mass actinides of curium and californium that were generated during the target irradiation to be diluted over a larger fuel inventory. This dilution is intended to reduce the intensity of radiation fields and

hence shielding requirements to fuel fabrication workers dealing with recycled material. The 10 w/o Am+Cm+Bk+Cf concentration in targets was selected to retain the fuel performance characteristics observed in the AFC-1 irradiation experiments which were performed at INL. The AFC-1 tests and the reasons for proposing this specific combination of Am+Cm+Bk+Cf with Np+Pu, U and Zr is discussed in detail in Chapter 6.

Transmutation Target Physics

As mentioned in the introduction, the repository space benefit stems primarily from the removal of americium from the fuel cycle. This is because the repository's waste emplacement drift spacing is limited by the maximum rock temperature at the midpoint between them. This rock temperature is principally a function of the decay heat produced by Am-241 in the SNF [13]. Because of its long half-life, radiotoxicity, high solubility and low sorption in Yucca Mountain tuffs, Np-237 is the principal environmental concern to the biosphere, if water does come into contact with the SNF. Because, Np-237 is the alpha decay product of Am-241, americium destruction in transmutation targets also minimizes the Np-237 accumulation in the repository.

Am-241 and Np-237 have an even neutron number and thus the binding energy contribution of an absorbed neutron is not sufficient to overcome the critical energy required for fission. In fact, the addition of a neutron to an odd-neutron nucleus (fissile isotope) to form an even-neutron compound nucleus gives a binding energy change that is about one MeV greater than for changing an even-neutron nucleus into an odd-neutron compound nucleus. This explains the fission threshold at one MeV for the long lived MAs, Np-237 and Am-241. A neutron capture in Np-237 generates the fissile Np-238 nucleus. However, Np-238 quickly beta decays into Pu-238 with a short 2.117 day half-life. A neutron capture in Am-241 produces the fissile Am-242,242^m isotopes. The yield fraction to the ground state is estimated to be

approximately 85% in the fast spectrum [10]. This Am-242 ground state beta decays into Cm-242 with a branching ratio of 83%. The other 17% of Am-242 electron captures to become Pu-242. Cm-242 decays into Pu-238 with a 163 day half-life.

Because of the fission threshold, the Am-241 fission cross section below one MeV and above the resonance range (where the SFR neutron spectrum is very small) is two orders of magnitude less than for fission above one MeV (Figure 3-5). However, the capture cross section is almost as high as the Pu-239 fission cross section in the same energy range.

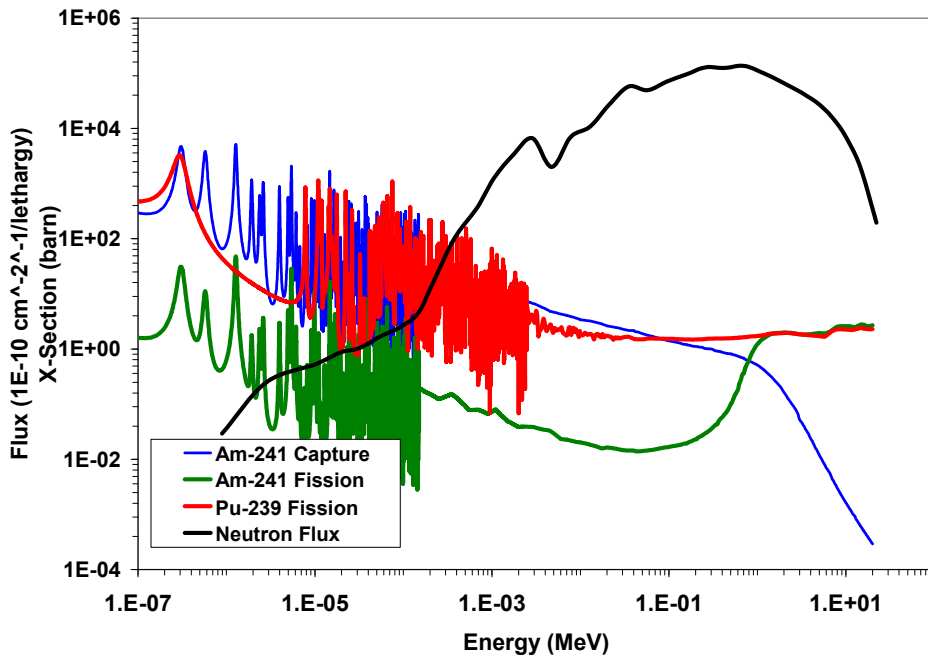


Figure 3-5. ENDF-VI americium and plutonium cross section plots versus a metal fuel SFR neutron spectrum

Therefore, the AHFTR axial target neutron spectrum is moderated slightly in order to reduce the neutron energy to just below one MeV. This increases the neutron capture in americium relative to plutonium fission in the targets. The effect can be seen by evaluating the ratio of total absorption in americium over total absorption in Pu-239. This increase can be seen by observing a capture and a fission based fuel utilization factor for the driver and the targets. In Table 3-3, a transmutation utilization factor is used to quantify the reaction probability of capture

in a given isotope divided by any absorption in the region of space being studied. The transmutation utilization factor is defined in the equation below.

$$\text{transmutation utilization} = \frac{N_i \sigma_i^r}{\sum_i N_i \sigma_i^c + N_i \sigma_i^f} \quad (3-3)$$

Where: i represents a given isotope in targets or driver fuel and r represents capture or fission

Similarly, the fission utilization factor is defined as the reaction probability of fission in a given isotope divided by any absorption in the region of the core being studied. Also supplied in Table 3-4 is a single group cross section ratio. The cross section ratio shows the spectral effect on the microscopic cross sections alone without being weighted by number density.

Table 3-3. Transmutation utilization factor (MCNP*)

	Driver		Target	
	CAP/ABS	FISS/ABS	CAP/ABS	FISS/ABS
Am-241	1.59%	0.34%	15.64%	0.93%
Pu-239	6.02%	30.36%	8.24%	15.43%

*Single group cross sections for Table 3-3 and Table 3-4 were performed by MCNP benchmarks of REBUS calculations using the final AHFTR core design.

Table 3-4. Single group cross section ratio (MCNP)

	Am-241 CAP over Pu-239 FISS	Am-241 ABS over Pu-239 ABS
Driver	0.77	0.78
Target	1.33	0.91

It is important to note that the ratio of the Am-241 capture to the Pu-239 fission cross section is greater in the target than the driver fuel because of moderation. It is also apparent that the total absorption cross section ratio of Am-241 over Pu-239 is greater in the targets than the driver fuel because of this increased neutron capture. This effect explains how the capture utilization factor for Am-241 is nearly equivalent to the fission utilization in Pu-239 in the targets.

The slight target moderation results in a relatively epithermal flux compared to that for the active driver regions as shown in Figure 3-6. It is important to note, that though the total flux in the targets is less than in the active driver, much of it is being depressed by resonance absorption

in the epithermal range. Much of this resonance absorption is in Pu-239 and U-238. However, resonance absorption in Pu-239 leading to fission serves to generate more neutrons. These neutrons have a relatively short mean-free-path because of the softer spectrum. Therefore, they remain locally within the target's neutron population. Moreover, resonance absorption in U-238 serves to generate more Pu-239. The combination of epithermal spectrum and plutonium breeding by both Am-241 and U-238 creates enough plutonium to replace the initial plutonium loaded in the targets at BOEC.

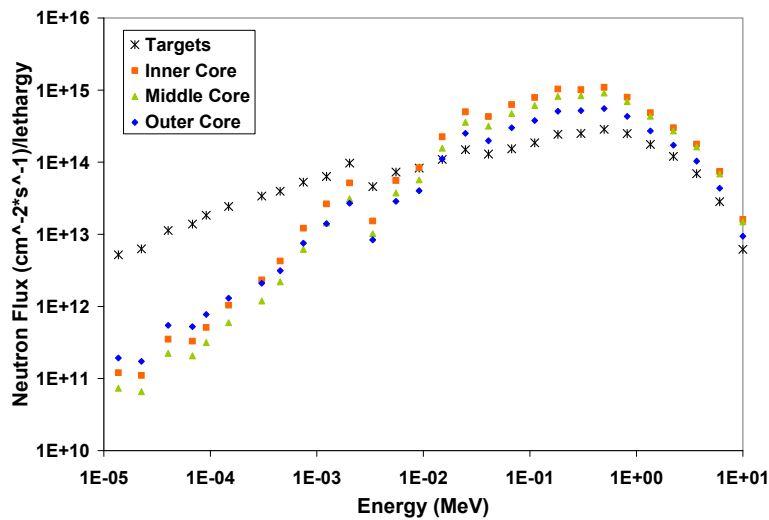


Figure 3-6. Target flux spectrum compared with the inner, middle and outer core for a 101.6 cm tall AHFTR with p/d of 1.1 (REBUS)

This breeding gives a τ_{CR} in the targets close to one but a τ_{CR} more near to 0.75. As can be seen by Figure 3-7, the total amount of Pu-239 stays relatively constant. However, the total plutonium content increases slightly, mainly from Pu-238,242 production from Am-241 transmutation. However, the total transuranic mass is being reduced as americium is being transmuted.

Parametric Study

Because the transmuted plutonium remains in the fuel cycle via the pyroprocessor, the amount of space reserved in the reactor for targets plays a significant role in the demand for the

UREX+3 supplied Np+Pu. From a geometry standpoint, the ratio of target volume to core volume is dictated by the active core axial height. From a physics standpoint, the amount of Pu-239 breeding in the active core is a function of core flattening. Since, breeding excess Pu-239 in the active core is not a primary objective of the AHFTR, it is desirable to minimize the active core's CR. Conversely, since breeding even-plutonium is an indicator of americium destruction, it is not obligatory to minimize the conversion ratio in the target region.

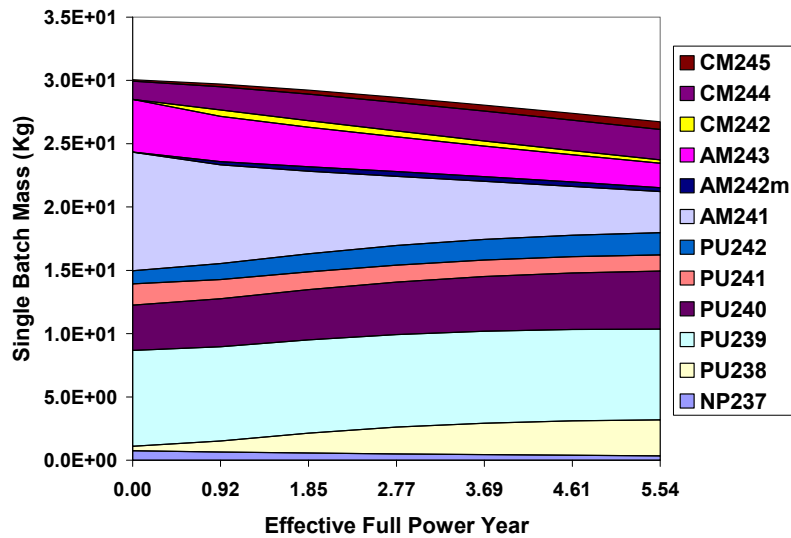


Figure 3-7. Isotope masses as a function irradiation time within the target region a 101.6 cm tall AHFTR with p/d of 1.1. Each color bar represents an isotope's mass (REBUS)

Effects of Pin Diameter and Core Height

Because of the vast range of options presented that affect the reactor's overall physics and transmutation performance, the following assumptions are made for the purpose of confining the parametric analysis of pin and core dimensions.

- Core design from Figure 3-1.
- Core height varied from 101.6 cm to 51.6 cm (Table 3-1)
- Fuel pin diameter varied from 0.808 cm to 0.464 cm (Table 3-2)
- Number of fuel pins per assembly (both driver and target region): 271 (Table 3-2)
- Peak fuel burnup constrained to 18 at. % (Figure 2-1)
- Ratio of zirconium hydride to target rods is: 1/5

The rate of americium destruction is a function of the target spectrum, active core axial leakage and target rod volume. Increasing the diameter of the target rod also increases the volume of americium charged to the AHFTR per cycle. If the reactor cycle is shortened, then the time rate of americium fed to the core is increased because the target mass loaded per cycle is constant due to the fact that the target rod composition has been fixed. This does not, however, indicate the spectrum effect of the zirconium hydride content or flux intensity in the targets. Because the target irradiation time is not held constant, simply comparing the ratio of charged to discharged target americium is not an adequate indication of the destruction efficiency. Instead, a half-life is defined for Am-241 transmutation which quantifies the magnitude of the capture reaction rate. Because the rate of Am-241 production rate via beta decay from Pu-241 is relatively slower than its destruction rate via neutron capture, the transmutation half-life can be approximated using a first order differential equation. Therefore, Am-241 destruction can be characterized with a purely exponential behavior just as with radioactive decay. This exponential behavior is given by the Am-241 production and decay rate equation. Table 3-5 shows the irradiation time required to reduce the americium mass by half.

$$\frac{dN}{dt} = \lambda_{Pu-241}^{decay} N - N \sigma_{Am-241}^{capture} \phi \Rightarrow \frac{dN}{dt} = \lambda_{Am-241}^{capture} N \Rightarrow T_{1/2}^{transmutation} = \frac{\ln(2)}{\lambda_{Am-241}^{capture}} \quad (3-4)$$

Table 3-5. Transmutation half-lives for a preliminary AHFTR design (Years) (REBUS)

Pitch/Diam.	p/d=1.1	1.176	1.293	1.357
101.6 cm	2.49	2.31	2.04	1.87
70.6 cm	2.73	2.54	2.24	2.06
50.6 cm	3.23	2.99	2.64	2.44

Notice the half-life decreases for decreasing pin diameter. This can be explained by the higher sodium fraction in the active core for decreasing fuel pin diameter. Increased leakage invests more neutrons in the targets. The decreasing half-lives with height are also related to axial leakage. However, the expected result is a decrease in half-life due to an increase in

leakage with the core height reduction. This contradiction in the half-life trend with core height can be explained by more evenly distributed neutron utilization in the active driver core.

Because of the enhanced axial leakage, the driver fuel radial power profile develops a depressed region in the inner core with decreasing height. The increase in the americium transmutation half-life with decreasing core height in Table 3-5 is caused by a reduction in the intensity of neutrons leaving the inner core region.

It is important to note the conformity of the three power profiles plotted in Figure 3-8 in the area of the outer core. This behavior is indicative of the cosine shape of the radial flux profile as neutrons leave the core. The increased axial leakage shown in Figure 3-9 affects the curvature of the radial power profile in the inner core region more so than in the outer region. This is because the axial flux gradient is decreased more in the inner core than the outer core. The flux in the outer core regions are already suppressed everywhere by radial leakage. This explains the conformity of the three different radial power profiles in Figure 3-8 at the outer edge. Because the power density becomes more evenly distributed axially and radially, the power density on the active core top surface becomes reduced.

A flatter radial power profile also reduces the radial power peaking. The reduction in power peaking in the inner core makes possible raising the reactor power, which was reduced in the parametric study for decreasing core height. Even though the decrease in core height increases axial buckling and hence axial leakage, the larger buckling in the radial direction relative to the axial direction causes flux in the inner core to be reduced which gives the flat radial power profile. This reduction of the inner core flux is also a result of the reduction in power for each reduction in core height which was done for the purpose of the parametric study.

Because of the depressed flux in the inner core, the power of the final flattened AHFTR core geometry is increased to give a more realistic power density.

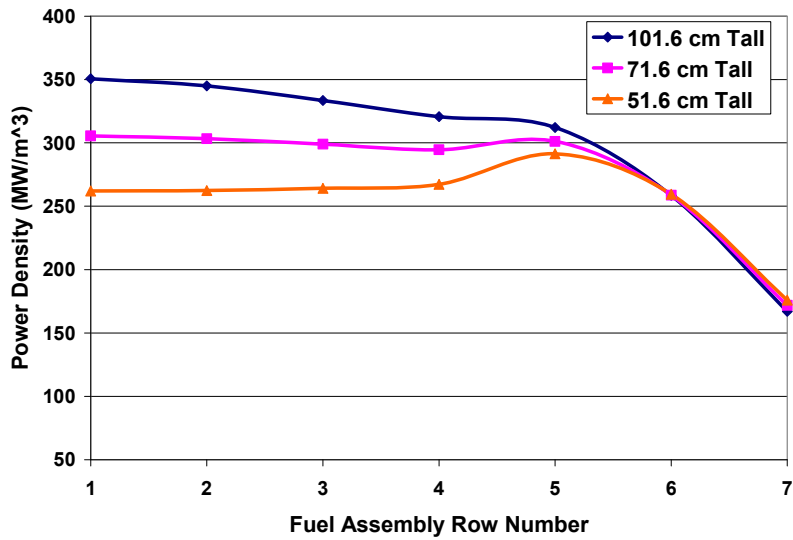


Figure 3-8. Active core radial power density profile for a preliminary AHFTR with active core height: 101.6, 71.6 and 51.6 cm (p/d=1.1) (REBUS)

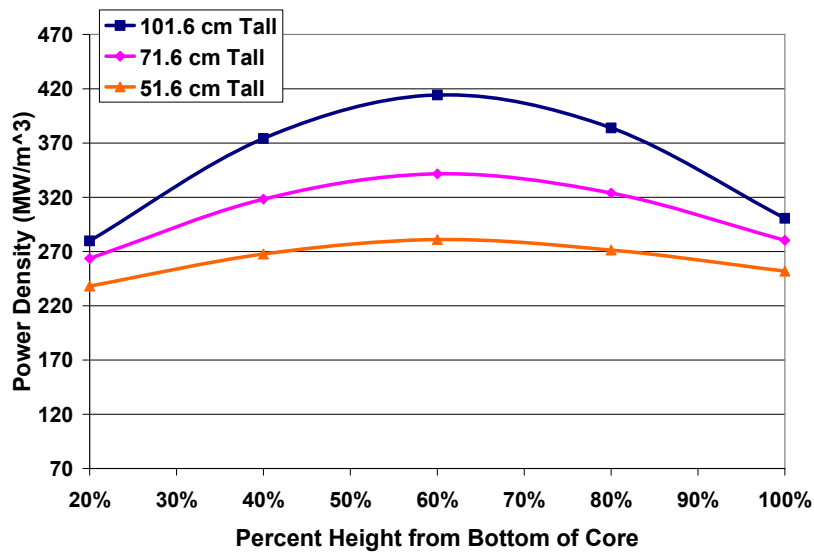


Figure 3-9. Inner core axial power density profile for a preliminary AHFTR with active core height: 101.6, 71.6 and 51.6 cm (p/d=1.1) (REBUS)

After increasing reactor power back to the practical limit, the increased power density in the targets will translate into a higher flux density for transmutation. Therefore, the transmutation half-life for the targets with a more realistic thermal power rating will be higher

than for the parametric study. A following section describes two possible AHFTR core geometries with two different active core heights and a 1000 MW power level.

Effects of Moderating Pins

The affect of moderation on the transmutation efficiency of the target region was also evaluated. Using a pin pitch-to-diameter ratio of 1.176 from Table 3-2 and a core height of 101.6 cm, the number of zirconium hydride rods per target rods was varied. The ratio of zirconium hydride rods per target rods was varied from: 1/5, 1/6, 1/7, 1/8 and 1/9. All of the other design variables used in the previous section were kept the same:

- Core design from Figure 3-1.
- Core height of 101.6 cm, Fuel pin diameter of 0.755 cm (Table 3-2)
- Number of fuel pins per assembly (both driver and target region): 271 (Table 3-2)
- Peak burnup constrained to 18 at. % (Figure 2-1)
- Vary the number of zirconium hydride to target rods from 1/5 to 1/10

It was found that the affect of moderator did have an affect on transmutation efficiency.

Table 3-6 gives the transmutation half-life of Am-241 for each moderator-to-target rod ratio.

Table 3-6. Transmutation half-life of Am-241 for varying number of moderating rods per target rods in the target region for the preliminary AHFTR design (REBUS)

Description*	Transmutation Half-life (Years)
One ZrH _{1.6} per Nine Target Rods	3.903
One ZrH _{1.6} per Eight Target Rods	3.759
One ZrH _{1.6} per Seven Target Rods	3.605
One ZrH _{1.6} per Six Target Rods	3.411
One ZrH _{1.6} per Five Target Rods	3.193

*Total number of pins is held constant by the fuel assembly design

It is important to note that the transmutation half-life decreases for increasing moderator. This means that the addition of hydrogen to the target region does contribute a spectrum effect to the transmutation efficiency. Figure 3-10 and Figure 3-11 shows the average neutron spectrum in the target region for each moderator-to-target rod ratio.

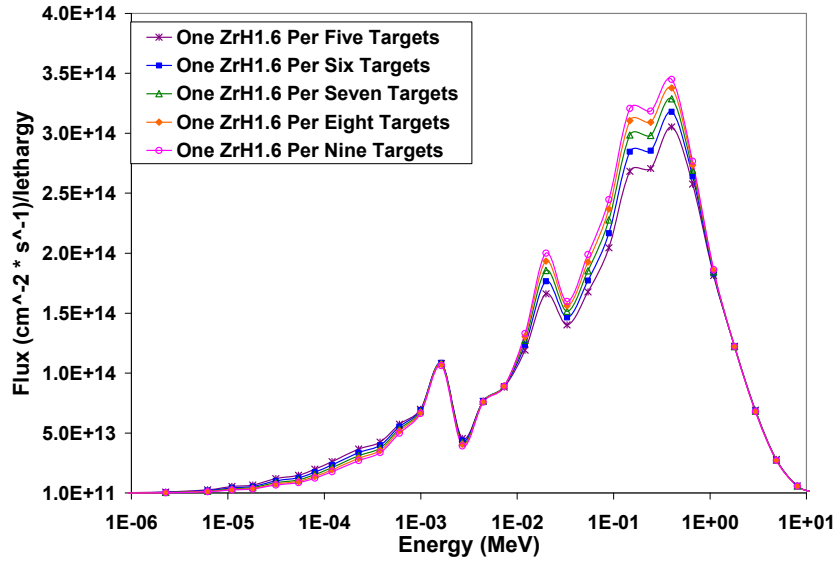


Figure 3-10. Average neutron flux in the target region of a preliminary AHFTR design for a varying number of moderating rods per target rods (lin.-log. scale) (REBUS)

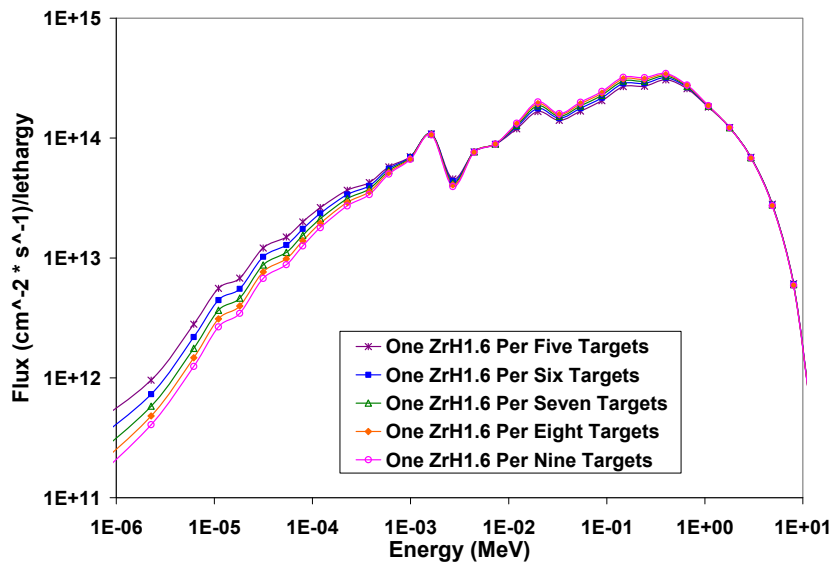


Figure 3-11. Average neutron flux in the target region of a preliminary AHFTR design for a varying number of moderating rods per target rods (log.-log. scale) (REBUS)

Notice that the fast flux decreases for increasing concentration of moderating rods. This is a sign that the fast component of the flux is being reduced by the moderation. However, because the y-axis of Figure 3-10 is linear, it is difficult to see from the plot whether or not there is an

increase in the neutron flux at lower energies. Figure 3-11 shows the same data that was plotted in Figure 3-10 but on a logarithmic scale.

Notice that the thermal-epithermal component of the spectrum increases for increasing number of moderator per target rods. The increase in thermal-epithermal flux for increasing zirconium hydride rods explains the improvement in transmutation half-life. As the spectrum softens, more of the flux is placed in the resolved-unresolved resonance range below one MeV. Recalling the cross section plot in Figure 3-5, the Am-241 capture cross section in this range has the same overall magnitude of that of the Pu-239 fission cross section. Because, the Am-241 loading and Pu-239 loading are approximately equal, the Am-241 capture reaction rate provides a degree of energy shielding effect over the fission rate of Pu-239 (and the other plutonium isotopes). The small amount of energy shielding gained by Am-241 allows neutrons invested in the target region by leakage from the active core to be invested in neutron captures in Am-241 as opposed to fissions in the Pu-239 which enables high transmutation efficiency.

The transmutation efficiency gained by the moderation can be visualized by tracking the change in the relative Am-241 content of the fuel normalized to the initial Am-241 loading of the fresh fuel, which is shown in Figure 3-12. In addition to the destruction of Am-241, the gain in transmutation efficiency by increasing neutron captures (i.e., transmutation) can be visualized by tracking the change in the relative Pu-238 content of the fuel normalize to the initial Pu-238 loading in the fresh fuel, which is shown in Figure 3-13.

Because the case with one zirconium hydride rod per five target rods demonstrated the highest transmutation efficiency over all other cases, this combination was selected for the final down selection of the AHFTR design. A decision was made to limit the concentration of moderator rods to one per five targets due to a concern that too much moderation would cause

power peaking effects in the target region and near the interface with the driver fuel. Increasing the thermalizing effect decreases the neutron mean-free-path. The concern over power peaking arises from the possibility that discontinuities in the neutron flux between regions with dissimilar neutron spectrums (due to isotope depletion) could emerge if the neutron mean-free-path becomes too short. These discontinuities would not only lead to unacceptable power peaking, but would also invalidate the accuracy of the fast reactor codes, MC²-2 and DIF3D, for the target analysis. These codes assume minimal flux discontinuity from region-to-region in order to homogenize the fuel over large regions of the core.

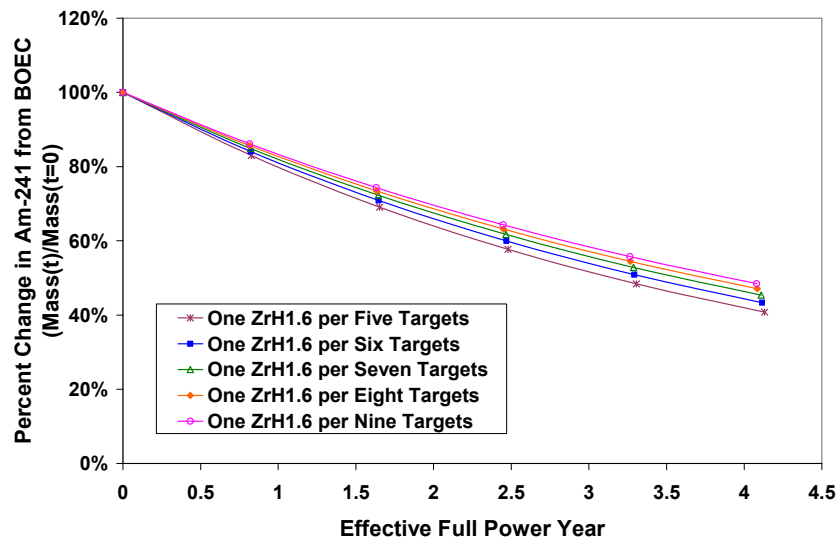


Figure 3-12. Percent of the initial Am-241 mass remaining in the target rod as a function of irradiation time for varying number of moderating rods in a preliminary AHFTR (REBUS)

There is an additional feasibility limitation on the practical number of pins that can be loaded with zirconium hydride as opposed to targets. The addition of moderator rods reduces the number of target rods available for loading MAs. Therefore, to burn an equal amount of mass in the targets, the MA concentration in the target slug must increase for decreasing number of target pins. As will be discussed in Chapter 6, for metal alloy fuels there is a practical limit on the

concentration of MAs that can feasibly be loaded into the fuel which are related to the volatility of americium in its melted form.

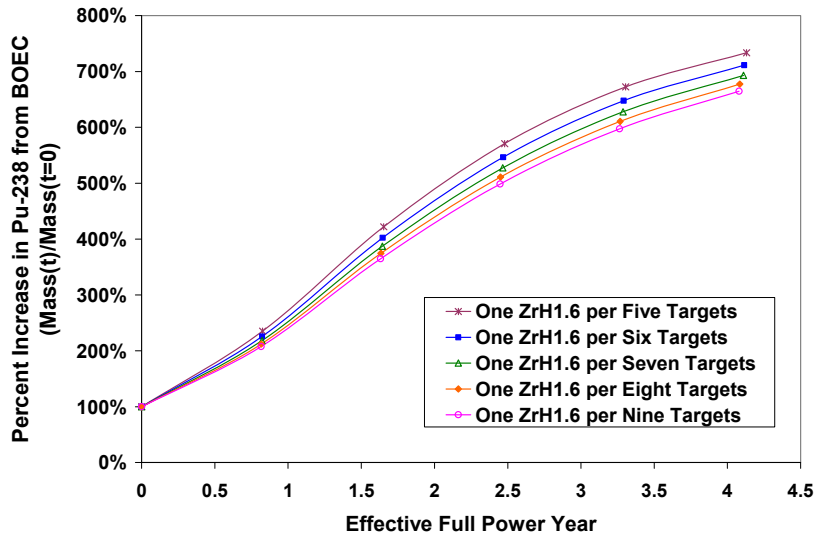


Figure 3-13. Percent of the initial Pu-238 mass created in the target rod as a function of irradiation time for varying number of moderating rods in a preliminary AHFTR (REBUS)

Tall and Flattened Axial Heterogeneous Core Designs

Using the reference ABR, with pin diameters from Table 3-2, as a standard for comparison, the AHFTR core height and pin diameter were varied. The reactor performance traits considered were the excess reactivity, total core void worth and Doppler coefficient. The largest diameter fuel pin design ($p/d=1.1$) from Table 3-2 is selected (for this section) to give a Doppler coefficient with increased negativity than the reference case. This is expected because the volume of fuel in the active core is increased and the percent of that fuel being uranium is also increased. After down-selection, the final active core geometry is 91.6 cm with a 1.1 pin pitch-to-diameter ratio. The 10 cm reduction in active core height was found to give a total core void worth that was slightly less than the homogeneous reference ABR with the 1.1 pin pitch-to-diameter ratio (Table 3-2). Though the active driver core height is 10 cm less than the reference ABR, the total core height is 10 cm “taller” due to the addition of the 20 cm height of the targets.

This core design, as well as a much “flatter” core design, is compared to the reference ABR in Table 3-7. It should be noted that these comparisons are made for a pin pitch-to-diameter ratio of 1.1. The flat AHFTR core design, discussed next, is given in Figure 3-14.

Table 3-7. Core design summary for the reference ABR with tall and flat AHFTR (REBUS)

	ABR (Ref.)	Tall AHFTR	Flat AHFTR
Total Core Height	101.6	110.6	91.6
Active Driver Height	101.6	91.6	71.6
Total Core Volume (m ³)	3.3	3.6	4.0
Active Core Volume (m ³)	3.3	3.0	3.1
Rows of Driver Fuel	7	7	8
Pitch-to-diameter ratio	1.1	1.1	1.1
Inner Core Enrichment	14.92%	16.07%	18.65%
Enrichment Split (IC/MC/OC)	1.0/1.25/1.50	1.0/1.25/1.50	1.0/1.12/1.25
Cycles per Enrich. Zone (IC/MC/OC)	6/6/7	6/6/7	6/6/7
Cycle Length (EFPD)	322.86	319.90	350.58

For the flattened version of the AHFTR, a 71.6 cm height is evaluated to observe a much larger target-to-driver volume ratio. An additional row of outer core drivers is added to this flat core so that the power density is made roughly comparable to the “tall” AHFTR (Figure 3-14).

Radial and Axial Power Profiles

Because of the inherently flatter power distribution, the gradient of enrichment splitting for the flat AHFTR can be decreased from that used for the ABR. Therefore, the “flat” core’s middle and outer zones are enriched to 1.12 and 1.25 times that for the inner core respectively. This tailored enrichment splitting gives the flat core a much more evenly radial power distribution than the tall core. The axial leakage works in parallel with the enrichment splitting to create an almost completely flat radial power profile across the inner and middle enrichment zone. Figure 3-15 shows the radial power distribution for six axial slices through the tall and flat versions of the AHFTR.

In Figure 3-15 and Figure 3-16, the power density of the flatter core geometry is noticeably greater than that of the tall core geometry. This greater power density is linked to the axial

leakage coming from the active core. As was seen in the transmutation half-life discussion in the parametric study, flattening the core reduces the radial curvature, or buckling, of the power (and flux) profile.

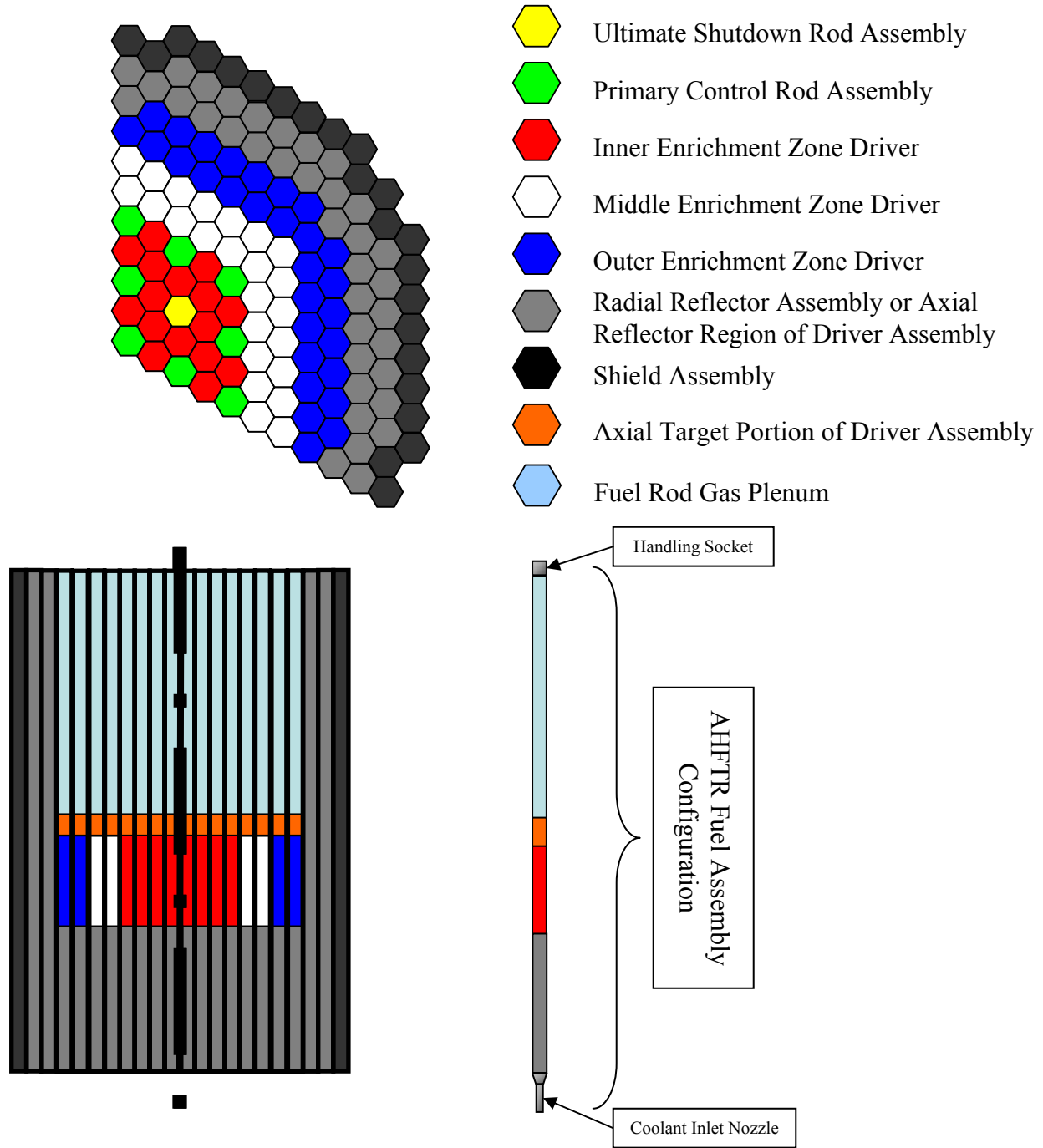


Figure 3-14. Preliminary “Flat” AHFTR design with eight rows of fuel instead of seven

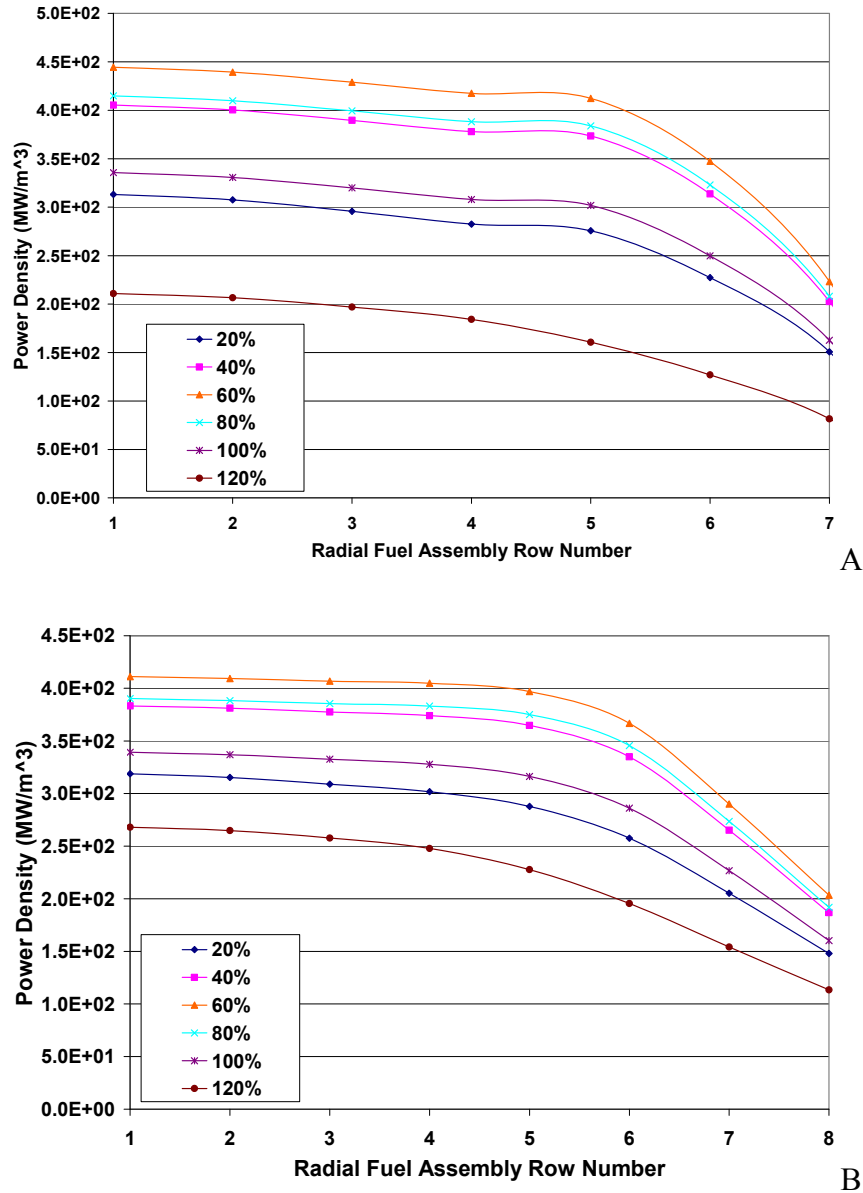


Figure 3-15. Radial power density profile for six axial slices through the core: Axial height is represented as a percentage of the full core height. (A = “tall”, B= “flat” core designs) (REBUS)

As can be seen in Figure 3-15, the curvature of the radial power profile is less for the flat core than it is for the tall core. Remembering back to the discussion in Chapter 2 on the critical buckling of a hypothetical bare cylindrical SFR, the sum of radial and axial geometric buckling must be equal to the material buckling. Therefore for approximately equal materials buckling between tall and flat geometries, a decrease in radial buckling requires an increase in axial

buckling. Hence, the axial buckling of the flat core is greater than that of the tall core. It is because of this increase in axial buckling that the flat core has more axial leakage than the tall core. The greater axial leakage gives the flat core a greater power density in the target region than in the tall core, which is shown in Figure 3-16.

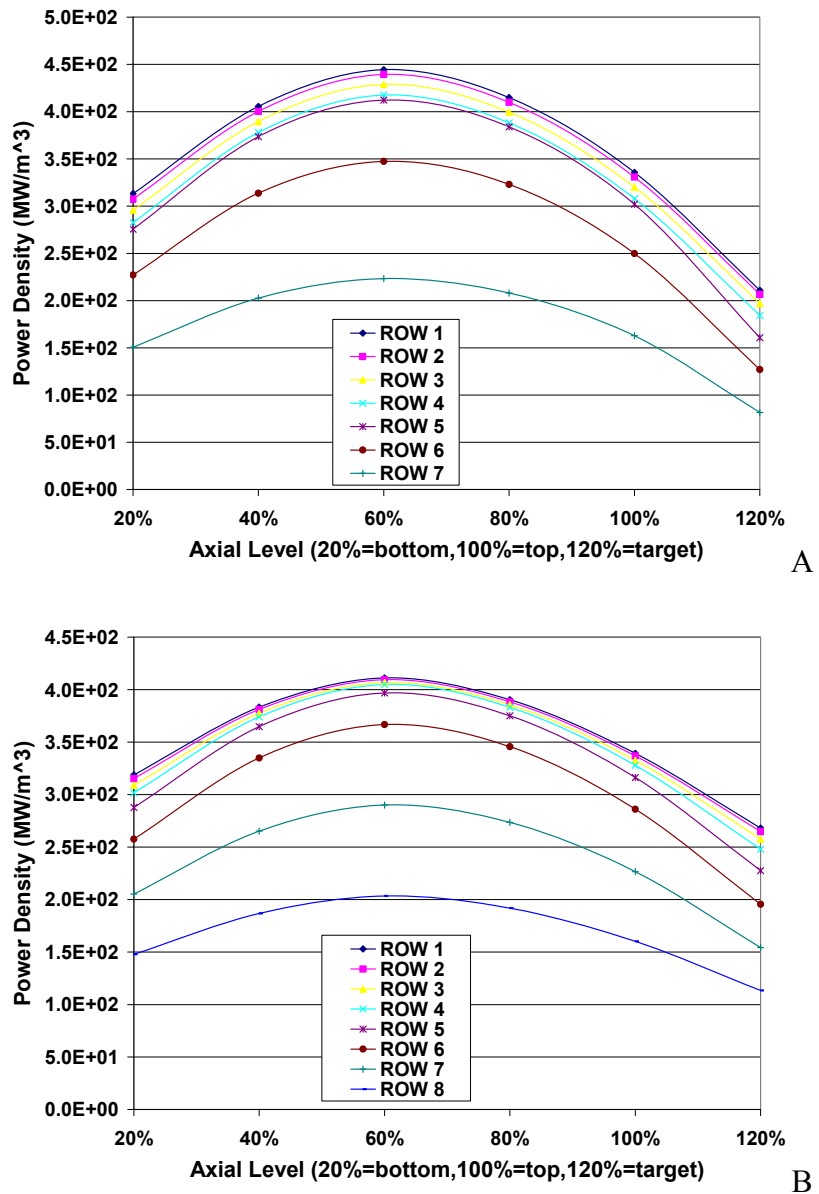


Figure 3-16. Axial power density profile for each row of fuel: Axial height is represented as a percentage of the full core height. (A = “tall”, B = “flat” core designs) (REBUS)

The increased power density in the target region also provides for a reduced transmutation half-life of 2.22 years. This transmutation half-life corresponds to a transmutation efficiency which is comparable to the small pin diameter ($p/d=1.357$) from Table 3-5. This small pin diameter was used by Hoffman et al to attain a τ_{CR} equal to 0.25. Therefore, the flat AHFTR core design achieves the MA destruction efficiency of a core with a thin fuel pin but does this using a larger pin diameter. The larger pin diameter used for the flat version of the AHFTR is more representative of the ABR with a $\tau_{CR}=1.0$.

This higher efficiency combined with an increased volume of the target region (physically more fuel assemblies) gives a higher destruction rate of $Am+ Cm+ Bk+ Cf$ when compared with the tall core. This higher $Am+ Cm+ Bk+ Cf$ destruction rate equates into a higher plutonium transmutation breeding rate. This increases the amount of $Am+ Cm+ Bk+ Cf$ and reduces the amount of $Np+ Pu$ drawn from the UREX+3 plant. Hence, the size of the surplus $Np+ Pu$ feed (outside the boxed off portion of Figure 3-4) decreases.

In fact for both the tall and flat designs, the external $Np+ Pu$ feed for the active core is reduced to zero for the equilibrium fuel cycle. Consequently, for both the tall and flat core designs, the UREX+3 plant only needs enough $Np+ Pu$ and $Am+ Cm+ Bk+ Cf$ to produce fresh targets.

For either case, the radial power profile falls off sharply in the outer two rows of fuel. This is attributed to the dominating radial leakage effect on the flux gradient in the outer core. It is important to note, the volume ratio of these outer two rows to the rest of the fuel is 0.5 and 0.44 for the flat and tall cores respectively. So the volume of the target material located in the low flux of these outer two rows decreases as the core radius is increased. Hence, the flat AHFTR has the smallest fraction of targets located above the low flux, low power driver fuel. This gives

the flat AHFTR the advantage of having the highest achievable transmutation rate over a greater share of the targets than the tall AHFTR.

In addition to the geometrical improvement in target exposure in the radial direction, the axial volume ratio of target to driver fuel increases with core flattening. This is because the target volume in the numerator of this ratio is fixed for a given radius by its 20 cm height, but the denominator is decreasing as the core height is decreasing.

$$\frac{V_{target}}{V_{driver}} = \frac{\pi R_{core}^2 \times (20 \text{ cm})}{\pi R_{core}^2 \times h_{active_core}} = \frac{(20 \text{ cm})}{h_{active_core}} \quad (3-5)$$

Where: V_{target} is the approximate volume of the targets in the core. V_{driver} is the approximate volume of driver fuel in the core. R_{core} is the core radius. h_{active_core} is the height of the active core. The height of the targets is held constant at 20 cm.

Therefore, the overall MA charge rate per cycle increases as the active core height is decreased. The combined effect of the increased axial leakage from the active core, the increased share of fuel having a higher power and an increase in the MA charge rate per cycle makes the flat AHFTR design the most attractive transmutation system because of its physical ability to consume MAs.

Table 3-8 shows the fuel cycle parameters for the homogeneous reference compared to the tall and flat AHFTR designs. As expected, the flat AHFTR has a greater amount of Am+Cm+Bk+Cf being destroyed in the targets. This can be observed by examining the americium transmutation half-life for the flat versus the tall core design. In addition to a decreased transmutation half-life (increased capture reaction rate), the overall Am+Cm+Bk+Cf target destruction rate is also increased. The enhanced destruction rate is the combined effect of transmutation half-life and the target assembly charge rate.

Despite having a larger destruction rate in the targets, the flat core has a smaller overall Am+Cm+Bk+Cf consumption rate (Table 3-8). This is because the flat core has a longer cycle length (i.e., refueling interval) than the tall core which is also equivalent to a smaller fresh target charge rate. Though the tall AHFTR has a more efficient target (shorter transmutation half-life), these targets discharge a larger Am+Cm+Bk+Cf volume to the pyroprocessor. The tall core has a less efficient target but the shorter cycle length increases the rate that Am+Cm+Bk+Cf is charged to the targets and consequently the rate that un-transmuted MA mass is received by the pyroprocessor. The difference in target destruction rate and total core consumption rate illuminates the importance of distinguishing between the transmutation rate of a given isotope and the actual charge rate of that isotope. The isotope destruction or reaction rate is a function of neutron flux and energy in any given region of the core, whereas the charge or consumption rate is more influenced by the logistics of the fuel cycle operating at steady state.

Table 3-8. Fuel cycle comparison for the reference ABR with tall and flat AHFTR (REBUS)

	ABR (Ref.)	Tall AHFTR	Flat AHFTR
Active Driver Height	101.6	91.6	71.6
Maximum MA in Driver Fuel			
OC Am/HM	0.00%	1.72%	1.79%
OC MA/HM	1.06%	3.20%	3.40%
TRU Externally Supplied Feed Rate			
Am+Cm+Bk+Cf Feed* Rate (kg/EFY)	2.79E+00	3.63E+01	3.31E+01
Np+Pu Feed Rate* (kg/EFY)	4.84E+01	3.60E+01	4.31E+01
HM Feed Rate (kg/EFY)	3.75E+02	3.80E+02	3.75E+02
Transmutation Half-Life			
IC Target Am Half-Life (Yr)	--	2.49	2.22

*See Figure 3-4 for a pictorial representation of the source of the external feed.

In both cases, the amount of MAs diluted in the driver fuel is comparable to that of the reference ABR and is less than the 5% limit set by the CAPRA recommendation as discussed earlier. Note that the MA concentration in the outer core is higher than the other two zones because the transuranic enrichment is the highest in that region due to enrichment splitting

(Table 3-8). The Am+ Cm+Bk+Cf in the driver fuel is effectively burned in the active core region and does not accumulate in the AHFTR fuel cycle.

Reactivity Feedbacks

The Doppler coefficient and total core void worth are compared in Table 3-9. These performance parameters are calculated for the cores at BOEC, using the calculation methods discussed in Chapter 2. The Doppler coefficients for these cores are fairly comparable with the values reported by Hoffman et al [7]. It should be noted that the ABR reference considered in these scoping calculations is not the exact same core design proposed by Hoffman et al [7]. The core layout, cycle length, number of batches, etc. were not conserved between this analysis and that of Hoffman's. The core layout given in Figure 1-5 is the one proposed by Hoffman for a ρ_{CR} of 0.5. The core design that Hoffman proposed for the larger fuel pins ($p/d=1.1$) is slightly different (Table 3-9). The $\rho_{CR}=0.5$ core layout was considered a middle-of-the-road design that could be used for comparison purposes in the scoping calculations in this chapter.

The reference ABR design and the flat version of the AHFTR both have a slightly negative Doppler coefficient. However, the tall version of the AHFTR has a slightly positive Doppler coefficient. The positive void coefficient of the tall core is due to the higher concentration of MAs in the driver fuel than the reference ABR and an absence of core flattening. The affect of fuel temperature increase, for the tall core causes resonance broadening of the U-238, TRU and fission products. This resonance absorption can cause the neutron spectrum to harden which causes an increase in multiplication. The positive worth of this multiplication can be greater than the negative feedback of the U-238 resonance absorption if the core has inadequate leakage to remove this extra reactivity. Hence, a degree of leakage is beneficial for Doppler feedback to ensure that the inner regions of the core are not overly reflected. An increase in axial leakage

also decreases the positive void worth, because of an improvement in axial streaming compared to the other two more symmetric cores.

As discussed in Chapter 2, the conversion ratio is also sensitive to core flattening. As leakage is enhanced, the concentration of fissile material must increase. Hence, the TRU increases. The excess reactivity may be viewed in the same way. As leakage increases, the TRU enrichment required to achieve the maximum fuel burnup (taken to be 18 at. % in these scoping calculations) also increases. This can be seen in Table 3-9. For the homogeneous case, this would normally reduce the cycle length because a reduction in U-238 capture also reduces the production of Pu-239 which is needed to achieve the fuel burnup. However, the flat AHFTR design has the longest cycle length. This is attributed to the reactivity breeding effect of the axial target region. Since, the overall core size is larger for the flat versus the tall or ABR cases, there is actually less neutron escape when the targets are factored into the consideration. Therefore, neutrons are efficiently invested in creating fissile material in the targets as the initial plutonium charge in the driver burns out.

Also shown in Table 3-9 is the effect of total core size on the AHFTR dominance ratio. The dominance ratio gives an indication of the closeness of the first and second lambda-mode eigenvalues and is generated by the DIF3D calculation [42]. A larger dominance ratio (nearer to 1.0) indicates less neutronic coupling between regions of the core. Because the mean-free-path for fast neutrons is much larger than for thermal neutrons, fuel regions in an SFR are normally well coupled. This is confirmed by the small dominance ratios in Table 3-9. It is desirable to have a tightly coupled fast reactor from the standpoint of transient response. Since, the effective delayed neutron fraction for fast reactors is significantly less than for thermal systems; it becomes advantageous to reduce the complexity of the types of reactivity feedbacks that are

expected to occur in the fast reactor. The flat AHFTR has the largest total core volume compared to the other two designs and also has a moderated region (reduced mean-free-path).

Nevertheless, the increase in dominance ratio from the reference ABR is not significant.

Table 3-9. Physics comparison for the reference ABR with tall and flat AHFTR (REBUS)

	Hoffman [7]	ABR (Ref.)*	Tall AHFTR	Flat AHFTR
Active Driver Height	101.6	101.6	91.6	71.6
Pin Pitch-to-Diameter Ratio	1.1	1.1	1.1	1.1
Total Core Void Worth (\$)	6.29	9.16	8.82	8.27
Doppler Coefficient (ρ/K)	-0.11	-0.13	0.06	-0.14
Excess Reactivity (%)	-0.06	1.31	1.12	1.70
BOEC k-eff	1.0	1.01325	1.01312	1.01727
Cycle Length (EFPD)	370	322.86	319.90	350.58
Max. Burnup (at.%)	11%	18%	18%	18%
Dominance Ratio**	--	0.3798	0.3813	0.3958
Conversion Ratio (ρ_{CR})				
Core Conversion Ratio	--	0.89	0.87	0.84
Target Conversion Ratio	--	--	0.91	0.90
Inner Core Conversion Ratio	--	1.01	0.97	0.90
Middle Core Conversion Ratio	--	0.85	0.82	0.81
Outer Core Conversion Ratio	--	0.77	0.75	0.77

*The performance characteristics for the reference ABR listed here are not that of the actual point design of the GNEP ABR design which is currently evolving and not final. See Chapter 2 for an explanation of kinetics calculations. **The dominance ratio is not reported by Hoffman et al in the report, ANL-AFCI-177.

Fuel Performance Indicators

One issue identified in previous heterogeneous target studies, by Sanda et al, was that the transmutation of MAs into plutonium can create an undesirable power peaking effect [28]. This issue was most pronounced for target irradiations in high flux regions in the inner core or for long “deep-burn” irradiations in the outer core. This work sought to diminish or eliminate any changes in the target thermal power throughout its life in the core (i.e., from beginning-of-life (BOL) to end-of-life (EOL)). For axial targets this is especially important because the targets share the same coolant channel flow orifice as the driver fuel.

SFR fuel assemblies often are, by-and-large, designed with a metal shroud that encompasses the fuel pins. This shroud prevents cross-flow of sodium to adjacent fuel

assemblies. Therefore, sodium coolant flow in the fuel assembly is controlled on an assembly basis using an orifice at the bottom of the fuel assembly near where it meets the bottom grid plate. The shroud prevents differences in pressure losses in each fuel assembly that would otherwise cause sodium coolant to move laterally in order to equalize the lateral pressure gradient. Therefore, despite a large radial power gradient (even for the AHFTR) compared to LWRs, the flow orifices are used to make the coolant outlet temperature at the top of the core fairly constant.

If there were to be a wide change in thermal power of the target region, the amount of flow could be sufficient to cool the target at BOL and inadequate for EOL. Also, undesirable power peaking in the driver fuel could result if the power sharing between driver and targets shifts significantly throughout the irradiation. Power peaking and shifting was minimized by choosing a target composition with a small amount of starting plutonium and uranium to ensure a slow net destruction of Pu-239 over the course of the irradiation. Also, the high importance of the Am-241 capture cross section in the epithermal flux ensured that neutrons could be equally absorbed in americium, as could be absorbed into Pu-239 (Table 3-3 and Figure 2-11). This gives the americium the purpose of a burnable poison in the target region as well as a fertile source for breeding even-plutonium isotopes. The power produced by these even-plutonium isotopes are sufficiently suppressed by the capture reactions in Am-241. Table 3-10 evaluates the fuel performance indicators for the AHFTR.

The peak Linear Heat Generation Rate (LHGR) in the targets was highest for the flat case. In all cases, the peak LHGR for the entire core occurred in the driver fuel not the targets. This peak driver LHGR occurs in the innermost row of fuel at the active core's mid-plane. This is also true of the volume and exposure integrated fission density for the target and driver fuel.

Table 3-10. Fuel performance comparison for the reference ABR with tall and flat AHFTR

	ABR (Ref.)	Tall AHFTR	Flat AHFTR
Active Driver Height	101.6	91.6	71.6
Linear Heat Generation Rate (kW/m)			
Peak Driver LHGR (kW/m)	38.1	36.9	35.5
Peak Target LHGR (kW/m)	--	20.1	25.3
Peak Fast Fluence: E>0.1 MeV (1E23 cm-2)			
Inner Core	5.72	5.66	5.53
Middle Core	5.58	5.49	5.61
Outer Core	5.05	4.95	5.88
Max Integral Fission Density: (f/cm ³)			
Driver Fission Density (1E21 f/cm ³)	6.96	7.67	7.09
Target Fission Density (1E21 f/cm ³)	--	3.64	4.62
Average Discharge Burnup (MWD/kgiHM)	124.4	127.3	134.1

Historically, the fission density has been used as an indicator of irradiation induced swelling and gas release in metal fuels. It allows equal comparison of fuel performance when the amount of HM loading is not constant in the comparison. This is the case for the AHFTR because the metal driver fuel and targets have different zirconium contents in their alloying. For all cases, the peak fission density is less in the targets than it is in the fuel. Hence, the expected swelling and gas release, including transmutation helium, should be similar to that of past experience with metal driver fuel for equivalent fission density. This assumes that the rate of void formation and interconnected porosity in the target is roughly equivalent for the lower zirconium content driver alloy. The irradiation induced interconnected porosity of fission gas bubbles coming together early in the irradiation was one of the significant developments of the Mark II driver fuel used at the EBR-II [60,61]. The effect slows the rate of swelling by allowing fission gas to escape to the plenum and increases the time before cladding interaction. Because of the high LHGR and burnups associated with both metallic and oxide based SFR fuels, typically 60-80% of all fission gas is released to the plenum [62]. This explains a plenum height of about 1.5 to two times the height of the core in Figure 1-7, Figure 3-1, and Figure 3-14.

The smaller radial power gradient for the flat case gives its driver fuels the smallest peak LHGR. The flatter power profile also explains the higher peak fast fluence in the outer core for the flat case than the other core designs. A more evenly distributed fast flux also results in a more level fast flux exposure between the inner, middle and outer core regions. Note that the peak fluence limit for all the core designs mentioned is greater than $4 \times 10^{23} \text{ cm}^2$. This number is the fast fluence limit assumed in the Hoffman report in consideration to the maximum displacements-per-atom (dpa) for fast reactor grade steel. HT-9 is a fast reactor grade martensitic/ferritic steel that was used for cladding and in-core structures for EBR-II and the Fast Flux Test Facility (FFTF) [63]. For the final down selection discussed in the next section, a limit of 200 dpa is assumed. The design basis and performance criteria for the AHFTR driver fuel and targets are discussed in detail in Chapter 6.

Similar to the LHGR distribution, a flatter fluence distribution allows more of the fuel to be irradiated to a level closer to the $4 \times 10^{23} \text{ cm}^2$ limit. As discussed in Chapter 2, the constraining parameter on the fuel cycle for the parametric study was the peak fuel burnup at the midpoint of the first row of fuel. The limit on fuel burnup as opposed to maximum cladding damage during the equilibrium cycle convergence process is a limitation of the REBUS code (Figure 2-1). The next section discusses a final down selection that reduces the cycle length such that the technical irradiation damage limits for the HT-9 structural components are met.

Final Down-Selection: The AHFTR Design

A final down selection in the AHFTR core design is made based on the transmutation and reactor physics attributes of the above flattened design case. In order to give a more favorable fluence and dpa, the cycle length from this case is reduced. In order to give a shorter cycle length, the pin diameter of the flat design is reduced to increase the TRU enrichment. The only parameter changed in the fuel assembly design is an increase in the pin pitch-to-diameter ratio

from 1.1 to 1.176. The resulting pin diameter (0.755 cm) is equal to the ABR version with a t_{CR} of 0.75 which was proposed by Hoffman et al (Table 1-6 and Table 3-2) [7]. This pin diameter and number of pins per assembly also closely matches the S-PRISM driver fuel assembly design (Table 1-3) [8]. The slight increase in enrichment also had the benefit of decreasing the AHFTR's CR (both t_{CR} and t_{CR}) from the case analyzed above.

The core geometry of the flat case was also modified slightly. Due to the low neutron flux in that part of the target region residing in the outer core (row 7 and 8), the target region above these assemblies was removed. Without these outer targets, the core design shown in Figure 3-14 now becomes the core design originally shown in Chapter 1 in Figure 1-7. Additionally, the removal of these outer core targets resulted in a reduction in the un-transmuted MAs discharged from the target region and sent to the pyroprocessor. Because of the higher efficiency, a higher concentration of transmuted plutonium and a smaller concentration of un-transmuted MA in the mass flow were sent to pyroprocessing from the target region.

Fuel Cycle Performance of the Final AHFTR Design

The generation of plutonium isotopes by the transmutation of MAs can be seen by comparing the mass flow rate of Am-241 entering and the Pu-238 exiting the target region. The resulting mass flow rate of plutonium exiting the target region can then be viewed as a supply rate (via pyroprocessing) of internally provided plutonium to the driver fuel. This internal plutonium supply rate can then be compared with the external plutonium supply rate from the aqueous reprocessor.

From Table 3-11, it can be seen that the *discharge rate* of Am-241 coming out of the target region (0.0202 g/MWD) is 40% that of the Am-241 *charge rate* entering the targets (0.0580 g/MWD). Therefore, 60% of the Am-241 mass entering the target region is destroyed by transmutation or by fission. Also, it is important to note that the target region's Pu-238 discharge

rate (0.0175 g/MWD) is 6.7 times the charge rate going into the targets (0.0026 g/MWD). Also, it can be seen from Table 3-10 that the target region's Pu-238 discharge rate (0.0175 g/MWD) is three times the externally supplied Pu-238 feed rate from the aqueous reprocessing center (0.0058 g/MWD). This means that the target region provides more than three times the supply of Pu-238 to the active core via pyroprocessing than the Pu-238 supplied by the "make-up" transuranic supply from the aqueous SNF reprocessing.

Table 3-11. Final AHFTR mass flow of each isotope entering and exiting the target region and active core region per MWD

	Charge and Discharge Rate of Mass Flows Normalized to grams/MWD			
	Entering Target	Exiting Target*	Entering Core**	Exiting Core*
Np-237	0.0053	0.0024	0.0264	0.0207
Pu-238	0.0026	0.0175	0.0969	0.0736
Pu-239	0.0480	0.0471	0.9963	0.9201
Pu-240	0.0217	0.0284	0.6255	0.5802
Pu-241	0.0105	0.0086	0.0947	0.0850
Pu-242	0.0062	0.0108	0.1457	0.1312
Am-241	0.0580	0.0202	0.0829	0.0577
Am-243	0.0302	0.0138	0.0761	0.0623
Cm-244	0.0116	0.0188	0.0815	0.0666
	Supply Rate from Aqueous Reprocessing to Target Region	Supply Rate from Aqueous Reprocessing to Active Core Region		
Np-237		0.0053	0.0033	
Pu-238		0.0026	0.0058	
Pu-239		0.0480	0.0291	
Pu-240		0.0217	0.0169	
Pu-241		0.0105	0.0011	
Pu-242		0.0062	0.0037	
Am-241		0.0580	0.0050	
Am-243		0.0302	0.0000	
Cm-244		0.0116	-0.0039	

*The sum of these two columns is the total mass stream seen by the pyroprocessor. **This column is the total mass of externally supplied and the internally supplied "pyroprocessed" TRU.

The balance between Am-241 destruction versus Pu-238 generation can also be seen by examining the isotopic inventory of the core at BOEC and EOEC which is given in Table 3-12. Also from Table 3-12, it can be seen that the total concentration of MAs per HM is maintained to be much less than the imposed 5% limit imposed on the active core composition.

Table 3-12. Target and active core region isotopic fuel inventory compared with the ABR at BOEC and EOEC (REBUS)

	Target Region		Active Core Region		ABR (CR=0.5)	
	BOEC	EOEC	BOEC	EOEC	BOEC	EOEC
Heavy Metal Loading (kg)	714	698	12,583	12,380	9,368	9,127
TRU Loading (kg)	244	240	2,791	2,741	3,021	2,913
MA Loading (kg)	115	106	374	360	343	332
Pu Loading (kg)	129	134	2,417	2,381	2,678	2,581
Pu-238 Loading	13	16	110	105	100	97
Pu-239 Loading	61	61	1,236	1,220	1,140	1,088
Am-241 Loading	50	42	92	86	88	83
MA/HM Ratio	16.11%	15.23%	2.97%	2.91%	3.66%	3.64%

The buildup and depletion curve for both the target region and the active core region is given in Figure 3-17 and Figure 3-18, respectively. These curves give the change in fresh driver fuel and target composition as a function of irradiation time. Notice the small relative change in the overall plutonium content of the fuel with irradiation time. This verifies the statement made in Chapter 2 regarding the lack of spectrum shifting as a result of depletion in the SFR. Because, the “relative” fuel composition of the core does not change considerable during the course of the irradiation, the change in resonance and unresolved resonance shielding between various isotopes is negligible.

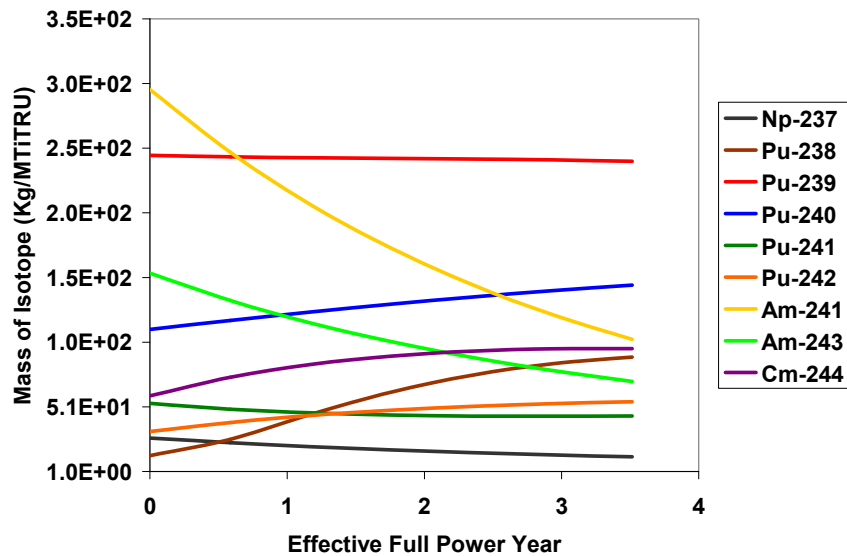


Figure 3-17. Buildup and depletion curve for fresh fuel in the target region of the final AHFTR design (REBUS)

The same can be said about the target region to a limited extent. Though the change in MA concentrations is significant as intended, the Pu-239 concentration varies slowly with irradiation. This slow Pu-239 depletion was intended by design by adding a small amount of uranium to the metal alloy of the target slug in order to buffer changes in spectrum with irradiation. The insensitivity of the target region's neutron spectrum to burnup is verified by calculations performed in Chapter 5.

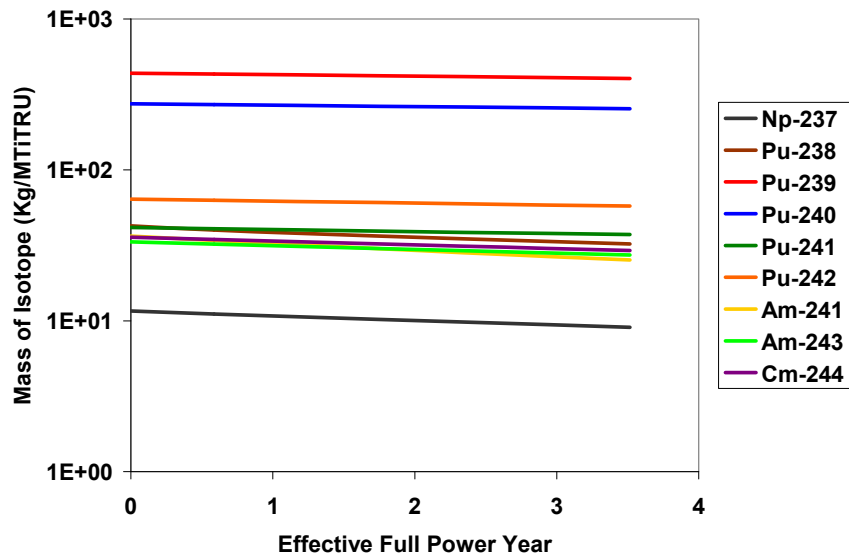


Figure 3-18. Buildup and depletion curve for fresh fuel in the active core region of the final AHFTR design (REBUS)

Reactor Performance Characteristics of the Final AHFTR Design

A comparison is made between the final AHFTR down-selection and the homogeneous metal ABR (CR=0.5) design proposed by Hoffman et al [7]. It was the lateral core layout of this ABR (CR=0.5) design case that was adopted for the ABR reference cases which was used for comparative analysis of the earlier parametric study. This is also the lateral core layout shown in Figure 1-5 and Figure 3-1. To achieve the conversion ratio of 0.5, Hoffman used a pin diameter of 0.623 (p/d=0.623) which is less than the pin diameter of 0.808 (p/d=1.1) which was used in the previous section to compare the tall and flat versions of the AHFTR. Also, Hoffman

increased the number of fuel pins from 271 ($t_{CR}=1.0$ and $t_{CR}=0.75$ designs) to 324 for a t_{CR} of 0.5.

Because of the significant change in fuel pin size and assembly design, the ABR (CR=0.5) design is somewhat more exotic than the fuel designs used in past reactor designs such as EBR-II, FFTF and the proposed S-PRISM. This is why the AHFTR fuel assembly design is based on the ABR with a $t_{CR}=0.75$ instead of the $t_{CR}=0.5$ design. Table 3-13 gives a comparison of various reactors and fuel cycle attributes of both the final AHFTR and two ABR designs.

The AHFTR's transuranic enrichment is just inside the current experience database with Pu-U-Zr fuel alloys tested during the IFR program in the 1980's [64]. Also because of the smaller enrichment, the excess reactivity for the AHFTR is less than the ABR. It is important to note the selection of the pin diameter of 0.755 cm ($p/d=1.176$) for the AHFTR was not optimized to make the fluence and dpa limit as close to the $4 \times 10^{23} \text{ cm}^{-2}$ and 200 dpa limits as possible. Instead, it was statically selected on the basis of most probable and feasible fuel composition and assembly design. Extending the cycle length is possible by decreasing the driver fuel enrichment. However, as discussed in Chapter 2, an increasing conversion ratio results from decreasing TRU enrichment.

The AHFTR core design was made to have approximately the same cycle length as the ABR (CR=0.5) case. However, because of the higher neutron leakages from the AHFTR active core, due to the flattened geometry, a larger uranium fraction in the core is required to increase internal breeding, which extends the fuel burnup, in order to meet the cycle length requirement. However, per the discussion Chapter 2, the addition of uranium (i.e., reducing the transuranic enrichment) does not necessitate the removal of fissile TRU. It does however indicate that the fuel fraction is increased and the sodium fraction in the core is decreased (i.e., a larger fuel pin

diameter). Therefore, the transuranic enrichment of the AHFTR driver fuel is less than that of the ABR (CR=0.5), but the transuranic loading is comparable and actually slightly larger (Table 3-12).

Table 3-13. Initial reactor physics and fuel performance comparison between the AHFTR and ABR design proposed by Hoffman et al

	ABR (CR=0.5)	ABR (CR=0.75)	AHFTR
Fuel and Reactor Dimensions*			
Total Core Height	101.600	101.600	91.600
Active Driver Height	101.600	101.600	71.600
Pin Pitch-to-Diameter Ratio	1.293	1.176	1.176
Pin Diameter (cm)	0.623	0.755	0.755
Pins per Assembly	324	271	271
Calculated Conversion Ratio			
Fissile Conversion Ratio (f_{CR})	0.64	0.84	0.84
Transuranic Conversion Ratio (t_{CR})	0.53	0.77	0.72
Excess Reactivity and Cycle Data			
Inner Core Enrichment	26.6	16.1	20.77%
Excess Reactivity	2.85%	1.47%	1.23%
Cycle Length (EFPD)	219	232	214
Fuel Assembly Residence Times (cycles)			
Inner Core	6	6	6
Middle Core	6	6	6
Outer Core	7	6.5	6
Enrichment Splitting Factor (multiple of Inner Core)			
Inner Core	1.00	1.00	1.00
Middle Core	1.25	1.25	1.12
Outer Core	1.50	1.50	1.25
Reactivity Kinetics and Feedbacks			
Delayed Neutron Fraction**	0.0035	0.0035	0.0033
Total Core Void Worth (\$)	9.17	6.82	8.34
Doppler Coefficient (ρ/K)	-0.08	-0.10	-0.14
Peak Fast Fluence: $E>0.1$ MeV ($1E23$ cm ⁻²)			
IC: Row 1 - Mid-plane	4.00	3.86	3.55
Displacements per Atom in HT9 (dpa)			
IC: Row 1 – Mid-plane	182.7	176.3	160.4

*These dimensions are also given and discussed in more detail in Table 1-6 and Table 1-7 in Chapter 1. **The delayed neutron fraction was calculated with MCNP using fission source libraries with and without delayed neutron fraction data [65].

Because of the higher concentration of uranium in the AHFTR fuel, it should be noted that the Doppler coefficient of the AHFTR design is slightly more negative than that of the ABR (CR=0.5). Also, because the transuranic, particularly MA, concentration in the AHFTR driver

fuel is less than that of the homogeneous core, the positive void worth of the AHFTR is slightly less than that of the homogeneous reference (Table 3-13).

Transmutation Analysis of the Final AHFTR Design

Table 3-14 shows the rates of MA and plutonium consumption for the AHFTR versus the ABR designs. From Table 3-14, the AHFTR burns less total TRU per fission energy generated than the ABR (CR=0.5) but roughly twice the amount of MAs. Also the AHFTR burns almost as many MA as it does plutonium. For comparison, Table 3-14 also shows the amount of TRU produced for a typical PWR design fuel assembly with the composition given in Table 2-1.

Table 3-14. Mass production and destruction rates per installed megawatt per year

	ABR (CR=0.5)	ABR (CR=0.75)	AHFTR
External Supply Mass Streams Provided by UREX+3 Aqueous Plant*			
External Np+Pu Supply (kg/MWY)	0.1596	0.0695	0.0549
External Am+Cm+Bk+Cf Supply (kg/MWY)	0.0092	0.0051	0.0370
External Mass Supply Broken Down by Pu and MA			
Pu Consumption (kg/MWY)	0.1516	0.0654	0.0519
MA Consumption (kg/MWY)	0.0172	0.0092	0.0400
	UOX PWR**	MOX PWR**	
Pu Consumption (kg/MWY)	-0.0758	0.2033	
MA Consumption (kg/MWY)	-0.0074	-0.0482	

* Mass streams calculated from the equilibrium cycle search calculation performed by REBUS on the fuel management scenario in the boxed off region of Figure 3-4. **UOX PWR calculations were performed using TRITON for an initial enrichment of 4.5% and burned for 50 MWD/kg. MOX PWR calculations were performed using TRITON for an initial Np+Pu concentration of 10% and burned for 50 MWD/kg.

Also shown in Table 3-14, is the amount of plutonium consumed and MAs produced in a typical PWR MOX fuel assembly. As a side note, it is worth mentioning that the MOX-PWR fuel assembly has approximately the same *net* TRU consumption rate as the ABR. In fact, it can be easily calculated that most PWR MOX fuels have a conversion ratio between approximately 0.6 and 0.8 depending on the TRU enrichment. However, the MOX has a negative net consumption (i.e., production) of MAs. This emphasizes the fact that a reactor design can have a low CR with a high net destruction of TRU but still do very little for reducing the isotopes most

important to HLW management and the repository design (i.e., MAs and long lived fission products)

By comparing the mass flows per unit of installed thermal reactor capacity, the ABR (CR=0.5) would require approximately one MWth to destroy the transuranics produced by two MWth of UOX PWRs. Coincidentally, if the fuel design and core layout of the metal ABR (CR=0.75) is used, the ratio of ABR installed power to PWR installed power is near unity.

The AHFTR also destroys TRU at about the same rate that it can be produced in a PWR UOX. However, the TRU destroyed by the AHFTR is more than 40% MAs. Hence, the AHFTR's MA consumption is roughly 2.3 times greater than that of the ABR (CR=0.5) design. These comparisons demonstrate that the transuranic consumption of the AHFTR is comparable to the range of ABR options. More importantly, the fissile (i.e., plutonium) requirements of the AHFTR are significantly less than the ABR. The AHFTR requires only a third of the externally supplied plutonium than the ABR (CR=0.5) and 70% of the plutonium burned in the ABR (CR=0.75). Note that the use of the term "externally supplied" can be used synonymously with the "consumption rate". The fact that the fission cross section for most MAs is much smaller than that of fissile plutonium suggests that the 40% MA concentration in the AHFTR TRU requires transmutation before ultimately being destroyed by fission. In order to show that the MAs are not producing 40% of the fission reactions in the core, the contribution to the reactor average fission rate for each actinide isotopes is broken down in Table 3-15.

Because 81% of the reactor's thermal power is produced by fissions of plutonium isotopes but only 14% of the externally supplied HM is actually plutonium, Table 3-15 shows that the remainder of the plutonium that is undergoing fission is provided by transmutations from the fertile isotopes: U-238 and the MAs. A closer look at the amount of plutonium supplied to the

core versus actually undergoing fission shows that 92% of the TRU that is undergoing fission at any given time is plutonium. In actuality, only 56% of the TRU being supplied to the core is plutonium. One important fact to observe is that the total rate that HM is actually supplied to the core is 0.00103 kg/MWD (1.03 g/MWD). This is equivalently the amount of HM mass that is destroyed by fission in order to produce one megawatt of power in one day. Am-241 is supplied to the core at a rate of 5.8E-05 kg/MWD. The fraction of Am-241 in the HM make-up feed is 5.65%. This is equivalent to saying that 5.65% of all fission reactions in the core are derived from the introduction of Am-241. However, only 1.01% of the fission power is being produced by Am-241.

Table 3-15. Concentration of isotopes supplied to replace the mass destroyed by fission compared to the contribution to fission by each isotope (REBUS)

	External Heavy Metal Supply (Kg/MWD)	Fraction of Each Isotope per HM of External Feed	Fraction of Each Isotope per HM of All Fission Reactions	Fraction of Each Isotope per TRU of External Feed	Fraction of Each Isotope per TRU of All Fission Reactions
U-234	7.61E-08	0.0074%	0.16%	--	--
U-235	3.96E-06	0.3860%	0.48%	--	--
U-236	2.34E-06	0.2278%	0.07%	--	--
U-238	7.68E-04	74.8441%	11.57%	--	--
Np-237	8.38E-06	0.8170%	0.33%	3.33%	0.37%
Pu-238	4.15E-06	0.4047%	3.58%	1.65%	4.09%
Pu-239	7.65E-05	7.4637%	59.36%	30.42%	67.66%
Pu-240	3.46E-05	3.3718%	8.55%	13.74%	9.75%
Pu-241	1.68E-05	1.6334%	7.64%	6.66%	8.71%
Pu-242	9.96E-06	0.9714%	1.43%	3.96%	1.62%
Am-241	5.80E-05	5.6534%	1.01%	23.04%	1.15%
Am-242 ^m	1.97E-07	0.0192%	1.17%	0.08%	1.33%
Am-243	3.02E-05	2.9460%	0.70%	12.01%	0.79%
Cm-242	1.92E-09	0.0002%	0.03%	0.00%	0.03%
Cm-243	9.33E-08	0.0091%	0.14%	0.04%	0.16%
Cm-244	1.16E-05	1.1342%	1.34%	4.62%	1.52%
Cm-245	1.01E-06	0.0989%	2.21%	0.40%	2.52%
Cm-246	1.19E-07	0.0116%	0.16%	0.05%	0.18%
Total	0.00103	100%	99.9%	100%	100%

As an appropriate comparison, for the same analogy applied to the ABR (CR=0.5), the Am-241 concentration in the HM make-up feed is only 1.5% which is set by the isotopic content

of SNF TRU and the TRU enrichment in the fuel. Also, the fraction of fission power contributed by Am-241 in the ABR (CR=0.5) is only 0.8%. Hence, about half of the Am-241 externally supplied to the core is destroyed by fission (as Am-241) and the remainder is transmuted. In contrast, the AHFTR destroys only 20% of the externally supplied Am-241 through direct fission of Am-241 atoms. The remaining 80% of the Am-241 external mass supply is transmuted. This result demonstrates that the AHFTR use MAs for conversion into fissile isotopes. This strategy is different from the ABR which does not use transmutation targets to precondition the americium into plutonium.

CHAPTER 4 REACTOR REACTIVITY CONTROL STRATEGY

The standard control rod poison for most SFR designs has historically been natural boron or boron enriched in the more absorbing isotope: B-10 [29]. The preference of boron over other poison materials, such as silver or gadolinium, is primarily due to the order of magnitude larger unresolved resonance cross section of B-10 over other conventional neutron poisons in the fast spectrum. The necessity to enrich the boron in B-10 is determined by the excess reactivity of the core. The ABR, like the EBR-II and many other SFR designs, has been proposed to have enriched B₄C as the control rod material. As a side note, FFTF used a sintered boron powder as the control rod material.

Because the AHFTR has a smaller excess reactivity than the ABR reference case (Table 3-13), it requires less control rod worth to suppress this reactivity. Therefore, boron enrichment is not required. As demonstrated by calculations performed by Hoffman et al and Morris et al, the excess reactivity of an actinide burner SFR (such as the ABR) increases with decreasing conversion ratio [7,20]. The increase in excess reactivity is a result of the requirement to enhance neutron losses by leakage in order to attain the low ρ_{CR} . As mentioned before, for homogeneous cores, the ρ_{CR} is closely coupled to the ρ_{CR} because transuranic breeding is a function of the neutron balance between parasitic absorption and neutron escape losses. The AHFTR has less neutron losses because the axial targets lessen their probability of escape.

Tc-99 versus B-10 as a Control Rod Neutron Poison

Though it will be demonstrated in this chapter that B₄C would be an acceptable neutron poison for the AHFTR, the fundamental objective of this work is to destroy TRU, and if possible other HLW, separated from SNF such as fission products. As identified in the introduction, Tc-99 has a non-trivial concentration in SNF (approximately equal to the MA concentration). Also,

because of its radiotoxicity, and long half-life (in a geologic time frame), it requires a permanent disposal solution, such as in a geologic repository. Because of this need to remove Tc-99 from the fuel cycle, previous studies have focused on ways of transmuting it in a SFR. It is noteworthy that the UREX+ aqueous reprocessing technology was developed partly for the purpose of removal of Tc-99 from the repository destined SNF waste stream. For destroying Tc-99 by transmutation, Yang et al proposed burning metallic Tc-99 in moderated targets within an accelerator driven SFR system [66]. However, Yang's studies concluded that the transmutation half-life of Tc-99, even in a moderated target within the SFR, is in the range of decades.

This result precludes the use of Tc-99 as an Integral Burnable Absorber (IBA). IBAs are burnable poisons that are an integral part of the fuel assembly that can not be removed once it has been manufactured [3]. An example of an IBA is the Westinghouse Integral Fuel Burnable Absorber (IFBA) fuel rod which has a coating of zirconium diboride on the fuel pellets [3]. IBAs are used extensively in many PWR fuel designs for the purpose of leveling power peaking and power shifting that can occur between beginning-of-cycle (BOC) and end-of-cycle (EOC). Using IBAs allows all the fissile material in an LWR to be consumed at a more level rate which enhances fuel utilization and extends the fuel's reactivity limited burnup. In order to control pin and assembly power peaking between BOC and EOC, an IBA must be able to be almost completely depleted by the end of the first cycle. Otherwise, the presence of the IBA would penalize the excess reactivity of the core during the next irradiation cycle. Because a Tc-99 target can not be completely depleted during a single irradiation cycle, it is unlikely that it could be made a feasible IBA.

Despite the difficulty of burning Tc-99 as an IBA, there is still a cost advantage to using technetium as a neutron poison in control rods. The isotopic enrichment of boron is an

expensive process that could be avoided if Tc-99 were used instead. Since, the UREX+ process produces a technetium waste stream that is separate from the other fission products; it is a material that would be readily on hand in the LWR-to-SFR fuel cycle (Figure 1-9). If not used for the production of control rods, technetium would require geologic disposal as a HLW stream. If the AHFTR consumes Tc-99 as a service to the fuel cycle, it would be entitled a credit towards the cost of its fuel purchase as payment for the destruction of Tc-99, which is considered HLW. A detailed explanation of the economic incentive to destroy HLW is given in Chapter 6.

Tc-99 has a virtually identical unresolved resonance neutron capture cross section to that of U-238 in the fast spectrum (Figure 1-6). By comparison, the unresolved resonance capture cross section of Am-241 has a magnitude three times as great (Figure 4-1) as Tc-99. This fact explains why Tc-99 is more difficult to transmute than americium in a SFR. Similarly, when compared to B-10, the Tc-99 capture cross section is also less by approximately a factor of three (Table 4-1).

It is important to remember that it is B-10's highly absorbing property that makes enriched B₄C the primary candidate for reactivity control in the ABR. However, the excess reactivity hold down requirement (i.e., excess reactivity) of the AHFTR is less than that of the ABR (CR=0.5) by roughly a factor of two (Table 3-13). Therefore, enriching the B₄C is not as significant of a prerequisite for the AHFTR. Also it is important to note that metallic Tc-99 has an atomic density that is roughly 3.5 times greater than that of the B-10 constituent of 90% enriched B₄C (Table 4-1). Therefore, Tc-99 can be considered a candidate for the neutron poison in the movable control rods in the AHFTR. Because a control rod can be inserted or withdrawn per the excess reactivity requirements of the core, it is not necessary to completely burn out the Tc-99 by EOC as it would be if were implemented as an IBA.

Table 4-1. Atomic concentrations of absorber atoms in B₄C versus technetium metal (atom/barn×cm)

Atom Concentration	Natural B ₄ C	Enriched (90%) B ₄ C	Metallic Technetium
B-10	4.39E-03	1.98E-02	--
B-11	1.76E-02	2.20E-03	--
C	5.49E-03	5.49E-03	--
Tc-99	--	--	6.69E-02

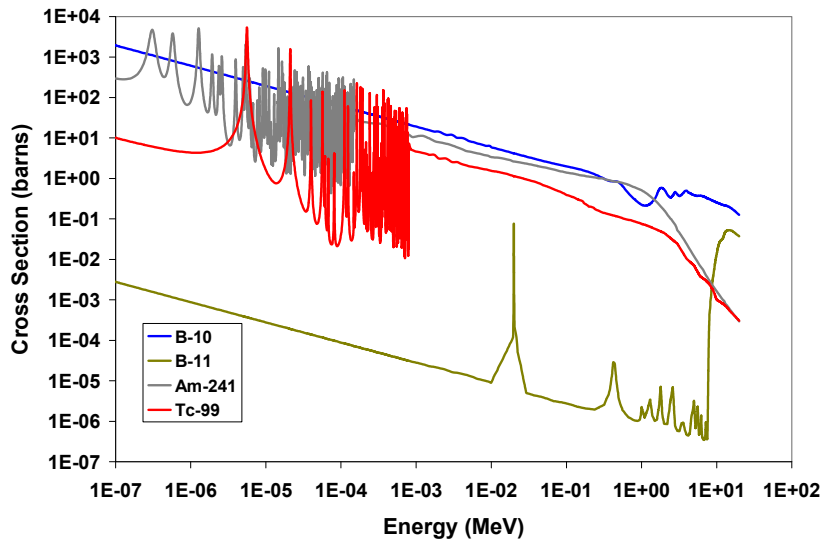


Figure 4-1. ENDF-VI total neutron absorption cross section plots for select AHFTR absorber materials

Because Tc-99 is not as strongly absorbing as B-10 or Am-241, it is more suited as a gray absorber material. As mentioned in the Introduction, Messaoudi et al proposed that Tc-99 could be used as a neutron absorber in dilution pins within the driver fuel assembly for the purpose of resonance feedback [32]. To minimize the affect of energy shielding with U-238, which could happen during a sodium void, Kim et al has shown that the poison rods should be concentrated in their own standalone poison assemblies as opposed to evenly distributed in the driver fuel. In the case of the study performed by Kim et al, B₄C was proposed as an IBA [31]. However, it should be expected that the same principle applied by Kim et al also applies to control rods. Therefore, distributing the control rods in evenly distributed clusters throughout the fuel, as is done in LWRs, is not practical in SFRs. In fact, in most SFR designs control rods are commonly

bunched together into a movable subassembly that travels inside a fixed *control assembly* that takes its own discrete location within the core. Therefore, the technetium control rods will be located in dedicated control assemblies as shown in Figure 1-7.

Control Assembly Design

The AHFTR reactivity control strategy consists of three different types of control rod mechanisms: (1) a reactivity shim control rod bank, (2) a safety shutdown rod bank and (3) an ultimate shutdown rod bank for achieving shut down margin. Technetium is selected to be the absorber material for the shim and safety rod banks. The shim and safety rod clusters operate independently of each other, but are together co-located in the primary control assembly locations (Figure 1-7). The ultimate shutdown rods compose a separate control assembly (Figure 1-7). The dimensions of each control system, which will be discussed in the following sections, are given in Table 4-2.

Table 4-2. Control assembly types and dimensions

Control Assembly Type	Ultimate Shutdown	Primary Control		Gas Expansion Module
Control Assembly Pitch (cm)	16.142	16.142		16.142
Assembly Duct Thickness (cm)	0.394	0.394		0.394
Inter Assembly Gap (cm)	0.432	0.432		0.432
Subassembly Duct Thickness (cm)	0.394	--		--
Intra Assembly Gap (cm)	1.000	--		--
Rod Type	Shutdown	Shim	Safety	Reflector
Poison Type	B ₄ C	Tc-99	Tc-99	Void
CRGT Outer Diameter (cm)	--	0.755	0.755	0.755
CRGT Inner Diameter (cm)	--	0.643	0.643	0.643
Control Rod Cladding Outer Diameter (cm)	0.755	0.455	0.455	--
Poison Slug Outer Diameter (cm)	0.643	0.343	0.343	--
Length of Poison Section (cm)	91.100	56.900	91.100	91.100
Number of Rods	271	133	138	271

Traditional SFR Control Assembly Design: B₄C Ultimate Shutdown Assembly

It is important to indicate the current state of typical SFR control assembly design such as that proposed for the ABR before discussing the details of the technetium primary control. To

illuminate this point, the design of the ultimate shutdown control assembly is selected to be based on that of the ABR. Therefore, the ultimate shutdown control assembly draws its design from more conventional SFR control designs. Similar to the ABR, a small number of the control rod assemblies are designated for attaining the ultimate shutdown margin of the core. This margin is considered necessary to bring the core reactivity down to the point of the cold shutdown condition [55].

Most of the length of the ultimate shutdown assembly consists of just the outer hexagonal HT-9 shroud (Figure 4-2). Sodium coolant is allowed to flow through this empty assembly structure. The ultimate shutdown rods make up a 271 pin bundle array that is located inside a secondary hexagonal HT-9 shroud which is concentric with the outer assembly shroud. This secondary shroud and pin bundle comprise a sub-assembly which is allowed to move freely inside of the outer assembly shroud. This control subassembly is connected to a drive shaft that extends to control motors outside of the reactor vessel.

Just as with traditional SFR core designs, the neutron poison material for the ultimate shutdown system is B_4C . For the AHFTR, natural boron is used instead of enriched boron. For the AHFTR primary control rods, technetium metal is adopted for the poison material for its high atomic density of Tc-99 atoms. Tc-99 metal was also proposed for the technetium transmutation targets by Yang et al. However, unlike the Tc-99 targets proposed by Yang et al, the primary control assemblies proposed in this dissertation are not implemented with a moderating material in their design.

Technetium Based Primary Control Assembly Design

Originally, an internal subassembly design, exactly the same as that proposed for the ABR, was considered for the AHFTR primary control system. In the ABR, the downward motion of a primary control hexagonal subassembly into the top of the active core is responsible for

reactivity shim. These rods used for reactivity shim also have a dual role as the ABR's safety rods. Thus, the ABR uses the same primary control subassembly to provide enough negative reactivity to shut the core down to a safe condition in case of an accident situation. Therefore, the ABR uses this subassembly design to provide reactivity shim as well as part of the shutdown margin.

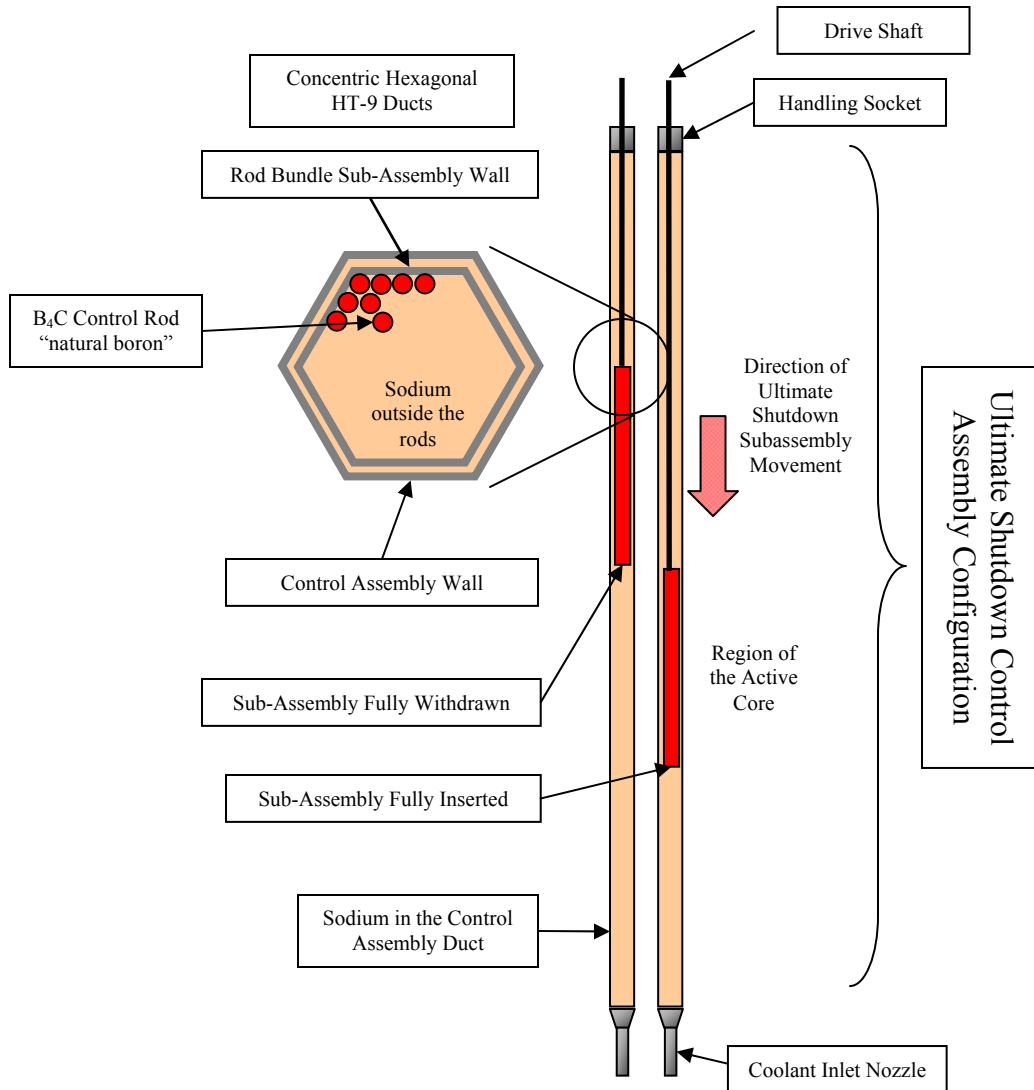


Figure 4-2. Ultimate shutdown control assembly configuration

When a top loaded primary control subassembly is inserted into the top of the AHFTR, the resulting absorption of the neutron flux in the upper half of the core also decreases the transmutation efficiency of the axial targets. Therefore, the mechanics of the primary control

assembly design diverges slightly from the ABR. This decision was made to allocate a portion of the primary control assembly rods, to be used for shim control, to be inserted through the bottom of the core so that they would not significantly perturb the flux in the axial target region.

Instead of a moveable subassembly filled with control rods, two separate clusters of control rods are created. Rods from both a shim rod cluster and a separate safety rod cluster are evenly distributed throughout the primary control assembly. Rods of the same cluster are attached to one another through a spider-like tie rod subassembly similar to that used in PWRs. Therefore, there is a spider-like tie rod subassembly for the shim rods and a separate one for safety rods within each primary control assembly. Because the shim rods are inserted into the core from the bottom, the shim rod cluster is attached to long tie-rods that are equal to the height of the core.

To insert shim rods into the core, its spider subassembly is pulled upwards by the action of the rod drive. When the shim rods are inserted to their desired location, a mechanical clamping mechanism can be actuated to prevent them from falling out of the core. Alternatively (or additionally), the shim rod drive mechanism can be designed with sufficient internal friction in the gearing system that unintentional rod drop out of the core is highly improbable. It is important to note that the incorporation of both top and bottom loaded control rods does not increase the physical size of the reactor and associated core externals because neither shim or safety rods are withdrawn beyond the extent of the gas plenum (top) or the axial reflector (bottom). Figure 4-3 shows the mechanical details of the primary control assembly design.

The AHFTR primary control assembly consists of a tube bundle of control rod guide tubes (CRGT) that are wrapped in a hexagonal assembly shroud. These CRGTs are capped at the bottom to prevent sodium coolant from entering the tube. Half of these CRGTs are allocated for

the shim control rods whereas the other half are allocated for the safety control rods. The shim and safety rod clusters move independently of each other in the CRGTs through the locomotion of their respective connecting spider subassemblies. These spider-like connectors are then each connected to two concentric drive shafts that extend to the control motors outside of the reactor vessel.

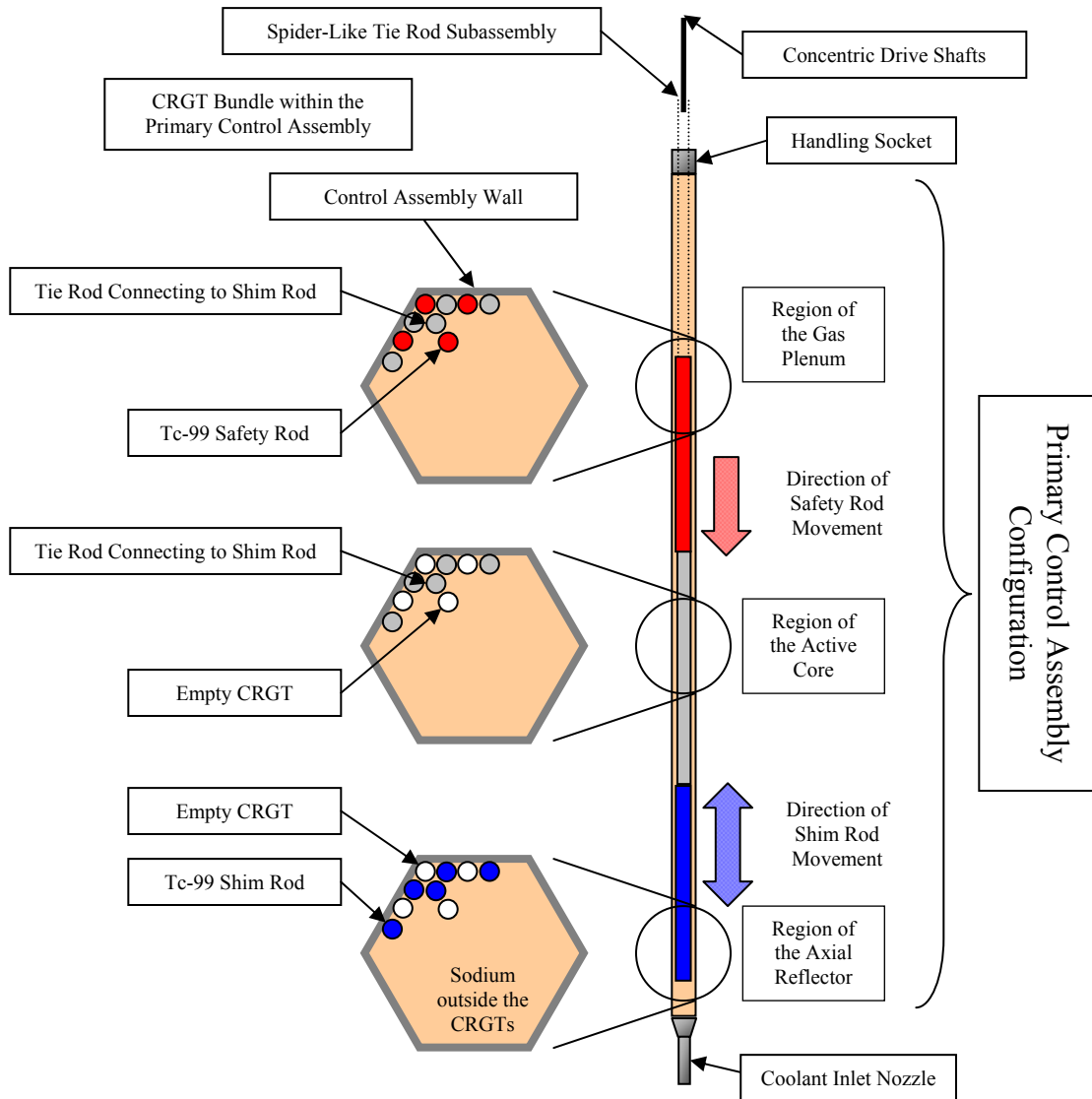


Figure 4-3. Primary control assembly configuration

It is envisioned that a rack-and-pinion style control rod drive motor would be used for the *inner* safety rod shaft. A worm-screw type drive mechanism would be used to move the *outer*

annular shim rod shaft. The safety system would operate on an electric servo with a circuit interrupter such that interruption of power to the servo would cause the safety rod clusters to fall into the core. The shim system would only move the shim rod cluster when power was applied to the worm gear servo. Hence, if power is interrupted to the system, the shim rods would not fall out of the core, but rather be held in place by the friction in the worm-gear system.

It is envisioned that the CRGT tube would be filled with helium. The lack of sodium flow through the tube prevents the action of hydraulic frictional drag on the control rod in the tube that could hinder its motion. This is an important design feature because of the possibility of a stuck control rod cluster due to a control assembly being axially bowed or warped. The lateral and axial temperature gradients, which are typical in a SFR core, frequently create expansion and bending forces that cause assembly bowing. In fact, assembly bowing is sometimes relied upon as a negative reactivity feedback mechanism related to leakage. This feedback mechanism will be discussed later in this chapter.

An additional design consideration is attributed to gamma ray heating of structural components, which is the result of gamma rays that are produced by fission and neutron activation, imparting kinetic energy into the atoms of structural materials. The number and dimensions of the CRGT tubes in the primary control assembly are exactly the same as that of the fuel cladding used in the fuel assemblies. Because the CRGTs receive the same level of sodium flow that fuel pins receive, it is expected that gamma ray heating of control assembly structures will be sufficiently dealt with by the coolant outside the tubes.

Gas Expansion Module

A measure of passive safety control is included by incorporating six gas expansion modules (GEM) in each six corners of the core periphery (Figure 1-7). GEMs are special assemblies placed at the perimeter of a SFR which are designed to enhance neutron leakage in

the event of the loss of primary coolant flow. GEMs were originally designed for reactor concepts of the IFR program [67]. A typical GEM design is shown in Figure 4-4.

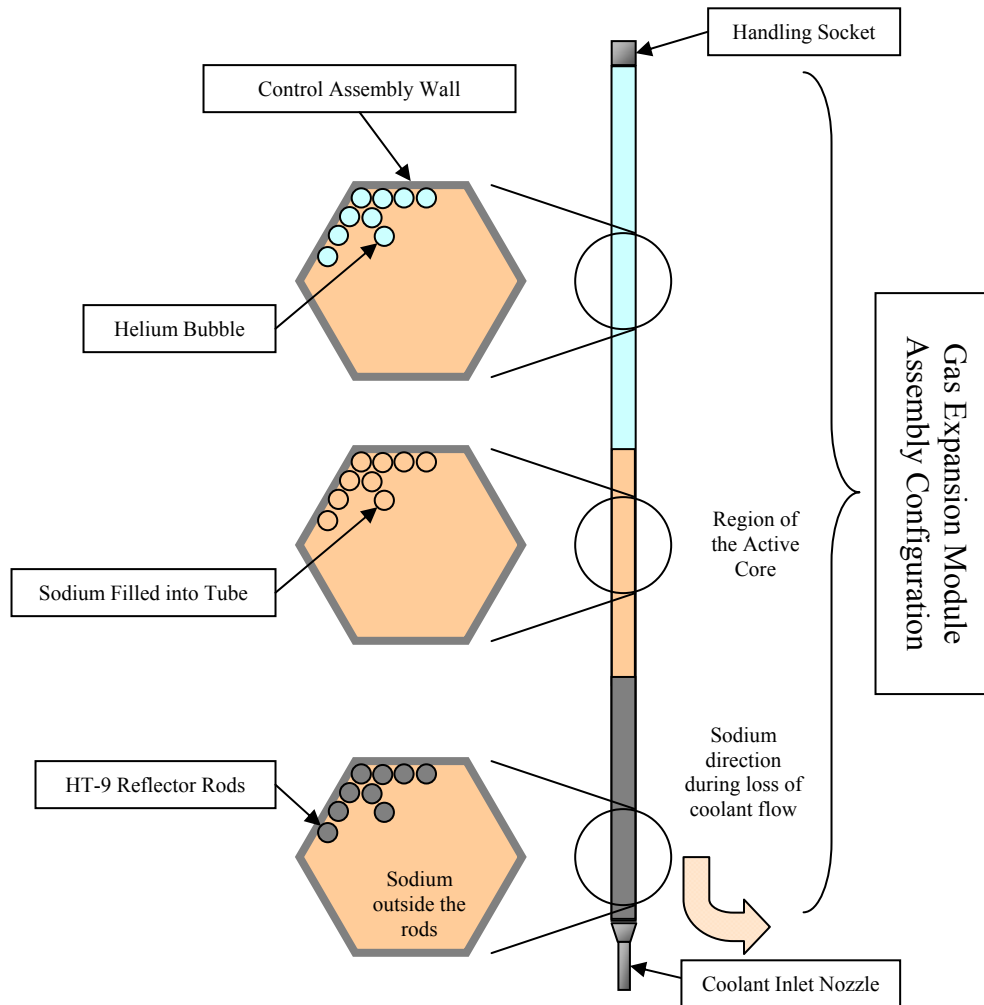


Figure 4-4. Gas expansion module assembly configuration

The lower end of the GEM assembly consists of a lower rod bundle of HT-9 pins that is an integral component of the core's lower axial reflector. A separate bundle of tubes fills the space above the axial reflector. These tubes are open at their bottom end to allow sodium coolant to enter the tube. A helium gas bubble fills the upper end of the tube, which is capped at the top near the handling socket to prevent the sodium from passing through the tube. In the event that the bulk coolant circulation pumps fail, the pressure differential between the non-circulating sodium and the helium gas bubble forces sodium out of the tube causing the gas bubble to

expand. The displacement of the sodium and expansion of the helium creates a voided space in the radial reflector that extends down into the active core region. The removal of reflection by the sodium at the core periphery enhances neutron streaming from the active core.

Control Rod Worth

The shim rods are inserted through the bottom of the active core by the withdrawal of the shim cluster spider subassembly. The purpose of the shim rods is to absorb the excess reactivity produced by the addition of fresh fuel at BOC. As can be seen in Figure 4-5, the reactor core's BOEC excess reactivity can be completely suppressed when the rods are inserted 55 cm. This distance is 75% of the height of the active core.

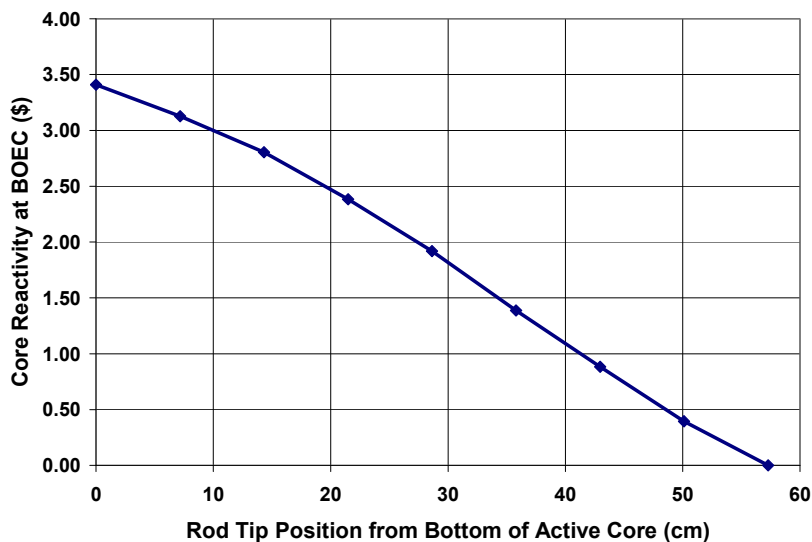


Figure 4-5. Shim control rod bank reactivity worth at BOEC

As the fuel is irradiated, the excess reactivity is consumed by the burnup of the fuel. Therefore, the shim rods are pushed out of the bottom of the core, by the downward motion of the spider subassembly, until they are fully withdrawn by the end of the irradiation cycle. The reactivity worth of the shim rod bank at EOEC is shown in Figure 4-6. Figure 4-5 and Figure 4-6 show the excess reactivity worth of the core at BOC and EOC as a function of the length of

control rod inserted into the core. Notice, that the relative reactivity worth of the shim rod does not change considerable between BOC and EOC.

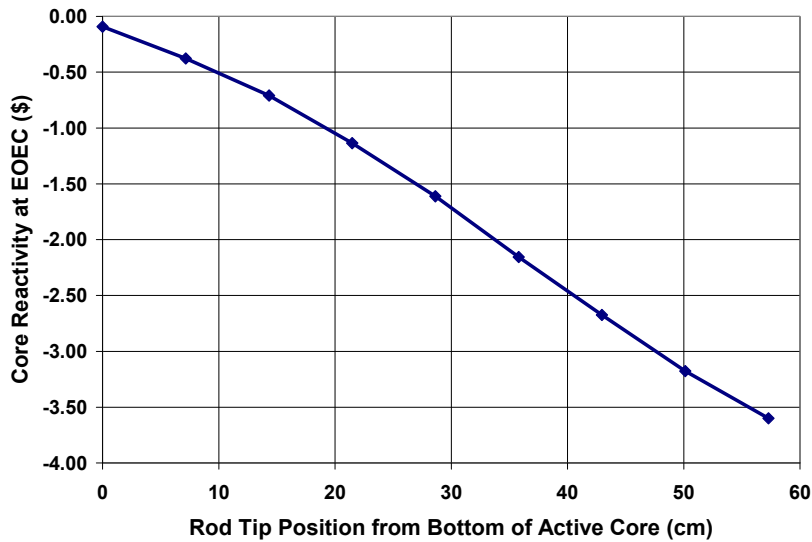


Figure 4-6. Shim control rod bank reactivity worth at EOE (DIF3D)

The safety control rods are inserted through the top of the core above the axial targets. These rods do not move throughout the irradiation. Instead they are raised to the top of the core during startup where they remain during normal operation. In the event that rapid shutdown is required, the reactor monitoring and safety systems can trigger the drop of these rods into the core by interrupting power to the control rod drive servo. The safety rod bank reactivity worth at BOEC and EOE is shown in Figure 4-7 and Figure 4-9 respectively.

There is a slight positive reactivity insertion as the rod tip passes through the axial targets. This positive reactivity feedback is caused by the spectrum hardening of the flux in the targets due to the epithermal absorbing worth of technetium. Figure 4-8 shows the flux spectrum in the targets when the safety rod tip is inserted into the axial target region. However, it is important to note that the preferential absorption of neutrons in Tc-99, as the control rods pass through the targets, can only be observed in the epithermal energy range. This is because, the capture cross section of Tc-99 falls off sharply at neutron energies above one MeV (Figure 4-1). It is also

important to note that the spectrums plotted in Figure 4-8 are virtually indistinguishable. Therefore, the spectrum hardening from Tc-99 entering the target region can be considered negligible. Hence, the initial positive increase in reactivity in Figure 4-7 has a total value of only ten cents. It is likely that this ten cents can be compensated by allowing for passive safety feedbacks such as the leakage control afforded by the GEMs.

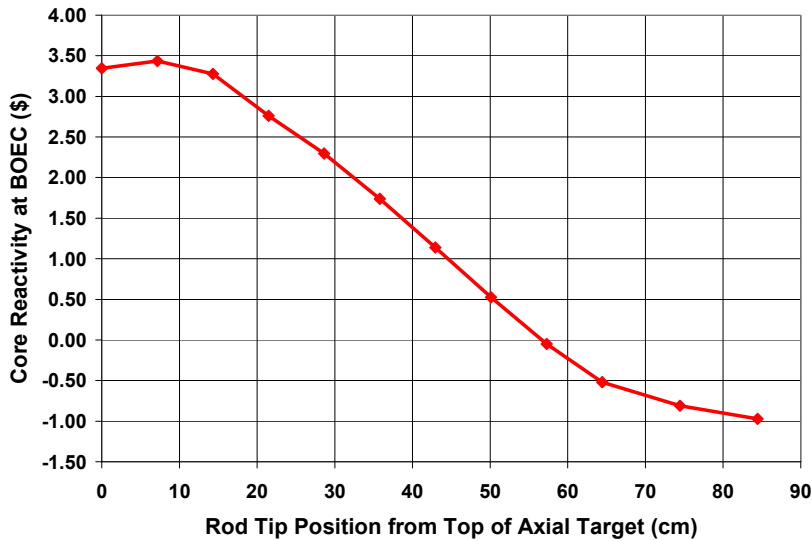


Figure 4-7. Safety control rod bank reactivity worth at BOEC (DIF3D)

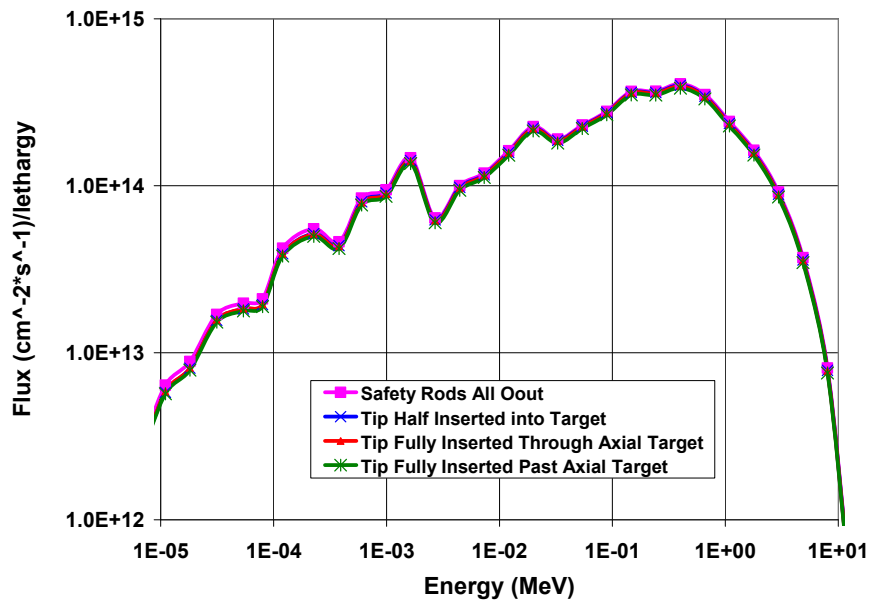


Figure 4-8. Neutron spectrum in the targets as a function of safety rod insertion (DIF3D)

It is important to note that the positive insertion exists only at the BOEC. As the americium is depleted in the targets, the local spectrum dependence on neutron capture is also lessened. This is because the reactivity suppression provided by the combination of moderation and americium capture is lessened. Therefore, the insertion of the rod and resulting absorption of neutrons in the epithermal range has less impact on reactivity at EOEC. This is reflected in the safety rod reactivity worth curve at EOEC in Figure 4-9.

As can be seen from Figure 4-7 and Figure 4-10, the safety rod bank has sufficient reactivity worth by itself to completely shut the reactor down to at least one dollar below critical. Therefore, even if for any reason, the entire shim rod bank were to be absent from the core during an emergency shutdown, the shim rod bank could completely take its place and still have one dollar of shutdown margin remaining.

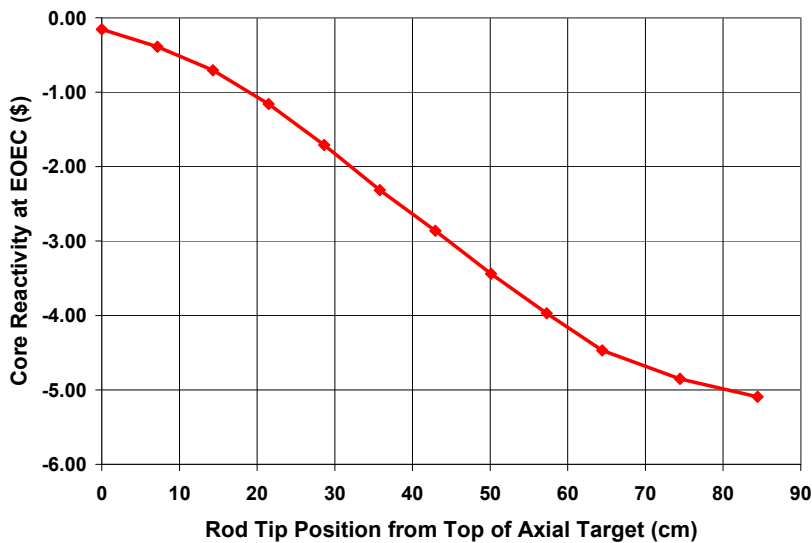


Figure 4-9. Safety control rod bank reactivity worth at EOEC (DIF3D)

Additional shutdown margin is provided by the ultimate shutdown subassembly bank. Like the safety rods, the ultimate shutdown subassemblies are inserted through the top of the core. These subassemblies are withdrawn through the top of the core during startup where they remain during normal operation. At the end of the irradiation cycle, the safety and ultimate

shutdown subassemblies are inserted to provide for the full shutdown margin of the core. Figure 4-10 and Figure 4-11 show the reactivity worth of the ultimate shutdown system for BOEC and EOEC respectively.

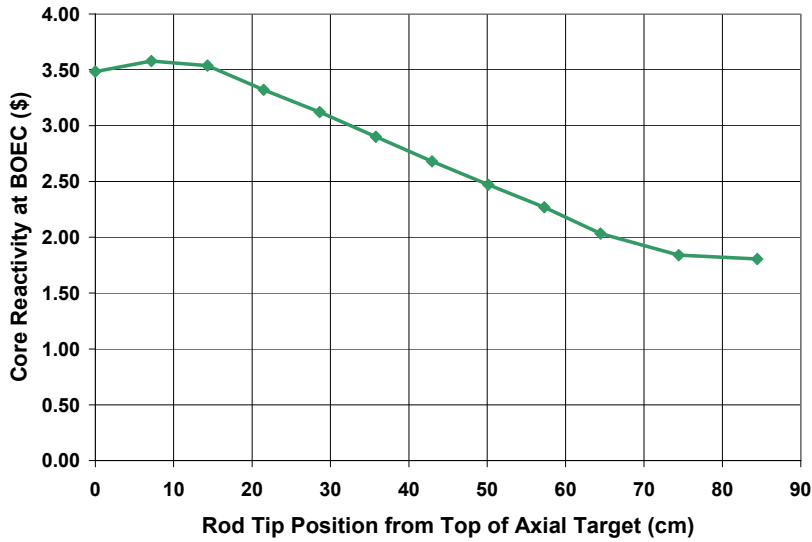


Figure 4-10. Ultimate shutdown system worth at BOEC (DIF3D)

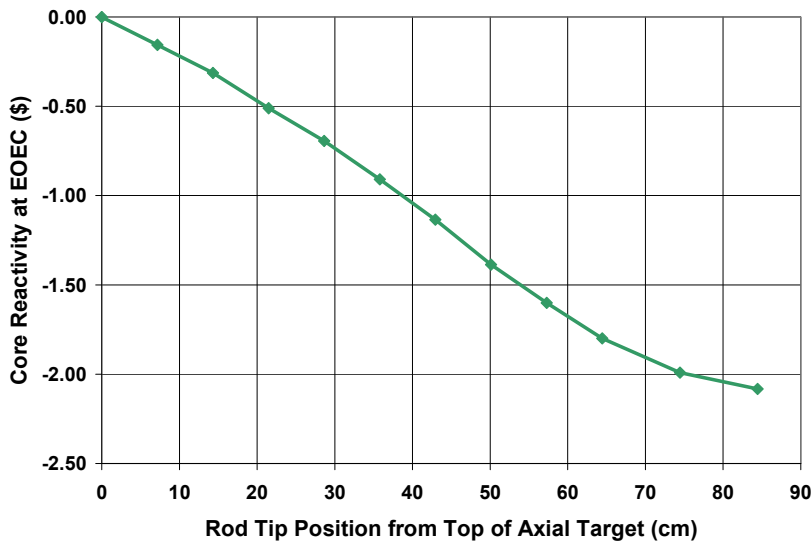


Figure 4-11. Ultimate shutdown system worth at EOEC (DIF3D)

It is important to note that the overall reactivity worth of the ultimate shutdown system is \$1.75 despite being composed of natural boron in B₄C. The three ultimate shutdown assemblies are located in the inner most region of the core where the flux is strongest. Therefore, despite

being composed of natural boron, the ultimate shutdown assemblies have the largest average reactivity worth per assembly. There are three ultimate shutdown assemblies with a combined worth of \$1.75 which gives an average reactivity worth of 58¢ per assembly. Conversely, the safety rod system and shim rod systems both only have an average reactivity worth of 22¢ and 28¢ per primary control assembly, respectively.

By inspection of Figure 4-7 and 4-10, it is apparent that the total shutdown worth of the reactor at BOEC is \$6.25. The complete shutdown at BOEC accounts for zero net reactivity when the shim rods are inserted and also \$4.50 and \$1.75 of total negative reactivity insertion by the safety and ultimate shutdown systems, respectively. By inspection of Figure 4-6, Figure 4-9 and Figure 4-11, it is apparent that the total shutdown worth of the reactor is \$9.75. The complete shutdown at EOEC accounts for the total negative reactivity inserted by the safety and ultimate shutdown systems as well as an additional \$3.50 by fully inserting the shim rod system. Thus, if an emergency shutdown is required at EOEC with all shim rods removed, the safety and ultimate shutdown system can provide \$6.25 of negative reactivity.

Reactivity Worth of Boron versus Technetium

It is important to compare the reactivity worth of metallic Tc-99 with the more conventional SFR reactor poison: B_4C . As noted earlier, the atom concentration of metallic Tc-99 is approximately 3.5 times that of B-10 in enriched B_4C . However, the unresolved resonance absorption cross section of B-10 is roughly three times greater than that of Tc-99 for most of the fast spectrum. Figure 4-12 contrasts the reactivity worth of the shim rod bank if natural boron or enriched boron is used in the form of B_4C as opposed to metallic Tc-99.

It is apparent from Figure 4-12 that enriched B_4C has a greater reactivity worth in the AHFTR than Tc-99. However, the use of B_4C would only reduce the length of control needed to

shut the core down by approximately 10 cm. Therefore, the technetium rod is considered as a viable alternative to enriched B₄C as a control material in the AHFTR.

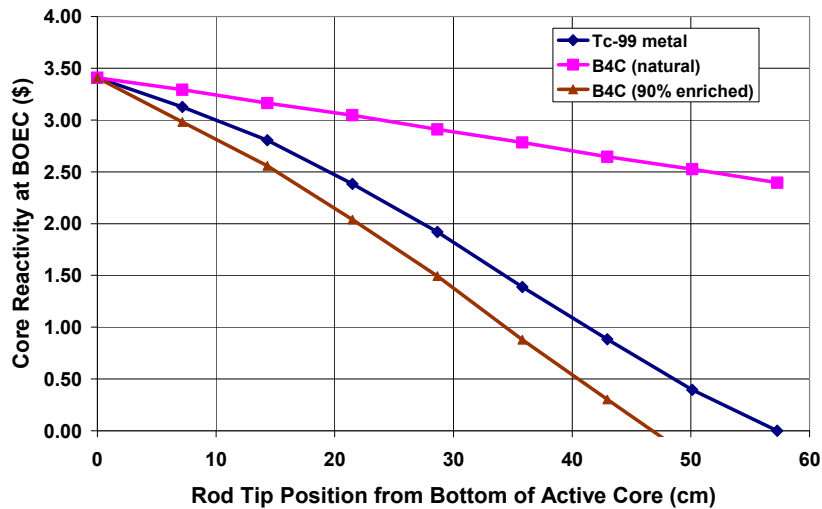


Figure 4-12. Shim control rod bank reactivity worth at BOEC for metallic Tc-99 compared to natural and enriched boron in the form of B₄C (DIF3D)

Top versus Bottom Inserted Shim Rods

One of the key design features of the primary control assembly was to have the shim rods inserted through the bottom of the core ensure that they did not steal neutrons away from the axial targets. For the sake of comparison, the volume average radial flux profile of the active core and targets has been plotted for the case where all shim rods are inserted through the bottom of the core versus all shim rods being inserted through the top of the core. These flux plots are given in Figure 4-13.

Notice that the flux in the targets is slightly less for the top inserted shim rods than it is for the bottom inserted shim rods. The reduction of flux indicates that the transmutation efficiency of the axial targets would be reduced if the shim rods were inserted through the top of the core. Unlike the safety or ultimate shutdown rods, the shim rods require being in the core at all times. Hence, the neutron absorbing effect of a top inserted control rod would have a constant impact

on the targets region's transmutation efficiency, regardless of its gradual removal from the active core. Thus it is more feasible to have a bottom inserted shim rod cluster design as was discussed in the primary control assembly proposed for the AHFTR.

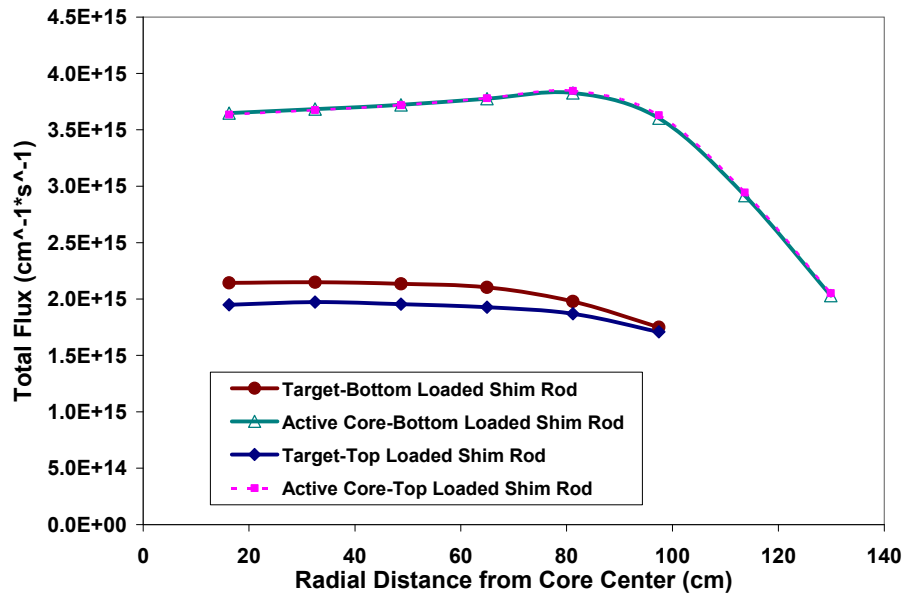


Figure 4-13. BOEC radial flux distributions of the active core (volume averaged over core height) and axial target fluxes for shim rods being inserted through: the top or the bottom of the core (DIF3D)

Axial Power Tilt and Shim Rod Insertion

Figure 4-14 shows the axial power distribution for various shim rod positions in the AHFTR core. As discussed previously, the large mean-free-path of neutrons in the core combined with the relatively gray neutron absorbing worth of technetium reduces the affect of localized flux depressions on the overall core flux distribution. Therefore, the axial flux distribution is virtually identical regardless of the length of control rod inserted into the active core region.

Other Reactivity Feedbacks

As indicated previously, the AHFTR, like the ABR and many other SFR designs has a positive void coefficient. The positive reactivity feedback is a direct consequence of neutron

energy spectrum hardening resulting from the loss of the slight moderation provided by the sodium coolant. When the spectrum hardens, the lack of down scattering causes the number of neutrons above the fission threshold of fertile isotopes (U-238 and MAs) to increase. An increase in above-threshold fissions causes an increase in the neutron multiplication contribution of these fertile isotopes. Figure 4-15 gives the neutron spectrum of the AHFTR inner core region during normal steady state operation and a scenario where all of the sodium coolant is voided from the core.

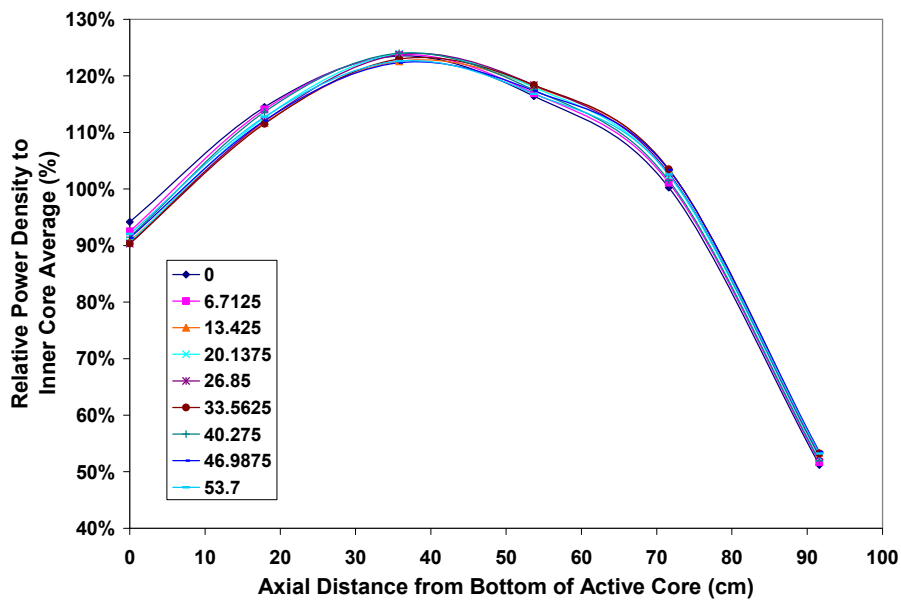


Figure 4-14. Axial power distribution for increasing shim rod length into the active core (inner enrichment zone) region (DIF3D)

This spectrum hardening can be unfavorable if there is no other competing feedback mechanism that can negate the void induced positive reactivity insertion. For SFRs, some negative reactivity feedback comes in the form of Doppler resonance broadening of capture cross sections as the fuel temperature increases. Additionally, because SFRs typically exhibit a high degree of leakage, they can rely on feedback mechanisms that increase leakage as the fuel and structural materials increase in temperature. The negative reactivity feedback caused by this fuel expansion is most pronounced in metallic fuels and was a key control aspect of EBR-II [35].

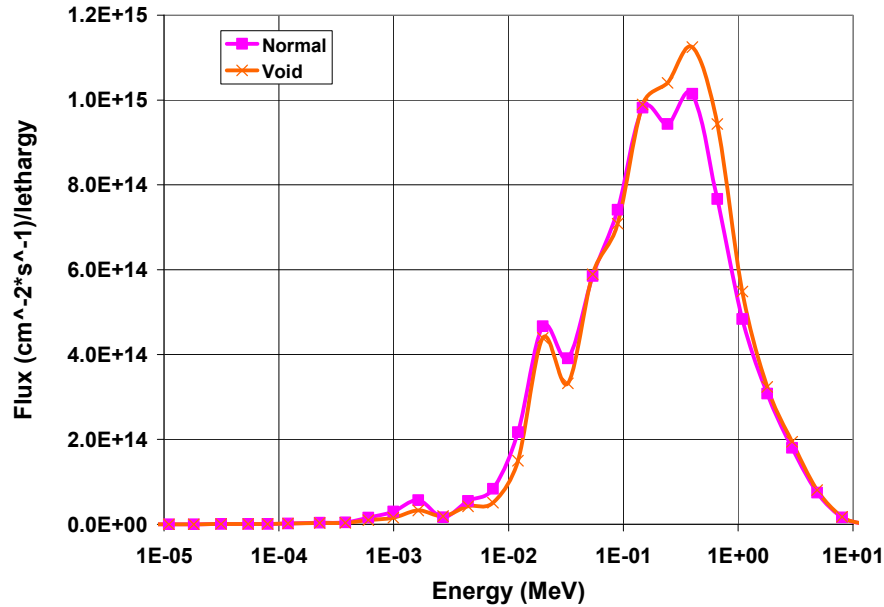


Figure 4-15. Neutron spectrum at BOEC of the inner core region for steady state operation versus a complete loss of sodium coolant (DIF3D)

The void and Doppler reactivity worth for the AHFTR are given in Table 4-3. Also given is the negative reactivity provided by leakage feedback when fuel expansion changes the radius and height of the active core. Leakage feedback is also provided by the GEM. The void effect of the helium bubble expansion in the GEM is also given in the table.

As can be seen from Table 4-3, if the sodium coolant is completely lost from the active core (coolant remains in the gas plenum, axial and radial reflectors), a positive reactivity insertion of about \$8.60 occurs. However, if thermal expansion effects cause both the height and diameter of the core to increase by only 2.5%, the core will lose approximately six dollars worth of reactivity. If both the height and diameter increase by 5.0%, the expansion would remove approximately \$13.30, which is sufficient reactivity to completely negate the positive reactivity insertion by the void. Also, an additional dollar of negative reactivity can be supplied by the combined contribution of the GEM and Doppler feedbacks. Assuming a loss of primary coolant flow, the GEMs provides can provide \$0.52 of negative reactivity. The Doppler feedback can provide an additional \$0.0014 per degree increase in fuel temperature.

Table 4-3. Core reactivity worth for independently separate reactivity feedback effects

	BOEC	Difference from Normal	EOEC	Difference from Normal
Normal Steady State (all rods out)	\$3.79	--	\$0.0	--
All Coolant Voided (all rods out)	\$12.13	-\$8.34	\$8.60	-\$8.60
Doppler (+100K) (all rods out)	\$3.65	\$0.14	-\$0.15	\$0.15
Normal Steady State (shim rods in)	\$0.0	--	n/a	n/a
All Coolant Voided (shim rods in)	\$8.62	-8.62	n/a	n/a
Doppler (+100K) (shim rods in)	-\$0.14	\$0.14	n/a	n/a
Values Below This Point Taken with All Rods Out				
GEM Voided	\$3.27	\$0.52	-\$0.50	\$0.50
Radial Expansion (2.5%)	-\$0.35	\$4.14	-\$4.17	\$4.17
Radial Expansion (5.0%)	-\$5.01	\$8.80	-\$8.88	\$8.88
Axial Expansion (2.5%)	\$1.82	\$1.97	-\$2.01	\$2.01
Axial Expansion (5.0%)	-\$0.71	\$4.50	-\$4.58	\$4.58

Axial Fuel Expansion

During the IFR program, axial fuel expansion of Pu-U-Zr (and U-Zr) EBR-II fuels were tested at the Transient Reactor Test (TREAT) facility. The results of these tests are summarized by Rhodes et al [68]. For these tests, fuel pins were first irradiated to varying burnups in the EBR-II. These irradiated fuel pins were then subjected to transient overpower (TOP) at TREAT. These power levels were in excess of four times their nominal power level in EBR-II. All overpower transients caused extensive melting in the test fuel which amounted to one-half of the original fuel inventory. The pre-failure data from these tests indicated that the metallic fuel slugs expanded axially in excess of the 1% attributed to purely thermal expansion. Rhodes et al attributed this additional expansion to swelling caused by dissolved fission product gasses being liberated by the partial melting of the metallic fuel. Post test examination of the fuel pins that did not exhibit cladding rupture showed large bubbles in the fuel that formed from fission gasses which coalesced into voids as the fuel partially melted and then expanded. It is this expansion of

coalesced gas bubbles that caused the fuel to expand during the TOP. The level of axial expansion was later quantified as a function of:

- The amount of molten fuel created during the overpower
- The concentration of fission gas made available when the fuel melted
- The initial bubble size due to surface tension effects
- The pressure of gas in the fuel pin gas plenum resisting the expansion

The results obtained by Rhodes et al showed that one of the test pins achieved an axial elongation of 3.7%. Also, the axial expansion could be well predicted using a simplified model where only gas trapped in the bubbles was available for expansion.

The results of these tests are promising from the standpoint of reactor control. If these models can be developed to a higher fidelity, they might be used to optimize the axial expansion to meet the TOP scenarios for a given SFR design with a safety margin to cladding breach.

Thermal expansion and fuel assembly bowing was used to validate the safety case for future ALMRs during the IFR program. This passive feedback capability was demonstrated in the Shutdown and Heat Removal Test (SHRT) conducted at EBR-II [69,70]. The SHRT tests demonstrated passive reactor shut down using fuel expansion and natural circulation during two LOCA scenarios: an Unprotected Loss of forced circulation Flow (ULOF) as well as an Unprotected Loss of Heat Sink (LOHS) [71,72].

Radial Fuel Bowing

Radial expansion of the core through fuel assembly bowing is a phenomenon that is highly coupled between the core physics of the TOP reactivity insertion (either by LOCA or other accident initiators) and the thermal-hydraulic and thermo-mechanical behavior of the sodium coolant and fuel assemblies. The bowing of fuel assemblies in the radial direction is caused by lateral temperature gradients across the cross-sectional area of the fuel assembly. The temperature gradient across the fuel assembly is related to the power gradient in the reactor

during the transient. The temperature gradient causes differences in the axial thermal expansion of the assembly's HT-9 duct wall from one side of the fuel assembly to the other. It is this difference that induces a bending moment on the length of the fuel assembly. Assuming the core temperature gradient during the transient is positive for decreasing radius (core hotter at the center), the bending moment pushes the fuel assemblies outwards. At a fundamental level, the amount of bowing created by these temperature gradients is roughly approximated by treating the assembly as a tubular beam with an applied bending moment. Varying complexities of calculations of this type have been implemented in computer codes since the 1970's to try to accurately predict fuel bowing. However, these codes to date have all assumed steady state conditions and were typically benchmarked against critical pile simulations (also at steady-state) using perturbation theory [73,74,75,76].

Fuel bowing was used to enhance the passive safety of the EBR-II. The EBR-II fuel assembly was located in the core by two closely placed lower grid plates. To minimize radial expansion below the mid-plane of the core, a metal button was incorporated onto the surface of each six of the hexagonal sides approximately half-way up the length of the fuel assembly. These buttons held the fuel assemblies tightly in place below the mid-plane. EBR-II did not have an upper grid plate. The combination of the buttons and the two lower grid plates effectively cantilevered the fuel assembly below the core mid-plane. If a strong bending moment were to be induced on the fuel assembly, the lack of an upper grid plate would allow the fuel to blossom (analogous to a flower) at the top of the core. This blossoming effect was an integral feature of the passive safety attributes of the EBR-II. The EBR-II passive reactivity feedback by expansion forces was demonstrated by the SHRT tests. Similar negative reactivity feedbacks for

fuel assembly bowing have also been verified in critical pile tests performed at steady state conditions by various groups [73].

Despite the success of these tests, the transients initiated were demonstrated on fairly long time periods compared to the neutron lifetime in a fast reactor. Due to the small delayed neutron fraction in fast reactors compared to thermal reactors, the neutron lifetime is much shorter and is in the range of tenths of micro-seconds. If a void were instantaneously introduced into the core for some hypothetical situation, the reactivity insertion and resulting TOP could possibly occur on a timescale much faster than fuel bowing could occur.

However, it is important to realize that the total core void worth calculations in Table 4-3 were performed assuming that sodium was only voided in the core and not the surrounding reflectors. The likelihood of such a hypothetical reactivity insertion from void formation in the fueled region alone may not be probable. If this is the case, this hypothetical void insertion may be considered in the realm of core disruptive accidents (CDA) and may or may not require a robust reactor design for compensating for this remote possibility [77]. If such a robust design is required, then it is outside the realm of this dissertation work due to the fact that the ABR designs currently under consideration also have large positive void induced reactivity insertions for this accident event (Table 3-13).

It should be briefly mentioned that the coolant outlet temperature of the current ABR design is approximately 780 K. The boiling point of sodium (at atmospheric pressure) is 1156 K. If a pool type reactor with the bulk sodium at or just above atmospheric pressure is assumed, the temperature margin before sodium boiling occurs is roughly 370K. Sodium has a large thermal conductivity (60 W/m-K) and fairly large heat capacity (1,250 J/kg-K). Therefore, a pool type design could offer a large thermal momentum which minimizes the rate of increase in the core

coolant temperature. If a loop type design is used, the pressurization of the sodium could increase the margin to boiling. However, a loop design would possibly have to sacrifice the large thermal momentum offered by a large sodium pool. The decision for pool or loop type SFR reactor cooling strategies is currently the subject of much debate in the SFR community. Both methods have their own pros and cons. The choice for a pool or loop type reactor does not play a role in the transmutation performance of the reactor and does not enter into the calculations of this dissertation. For the purpose of discussion in the fuel performance discussion in Chapter 6, a pool type design is assumed.

Technetium Transmutation Rate

When Tc-99 absorbs a neutron, it transmutes into Tc-100 which decays with a half-life of 15.86 seconds by beta particle emission into a stable atom of Ru-100, ruthenium. Because, Ru-100 is followed by two more stable isotopes of ruthenium on the chart of the nuclides, it is unlikely that successive neutron capture from the original Tc-99 transmutation will produce a significant mass of radioactive material. Therefore, it can be assumed that Tc-99 transmutation by neutron capture will remove the radiotoxicity associated with Tc-99 from the fuel cycle. Hence, the technetium shim rod, though not a true transmutation target such as that proposed by Yang et al, performs a secondary purpose as a Tc-99 burner.

Given that some Tc-99 material is inserted into the reactor to some extent in the form of the shim rods, it is expected that some Tc-99 will be destroyed as a function of the amount of rod that is inserted into the core. To evaluate the rate at which the shim rod Tc-99 is destroyed, a REBUS calculation was performed for a single cycle (non-equilibrium depletion mode) with the shim rods fully inserted into the core throughout the entire irradiation. Using this simulation, the overall depletion rate of Tc-99 was computed.

This depletion rate was then divided by the entire length of the shim rod to find the average Tc-99 depletion rate per length of rod. Thus, the average Tc-99 depletion rate per length of control rod is: $1.4E-6$ kg/MWD per cm or shim rod. If it can be assumed that the amount of excess reactivity is linear as a function of burnup, than it can also be assumed that the rate that the shim rod is removed is also a linear function of irradiation time. For a shim rod length of 55 cm and a cycle length of 214 days, the shim rod removal rate is: 0.26 cm/EFPD. Integrating the Tc-99 depletion rate per unit length of rod over the entire cycle length then gives the total Tc-99 consumption rate of the core accounting for the shim rod movement. Thus, the Tc-99 consumption rate of the shim rods is: 0.0143/MWY. A summary of results on Tc-99 consumption by the AHFTR is given in Table 4-4.

Table 4-4. Summary of Tc-99 consumption by the AHFTR

Tc-99 Depletion Rate per Unit Length of Shim Rods (kg/MWY/cm)	1.4E-6
Shim Rod Removal Rate (cm/EFPD)	0.26
Cycle Length (EFPD)	214
Tc-99 Consumption Rate by Shim Rods (kg/MWY)	0.0143
Tc-99 Production Rate by Fissions in the Fuel (kg/MWY)	0.0053
Tc-99 Net Consumption Rate by the AHFTR (kg/MWY)	0.0089
Tc-99 Production Rate of reference PWR fuel (kg/MWY)	0.0074

Using the TRITON calculation of the reference UOX PWR fuel assembly, which was used to generate the isotopic vector of the ABR and AHFTR external feed, the rate of Tc-99 produced by the LWR fleet was found to be: 0.0074 kg/MWY. Therefore, the AHFTR shim rods can consume approximately 1.9 times more Tc-99 than that produced by a PWR for equal amounts of energy produced by each reactor type. In other words, the shim rods associated with one megawatt of installed AHFTR capacity can consume the Tc-99 produced by 1.9 megawatts of installed PWR capacity.

Despite the attractiveness of burning Tc-99 in the shim rod system of the AHFTR, these calculations up till now have not reflect the Tc-99 produced by the ABR or the AHFTR in the

fast reactor fleet. This is partly because, unlike the UREX+ aqueous reprocessing technology, pyroprocessing does not currently offer a separation strategy for Tc-99.

However, if Tc-99 separation were possible with pyroprocessing the *net* Tc-99 consumption of the entire AHFTR core can be found. The AHFTR fuel produces approximately 0.0053 kg/MWY of its own Tc-99 through fissions of fuel atoms. Therefore, the net destruction of Tc-99 by the AHFTR is only: $0.0143 \text{ kg/MWY} - 0.0053 \text{ kg/MWY} = 0.0089 \text{ kg/MWY}$. Hence, if it were possible to recover the Tc-99 produced by fission, the support ratio of PWRs to AHFTRs would be reduced to 1.2.

CHAPTER 5 DIFFUSION VERSUS TRANSPORT BENCHMARKS

A benchmarking effort is conducted to evaluate the validity of the diffusion theory calculation used for the core physics and transport analysis. The Variational Anisotropic Nodal Transport (VARIANT) code is an “add on” module that comes with the current publicly available version of the DIF3D code [78]. The VARIANT spherical harmonics treatment can be applied to the hexagonal-z nodal discretization which describes the AHFTR geometry. VARIANT can be invoked with minimal changes to the DIF3D input. Therefore, the equilibrium cycle calculation performed by REBUS is re-evaluated using the VARIANT option of the DIF3D code.

Due to the inherent archaic memory allocation structures available in the DIF3D/REBUS system, only three moments of the angular flux (P3) were calculated. Also, because of these memory restrictions, the number of energy groups was reduced from 33 to eight. Therefore, the amount of energy information is reduced in lieu of increased angular information. Because of these limitations, the MCNP code was used to evaluate the axial and radial spatial flux profiles as well as the driver and target energy spectrums. A short FORTRAN processing code was written for copying the batched homogenized isotopic number densities from each core region in DIF3D/REBUS model into the MCNP model. The corresponding hexagonal-z nodal geometry scheme used in the DIF3D model was also preserved in the MCNP model.

Also tested in this chapter is the spatial and energy shielding treatment used in the MC²-2 cross section collapsing algorithm. The collapsed cross sections (group constants) used for the deterministic calculations are generated by completely homogenizing the pin and fuel assembly geometry detail into a representative zero-dimensional infinitely dilute mixture. One of these mixtures is defined for every region in the core sharing a similar isotopic composition and,

hence, neutron spectrum. These regions include the: inner, middle, outer enrichment zones and the axial target region above the active core. Also, a mixture is created for the shield and reflector compositions. Using a critical buckling search calculation, the group constant library is generated for each zero-dimensional mixture in separate calculations performed by MC²-2. Therefore, the spatial shielding and the region-to-region neutron shadowing effects in the reactor core are not accounted for during the cross section generation. This task would generally be performed in a lattice calculation at the pin or assembly level for most thermal spectrum applications before using the group constant set in a core simulator.

For fast reactors, the mean-free-path is significantly longer than in thermal spectrums allowing for the homogenization over the fuel assembly. However, the axial targets are slightly moderated to an epithermal or hard-epithermal spectrum. Thus, it is important to test whether or not spatial shielding occurs within the target fuel rod placed adjacent to a moderator rod. A unit cell calculation of one zirconium hydride rod surrounded by six targets with reflective boundary conditions is modeled using the MCNP code. The flux for one of these six targets is evaluated as a function of radius going into the fuel slug. This radial distribution is determined by dividing the fuel slug into five equal volume zones and tallying the neutron flux entering each of these zones.

The region-to-region shadowing effect is also evaluated using the MCNP code. The six pins from the cell calculation are homogenized into an annular region of equal volume surrounding the zirconium hydride pin. Shadowing is determined by tallying the neutron flux as a function of radial distance away from the center of the annulus.

DIF3D, VARIANT and MCNP Methods

VARIANT solves the multigroup steady-state neutron diffusion and transport equations in two and three dimensional Cartesian and hexagonal geometries using variational nodal methods.

Anisotropic scattering is treated in these calculations. However, for the coupling of VARIANT with REBUS, it was found out that the REBUS code is ill-equipped to accept the higher order scattering matrices in the microscopic cross section data file format (ISOTXS) provided by the MC²-2 code. ISOTXS is a binary data file for transferring microscopic cross section data between codes by different authors which uses the standardized format adopted by the Committee on Computer Code Coordination (CCCC). The difficulty of REBUS to process the higher order scattering data in ISOTXS is caused by the method in which REBUS homogenizes fuel isotopic number densities over each region of the core (i.e., Inner, Middle, Outer Core and Targets).

Recalling Figure 2-1, REBUS homogenizes fuel compositions of all fuel batches independent of depletion stage within a user defined “same spectrum” region. This new region averaged number density is then used in the physics calculation to generate the flux in that region. This flux is then multiplied by the original un-homogenized number densities at each region to get the reaction rate at that location in the core. These reaction rates are then applied to the original isotopic compositions of each fuel batch at each stage within that region to perform the depletion process.

Therefore, the exact position of each individual fuel assembly within the core is not tracked. It is only necessary to track the mass of each batch as it moves from region to region as a function of cycle or stage number of its depletion. For many fast reactor core designs (ABR, AHFTR, etc.), the fuel is not shuffled. Instead, a fuel assembly typically resides in the same location in which it was originally loaded from BOL through EOL. Because the fuel is not shuffled, the core can be divided into separate enrichment zones throughout the core.

For this reason, even though the MC²-2 code provides the higher order scattering data, REBUS does not have the data storage structures to receive it. The creators of VARIANT made substantial modifications in DIF3D to handle the input of anisotropic cross sections. However, the VARIANT module expects this data to be input in macroscopic data file format (COMPXS). Very little formatting changes were made for the absorption and fission “principal” cross sections, which can be in ISOTXS or COMPXS form. Nevertheless, REBUS can only accept the ISOTXS format due to the homogenization routine. Logistically, it is impossible to input COMPXS formatted data into REBUS because the nature of the equilibrium search manipulates the atom densities of the fresh fuel composition (i.e., TRU enrichment) in order to meet the constraints of equilibrium cycle length and burnup. Because of these limitations, the higher order approximation of the scattering cross section had to be dropped for the coupling between VARIANT with REBUS.

Flux Spectrum Analysis

A P3 approximation of the flux and current are performed by VARIANT but with zero order scattering in the P_N equations. To this end, MCNP is used to compare the BOEC radial and axial flux distributions as well as neutron energy spectrum with the DIF3D/REBUS and VARIANT/REBUS results. Figure 5-1 shows the flux spectrum for the AHFTR mid-plane at the inner most row of fuel.

It is important to note the close agreement between the MCNP and the DIF3D spectrum. The major observable difference between the two curves is the general magnitude of the flux which can be seen to be centered on 0.25 MeV. The flux depression at 0.25 MeV is a result of several well resolved but overlapping sodium resonances in that energy range. Note the flux depression at 30 keV which corresponds to the well resolved iron capture resonance at that energy. The VARIANT spectrum does not capture the true shape of the energy distribution due

to the eight energy group resolution. Figure 5-2 shows the flux spectrum for the target zone for the innermost row of fuel.

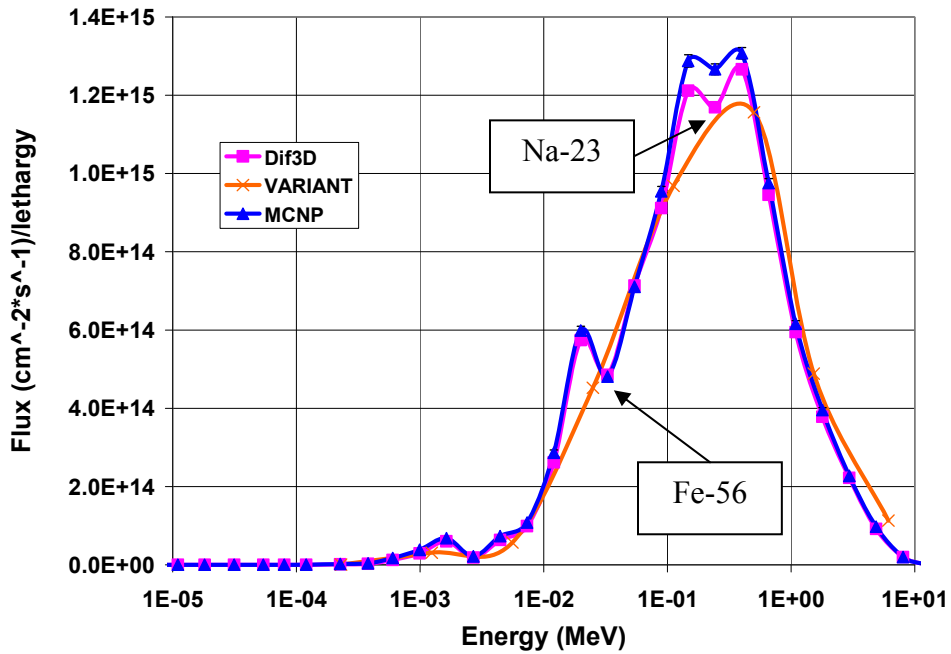


Figure 5-1. Neutron energy spectrum for the AHFTR at the core mid-plane for the inner most row of driver fuel (taken at BOEC)

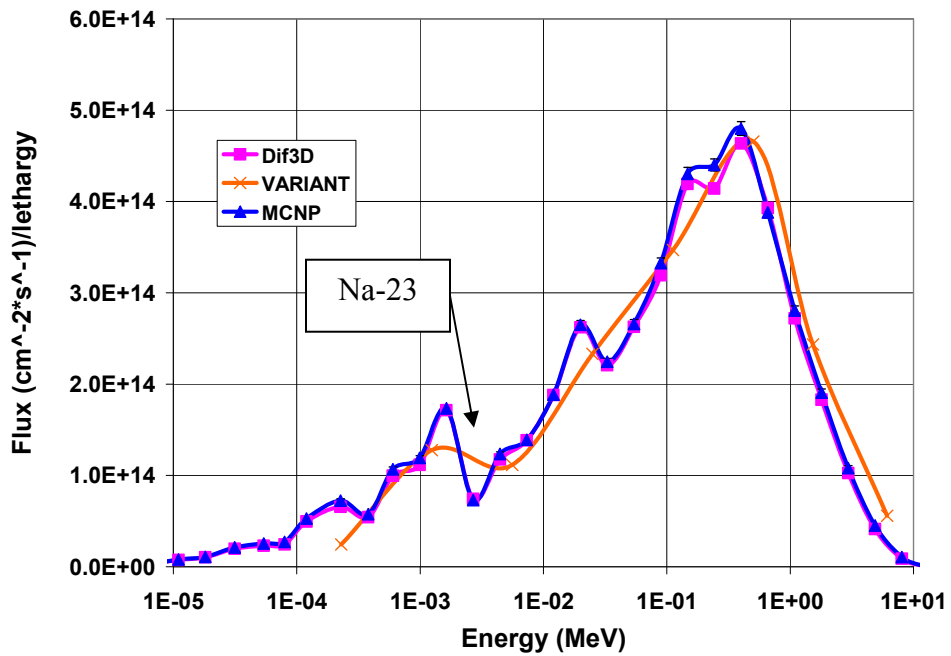


Figure 5-2. Neutron energy spectrum for the AHFTR at the target region located directly above the inner most row of driver fuel (taken at BOEC)

Here again, the DIF3D spectrum shows good agreement with the MCNP spectrum. In fact, the difference in overall magnitude is less than in the driver fuel. Note that because of the epithermal spectrum, the sodium resonance at 3 keV is much more pronounced than in Figure 5-1. However, much of the flux is still in the epithermal-to-fast energy range such that heavy metal resonances dominating from 0.1 eV through 100 eV have very little importance. For a later discussion, it appears that the resonance shielding of the lighter metal elements (comprising the structure and coolant), with resolved resonances between 1 keV and 1 MeV, have the most affect on the flux.

The difference in total flux magnitude between the three calculation methods may be attributed to an increasing accuracy of the angular treatment provided by VARIANT and REBUS. VARIANT provides a better approximation of the angular distribution of the flux and transport cross section. MCNP provides full anisotropic treatment of scattering as well as the flux gradient as opposed to the diffusion approximation made by DIF3D or the isotropic scattering assumption made with VARIANT.

Spatial Flux Analysis

The diffusion approximation under predicts the curvature of the axial and radial flux gradient [79]. This is observed in the axial and radial flux profile for the AHFTR. The axial flux profile for the inner most row of fuel is given in Figure 5-3. The error bars for two standard deviations of the flux in the MCNP calculation are shown in the plot but are of the same size as the plotted data point. Notice the peak flux occurring at the mid-plane is less for the DIF3D calculation than the other two curves. The total flux calculated by VARIANT is actually much closer to the MCNP result than the DIF3D result. This indicates that the fewer energy groups used in the VARIANT calculation was a valid simplification even though the fine spectral

resolution of the flux energy spectrum is lost. Figure 5-4 shows the radial distribution of the flux at the core mid-plane.

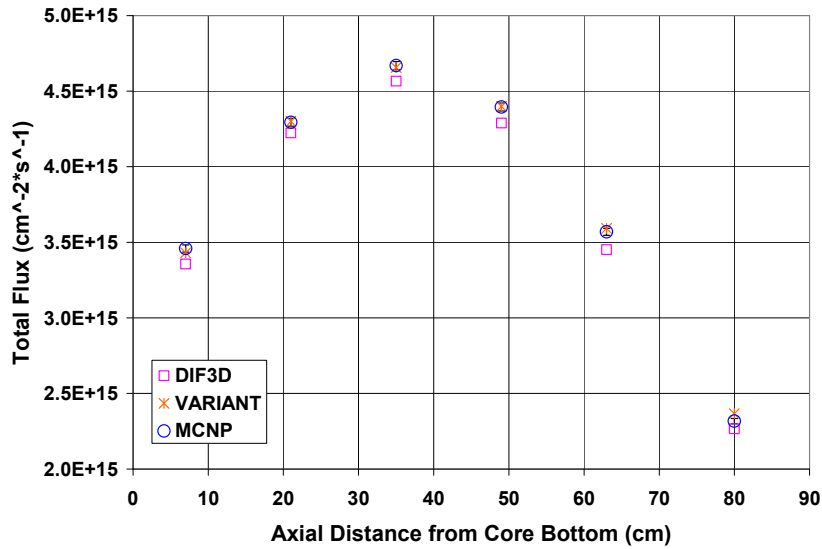


Figure 5-3. Comparison of the total BOEC flux axial profile for the inner most row of fuel

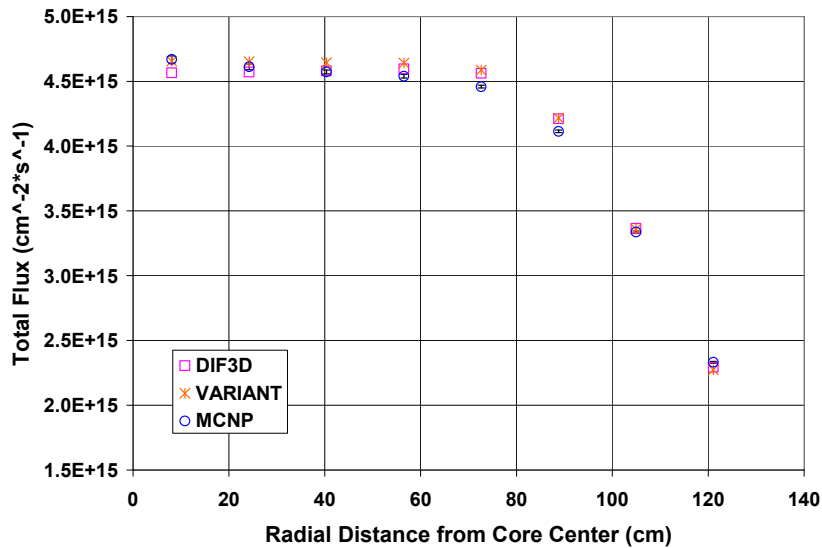


Figure 5-4. Comparison of the total BOEC flux radial profile calculated at the core mid-plane

The differences in the mid-plane radial flux distribution between calculation methods are negligible for the inner regions of the core. However, for increasing radial and axial distance from the center, some differences in the flux gradient become observable. The target region radial distribution (Figure 5-5) shows notably more difference for regions nearest the center of

the core. These differences may be explained by the differences in angular treatment between the three methods. It is interesting to note that the target flux calculated by VARIANT is greater than the MCNP calculation for the inner rows of targets. This may be attributable to the lack of anisotropic expansion of neutron scattering used for this calculation. The anisotropic scattering off of target hydrogen could cause more neutrons to pass through the target without being absorbed. Not having this anisotropic effect in the VARIANT calculation causes some of the neutrons to be reflected back into the target and active core regions.

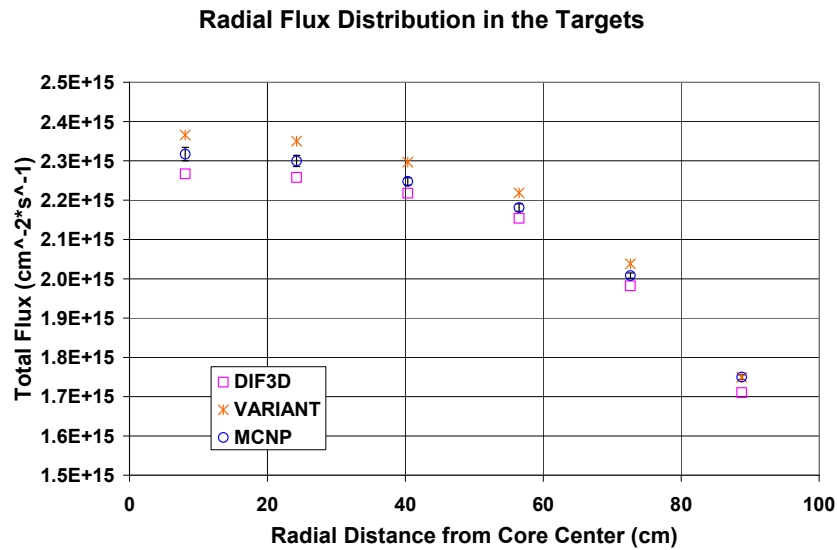


Figure 5-5. Comparison of the total BOEC flux radial profile calculated for the axial target region

The DIF3D curve under predicts the flux given by both MCNP and VARIANT.

Therefore, it is expected that the MA destruction rate should be on the conservative side of the full transport flux evaluation. This result can be seen in Table 5-1. As expected, the rate of transmutation is higher for VARIANT than it is for the DIF3D calculation. However, all of the values in the comparisons made by Table 5-1 are in close agreement with each other. Therefore, the use of the diffusion theory is deemed as an acceptable solution to the transport equation for fast reactor core and epithermal target physics analysis. It is important to make the connection

that there is very little impact on the fuel cycle performance evaluation when using diffusion or transport theory to calculate the AHFTR's reactor and transmutation performance.

Table 5-1. Select reactor parameters for the AHFTR given by DIF3D and VARIANT.

	DIF3D	VARIANT
BOEC k-eff	1.012377	1.013683
β_{eff} CR	0.718088	0.715677
Cycle Length (EFPD)	213.957	212.078
Inner Core Enrichment	20.77%	20.70%
Am-241 Transmutation Half-Life (EFPY)	2.31	2.26
Am-241 Consumption Rate (kg/EFPY)	2.12E+01	2.14E+01
MA Consumption Rate (kg/EFPY)	4.00E+01	4.04E+01

Differences between BOEC and EOEC Fluxes

As discussed in the Chapter 2, the relative or percent change in the initial fissile concentration in the fuel as a function of burnup is small. This is the fissile requirement of the core is high due to the high leakage (i.e., geometric buckling). Therefore, it should be expected that the neutron spectrum in the core is fairly insensitive to the fissile atom depletion. Figure 5-6, shows the neutron spectrum at the mid-plane and target level in the first row of fuel in the AHFTR.

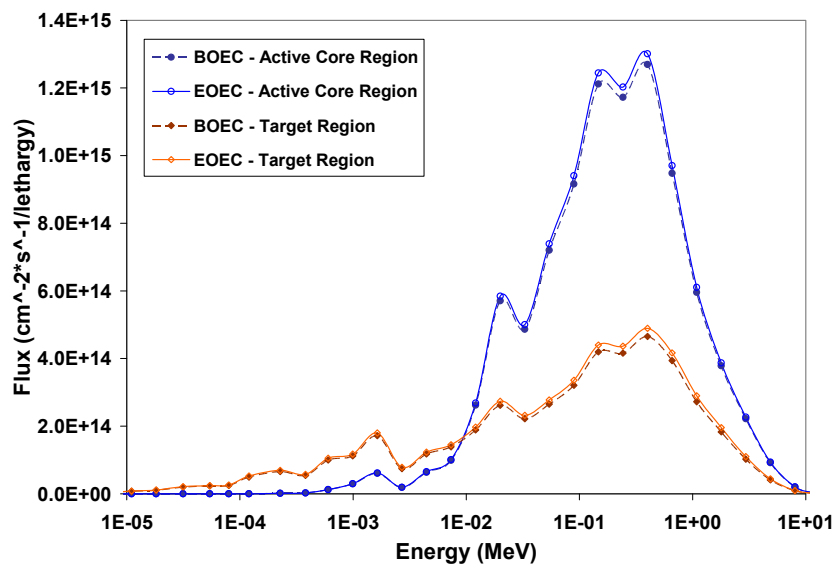


Figure 5-6. Comparison between the BOEC and EOEC neutron spectrums for the inner most row of fuel (DIF3D)

Notice that there is a slight change in the magnitude of the flux between BOEC and EOEC. This difference is attributed to the slight change in the average fissile concentration in the core between BOEC and EOEC from the fuel burnup. It should be expected that the average flux in the core should generally increase as the fissile material is being decreased by depletion due to the fact that generally number density and flux are inversely proportional to each other. To illustrate this point, the radial flux distribution at the core mid-plane is plotted for both BOEC and EOEC in Figure 5-7. The axial flux profile is plotted for the innermost row of fuel for both BOEC and EOEC in Figure 5-8.

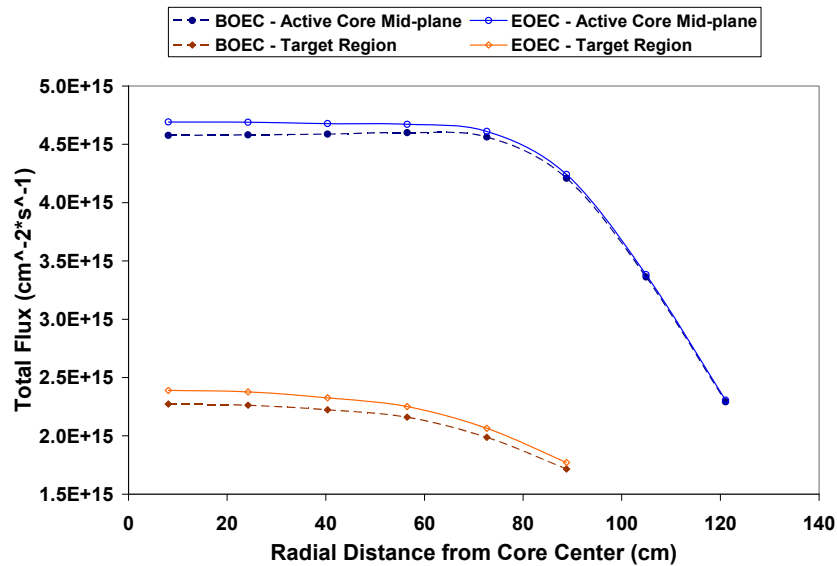


Figure 5-7. Comparison between the BOEC and EOEC radial flux profiles (DIF3D)

Depletion Test

To check the affect of the difference in flux values on the results of the REBUS depletion calculation, a benchmark with MONTEBURNS was performed to compare the k-eff as a function of irradiation time.

In equilibrium-mode, the REBUS code performs a minimum of two DIF3D calculations: BOEC and at EOEC. The BOEC calculation is performed to determine the flux values needed to deplete the fuel. The EOEC calculation is performed to determine whether or not the

uncontrolled k-eff has converged to one, indicating that the code has reached the end of the irradiation (Figure 2-1). A middle-of-equilibrium-cycle (MOEC) calculation is performed to update the flux values during the depletion to ensure that any spectrum changes, though small, will be reflected in the depletion. Due to the small change in flux spectrum and intensity throughout the irradiation (Figure 5-6, Figure 5-7 and Figure 5-8) this three-point check is usually acceptable. The limitations of the REBUS code in equilibrium-mode, only allows a maximum of two DIF3D calculations to be performed between BOEC and EOEC. For the many core design calculations performed in this dissertation, using the equilibrium-mode, only one MOEC calculation was performed between BOEC and EOEC. This decision was made in order to minimize computational time.

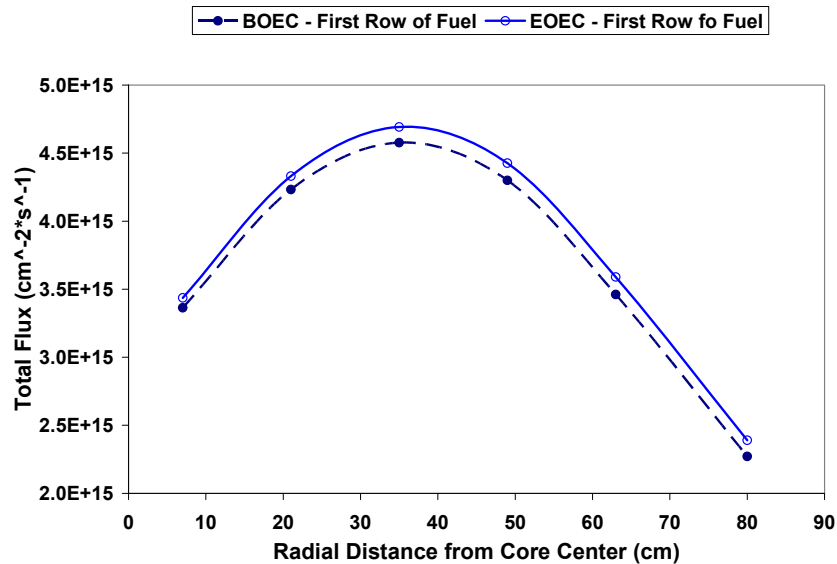


Figure 5-8. Comparison between BOEC and EOEC axial flux profiles (taken at the inner-most row of fuel) (DIF3D)

To check the validity of this three-point check, a *non-equilibrium-mode* REBUS calculation was performed using the geometry and atom density data extracted from the equilibrium-mode output. In non-equilibrium mode the REBUS code allows an arbitrary number of DIF3D calculations to be performed between BOC and EOC. Therefore, the BOEC atom

density and geometry used in the previous standalone DIF3D calculations (Figure 5-1 through Figure 5-8) of this chapter was also used for BOC values in a representative non-equilibrium coupled DIF3D/REBUS calculation. In a similar manner, the atom density and geometry data used in the previous standalone MCNP calculations of this chapter was applied to a coupled MCNP/MONTEBURNS calculation. Figure 5-9 shows the k-eff results from the non-equilibrium DIF3D/REBUS calculation and the MCNP/MONTEBURNS calculation.

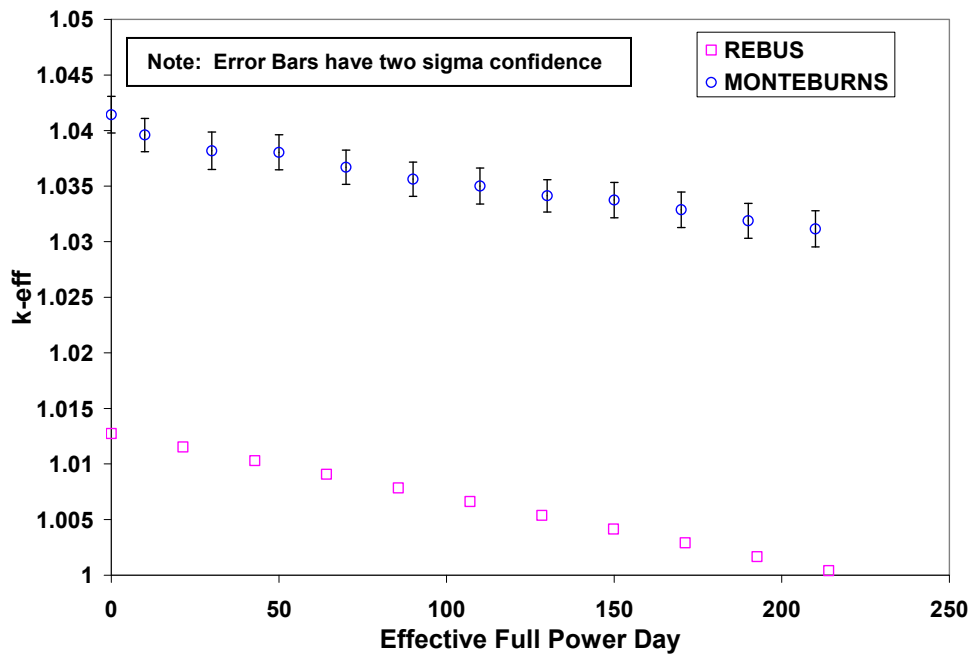


Figure 5-9. Reactivity curve comparison between REBUS and MONTEBURNS

There is a bias of approximately 30 milli-k-eff between the REBUS and MONTEBURNS calculations. Part of this difference can be attributed to the difference in the diffusion approximation made by DIF3D and the transport calculation performed by MCNP. However, much of the difference exists due to a discrepancy between fission product masses at BOC in the DIF3D and MCNP models. This discrepancy is caused by the MC²-2 cross section library (used by DIF3D and REBUS) having more fission product isotopes than the standard ENDF libraries available to MCNP and MONTEBURNS. MC²-2 also uses ENDF libraries to produce the group

constants used in DIF3D/REBUS. However, the reason MC²-2 has more ENDF isotopes than MCNP is because almost all of the fission products in the comprehensive ENDF database are important to fast reactor calculations. In general, all fission products have approximately the same cross section value in the unresolved resonance range. However, not all of these fission products have appreciable value in the thermal range. Therefore, for thermal reactor calculations these extra fission product isotopes are not needed and do not come standard with the publicly available release of MCNP.

There is also a slight difference in the slope of the reactivity curve between REBUS and MONTEBURNS. The smaller MONTEBURNS slope is explained by the difference in fission product isotopes, which are generated by the ORIGEN part of MONTEBURNS, which do not exist in the MCNP cross section library. When these isotopes are generated by the ORIGEN code but can not be recognized by the MCNP code, MONTEBURNS simply decides not to continue tracking these isotopes in the depletion calculation. Therefore, the neutron absorption of these dropped fission products are not reflected in the MONTEBURNS reactivity curve causing the shallower slope.

Before REBUS was adopted for fuel cycle analysis in this work, a benchmark calculation was performed between REBUS and MONTEBURNS using the Advanced Burner Test Reactor (ABTR) design as a reference for fuel composition and geometry [80]. The ABTR is a smaller prototypic version of the larger ABR design, proposed by ANL as a proof of concept reactor with a primary function for materials testing. The ABTR benchmark started with a fresh fuel composition and not one obtained from an equilibrium cycle. The results of this “fresh core” benchmark calculation are given in Figure 5-10.

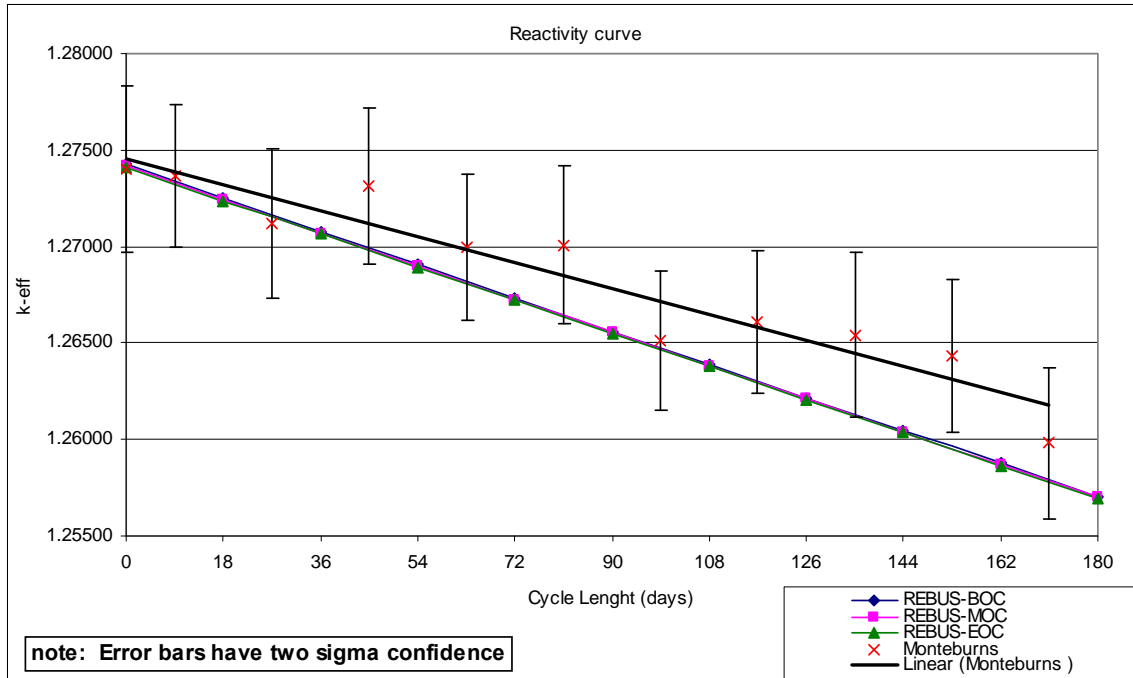


Figure 5-10. Advanced Burner Test Reactor benchmark using “fresh core” fuel composition showing the gradual departure of MONTEBURNS from REBUS¹

This benchmark was conducted “internally” by the members of the INL fuel cycle analysis team (which the author is a member of) to identify the practicality of using REBUS (an ANL code) for fast reactor calculations. The non-equilibrium REBUS and MONTEBURNS calculations in the ABTR benchmark showed very good agreement with each other at BOC. However, as fission products were dropped from the MONTEBURNS calculation, the EOC result by MONTEBURNS diverged from the REBUS calculation.

Spatial Self-Shielding Test

The method by which the group constants are generated in MC²-2 is consistent with zero dimensional slowing down theory techniques that were in common use at the time the MC²-2 code was developed. The use of such methods is generally considered an acceptable practice for fast reactor core simulation due to the fast neutron mean-free-path being generally larger than the

¹ The non-equilibrium REBUS calculations were performed using BOC, MOC “Middle-of-Cycle” and EOC isotopics to generate the MC2-2 cross section library.

pin-cell. There is little change in the neutron spectrum over the local space domain due to this long mean-free-path. Therefore, the use of corrections of the flux at node, cell or the boundaries between different fuel compositions such as discontinuity factors, is not applied in the DIF3D or VARIANT codes. However, incorporation of moderating pin-cells within the target geometry raises the question of the applicability of such generic assumptions.

An MCNP sub-lattice model of one zirconium hydride pin surrounded by six target pins was created to represent an equivalent lattice calculation for this arrangement (Figure 5-11). The neutron flux was tallied in five equal volume zones within the zirconium hydride pin. Similarly, the fuel slug of one of the six targets was sub-divided into five equal volume tally zones. The 33 energy bin group structure used in the MC²-2 calculation was used to tally these fluxes as a function of energy. The height of this MCNP model is 20 cm. Reflective boundary conditions were used on all sides to simulate a repeating lattice of this geometry.

It should be noted that the geometry shown in Figure 5-11 is not a true lattice calculation. This is because the geometry can not be simply folded over at the problem boundary condition into a hexagonal lattice.

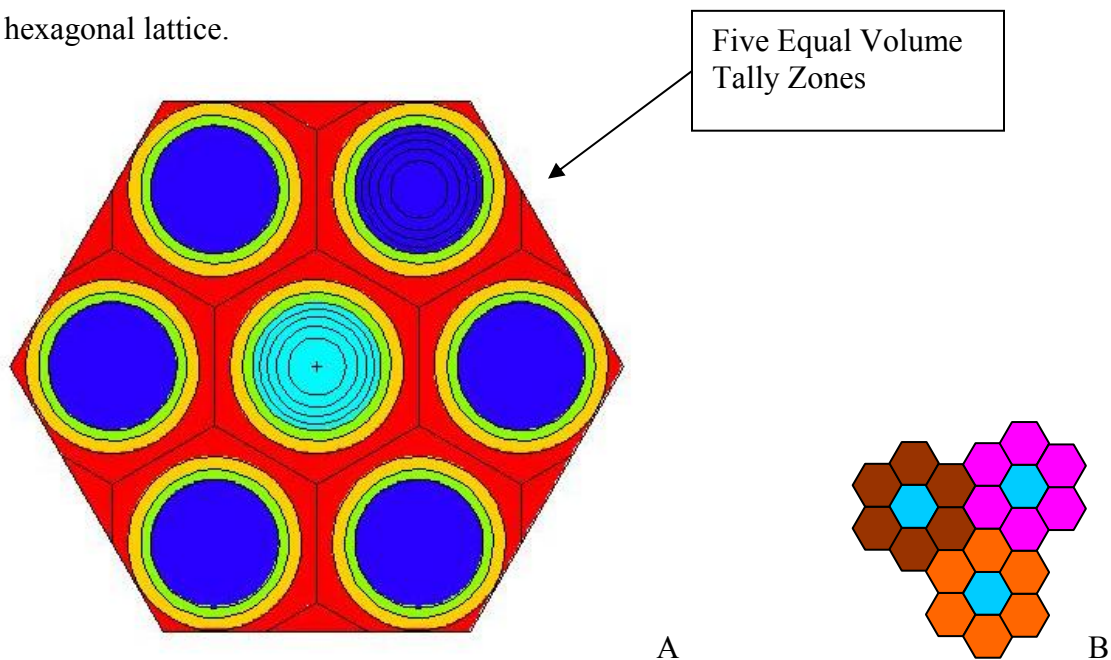


Figure 5-11. MCNP sub-lattice representation (A) of a repeating pin-cell arrangement (B)

The picture in the right-hand-side of Figure 5-11 shows how the seven pin arrangement would actually look within a hexagonal lattice. Nevertheless, it will be seen that the geometry shown can be used as a valuable analysis tool for evaluating the neutron spectrum variations within the repeating lattice. Figure 5-12 and Figure 5-13 shows the 33 group energy spectrum as a function of the five equal volume tally zones for both the zirconium hydride and target slugs respectively. These plots show a similar spectrum shape and magnitude to that shown in Figure 5-2. Indeed both of these plots are very similar to each other. The small change in neutron spectrum as a function of penetrating depth into the moderator is similar to that found by Konashi et al [81]. Therefore, there is virtually zero spatial shielding as a function of fuel slug radius. Because of this uniform irradiation, the target slug should not experience a non-uniform radial burnup distribution or “rim-effect”.

The uniform irradiation across the fuel slug radius can be attributed to the epithermal mean-free-path in this target spectrum to be greater than that of the pin diameter in the seven pin model of Figure 5-11. The hexagonal flat-to-flat dimension of the model is 2.31 cm, whereas the neutron mean-free-path (for all reaction types including scattering) is 2.97 cm. Note the fuel slug outer diameter is 0.557 cm. As a comparison, the mean-free-path calculated for a generic PWR IMF fuel assembly (Table 1-2) is 2.34 cm, whereas the lattice pitch and pellet diameter is 1.26 and 0.82 cm respectively.

Spatial Shadowing Test

Now that the irradiation distribution in the pellet has been analyzed, there is still one final check in the applicability of the infinitely homogeneous approximation used by MC²-2. The region-to-region neutron shadowing effect is evaluated by modifying the seven pin sub-lattice model shown in Figure 5-11. A new MCNP unit-cell model is created by homogenizing the six target pins into an annulus that surrounds the zirconium hydride pin (Figure 5-14).

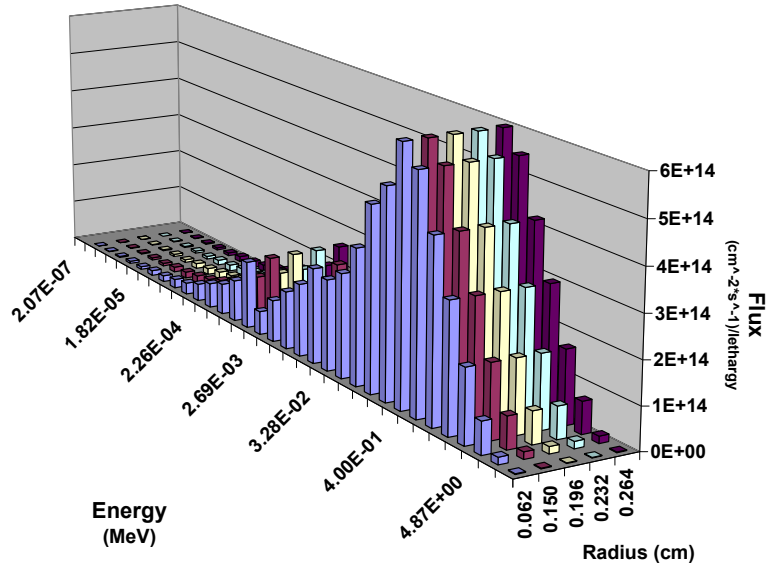


Figure 5-12. Neutron spectrum as a function of energy and the zirconium hydride slug radius (MCNP)

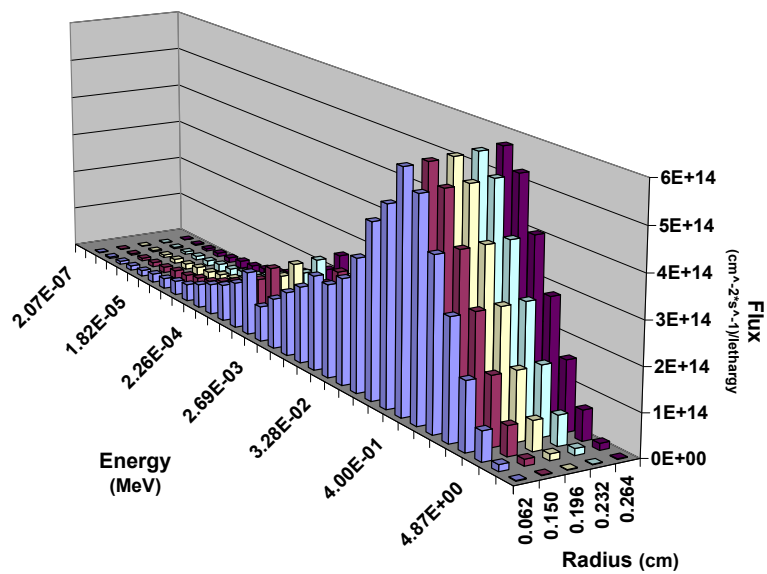


Figure 5-13. Neutron spectrum as a function of energy and the target slug radius (MCNP)

The inner and outer bounds of this annulus are the nearest and furthest points of the original six targets from the zirconium hydride pin. The HT-9 cladding and sodium bond and coolant are also homogenized with the fuel slug into the annulus’s composition. A “white albedo” boundary condition was used at the annulus outer perimeter. The white boundary condition replaces the incident angular dependence with an isotropic distribution. This is

different from a reflective boundary condition which reflects neutron flux with a reflection of the angular distribution that is incident upon it as if it were a perfect mirror.

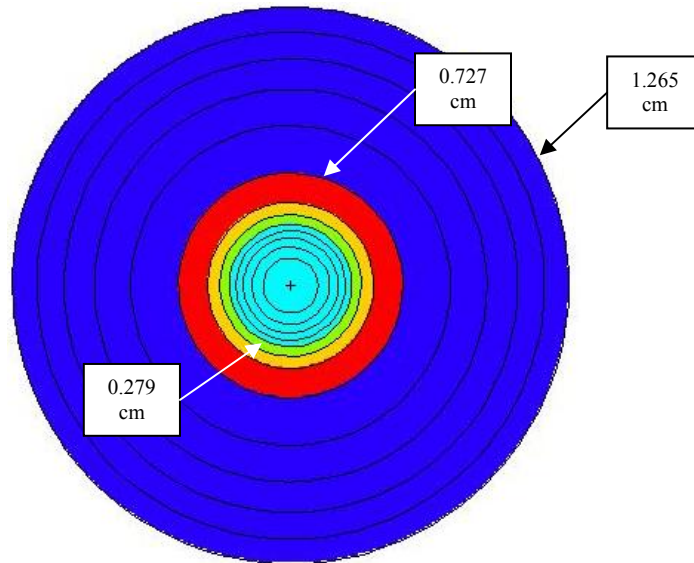


Figure 5-14. MCNP unit-cell model with homogenized fuel annulus: zirconium hydride (turquoise), sodium bonded gap (olive), HT-9 cladding (yellow), sodium coolant (red), homogenized fuel annulus (blue)

The white boundary condition was used for this problem to give the annulus a representative flux at the boundary to that of a hexagon despite using the circular shape. Similar to the sub-lattice geometry from Figure 5-11, the annulus is divided into five equal volume zones for tallying the neutron flux. Figure 5-15 shows the 33 group neutron spectrum as a function of radius for these flux tally zones.

As can be seen from Figure 5-15, there is very little difference in the neutron spectrum flux magnitude as a function of radial distance from the zirconium hydride pin. This is expected because the epithermal mean-free-path discussed in the previous section is on the dimensional level of the annulus which is filled with mostly sodium. The annulus outer diameter is 2.53 cm compared to a mean-free-path of 2.97 cm. This is compared to the LWR IMF case which has a mean-free-path of 2.34 cm which is roughly twice the rectangular pitch of 1.26 cm. Note, the

volume fraction of water in a PWR pin-cell is approximately 65 v/o, whereas the volume fraction of $ZrH_{1.6}$ in the annular pin cell is approximately 5 v/o.

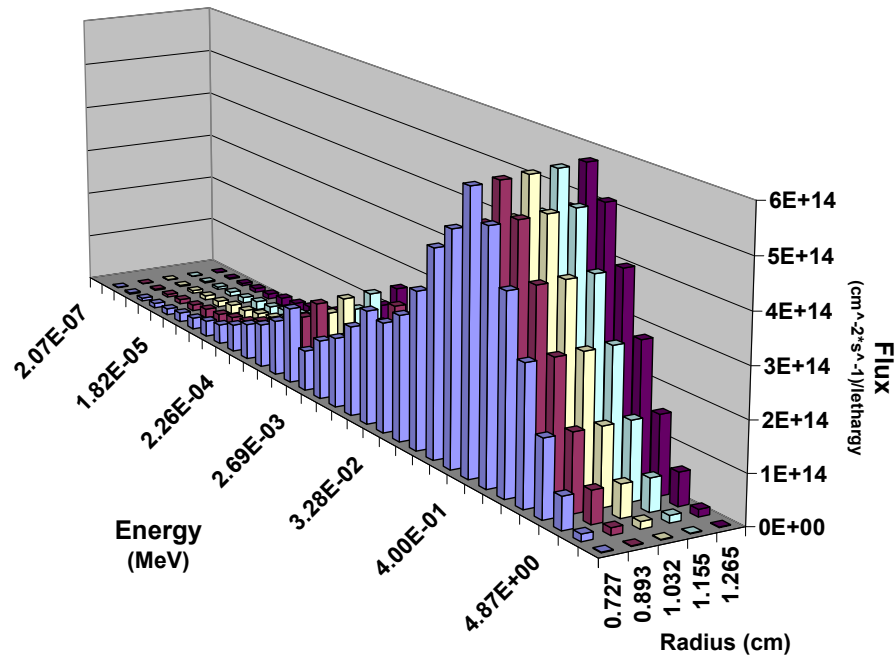


Figure 5-15. Neutron spectrum within the homogenized annulus as a function of radial distance from the unit-cell origin (MCNP)

It is important to distinguish between the mean-free-path between total interactions versus the mean-free-path between fission events. Table 5-2 indicates the mean-free-path for total interactions versus that for only scatter, capture or fission reactions.

Table 5-2. Comparison of mean-free-paths of different reaction types for various irradiation regions having different spectrums (MCNP)

	Total Interaction (cm)	Scatter (cm)	Capture (cm)	Fission (cm)
ABR (CR=0.5)	4.15	4.44	386.42	457.24
AHFTR Active Core	3.75	4.04	339.86	390.53
AHFTR Target Region	2.97	3.11	166.07	451.81
LWR IMF	2.34	2.97	21.16	27.89

The loss of energy per collision in sodium is significantly less than that of hydrogen in water. Therefore, without slowing down to thermal energies, neutrons are more likely to fission at fast energies, where the probability (i.e., cross section) is small compared to thermal energies. Therefore, the average length of travel between fission (or capture) reactions for a SFR neutron

spectrum is much greater than for an LWR spectrum. This is also true of the “slightly” moderated target region of the AHFTR as shown in Table 5-2.

Calculation Validation Remarks

Despite the lack of higher order scattering in the VARIANT/REBUS calculation, close agreement in the neutron spectrum and spatial flux distribution was found between DIF3D, VARIANT and MCNP. The DIF3D/REBUS and VARIANT/REBUS BOEC k-effective was 1.012377 and 1.013683 respectively. The MCNP calculation with BOEC isotopic number densities based on the DIF3D/REBUS calculation was 1.04071 with a standard deviation of 0.00024. As is seen in the benchmark analysis given in the VARIANT user’s manual, the full transport evaluation gives a k-eff that is higher than for diffusion by roughly 25 milli-k-eff [78]. Naturally, this bias is not constant for any core geometry. It is expected that for increasing core size, the difference between the core average fluxes of the full transport evaluation and the diffusion approximation would decrease as a result of spatial heterogeneities becoming less significant compared to the overall governing core physics. The much higher k-eff obtained by MCNP is a result of the lack of fission product isotopes that were available to the MCNP code. Despite the lack of these isotopes, the MCNP calculations showed similar trends with regards to flux values and a loosely representative reactivity curve in the MONTEBURNS calculation. Due to the close agreement in neutron spectrum and spatial distribution between all three calculation methods, little difference was observed in the MA transmutation rate. Therefore, the diffusion approximation is considered an acceptable method for evaluating the fuel cycle and reactor performance analysis of the AHFTR core design.

It was also found that the arrangement of moderating and target rods in the AHFTR demonstrate negligible resolved resonance spatial self-shielding and shadowing effects. Though neutrons are being slowed down by scatters in the zirconium hydride rod, the neutron energies

are still too fast to be considered a true thermal spectrum. Most of the neutrons in the target region's neutron spectrum have energies above 100 eV which is at the upper end (or above) the resolved resonance range for essentially all heavy metals. At these energies, the resolved resonances of heavy metals are poorly resolved. The flux depressions observed in the neutron spectrum of the AHFTR are, in fact, a result of the lighter sodium and iron atoms with resolved resonances in the fast range. The nearly fast epithermal spectrum has a mean-free-path sufficiently greater than the dimensions of the fuel slug; allowing neutrons to pass through it without being absorbed non-uniformly in the slug periphery which would give a "rim-effect". This uniform irradiation makes it possible to assume infinite dilution in the target region for the group constant calculation performed by MC²-2. Also because the epithermal neutron mean-free-path is on the dimensional level of the repeating target-and-moderating rod arrangement, the neutron shadowing effect is negligible.

CHAPTER 6 THE AHFTR FUEL DESIGN

The AHFTR design employs flattened core geometry, epithermal upper axial targets and metallic ternary alloy fuel. The combination of axial targets, combined with the co-pyroprocessing approach draws from the Integral Fuel Cycle (IFC) strategy demonstrated by the EBR-I and later by EBR-II. In the IFR program, it was envisioned that both driver blanket fuel would be used to breed fissile plutonium [40,82,83]. Once discharged from the core, driver and fuel assemblies (axial blankets were included as part of the driver fuel assembly) would be chopped into small segments. Next the sodium bond occupying the fuel-to-clad gap would be extracted and the remaining chopped cladding hulls and fuel slugs placed in perforated steel baskets. These baskets would be taken to the electrorefiner for processing. All of these processes were performed in a system of interconnected hot-cells at a facility adjacent to the EBR-II primary containment building. A more detailed synopsis of metal fuel electrorefining will be provided in a following section.

In the AHFTR design, the moderation effect in the targets suppresses the fission of plutonium isotopes while increasing the capture rate in Am-241. Similar to the Pu-239 conversion from uranium in the IFR blankets, plutonium isotopes are generated by this Am-241 transmutation. The moderating effect enhances this transmutation conversion process as discussed in Chapter 3. The combined effect of americium transmutation into Pu-238, and conversion of Pu-239 from the U-238 in the target, provides a plutonium source within the AHFTR fuel cycle analogous to the IFR blanket fuel. The co-pyroprocessing approach, envisioned by the IFR scenario, is also applicable to the AHFTR because of this plutonium creation. The feasibility of this scenario is validated by the fact that the MA concentration accumulating in the fresh driver fuel can be kept to below 5 w/o (MA/HM) as a guideline

adopted from the CAPRA program. The 5 w/o limit was imposed for the foregoing AHFTR parametric design study in Chapter 3, for the purpose of preserving the fuel irradiation performance established within the IFR experience database for U-Pu-Zr metal alloy fuels.

The 5 w/o limit was also considered important to maintain a low MA driver fuel concentration from the standpoint of reactor kinetics. As discussed in the introduction and Chapter 4, MAs can create an unacceptably high void coefficient due to the resulting spectrum hardening.

Fuel Pin Design

The neutron trap effect afforded by the moderated target region allows the neutron leakage leaving through the top of the reactor to be captured in the targets as opposed to being lost. In the absence of the targets, axially leaked neutrons would leak out of the top of the active core into the gas plenum region which is mostly voided space. Placing the axial targets below, in addition to above the driver fuel, is possible and was considered in the conceptualization of this design. However, including a second target region of equal size to that of the upper region would double the amount of unburned americium discharged to the pyroprocessor by the targets. Hence, the MA content in the driver fuel would roughly double. Remember, from a reactor kinetics and fuel reliability standpoint, it is desirable to maintain the americium content below the 5 w/o limit adopted for this work. Also lower axial targets would act as a neutron trap below the core thus robbing the AHFTR of the reflection necessary for optimizing the core's reactivity requirements. Therefore, a bottom axial reflector comprised of stainless steel, which is a traditionally common design aspect for SFR's, was adopted. For the AHFTR, S-PRISM and ABR designs, this axial reflector constitutes an HT-9 plug approximately a meter long which comprises the bottom end of the fuel pin. This end-plug could either be cast as an integral part of

the fuel cladding or inserted as a separate component and diffusion bonded into the pin. Figure 6-1 shows the general design configuration of the AHFTR fuel pin.

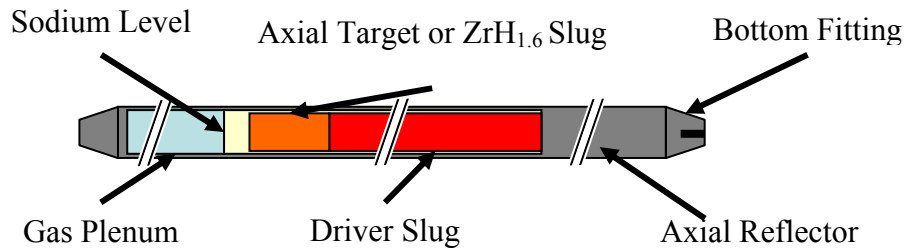


Figure 6-1. Conceptual AHFTR fuel pin design

In Figure 6-1, the axial target slug is a zirconium metal alloy similar to the driver fuel. The elemental constituents of this alloy are 0.5Np/9Pu/9Am/1.5Cm/40U/40Zr by weight. These weight percents are derived from the blending of the Np+Pu, Am+Cm+Bk+Cf and U mass streams produced by the aqueous separations plant shown in Figure 3-4. As mentioned in Chapter 3, these streams are blended with the ratios: 10Np+Pu/10Am+Cm+Bk+Cf/40U/40Zr. The SNF TRU isotopic vector was assumed to be that for a typical 17x17 PWR fuel assembly having a discharge burnup of 50 MWD/kg and cooled for five years before being transported to the aqueous separation plant. An additional decay time of two years was assumed for the time after separation which includes: reprocessing, fuel fabrication and transportation to the AHFTR. The SNF TRU isotopic data was generated by an infinitely repeating fuel assembly lattice calculation using the coupled NEWT/TRITON depletion module of the SCALE5.1 code system. The isotopic vector was given previously in Table 2-1.

Target Alloy Selection and Design Considerations

The elemental composition of the target was selected, based on the irradiation experience gained by the AFC-1B and AFC-1F tests performed at the Advanced Test Reactor (ATR) at INL [84]. The AFC-1B tests consisted of four uranium-free metal alloy fuel samples with varying MA, plutonium and zirconium concentrations.

- A1B1 and A1B4: 48Pu/12Am/40Zr
- A1B2: 40Pu/10Am/10Np/40Zr
- A1B3: 60Pu/40Zr
- A1B5: 40Pu/60Zr

The AFC-1F test consisted of four uranium bearing metal alloy fuel samples with varying MA, uranium and zirconium concentration.

- A1F1: 28Pu/4Am/2Np/66U/30Zr
- A1F2: 27Pu/3Am/2Np/28/40Zr
- A1F3: 34Pu/4Am/2Np/60U/20Zr
- A1F4: 29Pu/7Am/64U

The AHFTR target composition is a hybrid compilation of these test compositions: combining a modest amount of uranium (~40 w/o in some cases) and zirconium content (~40 w/o in some cases) and high MA (~10 w/o in most cases) content. The choice to mix fertile and fissile materials in this composition was made with the intent to decrease the expected fission density in the axial target fuel alloy.

Metallic fuels experience a swelling incubation period (low rate of swelling) followed by a transition period (high rate of swelling) as a function of burnup [60,85]. The AFC-1 test Post Irradiation Examination (PIE) performed by Hilton et al. revealed that the time of incubation is proportional to the amount of fission damage imparted to the overall fuel matrix. Because the zirconium content was varied in these tests, the total fission energy released per unit HM mass (MWD/kgiHM) (iHM stands for initial heavy metal of fuel) or equivalently atom % heavy metal destruction) could not be used as a metric to measure cumulative fission damage. As an alternative, the time integrated cumulative fissions per unit volume of fuel alloy was used instead.

As is common in metal fuel irradiation behavior, many of the metal fuel samples experienced fuel-to-clad contact due to swelling. This behavior was also common to metal fuels

tested at EBR-II. The samples that experienced this behavior were the ones placed in the highest flux and also had the highest plutonium content. However, also similar to EBR-II experience, there was no cladding breach despite this contact. Figure 6-2, borrowed from Hilton et al, shows the optical microscopy and fission gas release for three of the AFC-1B samples.

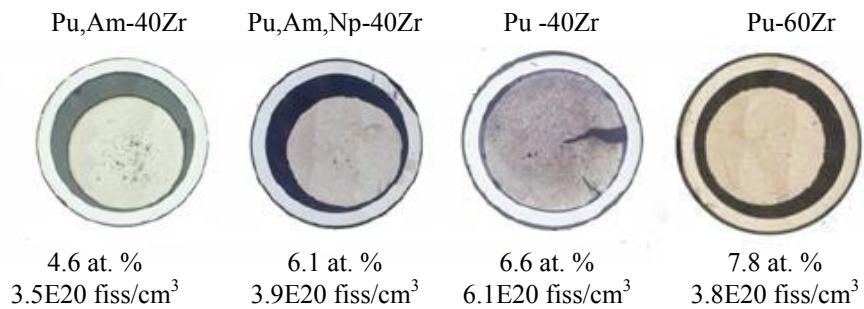


Figure 6-2. Optical microscopy for three of the AFC-1B samples performed by Hilton et al (PIE) [84]

As can be seen in Figure 6-2, the high plutonium content of the 60Pu/40Zr composition leads to greater fuel swelling than the low plutonium 40Pu/60Zr sample at equal burnup. This is expected because the amount of fission damage imparted to the total fuel volume (i.e., fission density) is greatest in the 60Pu/40Zr case. It is important to note that the correlation between atom percent burnup and fission density is roughly linear for equal zirconium content. Therefore, for equal zirconium volume and actinide volume, the fission damage is the same. This can be seen in the three TRU/40Zr cases. It appears that the transition swelling begins somewhere between 3.9E20 and 6.1E20 fiss/cm³. This result is reflected in the fission gas curve of Figure 6-3, which was borrowed from Hilton et al.

The fission gas release curve seems to also exhibit an incubation period followed by transition period. The metal fuel alloys used at EBR-II also exhibited this connection between swelling and fission gas release. Fuel transition swelling would occur early in the irradiation leading to a high incidence of cladding breach for the first generation of EBR-II fuel (Mark I).

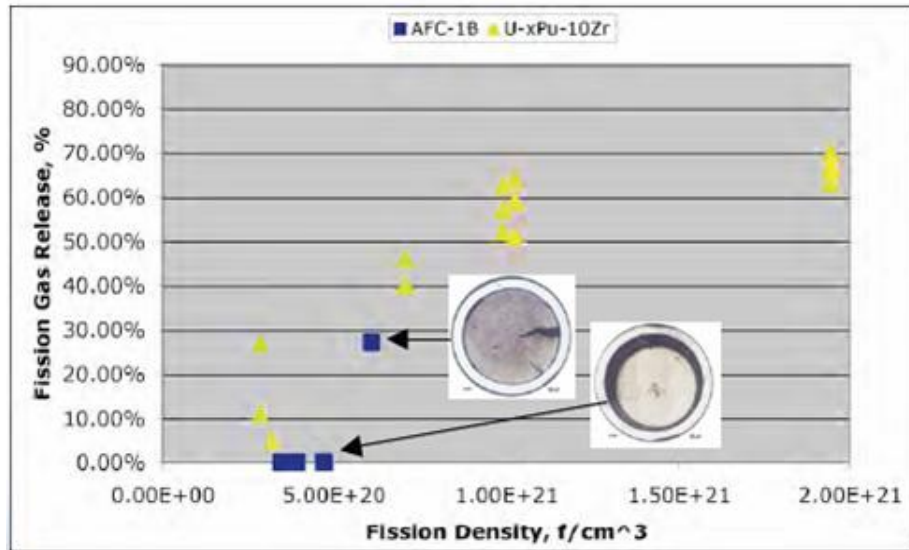


Figure 6-3. Fuel swelling performance for the AFC-1B samples by Hilton et al (PIE) [84]

The second generation of fuel (Mark II) used a much larger cladding-to-fuel gap distance, which allowed the fuel to expand inside of the larger gap and delay contact with the cladding [61]. It is important to remember that the bond material selected for metal fuels is sodium which provides high gap conduction. When the Mark II fuel was allowed to expand, it was discovered that the fission gas bubbles generated in the fuel would eventually interconnect after a certain burnup was reached, as documented by Walters [60,62]. This “interconnected porosity” allowed most of the accumulated fission gas to be released from the fuel where it would be collected in the gas plenum at the top of the fuel pin. This sharp increase in fission gas release slowed the rate of fuel swelling in the transition period, allowing a significantly higher burnup than the Mark I before the limiting inter fuel-to-clad contact pressure was reached. The Mark I fuel could only be irradiated to 2-4 at.% (19 MWD/kgiHM – 37 MWD/kgiHM). Whereas, the Mark II fuel could be irradiated to 15-18 at.% (140 MWD/kgiHM – 160 MWD/kgiHM) [86]. The high burnup and fission gas release for both metal and oxide SFR fuels stipulates a gas plenum approximately one and one-half times the length of the driver fuel [60,61,62].

Target and Driver Fuel Burnup Criteria

For the AHFTR targets, it was desirable to delay the transition from incubation to transition swelling as long as possible. To accomplish this, the plutonium concentration in the AHFTR axial target alloy was reduced from that used in the AFC-1B tests and replaced by U-238. The result is a better balance of reactivity suppression at BOL by neutron capture in both uranium and americium. The addition of uranium and americium gives a breeding contribution to reactivity at EOL. Table 6-1 and Table 6-2 give the peak and average burnup and cumulative fission density, respectively, for the inner, middle and outer enrichment zones for the driver fuel and targets.

Table 6-1. Peak burnups for the driver fuel and targets (REBUS)

Region	Peak Burnup (MWD/kgiHM)	Peak Burnup (at. %)	Peak Fission Density (fiss/cm ³)
Inner Core Mid-plane	119.18	12.76%	4.7456E+21
Middle Core Mid-plane	122.64	13.13%	4.8836E+21
Outer Core Mid-plane	96.52	10.33%	3.8434E+21
Inner Core Targets	201.78	21.60%	3.4435E+21
Middle Core Targets	173.85	18.61%	2.9669E+21

To ensure fuel reliability with no cladding failures, an average fuel burnup of approximately 100 MWD/kgiHM is common for both metallic and oxide fueled cores [62]. This is the case for both S-PRISM and the ABR (CR=0.75) designs [7,19]. The average burnup for the AHFTR is also in this range. Walters et al show that the corresponding fuel burnup for EBR-II Mark II fuel (90U/10Zr) could reach about 15 at. % with a low probability of cladding failure [60,61].

The AHFTR average and peak burnup stays below this limit with the exception of the targets. However, the target peak and average fission density, in the targets, is still below that of the driver fuel. Therefore, it is expected that the AHFTR fuel performance will be within the design criteria established by EBR-II experience.

Table 6-2. Average burnups for the driver fuel and targets (REBUS)

Region	Avg. Burnup (MWD/kgiHM)	Avg. Burnup (at. %)	Avg. Fission Density (fiss/cm3)
Inner Core Mid-plane	106.19	11.37%	4.2285E+21
Middle Core Mid-plane	102.79	11.00%	4.0928E+21
Outer Core Mid-plane	70.52	7.55%	2.8079E+21
Inner Core Targets	197.02	21.09%	3.3622E+21
Middle Core Targets	162.15	17.35%	2.7672E+21

The peak driver fuel burnups were taken at the active core mid-plane. It is important to note that the peak actinide burnup occurs in the targets. This is due to the higher zirconium content in the targets than in the driver fuel. In fact, because of the lower mass density of zirconium than the metal actinides, the 40 w/o zirconium fraction occupies 60 v/o of the alloy volume. However, the peak fission damage per volume occurs at the active core's mid-plane. Therefore, the fuel performance of the driver fuel is the actual limiting case with respect to fuel performance. The mid-plane also happens to be the location in the core that experiences the highest flux, volumetric power density and specific power. Therefore, it can be expected that the fuel at the active core mid-plane will experience the peak cladding damage, fuel swelling and fuel center-line temperature.

Cladding Damage Criteria

The time integrated fast fluence and dpa for the HT-9 cladding is given in Table 6-3 for the inner, middle and outer enrichment zones for the driver fuel and targets. As indicated in Chapter 5, the peak flux occurs at the active core mid-plane. Therefore, it is expected that the mid-plane is where the highest cladding damage occurs as verified in Table 6-3.

Table 6-3. Average and peak fast fluence ($E > 0.1$ MeV) and peak dpa (REBUS)

Region	Peak Fast Fluence* (cm^{-2})	Peak dpa
Inner Core Mid-plane	3.5360E+23	164.32
Middle Core Mid-plane	3.6125E+23	170.63
Outer Core Mid-plane	3.2986E+23	159.38
Inner Core Targets	2.0791E+23	89.04
Middle Core Targets	2.0614E+23	90.21

* Fast fluence is calculated by the REBUS code for energies greater than 0.1 MeV.

A fast fluence limit of $4.0E23 \text{ cm}^{-2}$ was assumed as the maximum allowable cladding exposure for the AHFTR based on the irradiation experience gained by the FFTF reactor. HT-9 qualification at FFTF showed no elongation or cladding breach after being irradiated up to $3.9E23 \text{ cm}^{-2}$ [63]. A cladding damage criterion of 200 dpa was selected as a secondary cladding performance standard for the AHFTR. The 200 dpa limit is the approximate damage function corresponding to a fluence of $4.0E23 \text{ cm}^{-2}$ in a “typical” SFR fast spectrum (such as that observed in the HT-9 tests at FFTF). The cumulative displacement damage was calculated by applying a 33 group displacement cascade response function library to the calculated neutron flux. As can be seen from Table 6-3, the target atomic displacement damage for the cladding in the target region is still less than in the active core. Also this peak cladding damage is within the $4.0E23 \text{ cm}^{-2}$ (or 200 dpa) design criteria for HT-9 established by experience gained at FFTF [63].

The use of irradiation tolerant steels for cladding and structural components in a SFR is critical to the reliable performance of the fuel. A cladding damage of at least 20 dpa, (corresponding to a fuel burnup of about 50 MWD/kg) is typical in the zirconium based cladding used by LWRs [87]. HT-9 would not make a favorable LWR cladding material due to its higher thermal neutron capture cross section and poorer oxidation performance than zirconium. However, HT-9 has been proposed for the S-PRISM’s and ABR’s cladding and structural materials due to its irradiation creep resistance, high tensile strength throughout irradiation and low irradiation induced swelling.

Because of the high fuel swelling and cladding damage, the SFR fuel pin is designed to accommodate the anticipated fuel-to-clad interaction, >90% fission gas release, etc. To have sufficient space to accommodate fuel expansion, the ratio of cross sectional area of the fuel slug divided by the cross sectional area of the gap and fuel region, “fractional smear density”, is

larger than for LWR fuel. The smear density adopted for the AHFTR is 0.75 as was done for the metal fueled EBR-II, S-PRISM and ABR. This is compared to a smear density of roughly 0.95 for LWRs, as well as oxide fueled SFR's. As a result of the larger smear density, the fuel-to-clad gap distance is larger. To achieve adequate heat conduction between the fuel and cladding, this gap is filled with sodium instead of helium. The sodium bond provides a much higher thermal conductivity than helium, which allows the difference in temperature between fuel surface and the inner cladding wall to be kept within 10-15°K. The thermal performance of the AHFTR metallic fuel and target will be discussed in a later section.

Though the gap is filled with sodium, the upper region of the fuel pin, allocated for the fission gas plenum, is filled with helium gas. Because a pool type design is assumed for the AHFTR, the coolant pressure is near one atmosphere (not including gravitational pressure head). Therefore, the helium in the fuel pin does not require significant, if any, internal pressurization. Hence, the gas plenum pressure at fabrication is assumed to be one atmosphere.

Fuel Pin Thermal Performance Criterion

The overall design rationale of the AHFTR is to minimize the excess reactivity required to achieve the lowest β_{CR} possible. It does this by increasing the core's axial buckling which increases axial leakage. If the sum of axial and radial buckling must be equal to the fuel material buckling (criticality condition), increasing axial buckling will reduce the required radial buckling. Since the AHFTR radius was increased by an additional row of fuel, the net effect results in a flattened radial flux and radial power density (i.e., a reduced radial buckling). This flattened radial power profile translates into a reduction in the ratio of peak-to-average power density and LHGR over the core. Therefore, the AHFTR design rationale is intended to inherently increase fuel performance by reducing peaking. The reduction in peaking enables most of the fuel to be irradiated evenly to within the same performance margins. This is

different from smaller SFR core designs, such as the ABR, with a higher radial buckling. Small cores have been proposed by Hill et al to decrease the τ_{CR} through increasing the radial buckling [54]. An increase in radial buckling translates into a higher radial power gradient than the flattened core. This effect was demonstrated by comparing the “tall” and “flat” AHFTR designs in Chapter 3. For the “tall” and homogeneous “ABR” designs, all of the peaking occurred in the inner core. Small SFR designs, such as the reference ABR design, require more enrichment in the outer core to overcome the reactivity lost through radial leakage. Without this enrichment splitting, only the inner core fuel could be irradiated to the limiting fuel and cladding design constraints, because the rest of the fuel would not have the reactivity to achieve the same fission density.

Fuel Temperature Criterion

There are two basic performance criteria. First, the power in the hottest fuel pins should be less than that necessary to melt the fuel. Secondly, the cladding inner wall temperature must be less than that necessary to cause eutectic melting between the fuel and cladding. As will be shown, the high fuel thermal conductivity of the metal alloy creates a large temperature margin between the peak fuel temperature and the solidus temperature for ternary alloy 19TRU/71U/10Zr fuel, taken to be about 1320 K (1100°C) [7].

As an interesting side note, cladding breach as a result of fuel melt is not probable due to the HT-9 melting temperature (~1500°C or ~1800K) being higher than that of the fuel. This result is illustrated by experimental irradiations of EBR-II Mark IA fuel, which was fabricated with only the bond sodium in the lower half of the fuel pins [61]. The absence of bond sodium caused extensive fuel melting. However when the fuel melted, it relocated, thus closing the fuel-to-bond gap, where it froze in place without melting the cladding. A small amount of eutectic interaction with the cladding was observed with a 10% penetration into the cladding wall.

Cladding Temperature Criterion

Eutectic phase formation between SFR metal fuel and cladding is a type of failure mechanism that can occur in SFR metallic fuels. Eutectic liquefaction is a result of metallurgical interaction between actinides (and fission products), and the iron in the HT-9 cladding, which produces a low melting point phase [86]. It is important to note that eutectic phase formation does not occur in all SFR fuel pins. It occurs only after sufficient chemical interaction between fuel and cladding has occurred to produce the low melting point phase, and if the temperature is high enough in this phase to cause melting. This fuel-to-clad chemical interaction (FCCI) begins as the inter-diffusion trading of fuel and cladding constituents. Unlike eutectic melting, the FCCI is a cumulative process as lanthanides are continuously produced by fission. Pahl et al described the results of FCCI tests, performed at EBR-II, as an inter-diffusion of lanthanides in the fuel and cladding constituents leading to formation of brittle layers in the cladding wall that were prone to failure [88]. Lahm et al discusses the erosion of the EBR-II Mark II cladding as a result of this FCCI inter-diffusion [89]. As the fuel slug swelled and came into contact with the cladding, the contact pressure led to creep damage and stress rupture later in life. Once the contact is made, FCCI occurs, allowing iron in the cladding to be traded with lanthanide fission product metals in the fuel. Lahm et al found that this newly formed uranium-iron phase had a eutectic solidus temperature below the melting point of the cladding. If the fuel was operated at temperatures above this eutectic temperature, a liquid interface between cladding and fuel would form accelerating the FCCI diffusion. The diffusion feedback causes the cladding to thin and lose its strength as iron in the cladding is consumed by the liquid interface. This cladding wastage serves to increase the frequency of stress rupture in the driver fuel.

Because, the EBR-II Mark II fuel did not contain plutonium, the eutectic phase was composed of uranium and iron. Lamb et al reports that cladding penetration was only observed

at temperatures above 985K (715°C), for the Mark II fuel [89]. However, plutonium and iron have a binary eutectic solidus temperature near 650K (280°C) [60]. This eutectic solidus temperature closely corresponds to the onset of FCCI at 930K (660°C) for the Mark II fuel, reported by Pahl et al [88]. The EBR-II Mark-V fuel was a 19Pu/71U/10Zr alloy with HT-9 cladding. For the AHFTR fuel pin design, the minimum value of 930K value was chosen as the limiting temperature, taken at the inner cladding surface. A similar approach was used for the S-PRISM design to show whether or not eutectic penetration could be tolerated during the bounding design basis of 113% over-power at SCRAM [19]. The full thermal-hydraulic analysis of the AHFTR over-power scenario is outside of the scope of this work which is more concerned with the fuel cycle aspects of the heterogeneous design. However, given the similarity of the AHFTR design to that of the S-PRISM and ABR, it is expected that the transient response issues of MA containing fuels will be dealt by future authors.

Thermal Analysis

The peak inner cladding and fuel centerline temperature was calculated using the region specific peak volumetric power density taken from the REBUS output. Given the poor neutronic communication amongst individual fuel rods, as discussed in Chapter 2, local pin power peaking, within the fuel assembly is considered to be a negligible effect. Therefore, pin power reconstruction within the hottest fuel assembly and/or core region is deemed unnecessary. Indeed, pin power reconstruction is not a feature provided by the DIF3D/REBUS code system. Therefore, the average fuel pin power for the hottest fuel assembly, in the hottest enrichment zone, is taken to also be the peak fuel pin power in the following thermal analysis.

Fuel Assembly Power Peaking

As noted previously, the enrichment zone homogenization routine in REBUS does not permit the specific tracking of individual fuel assemblies. Instead, a mass balance is used to

track the mass of each batch as it is charged and discharged from its enrichment zone within the core. Because the reactivity change of the average fuel assembly, and representative batch, does not change significantly with burnup, the shuffling of fuel assemblies is not required. Therefore, for the AHFTR, like the ABR and S-PRISM, the driver fuel is not shuffled during its irradiation. A fresh fuel assembly is simply loaded, irradiated and discharged from the same location within the core. For the sake of simplicity, the use of the term “fuel assembly”, being synonymous with the corresponding fuel batch, is used in place of the word “batch” for the remainder of this discussion.

It is evident from Figure 6-4, that the peak power density occurs at the core mid-plane of row five (yellow columns) which is in the middle core enrichment zone. This highlights the importance of enrichment zoning in SFR design. The reactivity contribution of a slightly higher enrichment for the middle and outer core provides for a flatter radial power distribution than can be achieved by radial buckling alone. The draw on reactivity by radial leakage can be inferred from the fact that the outer core fuel has the highest enrichment but also the lowest power density over the entire core.

The core region specific volumetric power density for the homogeneous ABR reference case with a $\tau_{CR}=0.5$ is given in Figure 6-5. Observing the yellow column of Figure 6-5, between row one and four, one can see the radial leakage affect on the curvature of the power density. The power density for the ABR decreases until the fuel reactivity is increased by the higher enrichment of the middle core. It can be seen from the yellow column of Figure 6-4, that the AHFTR exhibits virtually zero curvature between row one and four. In contrast, the ABR also has a relatively flat radial power density. This is because the ABR uses a higher gradient of enrichment splitting than the AHFTR (Table 3-13). The ABR enrichments in the middle and

outer core are 1.25 and 1.5 times, respectively, higher than for the inner core. Whereas for the AHFTR, the enrichments in the middle and outer core are 1.125 and 1.25 times, respectively, higher than for the inner core.

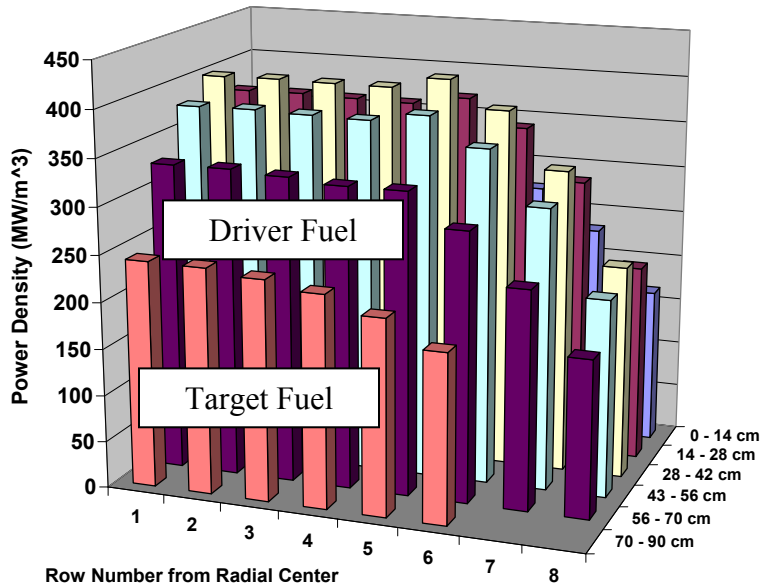


Figure 6-4. AHFTR power density profile as a function of fuel row and axial region (REBUS)

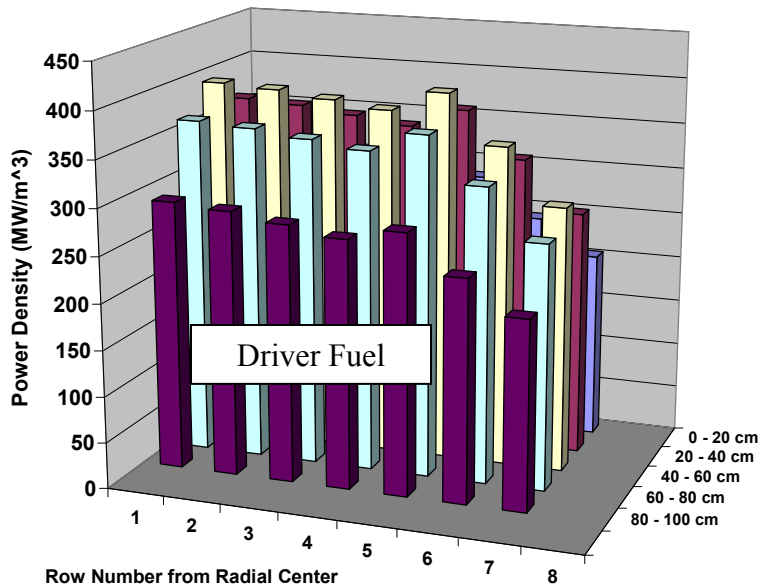


Figure 6-5. ABR reference power density profile as a function of fuel row and axial region (REBUS)

Because of the higher enrichment splitting, the ABR experiences a higher ratio of peak-to-average heat generation rate. The peak-to-average LHGR, at BOEC, is 1.5 for the ABR and 1.38 for the AHFTR. The peak-to-average ratio is defined as the hottest LHGR (mid-plane) for the hottest fuel assembly divided by the average LHGR taken over all fuel assemblies in the core. This core wide peaking factor also takes into consideration the peak-to-average of the axial LHGR distribution of the individual fuel assembly.

$$PF_{\text{axial}} = \frac{\max(LHGR(z))}{\left(\int LHGR(z)dz\right)/z} \quad (6-1)$$

$$PF_{\text{Fuel Assembly}} = \frac{\max\left(\left(\int LHGR(z)dz\right)/z\right)}{\left(\sum_{FA} \left(\left(\int LHGR(z)dz\right)/z\right)\right)_{FA} / \sum FA} \quad (6-2)$$

$$PF_{\text{Core}} = PF_{\text{Axial}} \times PF_{\text{Fuel Assembly}} \quad (6-3)$$

Where: PF stands for peaking factor and FA stands for Fuel Assembly. The LHGR(z) represents the axial LHGR distribution across the fueled portion of the fuel assembly and z is the total length of the fueled portion.

The ratio of the mid-plane LHGR to the average LHGR of the hottest fuel assembly is 1.2 and 1.23 for the ABR and AHFTR, respectively. The peak axial fuel assembly average LHGR to core average LHGR is 1.25 and 1.12 for the ABR and AHFTR, respectively. Multiplying the fuel assembly peaking factor by the axial peaking factor gives the core wide peaking factors, (i.e., $1.2 \times 1.25 = 1.5$ and $1.23 \times 1.12 = 1.38$). The fuel assembly peaking factors for the ABR and AHFTR cores are given in Table 6-4 and Table 6-5.

Note the small amount of change between the fresh and last burn of the fuel for any given row in the core. Hence, the peaking factor is generally insensitive to the amount of exposure received by the fuel assembly in any given row of the reactor. This is expected, given the impact

of leakage on the radial power distribution as noted above. Table 6-6 gives the fuel assembly average peaking factors for the AHFTR at EOEC.

Table 6-4. ABR fuel assembly peak-to-core average LHGR ratio taken at BOEC (REBUS)

Row Number	Batch Number						Sixth Burned
	Fresh Fuel	Once Burned	Twice Burned	Thrice Burned	Fourth Burned	Fifth Burned	
One	1.19	1.15	1.12	1.09	1.06	1.03	n/a
Two	1.18	1.14	1.11	1.08	1.05	1.02	n/a
Three	1.15	1.12	1.08	1.05	1.02	0.99	n/a
Four	1.12	1.09	1.06	1.03	1.00	0.97	n/a
Five	1.26	1.18	1.12	1.07	1.02	0.97	n/a
Six	1.07	1.01	0.97	0.92	0.89	0.85	n/a
Seven	0.78	0.74	0.71	0.68	0.65	0.62	0.60

Table 6-5. AHFTR fuel assembly peak-to-core average LHGR ratio taken at BOEC (REBUS)

Row Number	Batch Number					Fifth Burned
	Fresh Fuel	Once Burned	Twice Burned	Thrice Burned	Fourth Burned	
One	1.12	1.11	1.10	1.09	1.08	1.07
Two	1.12	1.11	1.11	1.10	1.08	1.07
Three	1.11	1.10	1.10	1.09	1.07	1.06
Four	1.10	1.09	1.08	1.07	1.06	1.04
Five	1.12	1.11	1.09	1.07	1.06	1.04
Six	1.02	1.01	0.99	0.98	0.96	0.94
Seven	0.92	0.90	0.88	0.87	0.85	0.83
Eight	0.64	0.63	0.62	0.62	0.61	0.60

Table 6-6. AHFTR Fuel Assembly Peak-to-Core Average LHGR ratio taken at EOEC (REBUS)

Row Number	Batch Number					Fifth Burned
	Fresh Fuel	Once Burned	Twice Burned	Thrice Burned	Fourth Burned	
One	1.14	1.13	1.12	1.11	1.09	1.08
Two	1.14	1.13	1.12	1.11	1.09	1.07
Three	1.12	1.12	1.11	1.09	1.08	1.06
Four	1.11	1.10	1.09	1.07	1.06	1.04
Five	1.12	1.10	1.08	1.06	1.05	1.03
Six	1.01	1.00	0.98	0.97	0.95	0.93
Seven	0.90	0.88	0.87	0.85	0.83	0.82
Eight	0.63	0.62	0.62	0.61	0.60	0.59

Comparing Table 6-5 with Table 6-6, it can be seen that the peak fuel assembly location shifts from Row Five in the middle core to Row One in the inner core. This can be attributed to a greater level of plutonium breeding in the inner core than in the middle core. The ϵ CR in each enrichment zone is given in Table 3-13 in Chapter 3. The conversion ratio is essentially a

function of the neutron balance between the probabilities of parasitic capture by U-238 versus neutron escape from the core through leakage. The inner core has the smallest enrichment of all the enrichment zones. It also sees the least amount of neutron escape from radial leakage. Therefore, the inner core stands to have the largest plutonium breeding gain and hence relative increase in power generation to the rest of the core.

The internal breeding effect on inner core reactivity can be seen by comparing the LHGR for the Row One (Inner Core) versus Row Five (Middle Core) (Figure 6-6 and Figure 6-7). The decrease in LHGR with irradiation is slightly less for Row One driver fuel than it is for Row Five driver fuel. Also important to note is the increase in LHGR for the targets. The increase in LHGR with irradiation is slightly more for Row One targets than it is for Row Five targets. However, the overall change in LHGR with irradiation for targets and driver fuel is relatively slow. If the conversion ratio of the active core is reduced, than the internal breeding would also be reduced, thus creating a greater loss rate in LHGR from BOL to EOL. For the targets, the composition was selected to have some initial plutonium and uranium at BOL so that the “external” breeding in the targets would maintain a fairly constant LHGR.

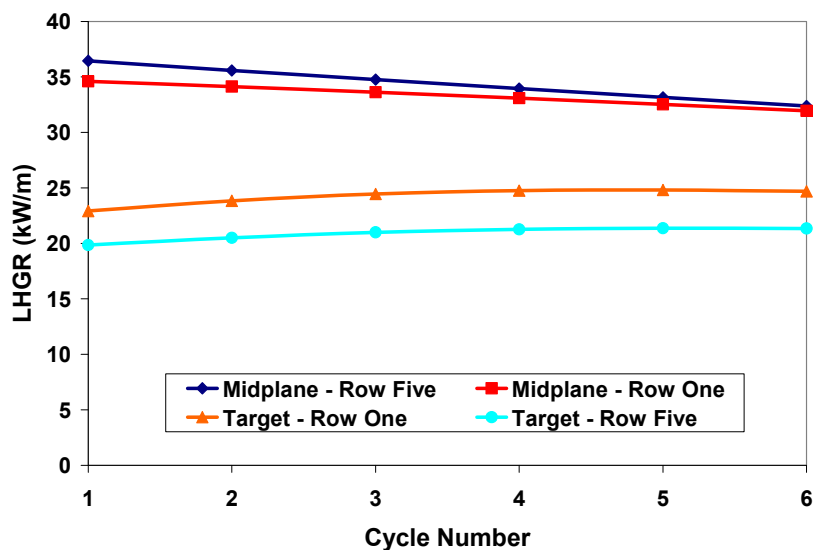


Figure 6-6. BOEC LHGR for the driver fuel mid-plane and target regions (REBUS)

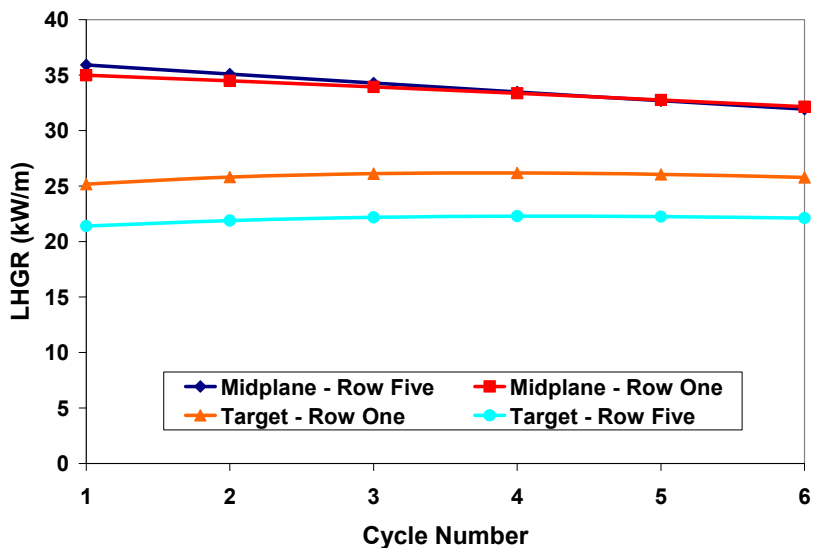


Figure 6-7. EOEC LHGR for the driver fuel mid-plane and target regions (REBUS)

Peak Fuel Pin Hot Channel Analysis

For the following analysis, the axial LHGR distribution for the hottest fuel assembly is used to determine the axial fuel centerline and inner cladding temperature profile. This “hottest” fuel assembly is located in Row Five of the AHFTR. The highest LHGR for Row Five fuel occurs at BOL. The sodium coolant channel surrounding a “typical” fuel pin within this hottest fuel assembly is considered. To perform sodium channel analysis, the coolant channel height is sub-divided into a series of axial temperature nodes. Steady state conditions are applied at each node to establish a Nusselt correlation as a function of axial height from the coolant inlet at the bottom of the active core. Using a curve fit to the axial LHGR data and an empirical formula for the sodium heat capacity, the coolant temperature drop across each axial node is determined. This information is used to determine the bulk coolant temperature at each axial node. Once the bulk coolant temperatures are known, established empirical correlations for the sodium Nusselt number and thermal conductivity is applied to calculate the convective heat transfer coefficient at each axial node.

Once the axial bulk coolant temperature and convective heat transfer coefficient distribution is known, a one-dimensional radial heat transfer model is applied at the channel wall to determine the: cladding outer and inner wall temperature and fuel surface and centerline temperature.

REBUS generates a snapshot of the average reactor power by region in the core (Figure 6-4) as a function of cycle number for each fuel batch (Figure 6-6 and Figure 6-7). The axial LHGR data for fresh fuel in Row Five was tabulated from the power generation data for each axial region in Row Five of the REBUS model. The REBUS model divides each row of fuel into six axial regions: five axial driver regions plus one target region. REBUS generates region powers for each of these six axial regions in each row of fuel. The code further breaks down the regional power data, which is homogenized over all fuel batches in that region, into the individual power contributions to that region by each fuel batch. These batch power values are given as a function of cycle number. Because each batch is assigned its own row, the average power produced by any given row (and axial region in that row) is the volumetric average of the batch power contribution at each stage (i.e., cycle) of its irradiation in that region.

This REBUS generated batch power “history” was then divided by the total length of all the fuel pins within the batch to give the LHGR in each axial region in each row as a function of batch and cycle number. This LHGR region specific power history data for Row Five was used to represent the “typical fuel pin” of fresh fuel occupying that region of the AHFTR. Figure 6-8 shows this axial BOL LHGR distribution. A fourth order polynomial was used to fit the REBUS tabulation for the 71.6 cm section of driver fuel. A linear curve fit was applied for the target region from 71.6 to 91.6 cm. A caveat must be noted here. The LHGR for each data point from the REBUS tabulation directly corresponds to the average power for that axial region in the

computer model. Given the scoping-calculation nature of the following one-dimensional channel Nusselt number calculation, the approximation by the “moving average” is deemed appropriate.

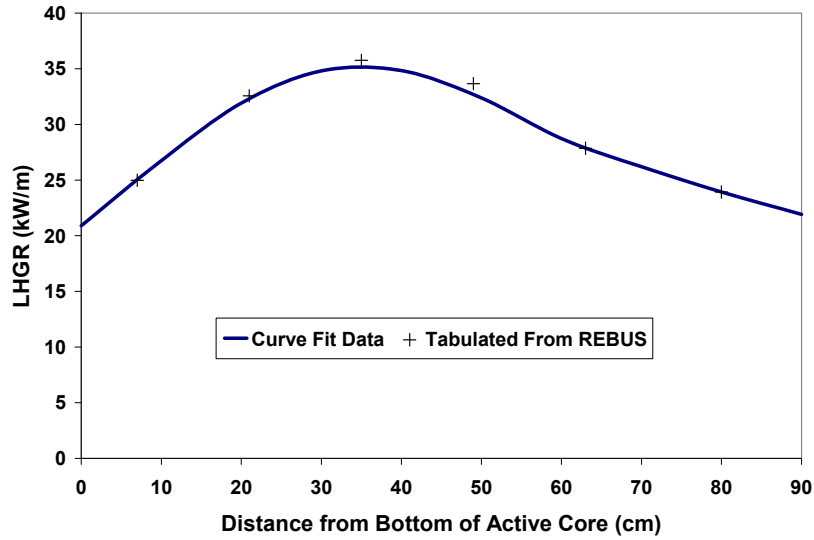


Figure 6-8. Peak pin axial BOL LHGR distribution (REBUS)

The LHGR curve fit is used to calculate the heat energy released “q” through the cladding, or channel wall, for each node by multiplying the node LHGR at a location “z” by the intra-node distance “Δz”. The node-to-node marching procession is illustrated in Figure 6-9.

$$q^i = q'(z^i) \times \Delta z \tag{6-4}$$

Where: q’ is the LHGR at “z”

Knowing that the first node is at the core inlet temperature, the axial bulk coolant temperature distribution is then calculated using the heat capacity relationship.

$$T_b^{i+1} = T_b^i + \frac{\dot{m}}{q^i \times Cp(T_b^i)} \tag{6-5}$$

Where: m is the average mass flow rate of a “typical” coolant channel, q is the amount of heat energy transferred to the channel cladding wall in Δz, Cp is the heat capacity of node “i” and T_b is the bulk coolant temperature at node “i” or “i+1”.

The average channel mass flow rate was approximated by considering the core inlet temperature and outlet temperature (after mixing above the core). Since the sodium heat capacity does not change appreciably in this temperature range, an average sodium heat capacity for the entire core was assumed for the channel mass flow calculation. Given the AHFTR core power, the heat capacity relationship is used to calculate the total core mass flow rate.

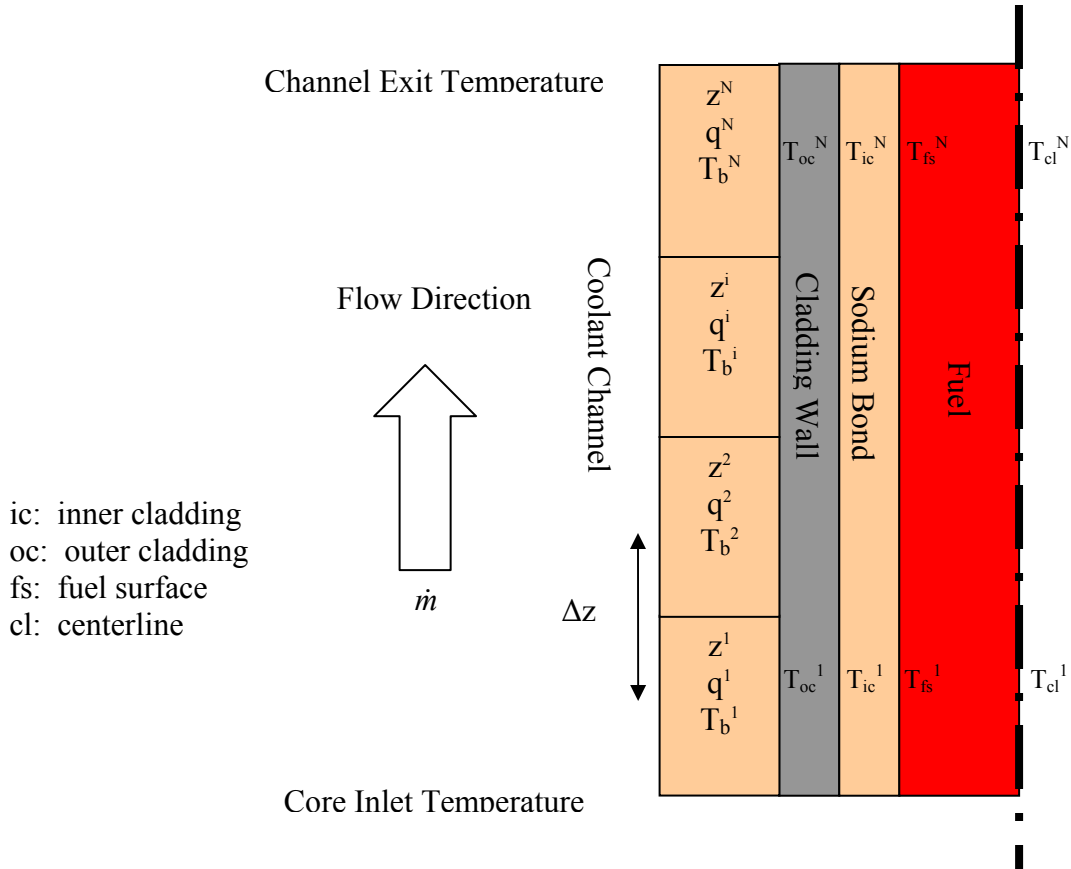


Figure 6-9. Axial node procession for Nusselt analysis

This total mass flow is then simply divided by the number of fuel pins in the core. This generic calculation gives a slightly conservative estimate of the hot channel mass flow rate. Typically a SFR thermal-hydraulic design would introduce a flow orifice at the coolant entrance at the bottom of the fuel assembly. Most modern SFR fuel assembly designs incorporate a hexagonal HT-9 shroud that encompasses the fuel pin sub-assembly. The HT-9 shroud prevents cross flow between fuel assemblies. This allows the mass flow through each fuel assembly to be

tailored specifically to meet the thermal requirements of the fuel in that assembly. Therefore, for the AHFTR, one might envision the inner, middle and outer core to have three different levels of flow orificing to ensure a fairly flat exit coolant temperature and average fuel temperature profile across the core. Since the hot channel mass flow rate has not been artificially increased to demonstrate this flow orificing, the fuel temperatures discussed in this analysis will be slightly higher than the expected operating value. However, as this analysis will show, even without flow orifices, the fuel still meets the thermal fuel performance criteria discussed earlier.

$$\dot{m} = \frac{Q}{C_p^{average} \times (T_{outlet} - T_{inlet}) \times No.^{FP}} \quad (6-6)$$

Where: Q is the thermal power of the AHFTR (1000 MW), $C_p^{average}$ is the average sodium coolant heat capacity throughout the core, $No.^{FP}$ is the total number of fuel pins in the core.

By repeating the axial marching procedure for all “N” nodes, the bulk coolant temperature is found as a function of z. Once the bulk coolant temperature profile is known, the Schadt-Modified correlation, as recommended by Todreas and Kazimi as well as Waltar and Reynolds, is applied to determine the Nusselt number for each node [62,90]. Once the Nusselt number is known for each coolant channel axial node, the radial temperature profile calculation is performed for all “N” nodes. For the remainder of the radial temperature analysis, the axial “i” subscript is dropped.

$$Nu = (-16.5 + 24.96(P/D) - 8.55(P/D)^2) Pe^{0.3} \quad (6-7)$$

For: $1.1 \leq P/D \leq 1.5$ and $150 \leq Pe \leq 1000$

Where: Nu is the Nusselt number at node “i”, Pe is the Pecklet number at node “i”, P is the hexagonal fuel pin-cell flat-to-flat pitch and D is the fuel pin diameter. Then the convective heat transfer coefficient for each node is as follows.

$$h = \frac{Nu \times k(T_b)}{D_H} \quad (6-8)$$

Where: h is the convective heat transfer coefficient, k(T_b) is the sodium thermal conductivity evaluated at the coolant bulk temperature and D_H is the fuel pin hydraulic diameter which is equivalent to D.

Assuming one-dimensional radial heat diffusion and constant heat current, Newton's Law of Cooling is applied to calculate the outer cladding surface temperatures at each node.

$$T_{oc} = T_b + \frac{q'}{\pi \times D_f \times h} \quad (6-9)$$

Where: D_f is the diameter of the fuel slug

With the outer cladding surface temperature known, Forrier's Law in cylindrical coordinates is used to calculate the inner wall temperature.

$$T_{ic} = T_{oc} + \frac{q'}{2\pi \times k_{HT-9}(T_{oc})} \ln(b/a) \quad (6-10)$$

Where: k_{HT-9} is the HT-9 thermal conductivity at the outer cladding wall temperature.

A gap heat transfer coefficient is approximated by dividing the thermal conductivity of the sodium bond, at the inner wall temperature, by the fuel-to-clad gap distance. This approximation does not take into account the surface roughness of the fuel or a jump distance approximation. Given the relatively large gap distance of 0.4 mm, compared to the allotted gap spacing for surface roughness (~0.01 mm), and the higher thermal conductivity of sodium, compared to helium, this is probably a reasonable approximation of the gap heat transfer coefficient. The temperature of the fuel slug surface is calculated using the gap conductance model.

$$T_{fs} = T_{ic} + \frac{q'}{\pi \times D_f \times k(T_{ic})/d} \quad (6-11)$$

Where: k is the sodium bond temperature taken at the cladding inner wall temperature and d is the fuel-to-clad gap distance.

The assumption was made that the fuel thermal conductivity does not vary widely with temperature. This is deemed as an acceptable “first glance” approximation by the recommendation of Hofman et al [86]. Given the higher thermal conductivity of metal fuel, as opposed to oxide, the radial temperature rise from the slug surface to centerline is only a few hundred degrees, as is verified by this calculation. Hence, it can be expected that the temperature dependent thermal conductivity will be relatively insensitive to this change in temperature.

In fact, the thermal conductivity is highest at BOL, as is the case for the hottest AHFTR fuel assembly, and remains high throughout most of the irradiation. Hofman et al discusses the effect of swelling and interconnected porosity phenomenon on the thermal conductivity of $^{19}\text{Pu}/^{71}\text{U}/^{10}\text{Zr}$ fuel irradiated at EBR-II [86]. In the first few at. % of burnup, pore formation, from fission gas retention in the fuel, causes the fuel to swell to nearly contacting with the cladding. During this free swelling time, the fuel thermal conductivity goes down. Also, much of the bond sodium is displaced and forced into the gas plenum volume. Near the point of fuel-to-clad contact the pores become mostly interconnected which releases fission gas to the plenum. The interconnected pores are large enough to allow the bond sodium to infiltrate the fuel causing the thermal conductivity to increase. The bond sodium infiltration was sufficient enough to restore most of the thermal conductivity that was lost during the initial swelling [60,83].

The approximate temperature independent thermal conductivity of $^{20}\text{Pu}/^{70}\text{U}/^{10}\text{Zr}$ metallic fuel is discussed by Hoffman et al for the ABR parametric study on conversion ratio. This summary is provided in Figure 6-10 which was borrowed from Hoffman et al [7]. It should be

noted that this data was not generated by Hoffman et al whose work was primarily focused in the reactor physics and fuel cycle analysis of the ABR. Hoffman referenced the data in Figure 6-10 to internal communications with Hofman and Pelton held at ANL in the 1980's and 1990's.

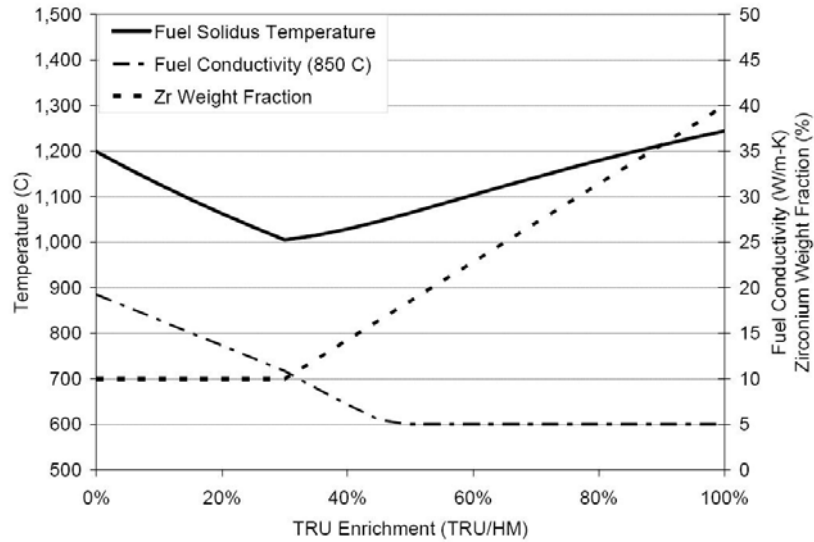


Figure 6-10. Assumed thermal properties of TRU-U-Zr metal alloy fuel borrowed from the ANL-AFCI-177 report by Hoffman et al [7]

Assuming the thermal conductivity was constant throughout the fuel slug, the centerline temperature was calculated by solving the heat diffusion equation with constant volumetric heat generation.

$$\frac{1}{r} \frac{d}{dr} \left(r \frac{dT}{dr} \right) + \frac{q'}{\pi D_f k_f} = 0 \quad (6-12)$$

Using the boundary conditions of a known temperature at the fuel surface and also zero temperature gradient when the radius is zero, a solution to the heat diffusion equation is found.

$$T_{fc} = T_{fs} + \frac{q'}{4\pi \times k_f (T_{fs})} \quad (6-13)$$

Where: k_f is the average fuel thermal conductivity taken at the fuel surface temperature.

The fuel centerline, fuel surface, and cladding inner and outer surface temperatures are plotted in

Figure 6-11. It is interesting to note that the axial fuel centerline temperature profile becomes fairly flat above the core mid-plane. The curvature of the axial LHGR distribution (Figure 6-8) gives the lowest heat generation at the upper and lower ends of the fuel rod. This reduces the heat input through the channel cladding, which is directly proportional to the difference in fuel centerline and surface temperature from Equation 6-13. It is an interesting finding that the reduction in $(T_{cl}-T_{fs})$ is roughly matched by the coolant temperature rise $(T_{oc}-T_b)$ with increasing z .

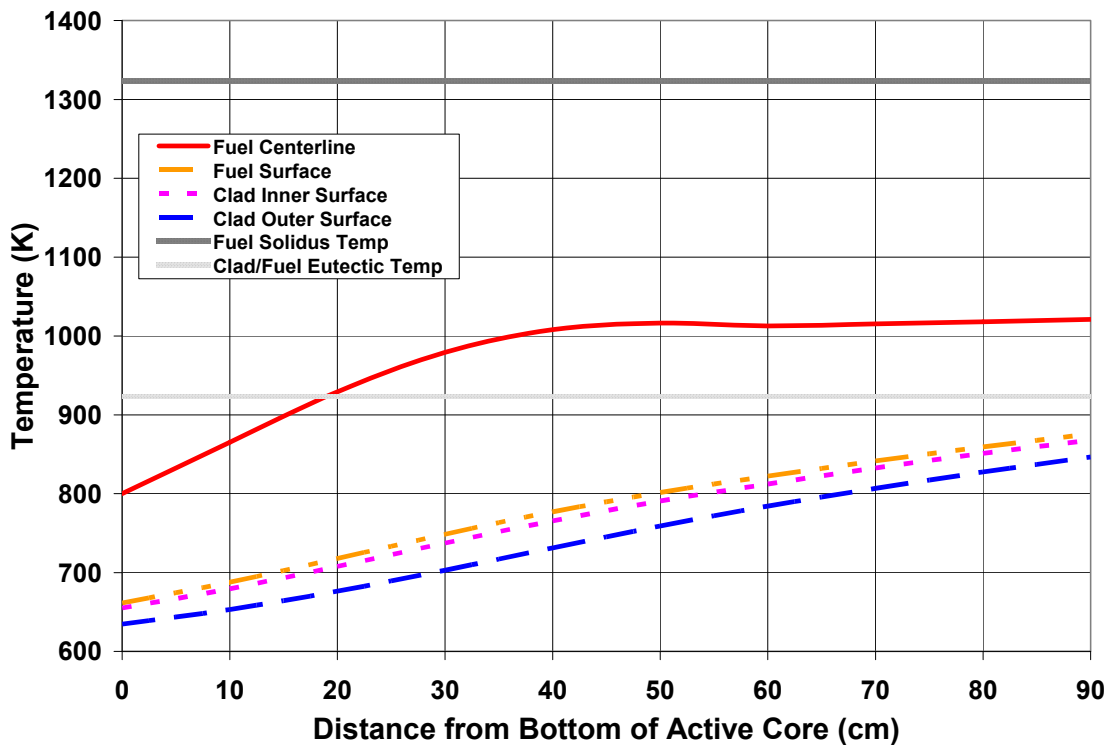


Figure 6-11. Axial temperature profiles for a “typical” fuel rod in the hottest fuel assembly

The resulting minuscule change in fuel centerline temperature, in the upper half of the AHFTR fuel rod, can be considered an important phenomenon for discussing the likelihood of atomic inter-diffusion between the target and fuel slug compositions in this region of the core. The anticipated metallurgical interaction between the fuel alloy and target alloy composition will be discussed in the following section.

The fuel centerline temperature is never more than 230 K greater than the fuel surface temperature. Due to the high thermal conductivity of the fuel, the fuel temperature is always at least 300 K less than its melting temperature. In contrast, the minimum difference between the inner cladding temperature and the eutectic melting temperature is only 55 K. Therefore, it is apparent that the eutectic melting temperature is the most constraining temperature limit. However, this feature is not a special property of the AHFTR, but is fairly common to all SFRs with metal fuel.

Hofman et al states that the most common failure mechanism for the EBR-II Mark II fuel was a small inter-granular crack caused by FCCI at the restrainer dimples (discussed in Chapter 4) [86]. The restrainer dimples (120 degrees apart) were three sharp indentations inside the fuel pin cladding. Their purpose was to prevent the fuel from somehow ratcheting upwards, due to bowing effects, inside the cladding during the irradiation and then later falling back down at an inappropriate time in the irradiation, resulting in positive reactivity insertion. These dimples became stress risers, as the fuel swelled and the plenum gas pressure increased. The failure rate at these high stress points was further enhanced by FCCI and a eutectic phase formation. PIE of the Mark II fuel showed that the ratcheting effect was not as significant as originally thought. When the dimples were eliminated from the EBR-II fuel pin design, much higher burnups could be achieved without clad rupture.

Metallurgical Diffusion Effects

Given the intimate contact of the axial target and driver fuel slugs, it is expected that some inter-diffusion of the alloy constituents, of the two different fuel types, should be expected. The targets and drivers slugs are essentially composed of the same primary elemental ingredients: plutonium, uranium and zirconium metal. They are simply mixed in different proportions. Since the axial fuel temperature gradient is nearly zero at the target-to-driver interface (Figure 6-11), it

is expected that the axial inter-diffusion between the target and fuel slugs will be driven only by the atom concentration gradients and not axial thermal gradients.

Inter-Diffusion Data

Inter-diffusion between these elements has been well characterized during the IFR program and its predecessors. This work was done to increase understanding of the radial redistribution of Pu, U and Zr induced by the thermal gradient between the metal fuel centerline and surface temperature. Isothermal diffusion coefficients of these constituents were measured by Petri et al [91]. Ternary inter-diffusion coefficients were calculated from the common composition between two diffusion couples with intersecting diffusion paths. In general, Petri et al found that the diffusion coefficients increased for increasing plutonium concentration and decreased for increasing zirconium concentration. This result suggests that it is more likely that driver fuel species are more likely to diffuse into the target than it is for the target species to diffuse into the driver fuel. The results of Petri et al's experiments are given in Table 6-7.

Table 6-7. Ternary inter-diffusion coefficients measured at the common composition (matino plane) between two diffusion couples*

Composition (a/o)			Inter-diffusion Coefficients (10^{-12} m ² /s)					
Pu	U	Zr	D_{ZrZr}^U	D_{ZrPu}^U	D_{PuZr}^U	D_{PuPu}^U	D_{ZrZr}^{Pu}	D_{UZr}^{Pu}
13	75	12	0.16	-0.33	-0.10	1.7	0.49	1.3
13	75	12	0.16	-0.29	-0.04	1.5	0.45	1.1
9	74	17		-0.45		1.3		
15	62	23		-0.62		1.4		
16	80	4					0.20	1.7
16	80	4					0.06	3.1
11	73	16					0.63	0.84
11	74	15					0.72	0.94

*Table borrowed directly from Petri et al [91]. D_{jk}^i stands for the ternary inter-diffusion coefficient for species j diffusing into species k within the solvent i.

The composition given in the left-hand side of the Table 6-7 represents the common composition at the *matino* plane between the two diffusion couple compositions. The matino

plane represents the original contact plane, between diffusion couples, where the accumulation on one side is balanced by the depletion of a species on the other side.

Petri et al describes a negative diffusion coefficient for zirconium indicating that zirconium inter-diffuses up a positive Pu concentration gradient to regions of higher Pu contents.

Therefore, it is expected that the high zirconium content of the targets is likely to diffuse toward the higher plutonium concentration in the driver fuel. For plutonium, the inter-diffusion coefficient with zirconium is more than an order of magnitude smaller than the plutonium-to-plutonium diffusion coefficient. Hence, plutonium inter-diffusion is affected strongly by its own concentration gradient, but is relatively uninfluenced by the Zr concentration gradient.

Therefore, it is expected that the higher Pu concentration in the driver fuel is likely to diffuse toward the lower plutonium concentration in the targets. The inter-diffusion coefficient of uranium into zirconium is of the same order as the plutonium-to-plutonium diffusion coefficient. Therefore, it is expected that the higher U concentration in the driver is likely to diffuse into the high zirconium concentration in the targets. The inter-diffusion coefficients for uranium and plutonium are all roughly three times higher than for any of the zirconium diffusion coefficients.

Penetration Distance

To quantify the inter-diffusion impact upon the target composition, an effective diffusion coefficient and penetration depth is offered by Petri et al.

$$\bar{x} = \sqrt{2 \times t \times \tilde{D}^{eff}} \quad (6-14)$$

Where: t is the annealing time, \tilde{D}^{eff} is the average effective diffusion coefficient.

The average effective diffusion coefficient is a proxy form of the ternary inter-diffusion coefficients that represents diffusion of a single species crossing the matino plane. Therefore, it can be applied in an analogous manner to a binary diffusion coefficient, which is easier to

conceptualize. The maximum D^{eff} is reported by Petri et al for each species. As expected from Table 6-7, Pu has the highest D^{eff} of $2.2\text{E-}12 \text{ m}^2/\text{s}$.

To calculate the expected penetration depth of driver plutonium diffusing into the target, the target-to-driver interface is assumed to be the matino plane in the AHFTR fuel rod. Given, isothermal conditions at the target-to-driver interface from the hot channel analysis, and assuming an annealing time equal to the fuel pin in-core exposure time, an effective penetration depth is calculated.

$$\bar{x} = \sqrt{2 \times \left(6 \text{ cycles} \times 221 \frac{\text{days}}{\text{cycle}} \frac{24 \text{ hr}}{\text{day}} \frac{3600 \text{ s}}{\text{hr}} \right) \times \left(2.2 \times 10^{-12} \frac{\text{m}^2}{\text{s}} 100^2 \frac{\text{cm}^2}{\text{m}^2} \right)} \quad (6-15)$$

$$\bar{x} = 2.2452 \text{ cm}$$

Therefore, it can be expected that about 11% of the length of the axial target length will be affected by the plutonium diffusion coefficient to some varying degree. As stated in Chapter 5, the mean-free-path of the epithermal neutrons in the targets is 2.97 cm. Therefore, it is unlikely that the plutonium diffusion gradient will have a significant impact on the local power produced in the area of the target-to-driver fuel interface. However, it should be pointed out that Petri's diffusion measurements did not include MAs. Therefore, further testing should be done to quantify the diffusion gradients including neptunium, americium and curium.

Transmutation Gas Generation and Plenum Sizing

The transmutation chain of the even neutron numbered americium isotopes, Am-241 and Am-243 ultimately lead to the production of Pu-238 and Cm-245, as shown in Figure 1-2 and Figure 1-3. The accumulation of these isotopes is favorable from a physics perspective because these isotopes can be used as fuel at a later time in the fuel cycle. However, in order to produce these fissile isotopes, a shorter lived intermediary non-fissile curium isotope has to be produced. For Am-241, this isotope is Cm-242, whose production and decay ($T_{1/2}=162.8 \text{ days}$) is

essentially in secular equilibrium with the beta decay of the neutron capture product Am-242. For Am-243, this isotope is Cm-244, which is sufficiently long lived ($T_{1/2}=18.1$ years) to accumulate in the AHFTR fuel cycle. Both Cm-242 and Cm-244 decay by emission of an alpha particle. The kinetic energy of this alpha particle is quickly lost by ionization interactions with atoms of the fuel matrix. Once, the alpha particle is stopped it will have picked up two electrons, becoming an atom of helium. These helium atoms accumulate in the fuel as a function of burnup. When the burnup drives the fuel swelling to the point of interconnected porosity, it is expected that these helium atoms will be released to the gas plenum in addition to the fission product gasses. This additional gas production requires quantification in order to determine the plenum height which in turn impacts the thermal-hydraulic design of the reactor. The major contributions to helium production by alpha decay for all the actinides in the targets are shown in Figure 6-12.

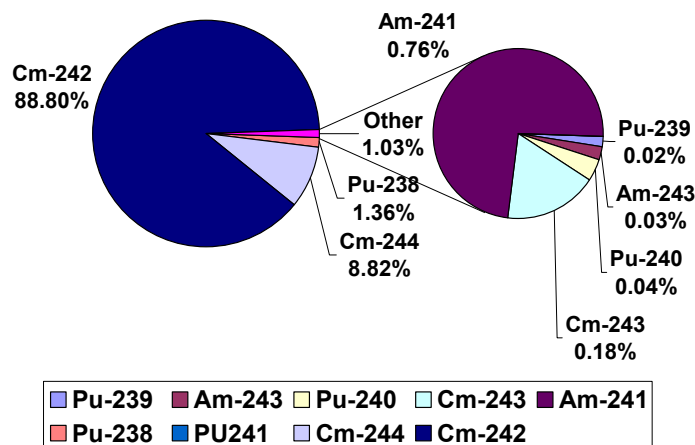


Figure 6-12. Percent contribution to helium production by alpha decay for target fuel actinides during the course of irradiation (BOL to EOL)

Almost all HM actinides decay by alpha decay. Most of these isotopes, like Pu-239 have half-lives ranging from decades to thousands of years. Therefore, most actinides have little

contribution to helium production in the fuel pin unless present in appreciably large quantities. This is the case for Pu-238 as well as Cm-244, whose alpha decays are not in secular equilibrium with the americium transmutation, but are present in the fuel in large enough quantities to produce a non-trivial amount of helium.

Since helium gas production is an unavoidable result of neutron capture by americium, it is an issue for the driver fuel as well. In fact, due to the fission threshold requirement for Am-241 and Am-243 to fission, all SFR designs with americium in the fuel, must account for transmutation helium. Helium production is discussed by Taiwo et al for americium bearing fuel pins for a multi-recycled heterogeneous PWR fuel assembly design [92]. Taiwo et al quoted the helium component to be about 20% of the total gas production for that particular fuel design. Taiwo et al also goes on to mention that there is a direct relationship between the presence of Am-241, Pu-238 and Cm-244 and the amount of helium produced. Hence, the percent helium per total gas production will increase as the ratio of americium to total HM loaded into the core increases.

Helium and Fission Product Gas Calculation

Since the REBUS calculation does not report total number of alpha decays as one of its outputs, a post processing code was developed to recreate the fuel buildup/depletion algorithm performed by REBUS. This was done in order to reproduce the exact alpha decay history of the fuel as a function of irradiation time. The depletion algorithm uses an exponential matrix method, similar to that used by the ORIGEN code, to calculate the number density of each actinide isotope as a function of discrete time steps [50]. With the depletion history of the fuel known in much finer time steps than reported in the REBUS output, these number densities are then converted into alpha decay activity. For the helium calculation, pure exponential decay is assumed within the time step. This alpha decay is numerically integrated in time for each time

step. The total cumulative number of alpha disintegrations throughout the entire irradiation is found by summing the integrated alpha decay over all time steps. The total integrated alpha activity corresponds to the total number of helium atoms generated.

The exponential matrix method provides a simultaneous solution of the generalized burnup equation for each time step. The generalized burnup equation is given in Equation 6-16.

$$\frac{dN_i}{dt} = Y_j \lambda_j N_j + B_j \left(\sum_g \sigma_c^g \phi^g \right) N_j - \lambda_i N_i - \left(\sum_g \sigma_a^g \phi^g \right) N_i \quad (6-16)$$

Where: N_i is the number of atoms of daughter i , N_j is the number of atoms of parent j , λ is the relevant radioactive decay constant, ϕ is the local neutron flux, σ_c is the capture cross section, σ_a is the total absorption (capture plus fission) cross section, g represents the 33 group neutron flux and cross section set, Y_j is the yield fraction of radioactive decay for isotope j going into i , and B_j is the branching ratio of isotope j going into isotope i . Equation 6-16 is determined for all combinations of i and j to form a list of first order ordinary differential equations for each daughter i . These equations are put into the matrix form shown below in Equation 6-17.

In matrix form, the Yield Fraction and Branching Ratio take on an additional numerical meaning. When i is not the radioactive decay daughter of parent j , then the yield fraction is zero. Similarly when a neutron capture in j does not create i , the branching ratio for j going into i is zero. Otherwise, when i is created by j the yield fraction or branching ratio is determined by the physics characterized by the radioactive decay or neutron reaction, respectively. The vector form of Equation 6-17 is expressed by Equation 6-18.

Given the non-linear behavior of buildup and depletion of isotopes throughout the entire irradiation, the solution can not be solved for in a simple integration, as is done for the scalar form of Equation 6-18. However, if the solution to this equation is assumed to be linear across a

small time step, then an accurate approximation can be found for each step. Therefore, the entire radiation time is broken into T time steps. Then the linear solution to Equation 6-18 is found for each step.

$$\begin{bmatrix} \frac{dN_1}{dt} \\ \frac{dN_2}{dt} \\ \dots \\ \frac{dN_N}{dt} \end{bmatrix} = \begin{bmatrix} \left[-\lambda_1 N_1 - \left(\sum_g \sigma_a^g \phi^g \right) N_1 \right] & \left[Y_1 \lambda_2 N_2 + B_1 \left(\sum_g \sigma_c^g \phi^g \right) N_2 \right] & \dots & \dots \\ \dots & \dots & \dots & \dots \\ \dots & \dots & \dots & \dots \\ \dots & \left[Y_N \lambda_2 N_2 + B_N \left(\sum_g \sigma_c^g \phi^g \right) N_2 \right] & \dots & \left[-\lambda_N N_N - \left(\sum_g \sigma_a^g \phi^g \right) N_N \right] \end{bmatrix} \begin{bmatrix} N_1 \\ N_2 \\ \dots \\ N_N \end{bmatrix} \quad (6-17)$$

$$\frac{d\hat{N}}{dt} = \hat{\Lambda} \hat{N} \quad (6-18)$$

$$\hat{N}_{t+1} = \hat{N}_t \left[e^{\Lambda(\Delta t)} \right] \quad (6-19)$$

Where: N_{t+1} is the N_t vector found at time $t+\Delta t$ after t and N_t , found during the previous time interval, and is also the initial condition to Equation 6-18 for the next times step. The exponential matrix is defined through a Taylor series expansion valid for small incremental times of Δt .

$$\left[e^{\Lambda(\Delta t)} \right] = \hat{I} + \hat{\Lambda} \Delta t + \frac{1}{2} \hat{\Lambda}^2 \Delta t^2 \quad (6-20)$$

Where: I is an identity matrix and Λ^2 is the vector multiplication of matrix Λ with itself.

Once the N_i vector is found for all T time steps, a vector for decay activity is defined by multiplying the number of isotope i atoms in each row by its alpha decay constant: λ_α .

Assuming that the change in N_i over Δt is negligible, the total number of decays, in Δt , can be found by simply multiplying the activity by Δt .

$$N_{He}^{(t+\Delta t)-t} = \frac{dN_i^t}{dt} \times \Delta t = \lambda_{\alpha}^i \times N_i^t \times \Delta t \quad (6-21)$$

However, in an effort to reduce the necessary time steps to give reasonably accurate results, a slightly more elegant integration within the time step is applied. First, the activity within the time step is defined.

$$A_i^t = \frac{dN_i^t}{dt} = -\lambda_{\alpha}^i \left(N_i^t e^{-\lambda_{\alpha}^i \times (\Delta t)} \right) \quad (6-22)$$

Where: A_i is the activity or rate of decay of isotope i . The helium production in the time step is found by integrating Equation 6-23 over Δt .

$$N_{He}^{(t+\Delta t)-t} = -\lambda_{\alpha}^i N_i^t \int_t^{t+\Delta t} e^{-\lambda_{\alpha}^i \times (t)} dt = N_i^t \left(1 - e^{-\lambda_{\alpha}^i \times (\Delta t)} \right) \quad (6-23)$$

The total helium generation over the irradiation time is found by summing the solution to Equation 6-23 over all time steps (t). A similar technique is used to calculate the atoms of krypton and xenon fission gas atoms produced by fission. Instead of λ_{α} , the fission reaction rate, in conjunction with the fission yield for krypton and xenon, is used instead: $B_{Kr}\sigma\phi$ and $B_{Xe}\sigma\phi$. The total fission gas yield for U-Pu fuel in a SFR is about 27 % [62]. This percentage accounts for all intermediate short lived decays, following fission, that ultimately lead to formation of a stable Kr or Xe atom.

Transmutation and Fission Gas Analysis

This depletion algorithm and gas production calculation is then applied for all regions of the core used in Figure 6-4. The code calculates the average number of helium and fission gas atoms produced per fuel assembly per cycle in each region of the core. Using the ideal gas law and the physical dimensions of the AHFTR fuel pin, the total number of He, Kr and Xe atoms, for each fuel assembly, are converted into pressure. For the conversion of atom density into

pressure, an approximate sodium coolant outlet temperature was assumed (~750 K). The dimensions used for this calculation are given in Table 6-8. The sodium coolant channel dimensions are also given. These dimensions were also used in the hot channel analysis in the previous section.

Table 6-8. AHFTR fuel pin dimensions

Total Fuel Pins Per Assembly	271
Pin Pitch-to-Diameter Ratio	1.1760
Pin Pitch (cm)	0.8879
Pin Diameter (cm)	0.7550
Cladding Thickness (cm)	0.0559
Cladding Inner Diameter (cm)	0.6432
Fuel Smear Density (%)	75
Fuel-to-Cladding Gap (cm)	0.0431
Fuel Slug Diameter (cm)	0.5570
Axial Reflector Height (cm)	114.6600
Active Fuel Height (cm)	71.6000
Target Fuel Height (cm)	20
Gas Plenum Height (cm)	191.1400

Fission gas release, due to interconnected porosity, is a function of fuel swelling, which in turn is a function of burnup for a given fuel composition. Extensive experimental data exists for the EBR-II Mark I, II, III and IV binary alloy 90U/10Zr fuels irradiated throughout the life of EBR-II. However, fuel qualification of the Mark V ternary 19Pu/71U/10Zr composition, of interest to the IFR program, had just begun before the program was terminated in 1992. The second phase of the AFC-1 program, at the ATR, is expected to achieve fuel burnups high enough to quantify swelling and interconnected porosity in high zirconium and high MA fuels. Therefore, without an established database correlating MA concentration with swelling, a gas release fraction of 75 % was assumed, as recommended by Tsai et al [64]. The average partial pressure contribution to the total plenum pressure is given for He, Kr and Xe as a function of row number in Figure 6-13.

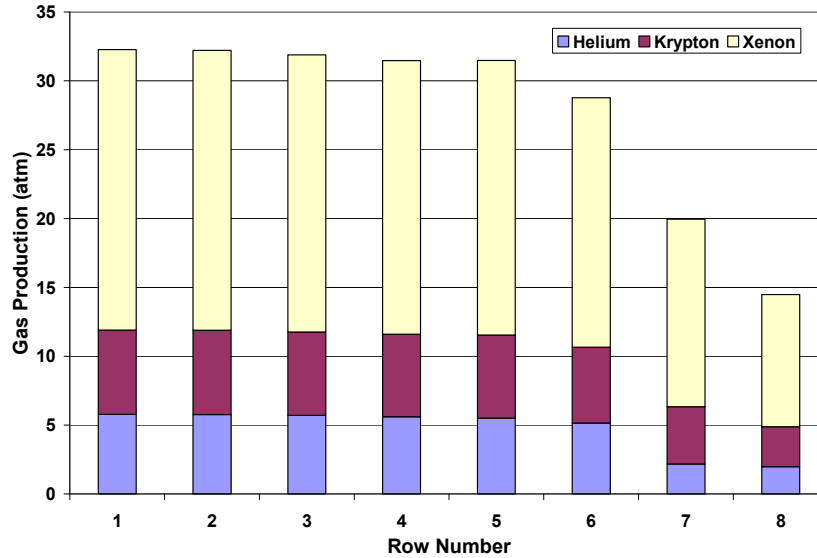


Figure 6-13. Gas plenum pressures resulting from transmutation and fission gas production (plotted as a function of fuel assembly row number)

Notice, the sharp fall in gas production for the outer core rows (seven and eight). The smaller gas production in this region is characterized by the smaller power generation in the outer core. Also, the outer core the outer core has no axial targets so the contribution to helium gas production is less in these outer two rows. However, it is important to note the percent of the total pressure represented by helium, even in the absence of targets. Even though the outer core does not have axial targets, the driver fuel still has a non-trivial concentration of Pu-238, Am-241 and Cm-244. Without the axial targets, the fraction of total helium generated by Pu-238 is 10% as opposed to the 1% shown in Figure 6-12.

These pressures are representative of plenum pressures observed at EBR-II for the Mark II through Mark V experimental irradiations [93]. Using empirical models for the peak strain, creep and cumulative damage fraction (CDF), a rule of thumb was adopted to allow a plenum length approximately 1.5 times the length of the driver fuel. As with the Mark II and Mark III fuel, the 75% smear density, for Mark V, was adopted to ensure low FCCI, respect the cladding tensile strength, and minimize the contact pressure due to fuel-to-cladding mechanical interaction

(FCMI). The end result is a low probability of cladding rupture. The corresponding plenum pressure ranged between 25 and 40 atmospheres for steady state operation depending on fission gas release, fuel radial and axial expansion, etc. Knowing that transmuted helium gas would create the need for additional plenum volume, a conservative estimate of two times the rod (driver and target) height was used for the AHFTR design. The resulting plenum pressures fall within the EBR-II database, indicating that the AHFTR fuels will experience similar tolerance of FCCI, FCMI or creep rupture.

Fuel Design Basis Summary

Though the design criteria for the AHFTR are quite different than for existing LWR technology, the standards applied have been proven to provide safe operating conditions for SFR in general. The design criteria used for the AHFTR are virtually identical to that adopted by the S-PRISM and ABR designs and is backed by over 40 year operational experience of EBR-I and EBR-II and the 14 years of experience gained at FFTF. The AHFTR pin design was approached in a way that could incorporate the axial targets as an integral feature of the overall driver fuel. Therefore, it is not surprising that the fuel performance, cladding damage and temperature profile fall within the same limitations imposed upon the driver fuel.

The similarities between target and driver fuel performance are principally related to the similarities in fuel composition. The choice to incorporate some fissile plutonium and uranium into the fresh target slug minimizes the power shift from BOL to EOL. The suppression of power and transmutation of fertile material (namely U-238 and Am-241) in the axial target region produces fuel atoms that can be used later as fuel. The transmuted material (which is mostly plutonium) experiences a spectrum shift from epithermal to fast neutron energies when it is re-fabricated for a second life as driver. When the transmuted plutonium isotopes are introduced as driver fuel, their fissile worth becomes very near that of fissile Pu-239. Efficient

conversion, of MAs into plutonium isotopes, eliminates the need to multi-recycle the unburned MAs back into fresh targets for additional irradiations. Only the target's initial pass through the reactor is required to transmute the majority of the SNF MA mass into plutonium fuel.

Fuel Processing Considerations

This recycling strategy (i.e. breeding plutonium outside the active core before combining it with recycled driver fuel) is exactly the same IFC scenario demonstrated during the IFR program. In fact the AHFTR fuel cycle uses all of the primary components of the IFR fuel cycle. All fuel processing and fabrication operations are expected to be performed by remote handling in a hot-cell facility adjacent to the reactor. A similar hot-cell facility, called the Fuel Cycle Facility (FCF), was used to develop pyroprocessing and associated process technologies “electro-refining” for EBR-II and the IFR program. The FCF was an annular argon gas filled hot-cell that encompassed all fuel dissolution and re-fabrication processes. Spent EBR-II fuel assemblies were passed from disassembly, to pyroprocessing, blending, casting and assembly fabrication in a clockwise fashion within this hot-cell.

The AHFTR “electrorefinery” would serve a similar form and function as the FCF, having a single interlock with the outside world, which would pass casks of imported Np+Pu, Am+Cm+Bk+Cf and uranium provided by a larger centrally located SNF aqueous separations facility (Figure 3-4). FCF fuel handler's manipulated objects in the hot-cell using hand operated master-slave manipulator arms. Unlike the FCF, the electrorefinery would be automated on an industrial scale with a system of conveyors and robotic manipulators.

In the pyroprocessor, the chopped cladding hulls, fuel slugs and zirconium hydride slugs are immersed in a eutectic solution of LiCl-KCl electrolyte. A direct current is applied with the positive pole connected to the fuel basket and the negative pole applied to a steel cathode that is also immersed in the electrolyte. The current that is passed through the salt bath induces electro-

transport of the uranium to the metal cathode. The transuranics are collected by a liquid cadmium cathode in a ceramic crucible at the bottom of the pyroprocessor. Hydrogen from the $ZrH_{1.6}$ slugs would be extracted by passing a current between the anode basket and a palladium cathode. Palladium metal becomes $PdLiH_x$ readily by immersion into a $LiCl-KCl-LiH$ system. Eutectic salt hydrogen recovery technology has been developed at the bench top level for fabricating tritium production targets as well as hydrogen batteries for fuel cell applications [93,94,95]. Further exploration of the hydrogen recovery technology, at the deployment level, is necessary to bring it to the same technology readiness level as pyroprocessing of SFR fuels.

After separations, the recycled and external feeds would be brought together to form the target and driver fuel slugs. For EBR-II and the IFR program, americium containing slugs were melted in an induction furnace and then injected into quartz molds. This process worked well for the $90U/10Zr$ and $19Pu/71U/10Zr$ fuels. However, when americium was added to the mix, 40 % of it was lost due to vaporization before the fuel slug solidified [96]. The vaporization loss was attributed to volatile contaminants and vaporization losses at the casting temperature of $1465\text{ }^{\circ}C$. This problem was overcome during the AFC-1 tests performed more recently (this decade) for testing at the ATR. To create the high MA compositions for the AFC-1 fuels, an arc smelter was used to reach much more rapid heating of the feedstock [97]. Also, the injection and cooling times were reduced by using a vacuum assisted injection process. These factors combined eliminated most of the americium losses. However, the arc melting technology was only applied at the table-top level and still needs to be demonstrated at the deployment level to prove that it can be consistently performed in an assembly line fashion.

The AHFTR electrorefinery is expected to work in conjunction with the S-PRISM power block concept [19,98]. The AHFTR design has the same thermal power rating as S-PRISM. In

the AHFTR power block model, two 1000 MWth cores, each having their own primary and secondary sodium coolant loops, share the same primary containment building, steam generator and turbine system. The power block business model is analogous to a power utility purchasing smaller fossil fuel boilers units to comprise a much larger plant. The nuclear utility purchases individual power blocks and adds them to the same reactor site in a similar fashion that a coal utility purchases additional boiler units depending on the rate of market growth for electricity demand in the local market. A cartoon of the power block reactor site is given in Figure 6-14.

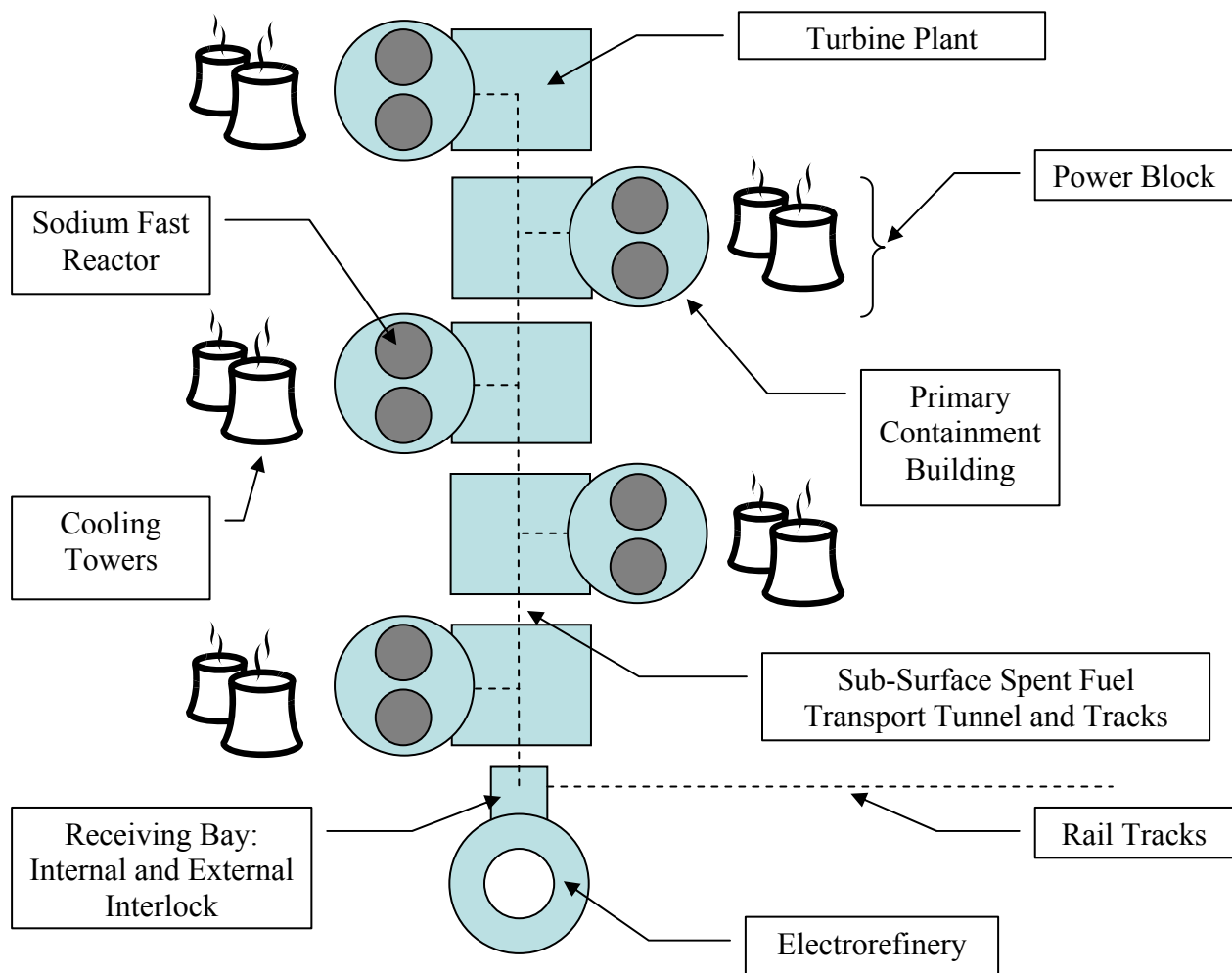


Figure 6-14. Envisioned power block reactor plant model describing the physical relationship between SFRs (ABR or AHFTR) and the electrorefinery

There is one important difference between the power block model and the boiler unit paradigm. The primary source of fuel is derived from the electrorefinery which is built at a set capacity. The utility must purchase the electrorefinery and co-locate it at the site where the power blocks are to be built. This virtually ensures that in order to achieve return on investment of the electrorefinery, the maximum amount of power blocks should be built early on. A high fuel throughput per unit of capital footprint pays down the interest on the electrorefinery capital investment more quickly.

For the AHFTR power block concept, it is envisioned that sufficient power blocks will be purchased, such that core reload operations will be a continuous, instead of cyclic, operation. The refueling of the AHFTRs would be conducted out of phase of each other, so that one reactor is going offline as the next reactor is going online. This ensures that the electrorefinery is, at all times, recycling the currently discharged fuel with a constant throughput. A cycle length of 220 EFPD days and a capacity factor of 0.85 gives an outage time of 36.56 days. Therefore, ten AHFTR reactors are required to ensure that one reactor is offline at any given time of the year. At any given time of the year, nine reactors are at full power and one is shutdown for refueling. Assuming a thermal efficiency of 0.37%, these nine reactors produce 8,990 MWth and 3,326 MWe of electricity.

Higher Mass Actinide Considerations

The choice of pyroprocessing eliminates the possibility of MA actinide partitioning and multi-reprocessing of the MAs in targets. Therefore, the buildup of curium and the higher mass actinides berkelium and californium in the driver fuel must be tolerated. This problem was encountered for multi-recycling IMF in studies of LWR recycling strategies. In IMF, each reactor pass depletes the concentration of neptunium, plutonium and americium while simultaneously generating curium, berkelium and californium. A similar result is observed in

multi-recycling all of the MAs in the homogeneous ABR [38]. The increase in decay heat, gamma and neutron emission in the recycled ABR fuel becomes an order of magnitude greater than if curium and the higher mass actinides are discarded.

Curium and the higher mass actinides are produced in the AHFTR targets as well as the driver fuel. Figure 6-15 shows the relative neutron emission activity per mass of initial TRU, after recycle and blending with the external feeds. In Figure 6-15, each reprocessing technology represents the actinide grouping assumed for the external transuranic feed from the SNF aqueous plant (Table 1-8).

- PUREX: Np, Am, Cm, Bk and Cf are discarded
- UREX+2/+3: Am, Cm, Bk and Cf are discarded
- UREX+4: Cm, Bk and Cf are discarded
- UREX+1a: All TRU is kept in the fuel and none is discarded
- UREX: All TRU is kept in the fuel and none is discarded

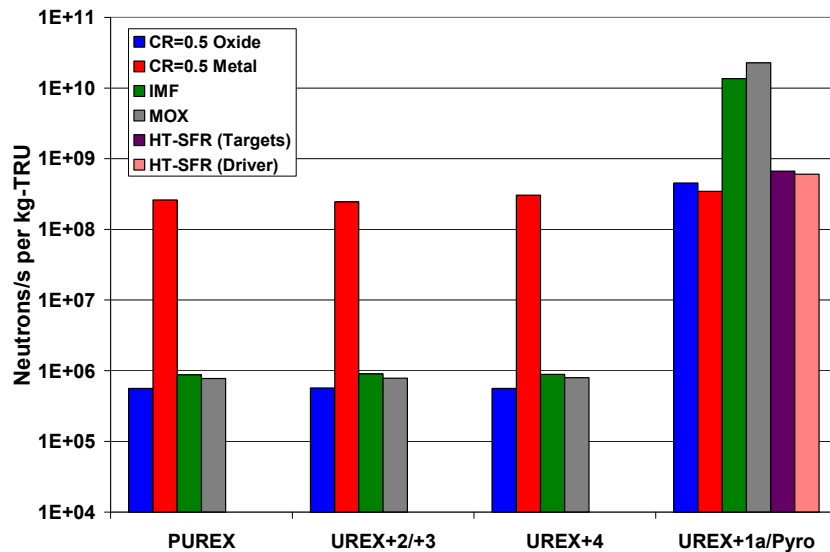


Figure 6-15. Average neutron emission rate for processed initial TRU in fresh fuel

In the case of the metal fueled SFR, the neutron emission rate remains more or less constant across the different levels of actinide partitioning. This is due to the lumped transuranic grouping limitation of pyroprocessing. In the case of oxide, however, different aqueous separation processes only allow specific isotopes to be fabricated into new fuel. In the oxide

fueled SFR, a UREX+ separation is assumed for the reactor discharge in addition to the SNF feed. With the exception of the metal fueled SFR, the neutron emission rate stays low until curium is kept in the fuel, as is the case for UREX+1a and pyroprocessing. Even MOX and IMF are found to have low emission rates when curium and the higher mass actinides are discarded.

However, it should be noted that even if curium, berkelium and californium are separated from the fresh fuel charge, the waste stream created is highly radioactive, and requires a long term storage solution. This is counterintuitive because the philosophy of an advanced “burner” reactor is to destroy nuclear waste.

The AHFTR appears to exhibit a much reduced neutron source compared to the thermal spectrum transmutation schemes. This may be attributed to the net destruction of Cm-244 in the driver fuel. In thermal reactors, the fission-to-absorption ratios for the fertile curium isotopes (Cm-244,246,248) are small and on the order of 10% to 20% (Table 1-2). The low fission importance provides an open gateway to produce higher mass actinides with each neutron capture. The AHFTR targets also have low fission-to-absorption ratios for these isotopes, thus allowing higher mass actinide generation. However, when these isotopes are processed and charged to the driver fuel, the much faster neutron spectrum of the active core closes the neutron capture gateway with significantly higher fission-to-capture ratios (Table 2-3). Therefore, the transmutation gateway towards higher mass curium, berkelium and californium is analogous to a diode. The transmutation diode is open for neutrons below the threshold for fission and closed at neutron energies above the threshold (one MeV).

The gamma decay energy rate per mass of initial TRU is shown in Figure 6-16. The trends are similar to the neutron emission data. However, gamma energy emission rate is less sensitive, than the neutron emission rate, to the separation of curium from the initial TRU. The AHFTR

targets show the highest gamma energy emission rate, even though this mass is processed directly from the SNF and not multi-reprocessed. Hence, there is inadequate time for buildup trends leading to high emission rates. The gamma decay rate from Am-241 and Cm-244 constitutes 66% and 20%, respectively, of the gamma energy produced.

Gamma decay is not the primary mode of decay for Am-241 and Cm-244. The secondary gamma emission of the excited daughter results in an associated gamma field (e.g., the Am-241 decay into various excitations of Np-237). The gamma emission rate of the AHFTR fuel is roughly 1.75 times that of the metal fueled reference ABR. The emission rate is not dominated by any single isotope as it is in the targets but rather is represented with relative equally by: Pu-238, Am-241, Cm-242, Cm-243 and Cm-244.

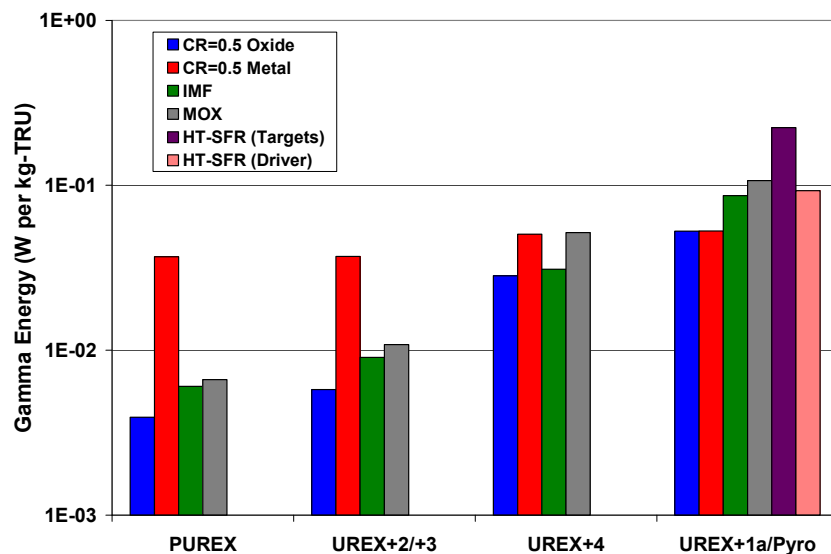


Figure 6-16. Average gamma decay energy rate for processed initial TRU in fresh fuel

The alpha decay heat rate per mass of initial TRU is shown in Figure 6-17. The trends are similar to the neutron emission data. The target and heat generation rate is dominated by the alpha decay of Cm-244 (targets) and also Cm-242 (targets and fuel) (Figure 3-17 and Figure 3-18). The AHFTR fuel heat generation rates are both roughly equal to the thermal recycling schemes and roughly twice as high as the metal fueled SFR.

Though the AHFTR driver and target fuels exhibit higher gamma and heat emission rates, these rates do not exceed the worst case scenario for multi-recycling in an LWR. Also, these higher emission rates should be expected, considering the high throughput of americium and curium feedstock in the AHFTR recycling center. Because of these high emission rates, it is assumed that all AHFTR fuel handling processes will be performed remotely in a dedicated hot-cell facility. However, the dedicated MA burning, performed by the AHFTR, provides for more economic fabrication of Np+Pu fuels for other reactors. The Np+Pu feedstock is free of curium and the higher mass actinides. Therefore, it could perceivably be handled using glove-box accessible processes. An economic evaluation of the cost savings of this “two-tier” strategy will be evaluated in a later section.

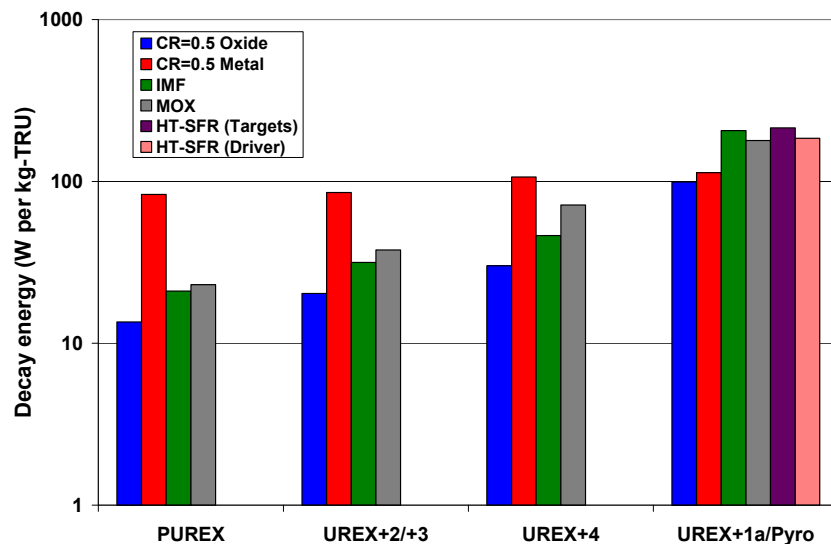


Figure 6-17. Average alpha decay heat rate for processed initial TRU in fresh fuel

Repository Considerations

Much emphasis has been placed on the importance of destroying Am-241 in this work. As can be seen in Figure 1-4, the heat contribution by Am-241 in UOX-SNF causes the heat generated in the repository to peak approximately 1000 years after it is closed. Therefore, transmuting Am-241 in the AHFTR should decrease the amount of heat generated in the

repository. However, as stated previously the irradiation of Am-241 results in the buildup of Pu-238 and Cm-244 in the fuel cycle. These two isotopes decay by alpha particle emission with half-lives ranging in the decades. As stated in the previous section, buildup of Cm-244 in the AHFTR fuel cycle results in a fresh fuel that is thermally hot within the time frame that fuel recycling occurs. Some of this material will be lost from the fuel cycle due to process losses at the reprocessing and fuel fabrication stages at the electrorefinery. These losses would be recovered as HLW and ultimately be sent to permanent geologic disposal in the repository. Therefore, it is necessary to quantify the thermal heat trends of the fuel within the time frame of the repository.

To do this, the ORIGEN component of the MONTEBURNS code was used. Using MONTEBURNS, the AHFTR fuel was depleted to the EOC (representing EOEC from the REBUS calculation) as was done in the benchmark calculation in Chapter 5. After the in-core buildup/depletion calculation was completed, the MCNP component of MONTEBURNS was switched off and only the ORIGEN code was used to decay the fuel out to the geologic time frames of the repository. Because the decay was performed on the entire core inventory at EOC, this calculation does not represent the repository performance due to the AHFTR spent fuel. Instead, the calculation offers a scenario where the core is shut down at EOEC, defueled and all fuel assemblies sent to the repository. Because the decay calculation represents HM in the fuel cycle averaged over its various stages of depletion in the core, it is a better representation of the isotopic composition of process losses than purely analyzing the spent fuel composition. The results of the coupled MONTEBURNS/ORIGEN calculation are shown in Figure 6-18.

Note that the total decay heat in Figure 6-18 does not have a hump at 1000 years as it does in Figure 1-4. Instead the near term repository heat is dominated by the presence of Pu-238 and

Cm-244 which decay away in the first few hundred years after emplacement. The heat contribution of Am-241 still peaks after 1000 years due to the fact that its production by Pu-241 beta decay is faster than its radioactive decay. However, the overall HM heat generation is relatively insensitive to the Am-241 peak due to the much higher concentration of Pu-238 and Cm-244 in the AHFTR fuel cycle than in SNF.

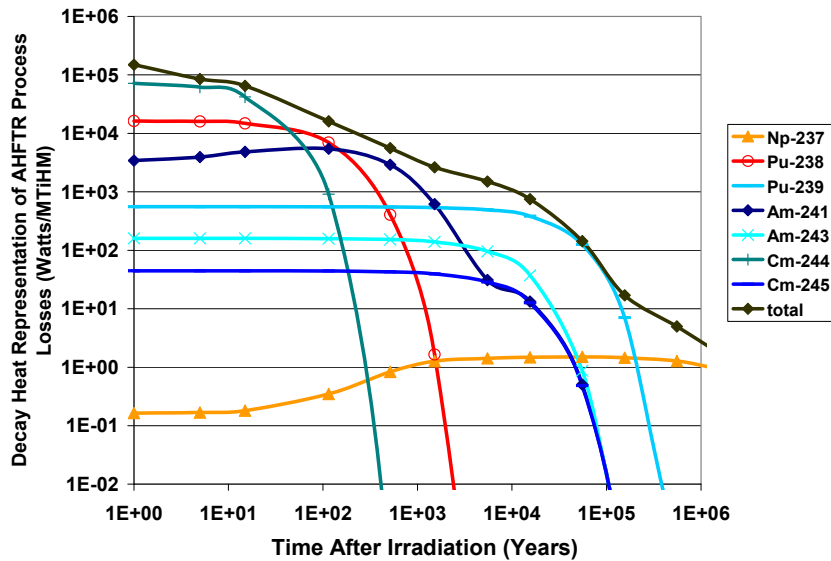


Figure 6-18. Decay heat plot for AHFTR for a scenario where the reactor is shutdown at EOE, defueled and all fuel assemblies sent to the repository¹

Because the AHFTR heat plateaus (due to the peak heat of Pu-238) earlier in the repository life than SNF, it can be argued that the waste stream produced by the AHFTR fuel cycle will be easier to monitor and manage in the repository than SNF. This is because the heat plateau occurs during the practical time that the repository can be operated and monitored by present day institutions. Very few human organizations, except for a select few religions, have enjoyed the longevity that would be needed to operate the repository for thousands of years. Therefore, if a

¹ Note the magnitude of the decay heat in Figure 6-18 is at least two orders of magnitude greater than Figure 1-4. To some extent, this is anticipated due to the one order of magnitude higher concentration of TRU in fast reactor fuel than in SNF. It is also important to note that reprocessing losses can usually be assumed to be less than one percent meaning that the amount of waste generated per energy extracted from the fuel is one to two orders less for a closed fuel cycle than an open fuel cycle [13].

sudden deviation from the predicted performance of a SNF repository occurs due to the Am-241 peak, it can not be expected that a human institution will exist that can respond to the safety implications of this change. However, in the AHFTR scenario, the heat generation peak would occur much sooner, in the first few hundred years. Many human institutions including the existence of the United States have subsisted in this few hundred year time scale. Therefore, the decay heat related performance of an AHFTR repository would be much easier to control using human influences.

CHAPTER 7 ECONOMICS OF THE TWO-TIER AHFTR FUEL CYCLE

Given the higher rate of MA consumption by the AHFTR compared to the ABR, the potential waste disposal attributes to the back-end of the fuel cycle are apparent. However, it is necessary to evaluate the overall AHFTR fuel cost in order to realize any cost reductions that MA waste burning can bring to a closed fuel cycle scenario. The cost attractiveness of fuel recycling versus direct-disposal of SNF has created an ongoing public debate on the subject for several decades. Two relatively recent independent reports, by the Massachusetts Institute of Technology (MIT) and Harvard University, state that the direct-disposal fuel cycle is currently more economically competitive from a fuel cost standpoint than plutonium reprocessing in a deregulated non-subsidized nuclear market [99,100].

Economic Issues of Reprocessing

The fundamental cost driver for SNF recycling is the reprocessing cost of separating the fissile (~1%) plutonium (or transuranic) component of the SNF from the non-fissile uranium (~95%) and fission products (~4%). Because of the low transuranic concentration in SNF, a large HM throughput of SNF is required to remove all of the unwanted uranium and fission products. Reprocessing costs are further complicated by plutonium proliferation and safeguards issues. Criticality safety and radiological protection adds additional costs to recycling and fabricating plutonium or transuranic bearing fuel. The combined effect is a fuel cost of a transuranic fuel cycle that is more expensive than the combined cost of mining, milling, conversion, enrichment and fabrication of UOX-LWR fuel.

For a fast reactor, the amount of energy extracted per mass of fuel (i.e., burnup) is at least twice as high as that attainable by irradiating MOX fuels in LWRs. This allows more revenue in electricity sales to be created per unit of fuel cost. However, fast reactors inherently require a

very robust and tolerant fuel and reactor design in order to achieve these high burnups and still operate safely. Therefore, commercial demonstration fast reactors have typically been built at a capital cost 10-50% higher than LWRs [99]. Also, because the spent fast reactor fuel (SFR) in many SFR fuel cycles (including this analysis) is reprocessed at the reactor site without allowing for fission product decay, a hot-cell is required for all fuel handling operations. This remote handling infrastructure requirement imposes a higher cost of fuel recycling than the glove-box type of infrastructure used for SNF plutonium recycling (i.e., MOX-LWR fuels).

Transuranic reprocessing also incurs a disposal fee for the HLW generated by the separation process. The HLW is mostly comprised of radioactive fission products that are removed during the separation process. In addition, a variety of low level wastes (LLW) and intermediate level wastes (ILW) are created by process losses and equipment contamination as a normal part of reprocessing and fuel fabrication plant operation¹. These waste materials can take on many forms from the mixed-waste (chemical plus radiological hazard) nitric acid solutions produced by aqueous processes that qualify as HLW to contaminated gloves and clothing that only qualify as LLW. These wastes comprise a non-trivial component to the front-end of the closed fuel cycle. For this analysis, a standard “base-case” HLW disposal fee is adopted for both aqueous reprocessing and pyroprocessing. Base-case values are also adopted for the unit costs of the following fuel cycle services.

- Price of Uranium ore, Conversion, Enrichment and UOX fuel fabrication
- NWPA SNF disposal levee
- Onsite SNF interim cask storage fee
- Cost of aqueous reprocessing, Cost of pyroprocessing

¹ It should be noted that ILW is not defined by United States laws and regulations. However, this term is adopted in the international community and is used in this dissertation as a nomenclature placeholder for reprocessing related waste streams such as chopped HT-9 cladding and/or the zirconium constituent of Pu/U/Zr fuels. This type of waste could be considered as “greater than class C LLW” in the United States as will be discussed in a later section.

- HLW disposal (including ILW and LLW in this cost)
- Fast reactor fuel fabrication – hot handling (hot-cell) or cold handling (glove-box)

A series of sensitivity studies will be applied to these base case unit costs to draw attention to the dominating fuel costs of the ABR and AHFTR fuel cycles.

Capitol Costs

The MIT report sites most Generation-III or III+ LWR plant overnight costs to be in the range of \$1,400/kWe to \$2,000 per 1 kWe of installed capacity. These values reflect the differences in plant infrastructure footprint, reactor vessel and component modularity, as well as a construction learning curve between the first-of-a-kind (FOAK) and the Nth-of-a-kind (NOAK) deployment of a particular plant design. The Harvard report mentions that the overnight costs of “proposed” commercial SFRs have been traditionally quoted to be 10% to 50% higher than for LWRs. This estimate is also summarized by Kochetov et al [101]. These higher capital costs are generally quoted as NOAK costs. However, many of these “proposed” commercial designs, such as the S-PRISM, are rooted in previous reactor experience with FOAK reactors. It is not an overgeneralization to say that all SFR plants to date were built without a standardized design or an established SFR regulatory framework. In addition, SFR power reactors have always had a dual role as a design concept demonstration and/or a fast flux fuel test facility. Because of the FOAK nature of past SFR power systems, a fair degree of over-engineering was introduced into their designs. This over-conservatism is necessary for a FOAK reactor plant to compensate for the lack of technological maturity. For this dissertation, no assumptions are made with regards to the learning curve or degree of technological maturity between, FOAK and NOAK of a commercial scale SFR fleet. However, it is assumed that most of the technological hurdles for an “economical” commercial SFR can be overcome by evolutionary design innovation and not limited by the fundamental physics of the SFR concept in general.

As an example, Konomura et al conducted a feasibility study of a conceptual commercial scale Japanese Atomic Energy Agency SFR (JSFR) to determine where design simplifications are necessary for reducing the construction cost [102]. Konomura et al identified the long piping of the secondary sodium loop as one of the largest construction expenses of the JSFR design. The secondary sodium loop transfers heat from the intermediate heat exchanger (IHX) in the sodium pool (or primary loop if a loop type system is considered) to the steam generator. The IHX and secondary loop sodium does not circulate through the reactor core which essentially eliminates neutron activated sodium from leaving the reactor vessel. This feature is a necessity in case of a leak between the reactor vessel and the steam generator that would ultimately lead to a sodium fire.

Historically, austenitic steels have been used for these pipes for their strength at elevated temperatures, sufficient ductility and compatibility with sodium. Ductility is a requirement for managing thermal stresses that arise during steady-state or transient operation. However, austenitic steels have a relatively high thermal expansion coefficient compared to other steels. The thermal expansion necessitates long piping designs with a number of elbows. On the other hand, high chromium content ferritic steels typically have a smaller thermal expansion than austenitic steels. High chromium steels were not used in the past due to their poor ductility. However, Konomura et al sites recent developments with tungsten and molybdenum alloying in 12-Cr steels in the 1990's that may give high chromium steels the advantage in ductility required to allow their use in the secondary loop plumbing. The HT-9 cladding developed in the late 1980's to early 1990's for SFR fuel pin cladding (and in-core structures) is also a 12-Cr ferritic/martensitic steel.

Konomura et al proposed that the shortening of piping in addition to: loop number reduction, a compact reactor vessel and structure and integration of certain components could significantly reduce the construction cost. These goals are also shared by the compact modularity and shared steam loop philosophy of the S-PRISM power block approach. Konomura et al used the Nuclear Utility Service (NUS) code of account, developed in 1969 for LWRs, in order to evaluate the JSFR construction cost. Using NUS, the total plant construction cost was evaluated as a sum of all facility and equipment unit costs multiplied by the mass or quantity of each component. Using this model and appropriately discounting the construction cost for each component, Konomura et al found that the overall JSFR cost would be in the range of 200,000 yen/kWe or equivalently about \$1,750/kWe in present United States dollars. This value is within the range of Generation-III options listed by the MIT report.

Due to the apparent similarities between the AHFTR power plant design and other proposed commercial SFR concepts (i.e., ABR, S-PRISM, JSFR, etc.), a rigorous component cost analysis is not necessary. However, if a base case overnight construction cost of \$1,800/kWe is assumed with a discount rate of 6% and a five year construction time, then the capital construction cost, at the time the plant goes on line, is \$2,140/kWe. After accounting for interest on the initial investment as well as taxes, insurance, etc., the capital cost contribution to the price of electricity is about 4.0 ¢/kW×hr(e). The economic model used to calculate the capital cost contribution to the price of electricity is discussed in a later section. A ballpark estimate of \$1,800/kW(e) is assumed for the AHFTR overnight capital cost. This assumes zero FOAK costs for a standardized SFR design with reactors built in succession at a preapproved site. Also, for the purpose of this analysis, the operations and maintenance cost contribution to the price of electricity will be assumed to be the same as for a LWR.

Fuel Costs

The Harvard report makes special mention of the fact that civilian plutonium separation practices to date have not kept in line with purchase of MOX fuel assemblies, resulting in a 200 metric ton commercial plutonium world stockpile. Therefore, the Harvard report stipulates that this stockpile could be used to constitute the “first-core” required to start the SFR and launch its closed fuel cycle. Hence, as was done in the Harvard report, the assumption is made for the AHFTR that this first-core at each new SFR (ABR or AHFTR) has zero fuel cost. The general transuranic loading of both the AHFTR and the ABR is approximately three metric tons (Table 3-12). Therefore, approximately 65 reactors can be started using the commercial stockpile. This is the equivalent of six reactor sites of ten SFRs per site (using the power block model) making 3,330 MWe per site. However, if more reactors are required, the commodity price of stockpiled commercial plutonium would be driven up by an increase in demand. Thus, it may be prudent to consider the approximate 600 metric tons of stockpiled weapons grade plutonium existing in the world, to supplement the commercial stockpile. If the weapons plutonium stockpile is considered, then 27 SFR power stations (using the power block model) may be constructed.

First-Core Reprocessing Cost

If the first-core plutonium must be separated from SNF, a significant capital cost is incurred of approximately \$200/kWe to \$300/kWe which corresponds to a reprocessing cost of approximately \$20,000/kgiHM to \$30,000/kgiHM, respectively, of separated plutonium. This estimate is based on a cost of aqueous reprocessing of SNF to be approximately \$1,000 to \$1,500 per kilogram of SNF and only 1% of this SNF being plutonium. Therefore, the cost to bring the plutonium concentration from 1%/kg in SNF to the 20%/kgiHM of TRU enrichment requirement for the SFR driver fuel is:

$$\frac{\$1,000}{\text{kg SNF}} \times \frac{1}{0.01} \frac{\text{kg SNF}}{\text{kg Pu}} \times \frac{0.20}{1} \frac{\text{kg Pu}}{\text{kg iHM}} = \$20,000 / \text{kg iHM}$$

or :

$$\frac{\$1,500}{\text{kg SNF}} \times \frac{1}{0.01} \frac{\text{kg SNF}}{\text{kg Pu}} \times \frac{0.20}{1} \frac{\text{kg Pu}}{\text{kg iHM}} = \$30,000 / \text{kg iHM}$$

Assuming, a \$2000/kWe overnight construction rate, the added cost of the first-core plutonium is equivalent to a 10% to 15% increase in the overnight capital cost of the reactor plant. Because, this “first-core” reprocessing cost is attached to the reactor’s total cost before actual operation begins, it can be considered as a capital or startup cost. This large pre-operational reprocessing cost is analogous to the cost of supplying the initial heavy water to a pressurized heavy water reactor (PHWR). The operational cost of resupplying heavy water to a PHWR is minimal. However, the pre-operational cost to supply the initial heavy water for a PHWR’s plumbing can be as high as 10% of a PHWR’s overnight cost [103].

Nth Core Reprocessing Cost

For all subsequent refuelings, a much smaller amount of SNF HM must be processed externally in order to retrieve the transuranic material needed to refuel the ABR and AHFTR. This is because much of the transuranic material needed for all Nth refuelings has already been pre-concentrated in the form of the fast reactor fuel, or more precisely the SFF. Hence, the throughput of HM required from SNF to reconstitute the TRU enrichment of fresh fuel is much less for a closed SFR fuel cycle than if the SFF were not recycled. The smaller HM throughput requirement stems from the fact that SFF needs less uranium to be subtracted in order to bring the spent fuel transuranic concentration back to that needed for fresh fuel. It is important to note, that as the SFR’s CR approaches zero, the concentration of TRU in the SFF relative to the initial TRU enrichment decreases, thus increasing the reprocessing cost of SNF. In the ABR fuel cycle, SNF is reprocessed at a centrally located aqueous reprocessing facility (presumably UREX+)

(Figure 1-1). Therefore, the HM mass throughput, and hence reprocessing cost per mass of product, of this aqueous facility is strongly dependent on the conversion ratio selected for the ABR (and/or AHFTR) design. The mass throughput requirements of the electrorefinery are similarly affected by the concentration of TRU in the SFF. However, because of the high TRU concentration per HM in SFF compared to SNF, the electrorefinery requires less SFF HM throughput “capacity” per unit mass of separated TRU produced.

The cost of fuel reprocessing is a function of the rate of return on investments made in its design and construction, the day-to-day operations and maintenance costs and the mass throughput of the SFR.

$$\$/\text{kgHM} = \frac{(\text{Design} \times \phi) + (\text{Construction} \times \phi) + (\text{O \& M})}{\text{Capacity}} \quad (7-2)$$

Where: “Design” and “Construction” are the design and construction overnight costs in millions of dollars (M\$), respectively. ϕ is the carrying charge on the initial investment per year (yr^{-1}). The carrying charge reflects the annual payment of the reprocessing facility capital cost plus interest, insurance and taxes. O&M is the operations and maintenance cost in millions of dollars (M\$/yr). Capacity is the annual HM throughput capability of the reprocessing facility (kg/yr).

Unfortunately, due to the technical requirements of remote fuel handling, the electrorefinery construction cost will be capital intensive. In order to have a pyroprocessing cost competitive with aqueous reprocessing, the design and construction costs must be reduced. To compensate the higher construction costs in Equation 7-2, the electrorefinery should have a modular design which could reduce the design cost of the facility to nearly zero. Because of the construction cost, the HM throughput capacity must be maximized to a feasible limit. This fact

requires that the electrorefinery service multiple SFRs as is proposed in the ten reactor power block model.

As stated before, reducing the SFR's CR will increase the HM throughput capacity. However, the reprocessing requirements of the SFR will also increase which would necessitate a larger electrorefinery be constructed in order to meet this demand. Therefore, the benefit of decreasing the CR to decrease the reprocessing service cost would be washed out by the cost to construct the reprocessing plants needed to keep up with fuel demand.

Operations and maintenance of the reprocessing facility is an unavoidable expense which is necessary for safe handling and protection of separated plutonium and transuranic material. The French La Hague plant employs 6,000 to 8,000 highly trained individuals that oversee operations and maintenance of equipment and processes [99]. A report by Smith et al and another by Kim, Kazimi et al details the expected fuel reprocessing plant costs for an Accelerator Transmutation of Waste (ATW) system and an ABR respectively [104,105]. Both reports indicate that the O&M cost is expected to be between 23% and 33% of the total reprocessing cost per HM throughput.

For the base case of this analysis, the reprocessing cost was allowed to vary from \$1,500/kgHM for the minimum aqueous processing cost to \$3,000/kgHM for the maximum electrorefinery cost. The \$1,500/kgHM is a common estimate of large scale commercial aqueous reprocessing costs for the United Kingdom's Thermal Oxide Reprocessing Plant (THORP) and France's UP2 and UP3 facilities in La Hague [99]. This number reflects the cost of reprocessing under government enforced pay-ahead contracts that required utilities to essentially pay off the entire cost of these plants over a ten year base load period with no required return to investors. The Harvard report estimated the reprocessing cost to be \$1,350/kgHM for a government owned

facility capable of borrowing money at low risk-free government rates and amortization of capital over a 30 year plant lifetime. The Harvard report also calculated the reprocessing cost to be greater than \$2,000/kgHM for a privately owned facility with a government guaranteed rate of return. If no rate of return is guaranteed, the reprocessing cost may be as high as \$3,000/kgHM. Since, it is considered likely that the electrorefinery will be privately owned and operated in a consortium with the reactor utility; this value is assumed as the maximum cost for pyroprocessing. The \$1,500/kgHM number (2003 dollars) was used for the fuel cycle calculations in both the MIT and Harvard studies. Despite the ATW reports that give a much more optimistic estimate, the MIT and Harvard value is considered for aqueous reprocessing for the purpose of this study. This value also closely matches a 1994 report by the French Nuclear Energy Agency of \$720 Euro/kgHM (1994 currency). Assuming a 3% rate of inflation and the present day conversion rate, this corresponds to approximately \$1,515/kgHM in 2007 US dollars.

High Level Waste Disposal Cost

As a byproduct of aqueous reprocessing HLW, ILW and LLW are produced. Low level waste generally consists of gloves, protective clothing and tools that have been contaminated with low levels of short lived radioisotopes. The definition of ILW includes resins, chemical sludge and metal reactor fuel cladding, as well as contaminated materials from equipment decommissioning [106]. It should be noted that ILW is not defined by United States laws and regulations. However, this term is adopted in the international community and is used in this dissertation as a nomenclature placeholder for reprocessing related waste streams such as chopped HT-9 cladding and/or the zirconium constituent of Pu/U/Zr fuels. If ILW contains transuranics, it may be considered transuranic waste which is a HLW that requires repository storage. It is common in Europe to cement ILW inside metal containers that are destined for geologic disposal. If this is the case, this type of waste could be considered as “greater than class

LLW” in the United States [107]. However, as a general rule, non-transuranic containing ILW such as fuel cladding hulls can be disposed of at surface burial sites with LLW. HLW consists of the separated fission products as well as pragmatic actinide losses that can not be fully recovered from the acid or molten salt solutions. The NEA study assumed that for aqueous reprocessing, these wastes would be vitrified into a glass waste form a few years after their creation and then held at the reprocessing site for 50 years.

Disposal practices for ILW and HLW have been demonstrated for pyroprocessing by the treatment of EBR-II spent fuel. For these treatment operations, EBR-II SFF is pyroprocessed to separate the uranium from the NaCl-LiCl eutectic solution. The transuranics and fission products are separated from this solution and then mixed with zeolite to form a ceramic waste form. The noble metals and cladding hulls from this process are added to zirconium and then melted down into a metal waste form.

The MIT and Harvard reports both assessed a fee of \$300/kgHM for disposing of these HLW, ILW and LLW for aqueous reprocessing. In this dissertation, this value is adopted for the electrorefinery as well.

Fuel Fabrication Cost

Similar to reprocessing, transuranic fuel fabrication also requires large capital-intensive facilities with a large workforce of highly skilled and trained personnel. The Harvard report suggested that the fuel fabrication cost of such a facility would be in the range of \$1,010/kgHM for a government operated facility; in the range of \$1,460/kgHM for a privately owned facility with a guaranteed rate of return; and approximately \$2,140/kgHM for a privately owned facility with no guaranteed rate of return. The Harvard report also mentions that a cost of \$120/kgHM should be assessed for transporting transuranic fuel from the fuel fabrication facility to the

reactor site. The MIT report assumed a value of \$1,500/kgHM for the cost of fabricating Pu-only MOX-LWR fuel.

Similar to the ABR and AHFTR reactor plants, the electrorefinery is expected to be privately owned with no guaranteed rate of return. Because, fuel fabrication is carried out in the same circuit as pyroprocessing, most of the transportation costs can be avoided at the ABR or AHFTR electrorefinery. However, some transportation cost is incurred in order to bring the make-up transuranic materials from the aqueous plant to the electrorefinery. Because of the additional shielding requirements (hot-cell environment) brought on by high gamma and neutron radiation fields, and also the additional complexity of target fabrication, a conservative fuel fabrication estimate of \$2,500/kgHM is for the reprocessing fee of the electrorefinery. This estimate is used for both the ABR and the AHFTR.

Due to the use of Lightly Enriched Uranium (LEU), the fuel fabrication safety requirements for LEU-UOX fueled LWRs are less than for transuranic fueled reactors. A fabrication cost of \$250/kgHM is the current average market price of LEU UOX-LWR fuel fabrication. This is the value used for the ABR and AHFTR fuel cycle study. The MIT report assumed a value of \$275/kgHM. The Harvard report assumed a value of \$250/kgHM.

Front-End Uranium Costs

The price of uranium ore has historically given a small contribution to fuel costs. In fact the primary reason why the LWR has become the work horse of the world's nuclear electricity industry is because uranium was found to be in much greater supply than originally expected during the early days of the industry. For the past 20 years, the price of U_3O_8 has stayed below \$20/lb U_3O_8 (\$40/kgU in the form of U_3O_8). However, this price has increased to as high as \$140/lb U_3O_8 between 2006 and 2007. The issue of the abundance of the world's "minable" uranium supplies, and hence price, is the center of much industry debate in recent years. Though

currently the price of uranium ore is in a state of flux, it is assumed for the purpose of this economic analysis that future prospecting will discover additional reserves. Therefore, the pre-2006 price of \$20/lb U_3O_8 is used for the ABR and AHFTR fuel cycle analysis.

Conversion of the U_3O_8 ore into UF_6 gas has been a relatively minor cost to the front-end of the fuel cycle. However, the price of conversion has also been in a relative state of flux over the past 10 years, varying from \$2/kgU in 2001 to \$11/kgU in 2006. For the following fuel cycle analysis, a value of \$11/kgU (in the form of UF_6) is assumed for the cost of conversion.

Uranium enrichment is the process of increasing the isotopic concentration of the fissile U-235 isotope in uranium above what is found in nature. The enrichment process produces a product stream, with a higher U-235 concentration, and a depleted uranium “tails” stream, with a lower U-235 concentration than that given by its natural abundance. The enrichment separative work unit (SWU) is defined as a metric of the cost of energy required by the enrichment process to achieve a desired U-235 concentration (i.e., enrichment). The more SWU that is applied to the natural uranium feedstock, the higher the U-235 enrichment in the product. Also, the more SWU applied leaves less U-235 concentration in the depleted uranium tails.

The price of the SWU has steadily risen since 2001 from a value of \$105/SWU to a value of \$145/SWU in 2006. The price increase of enrichment is driven by the price increase in uranium ore. As the price of uranium ore increases, fuel purchasers have specified a smaller U-235 concentration in the depleted uranium. The less amount of U-235 wasted in depleted uranium translates into more U-235 being extracted from the original uranium ore purchase. Therefore, the fuel purchaser does not need to buy as much uranium to arrive at the specified enrichment if more SWUs are purchased. This strategy is known as “underfeeding”. Because of rising uranium ore prices, underfeeding has been performed by the United States Enrichment

Corporation (USEC) since 2003 [108]. The increase in SWU demand has caused the price of enrichment to increase. For the following ABR and AHFTR fuel cycle analysis, an enrichment cost of \$145/SWU is assumed.

Back-End Uranium Costs

The NWPA was established to create a comprehensive national program for the safe long-term disposal of highly radioactive wastes. The NWPA directed the Department of Energy (DOE) to study suitable sites for a geologic repository for this long-term storage. The repository envisioned by the NWPA is an engineered disposal facility located deep underground that can store 70,000 metric tons of SNF and HLW. In 2002, Congress and the President approved the development of a geologic repository at Yucca Mountain, Nevada. The Yucca Mountain Environmental Impact Statement (YM-EIS) designated that the Yucca Mountain repository would receive 63,000 MTHM (metric ton heavy metal) of commercially generated SNF, 2,333 MTHM of DOE generated SNF and 4,667 MTHM of DOE generated HLW.

To finance the disposal of commercially generated SNF in the repository, the NWPA created the Nuclear Waste Fund (NWF) which imposes a flat fee of 1 mil/kW×hr(e) (1 mil is equal to ten percent of one cent) of electricity produced by nuclear fuel. This back-end fuel cost has been imposed on all nuclear electricity sold in the United States after the NWPA was passed in 1982.

Under the provisions of the NWPA, the DOE was required to accept SNF from the commercial industry for geologic disposal no later than January 31, 1998. This has not occurred due to logistical, legal and legislative delays. The delays have been driven by the Yucca Mountain site evaluation requiring a comprehensive understanding of its long term geologic behavior. Because of these delays and the fact that wet storage space provided by the spent fuel pool for most reactor plants is a finite premium, most nuclear utilities have been forced to

acquire interim storage capability in the form of dry storage casks. The cost of establishing this interim storage capacity has been estimated by the MIT and Harvard reports to be in the range of \$100/kgHM and is therefore used for the economics analysis of the ABR and AHFTR fuel cycle. This cost is determined by the cost to establish the storage facility (usually consisting of a concrete pad, fences, surveillance equipment, etc.) and purchase of the casks themselves. Since very little needs to be done with the casks once they are loaded on the pad, the operations, maintenance and surveillances costs are usually considered negligible and typically lumped in with the O&M cost of the power plant. It should be noted that if dry cask storage is needed for SNF at a reactor site that has been decommissioned, the cost of pad space for all of the reactor's legacy SNF can be much higher and in the range of \$300/kgHM because these costs would no longer be able to be rolled into the O&M costs of the reactor plant.

The assumption is made that it is probable that initial reprocessing capacity will not be able to meet the rate in which SNF is generated by LWRs. Therefore, it is foreseeable that interim storage will be necessary as a buffer between the rate of SNF generation and the rate at which it can be accepted by the reprocessing company. It is also assumed that these back-end costs will be credited to the reprocessing company as a fee for taking ownership of the SNF. The incentive for the LWR utility to pay the reprocessing company for SNF removal (\$100/kgHM), as opposed to waiting for repository disposal, comes from the avoidance of the \$300/kgHM dry cask storage fee in the event fuel is not removed before the plant is decommissioned.

Discounting and Financing

The cost of commercially generated electricity seen by customer ratepayers is broken down into four primary components: cost of reactor design, construction capital, fuel purchase, and operations and maintenance.

$$c_{elec} = c_{des} + c_{cap} + c_{fuel} + c_{O\&M} \quad (7-3)$$

For the ABR and AHFTR economics analysis, only the NOAK scenario is evaluated.

Hence, the cost of the reactor design is appreciably reduced and assumed to be zero.

Operations and Maintenance

For the sake of this analysis, the operations and maintenance cost per electricity generated is considered the same for SFRs and LWRs. Also the cost of decommissioning is rolled into this amount.

$$c_{O\&M} = \frac{C_{om} + C_{dd}F_{dd}}{8766 \times P \times \eta \times \varepsilon} \quad (7-4)$$

Where: C_{om} is the average operations and maintenance costs associated with payroll, equipment maintenance and update, etc. (\$). C_{dd} is the cost to decommission, dismantle and remediate nuclear materials from the reactor site at the end of its operational life (\$). F_{dd} is the amount of money paid each year by the utility into an annuity account for decommissioning activities. P is the reactor thermal power rating (kW). η is the reactor plants thermal-to-electric efficiency. ε is the availability of actual total heat energy produced in a year divided by the theoretical amount of heat energy produced if the reactor ran at full power throughout the same year. 8766 is the total number of hours in a year. The annuity factor (F_{dd}) is defined by the future value of a series of uniform payments into an account.

$$F_{dd} = \frac{i_{dd}}{(1 + i_{dd})^n - 1} \quad (7-5)$$

Where: i_{dd} is the rate of return on the decommissioning annuity fund. n is the number of years allotted for making payments into the annuity. For the ABR and AHFTR analysis the annuity is assumed to be paid over the five year construction time of the plant and i_{dd} is assumed to be 5.83 %/yr, which gives a value of 17.8% for F_{dd} .

Therefore, the c_{om} cost of electricity is \$0.0122/kW-hr(e), if $C_{om}/(P \times \eta \times \epsilon)$ and $C_{dd}/(P \times \eta \times \epsilon)$ are \$80/kW(e) and \$150/kW(e), respectively.

Construction Capital

Like the operations and maintenance model, the capital construction cost financing model of the ABR and/or AHFTR is borrowed from the Harvard report.

$$c_{cap} = \frac{C_{cap} (1 + F_{idc}) (1 + F_{preop}) (1 + F_{cont})}{8766 \times P \times \eta \times \epsilon} (F_{cr} + F_{tax} + F_{ins}) \quad (7-6)$$

Where: c_{cap} is the costs paid annually for the construction of the reactor (\$/kW×hr(e)). This is essentially the construction capital contribution to the cost of electricity. C_{cap} is the total overnight construction cost (\$). F_{idc} and F_{preop} are factors that account for interest during construction and other pre-operational costs. F_{cont} is a contingency factor to provide for cost overruns and other unforeseen costs. F_{cr} is the “fixed charge rate” which is the fraction of the total investment which must be repaid each year including interest rate and return on investment (yr^{-1}). F_{tax} and F_{ins} are the annual charges on property tax and insurance (yr^{-1}), respectively. For simplicity, it is assumed that F_{preop} and F_{cont} both equal 10%. Also, it assumed that the fixed charge rate, tax and insurance rates total to 10%/yr.

The interest rate factor during construction (F_{idc}) accounts for the interest charges collected during construction. The MIT and Harvard reports employ a special curve fit such as sinusoidal or binomial to generalize the amount of money borrowed for each year of construction. The amount of money borrowed at each of these years would then be discounted to the year the reactor goes online. For the ABR and AHFTR analysis, a flat distribution is assumed where the amount borrowed is the same for each year of construction before being discounted.

$$F_{idc} = -1 + \sum_{k=1}^n \frac{1}{n} (1 + i_{dc})^{n-k+1} \quad (7-7)$$

Where: n is the total number of years required for construction, k is the integer year of construction starting from ground breaking. i_{dc} is the interest rate on moneys borrowed during construction (yr^{-1}). For the ABR and AHFTR analysis, the construction time is assumed to be five years and the i_{dc} is assumed to be 5.83 %/yr, which gives a value of 19% for F_{idc} .

The fixed charge rate (F_{cr}) is the fraction of the initial investment that is paid each year to pay off the principal money borrowed with a return on investment. It is assumed that a fixed interest rate is applied over the lifetime of the reactor. Hence, the fixed charge rate may be determined by a simple “capital recovery formula”.

$$F_{cr} \equiv \frac{u}{p} = \frac{i(1+i)^N}{(1+i)^N - 1} \quad (7-8)$$

Where: u is the yearly required payment. p is the present worth of the capital investment. i is the discount rate for the return on the investment (yr^{-1}). N is the reactor lifetime in which the principal is paid off (yr). If a guaranteed discount rate of five percent and a reactor lifetime of 40 years are assumed, the fixed charge rate is 5.83 %/yr. If the sum of F_{cr} , F_{tax} and F_{ins} is 10%, the tax and insurance portion is 4.17 %/yr.

The discount rate i is treated in Equation 7-8 in a similar fashion to how interest is borrowed from a bank. However, in a broader sense, it is the “effective cost of money” for the investment made into the utility company by bonds and stockholders. This investment may be broken down into the percent of stocks and bonds invested in the utility and the taxes payable on the bonds.

$$i = f_s i_s + (1 - \tau) f_b i_b \quad (7-9)$$

Where: f_s is the fraction of the investment owned by stocks. f_b is the fraction of the investment owned by bonds ($f_b=1-f_s$). i_s is the stock rate of return (yr^{-1}). i_b is the bond rate of

return(yr^{-1}). τ is the effective percentage of the investment paid to federal, state and local taxes. If the tax rate is 45%, the stock rate of return is 10 %/yr, the bond rate of return is 8 %/yr and 90% of the investment is owned by stocks, the discount rate would be 5 %/yr.

If the SFR overnight capital construction cost is “ $C_{\text{cap}}/(P \times \eta) = \$1,800/\text{kW}(\text{e})$ ” then the c_{cap} capital cost of electricity from Equation 7-6 is $\$0.0427/\text{kW}(\text{e})$.

Fuel Investment

A simplified discounting model, similar to that used by the MIT report, is used to address the levelized cost of electricity corresponding to the purchase of fuel. Fuel costs are discounted in a similar manner to how interest is accrued during the construction capital investment. However, instead of reflecting just the discount rate, which is essentially another way of expressing interest or the investor rate of return, a broader “carrying charge” definition is applied for fuel costs. For this discounting model, the carrying charge is considered to be the total cost of money, taxes and insurance on funds borrowed at the time a fuel service is purchased. This carrying charge is used to discount the cost from the time the service is purchased to the midpoint of the irradiation of the fuel in the reactor.

$$c_{\text{fuel}} = \frac{1000}{24} \times \frac{1}{\eta} \times \left(\sum_i M_i \hat{c}_i + \sum_i M_i \hat{c}_i \phi \Delta t \right) \quad (7-10)$$

Where: M_i is the mass of HM processed at stage i per megawatt-day of energy that that mass produces in the core (kgHM/MWD). \hat{c}_i is the cost of the service to process the material at stage i (\$/kgHM). ϕ is the carrying charge on the investment to purchase the service i , Δt is the discounting time elapsed from the moment the service is purchased to the mid-point of the fuel irradiation in the reactor (days). 1000/24 is the unit conversion required to convert megawatts to kilowatts and days into hours. η is the reactor plants thermal-to-electric efficiency.

The carrying charge may be determined by summing the discount rate, tax rate and insurance rate of the fuel. For simplicity, these values are assumed to total to 10 %/yr. This is also the value used in the MIT report. This “lumped” carrying charge method is slightly different from the way that fuel purchases have historically been discounted with the carrying charge. In many fuel purchase arrangements, the fuel purchase including carrying charge is amortized in step with fuel burnup until the fuel is fully amortized when it is discharged from the reactor. However, for a general and straight forward comparison of fuel costs between SFRs and LWRs, the “lumped” carrying charge analysis is used as was done by the MIT report.

Fuel Cycle Base Cases

The choice of reactor type (or types) and their relationship with recycling centers has been the focus of much scientific debate since the late 1990’s when it became apparent that a second repository would be likely needed if nuclear electric generation was to expand without reducing the volume of SNF. This debate has caused the DOE to change the naming acronym of its fuel cycle research activity four times since the late 1990’s when research restarted after the IFR program was terminated (e.g., Accelerator Transmutation of Waste (ATW), Advanced Accelerator Applications (AAA), Advanced Fuel Cycle Initiative (AFCI), Global Nuclear Energy Partnership). The timeline of these research activities are not always in series to each other. Currently, the AFCI and GNEP programs are a parallel effort.

Each of these programs was highly focused on a single reactor technology (i.e. Large accelerator driven systems, water moderated reactors, fast reactors and graphite reactors) to solve all of the problems of the once-through fuel cycle in a single tier. A tier is referred to as a stepping off point in the fuel cycle where one reactor type accepts, as fuel, the nuclear waste generated by another reactor type. Each of these reactor concepts, and the fuel technologies developed for waste incineration, has demonstrated transmutation strengths and drawbacks for

each individual isotope within the SNF. As discussed throughout this dissertation, transmutation is highly sensitive to the neutron energies and flux intensities in which the fuel is exposed. The elemental partitioning technologies developed under the envelope of the UREX+ process has been demonstrated as a viable technology for partitioning SNF into specialized waste streams for individualized transmutation options and/or disposal options. This enables the feasibility for heterogeneous arrangements within the fuel and/or reactor.

The following analyses will demonstrate how the above cost calculations are employed to re-produce some of the fuel cycle scenarios and conclusions addressed by the MIT and Harvard reports. Then the symbiotic two-tier fuel cycle, as described in Figure 1-8 and Figure 3-4, with a heterogeneous fleet of ABRs and AHFTRs is analyzed.

The MOX Fuel Cycle

The MIT report focuses primarily on the cost competitiveness between the once-through irradiation of LWR UOX versus recycling SNF to create LWR-MOX fuel. This pseudo-closed MOX fuel cycle assumes that the UOX fuel is irradiated in an LWR and then recycled to create MOX fuel for a second reactor-pass in a LWR and then disposed of as MOX-SNF. This scenario, which is currently in practice in Europe, Russia and Japan, is not truly closed because it only reprocesses the SNF once, which still creates spent fuel assemblies that require repository storage. Such a fuel cycle, where fuel is only recycled once before requiring direct disposal, is considered an open fuel cycle with a single-tier recycling scenario. In theory, because additional energy is extracted from the fuel by the second reactor pass, such a fuel cycle reduces the mass of SNF destined for repository storage per uranium mined. However, the front-end cost of reprocessing and fabricating plutonium bearing fuels has historically made the MOX fuel cycle more expensive than the UOX fuel cycle. Figure 7-1 shows the mass flow relationships of the open one-tier MOX fuel cycle.

For the following fuel cycle calculations, the fresh UOX fuel is assumed to have a uranium enrichment of 4.5 w/o and is irradiated to 50 MWD/kg during three 500 EFPD cycles in a standard 17x17 PWR fuel assembly. For these calculations, the coupled NEWT-ORIGEN code, TRITON, is used to perform the buildup/depletion calculations for LWR fuel. Also, the TRITON code was used to decay the fuel in the time elapsed from UOX-LWR discharge to MOX-LWR fueling.

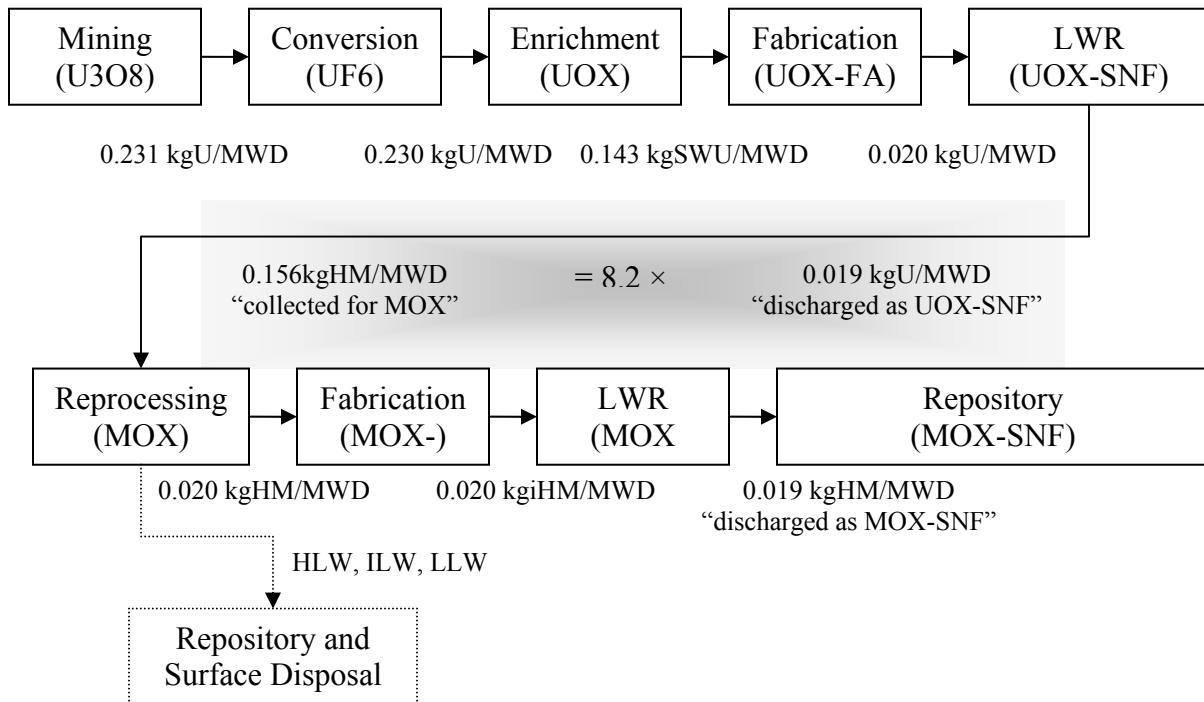


Figure 7-1. The open single-tier MOX fuel cycle

For this open single-tier fuel cycle, a theoretical Np+Pu-MOX is considered. Here, the Am+Cm+Bk+Cf stream is discarded as transuranic HLW and destined for the repository. This Np+Pu-MOX has a transuranic enrichment of 10% TRU per HM. The total fissile enrichment, including U-235, Pu-239 and Pu-241 is 6.8 w/o. Using the TRITON code, it was found that this composition could be irradiated for three 500 EFPD cycles to a burnup of 50 MWD/kg in a standard 17x17 PWR fuel assembly.

It is important to note the relatively large amount of UOX-SNF needed in order to produce a small amount of MOX. Performing a simple mass balance calculation shows that 8.2 times more SNF HM is needed at the MOX fuel cycle front-end than is produced per megawatt-day at the back-end of the UOX fuel cycle (Figure 7-1). Equivalently, roughly 8.2 UOX-SNF assemblies need to be reprocessed in order to create one Np+Pu-MOX assembly. The significance of this large front-end throughput becomes evident in the Np+Pu-MOX cost analysis. For the Np+Pu cost analysis, the following assumptions are made.

- Fresh UOX fuel enrichment: 4.5 w/o
- Uranium tails depletion: 0.3
- Process Losses: 1%
- LWR Fuel Burnup: 50 MWD/kg
- LWR Thermal Efficiency: 33%
- Reprocessed UOX-SNF uranium is used for the uranium in the Np+Pu-MOX

The unit costs for fuel cycle services and fees are listed in Table 7-1. Detailed descriptions of the background and assumptions of these unit costs are discussed earlier in this Chapter.

Using these assumptions and unit costs, the following fuel costs are calculated for the zero-tier or UOX-LWR component of the fuel cycle. These costs are tabulated in Table 7-2.

Table 7-1. Unit costs and fees for the open single-tier MOX fuel cycle

Item	Amount	Unit
Carrying Charge Rate: ϕ	10 %	--
Mined U	\$20.00	\$/lb U ₃ O ₈
Mined U	\$37.40	\$/kgU as U ₃ O ₈
Conversion	\$11.00	\$/kgU as UF ₆
Separative Work	\$145.00	\$/kg-SWU
Aqueous Reprocessing*	\$1,000.00	\$/kgHM Feed
HLW Disposal	\$300.00	\$/kgHM Feed
Fabrication UOX	\$250.00	\$/kgU Product
Fabrication MOX**	\$1,460.00	\$/kgHM Product
NWPA Levee	\$0.001	\$/kw-hr(e)
Interim Cask Storage	\$100.00	\$/kgHM Waste

*Note: For the Np+Pu-MOX it is assumed that no extra processing steps are required to extract a pure Am+Cm+Bk+Cf stream from fission product waste streams (e.g., UREX+2). **Note: Because Am+Cm+Bk+Cf is not involved in fuel fabrication, the requirement for a hot-cell facility is excluded and the cost of MOX fabrication is assumed to be performed in a glove-box operation at a cost of \$1,460/kgHM instead of \$2,500/kgHM].

Table 7-2. Fuel costs for the UOX-LWR tier, equivalently the once through fuel cycle

	\$/MWD	Sticker Price (\$/kgU)	Borrowing Time (Yr)	Carrying Charge (\$/kgU)
Mining & Milling	\$7.18	\$360.55	4.25	\$153.23
Conversion	\$2.10	\$105.53	4.25	\$44.85
Enrichment	\$16.35	\$821.60	3.25	\$267.02
UOX Fabrication	\$4.98	\$250.00	2.75	\$68.75
NWPA Levee	\$8.16	\$410.04	-2.25	-\$92.26
Interim Cask Storage	\$1.89	\$94.76	-2.25	-\$21.32

Combining the sticker price and carrying charges of the fuel purchase gives a total fuel cost of \$2,463/kgU. Dividing by the fuel burnup of 50 MWD/kg gives a fuel cost of electricity of \$0.0062/kW-hr(e). Repeating this calculation for the Np+Pu MOX-LWR tier gives the following fuel cycle costs shown in Table 7-3.

Table 7-3. Fuel costs for the MOX-LWR tier of the open single-tier MOX fuel cycle

	\$/MWD	Sticker Price (\$/kgiHM)	Borrowing Time (Yr)	Carrying Charge (\$/kgiHM)
Credit for UOX-SNF	-\$78.50	-\$3,944.84	4.25	-\$1,676.56
UREX+2	\$155.52	\$7,814.71	4.25	\$3,321.25
HLW Disposal	\$46.66	\$2,344.41	3.25	\$761.93
MOX Fabrication	\$29.35	\$1,474.60	3.25	\$479.25
NWPA Levee	\$8.16	\$410.04	-2.25	-\$92.26
Interim Cask Storage	\$0.00	\$0.00	-2.25	\$0.00

Combining the sticker price and carrying charge of the fuel purchase gives a total fuel cost of \$10,892/kgiHM. Dividing by the fuel burnup of 50 MWD/kgiHM gives a fuel cost of electricity of \$0.027/kW-hr(e). Therefore, the fuel cost of producing Np+Pu-MOX electricity is more than four times the cost of UOX electricity. The much higher Np+Pu-MOX cost is primarily due to the large sticker price ($\$155.52/\text{MWD} \equiv \$7,814.71/\text{kgiHM} \div 50 \text{ MWD}/\text{kgiHM}$) of reprocessing, which is a result of the reprocessing plants large HM throughput (0.156 kgiHM/MWD) and the price of reprocessing (\$1000/kg).

Notice the influence of the UOX-SNF credit. This is the fee that the UOX utility pays to the aqueous reprocessing company for assuming responsibility for the UOX-SNF. It is equivalent to the cost of interim storage at the aqueous reprocessing plant plus the NWPA levee

imposed on the UOX-SNF. Because, the aqueous reprocessing company assumes responsibility, it has the option of charging a removal fee equal to what the DOE would have charged to store the SNF in a repository. Also because the aqueous reprocessing company is providing the interim storage service as part of its regular operations, the reprocessing plant stores the dry storage casks and passes this cost along to the UOX-LWR utility. These credits are a significant source of income to the aqueous reprocessing company and alleviate some of the reprocessing cost. However, these credits are not sufficient to offset the total cost of reprocessing and the fuel fabrication cost. Note that the cost of MOX fabrication is more than five times as high as UOX fabrication.

It is an interesting finding of the MIT report, that because of the UOX-SNF credit, if the NWPA levee would have been set at approximately 3.0 mil/kW-hr(e), the fuel cost of MOX would be less than for UOX. In the calculations in Table 7-3, the 3.0 mil/kW-hr(e) would increase the UOX fuel cost to \$0.0078/kW-hr(e) and reduce the Np+Pu-MOX fuel cost to \$0.0060/kW-hr(e).

The ABR Fuel Cycle

The Harvard report offers a comparison of the once-through LWR fuel cycle with a SFR closed fuel cycle. Because the Harvard report considers the recycling of SFF, the system analyzed by the report is considered a truly closed fuel cycle. In such a fuel cycle, all fuel is recovered by reprocessing and only the HLWs due to fission product and/or MA separation requires a long term disposal solution. The Harvard report only considered SFRs with a conversion ratio equal to one or higher. Therefore, the only reprocessing cost considered was that for SFF. However for the ABR, two types of reprocessing plants are required: an aqueous facility for SNF and a pyroprocess facility for SFF. Therefore, the aqueous reprocessing cost associated with a continuous external supply of SNF TRU to the ABR must be considered.

Because ABRs, in this scenario, are the final destination of the TRU produced by LWRs, the ABR fuel cycle is considered closed with a single tier. Figure 7-2 shows the mass flow relationships of the closed one-tier ABR fuel cycle.

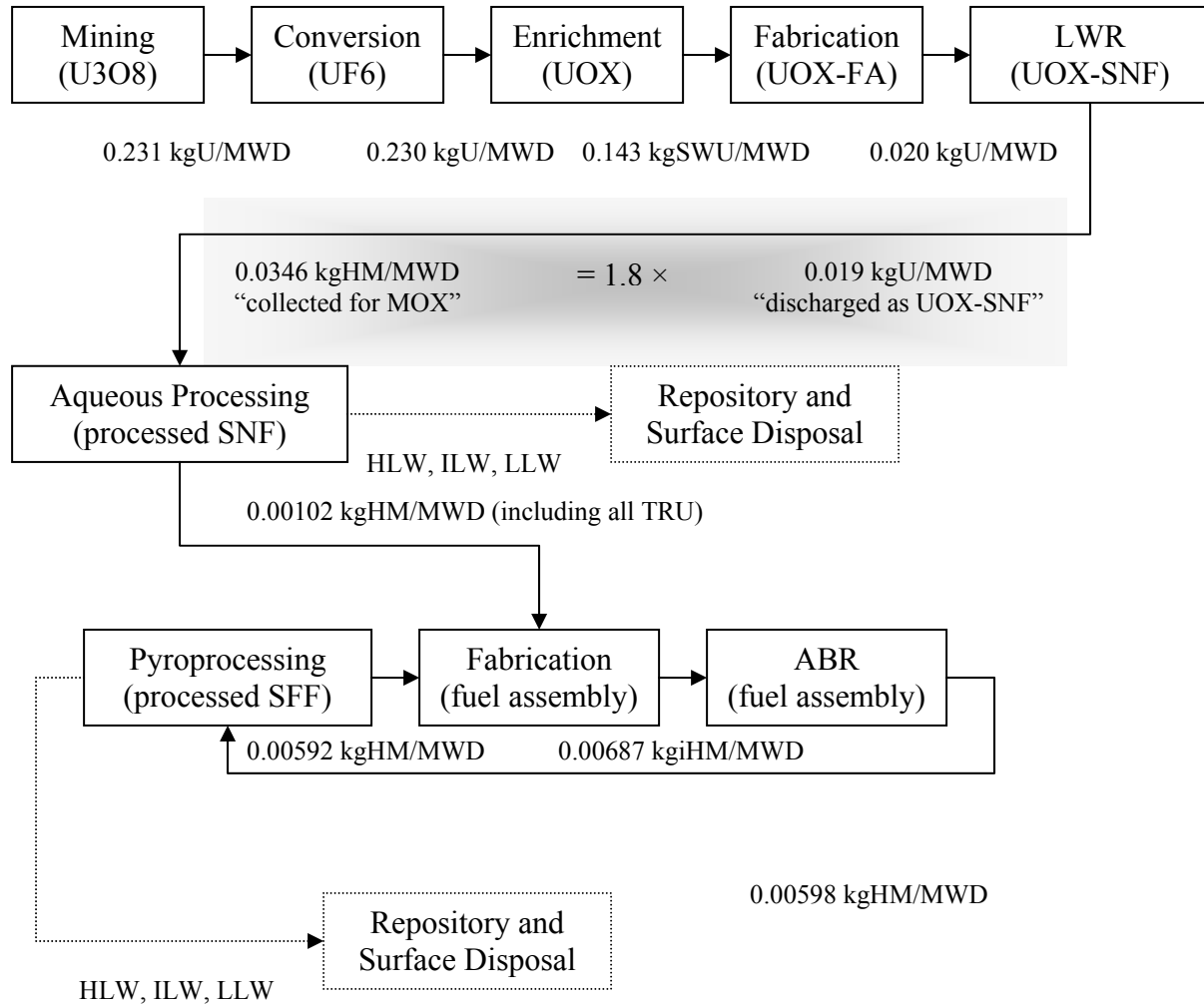


Figure 7-2. The closed single-tier ABR fuel cycle

Performing the mass balance calculation shows that only 1.8 times more SNF HM is needed at the ABR fuel cycle front-end than is produced per megawatt-day at the back-end of the UOX fuel cycle. For the ABR cost analysis, the following additional assumptions are made.

- All TRU, including Np+Pu+Am+Cm, is recycled at both reprocessing plants
- Metal fueled ABR with $\gamma_{CR}=0.5$
- Average ABR Fuel Burnup: 135 MWD/kgiHM
- ABR Thermal Efficiency: 37%

- Reprocessed UOX-SNF transuranics are used for the make-up TRU to the ABR
- Reprocessed UOX-SNF uranium is used for the make-up uranium to the ABR

The unit costs for the ABR fuel cycle services and fees for the closed single-tier fuel cycle are listed in Table 7-4. Using these assumptions and unit costs, the following fuel costs are calculated for the ABR tier of the fuel cycle. These costs are tabulated in Table 7-5.

Table 7-4. Unit costs and fees for the closed single-tier ABR fuel cycle

Item	Amount	Unit
Aqueous reprocessing	\$1,500.00	\$/kgHM Feed
Pyroprocessing	\$3,000.00	\$/kgHM Feed
HLW Disposal*	\$275.00	\$/kgHM Feed
Fabrication ABR	\$2,500.00	\$/kgHM Product

*Note: Since Am+Cm+Bk+Cf are not present in large quantities in the HLW, it may be assumed that vitrified HLW will not require deep geologic repository storage and could be stored in a surface repository at a cost of \$275/kgHM instead of \$300/kgHM

Table 7-5. Fuel costs for the ABR tier of the closed single-tier ABR fuel cycle

	\$/MWD	Sticker Price (\$/kgiHM)	Borrowing Time (Yr)	Carrying Charge (\$/kgiHM)
Credit for UOX SNF	-\$17.47	-\$2,340.62	3.74	-\$875.39
UREX+1a	\$51.90	\$6,955.14	3.74	\$2,601.22
Pyroprocess	\$17.94	\$2,404.30	3.74	\$899.21
HLW Disposal-Aqueous	\$9.52	\$1,275.11	3.74	\$476.89
HLW Disposal-Pyro	\$1.64	\$220.39	2.86	\$63.03
ABR Fabrication*	\$2.54	\$340.17	2.86	\$97.29
ABR Fabrication**	\$14.80	\$1,983.55	2.86	\$567.29
NWPA Levee	\$8.16	\$1,093.44	2.86	\$312.72

*Aside: Cost of fuel fabrication corresponding to the HM taken from SNF, **Aside: Cost of fuel fabrication corresponding to the HM taken from SFF.

Combining the sticker price and carrying charge of the fuel purchase gives a total fuel cost of \$16,073/kgiHM. Dividing by the fuel burnup of 135 MWD/kgiHM gives a fuel cost of electricity of \$0.014/kW-hr(e). Therefore, the ABRs fuel contribution to the cost of electricity is a little more than two times the fuel cost of UOX electricity and about one-half the fuel cost of MOX electricity. Similar to MOX, the cost of reprocessing SNF is principally responsible for the higher ABR fuel cost. However, the ABR can achieve 2.7 times the fuel burnup of the Np+Pu-MOX case. Therefore, even though the ABR fuel is about 1.5 times more expensive per

mass of fuel purchased than the Np+Pu-MOX it extracts more fission energy per fuel purchased. However, this higher energy extraction per mass of fuel purchased is still not sufficient to reduce the ABR fuel cost to less than that of the once-through UOX fuel cycle.

The Combined AHFTR and ABR Fuel Cycle

The AHFTR has essentially two fuel suppliers. It receives an external make-up supply of Np+Pu for supplementing the mass exhausted by fission in each cycle. It also receives an external make-up supply of Am+Cm+Bk+Cf for fabricating fresh targets. Both of these mass flows have origins in LWR SNF. However, the AHFTR receives a greater proportion of Am+Cm+Bk+Cf per total transuranic mass than exists in the initial SNF. This extra material is being diverted from ABRs which are receiving only Np+Pu based fuel. If the Am+Cm+Bk+Cf mass flow were not diverted to the AHFTR, it would be considered as part of the HLW stream created by the aqueous recycling center. Hence it would require a long term disposal solution and add to the HLW disposal cost. Conversely, if either the AHFTRs or ABRs accept this Am+Cm+Bk+Cf mass stream as part of its fuel, then the MA contribution of the HLW cost is avoided. However, the purpose of the AHFTR concept is to accept this unwanted material in order to alleviate material handling expenses for the ABR. Because, the AHFTR provides this service to the ABRs as well as consuming Np+Pu from LWRs, its fuel cycle is considered closed but having a two-tier recycling scenario. Figure 7-3 shows the mass flow relationships of the closed two-tier AHFTR fuel cycle.

Performing the mass balance calculation shows that only 0.63 kg of SNF is needed to produce one kg of fuel at the front-end of the AHFTR fuel cycle. The larger reprocessed fuel output than the SNF input is due to the contribution of MAs provided by the SNF partitioned for the ABR's fuel. This property of the AHFTR fuel cycle will be used to quantify the fuel savings afforded by recycling Am+Cm+Bk+Cf in the AHFTR as opposed to the ABR.

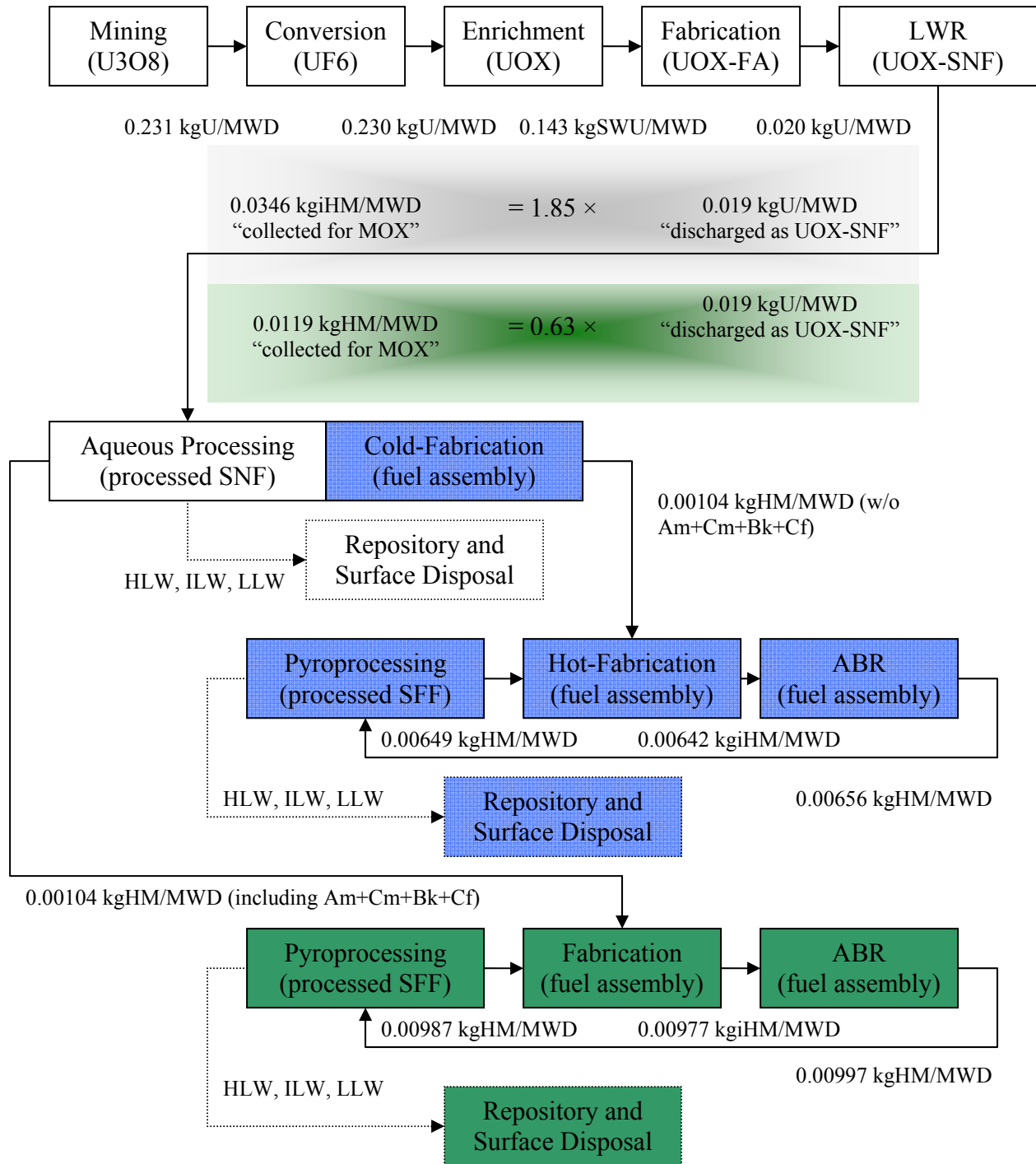


Figure 7-3. The closed double-tier AHFTR fuel cycle

It is important to note that the external supply of HM is identical for both the ABR and the AHFTR (0.00104 kgHM/MWD). These external feeds demonstrate the fact that one gram of HM is converted by fission into one MWD of energy. When the fuel cycle is evaluated from a

pure mass flow perspective, as it is shown in Figure 7-3, it is apparent that it is irrelevant whether or not this material is all plutonium, all MAs, all uranium or a mix in-between.

The rate that HM is discharged from the core and returned to the pyroprocessor is determined by how massive the core is and also the refueling rate. The AHFTR and ABR have approximately the same cycle length and batch-fraction. Therefore, the refueling rate is about the same (Table 3-13). However, the AHFTR has a HM mass approximately 1.3 times that of the ABR (Table 3-12). The larger core, explains the larger mass flow rate through the AHFTR pyroprocessor. For the AHFTR cost analysis, the following additional assumptions are made.

- The ABR and AHFTR draw HM from an infinite SNF reservoir at their own independent rates
- The external supply of TRU from the aqueous reprocessing plant, which is destined for ABR and AHFTR driver fuels, is only Np+Pu.
- All Am+Cm+Bk+Cf separated from SNF is diverted from HLW and sent to the AHFTR for target fabrication.
- Some of the ABR driver fuel can be fabricated in a glove-box facility collocated at the aqueous reprocessing plant using the Np+Pu separated from SNF.
- Metal fuel AHFTR with $t_{CR}=0.7$
- Average AHFTR Fuel Burnup: 93 MWD/kgiHM
- AHFTR Thermal Efficiency: 37%

The unit costs for the ABR component of the closed double-tier AHFTR fuel cycle services and fees are listed in Table 7-6. Using these assumptions and unit costs, the following fuel costs are calculated for the ABR tier of the fuel cycle. The ABR costs are tabulated in Table 7-7.

Combining the sticker price and carrying charge of the fuel purchase gives a total fuel cost of \$16,821/kgiHM. Dividing by the fuel burnup of 135 MWD/kgiHM gives a fuel cost of

electricity of \$0.014/kW-hr(e). As one recalls, the ABR fuel cost of electricity with Am+Cm+Bk+Cf in the driver fuel, was also \$0.014/kW-hr(e).

Table 7-6. Unit costs and fees for the closed double-tier AHFTR fuel cycle

Item	Amount	Unit
Aqueous reprocessing	\$1,500.00	\$/kgHM Feed
Pyroprocessing	\$3,000.00	\$/kgHM Feed
HLW Disposal	\$275.00	\$/kgHM Feed
Fabrication ABR – Cold Handling	\$1,500.00	\$/kgHM Product
Fabrication ABR – Hot Handling	\$2,500.00	\$/kgHM Product
Fabrication AHFTR	\$2,500.00	\$/kgHM Product

Table 7-7. Fuel costs for the ABR tier of the closed double-tier AHFTR fuel cycle

	\$/MWD	Sticker Price (\$/kgiHM)	Borrowing Time (Yr)	Carrying Charge (\$/kgiHM)
Credit for UOX SNF	-\$17.78	-\$2,384.83	3.74	-\$891.92
UREX+3	\$52.83	\$7,086.50	3.74	\$2,650.35
Pyroprocessing	\$19.67	\$2,637.87	3.74	\$986.56
HLW Disposal-Aqueous	\$10.57	\$1,417.30	3.74	\$530.07
HLW Disposal-Pyro	\$1.82	\$243.73	2.86	\$69.71
ABR Fabrication*	\$1.56	\$209.38	2.86	\$59.88
ABR Fabrication**	\$16.22	\$2,176.25	2.86	\$622.41
NWPA Levee	\$8.16	\$1,094.51	2.86	\$313.03

*Aside: Cost of fuel fabrication corresponding to the HM taken from SNF (assuming a glove-box facility for cold-fuel handling), **Aside: Cost of fuel fabrication corresponding to the HM taken from SFF (assuming a hot-cell facility for hot-fuel handling)

Therefore, reduction in the fuel fabrication costs using the glove-box facility had negligible impact on the fuel cost of electricity. This result indicates that the ABR fuel cost is fairly insensitive to whether or not some of it can be fabricated at the centrally located aqueous reprocessing plant. The negligible cost savings is a direct result of most of the HM being pyroprocessed as SFF at the electrorefinery. Repeating this calculation for the AHFTR tier gives the following fuel cycle costs. The AHFTR fuel costs are shown in Table 7-8.

Combining the sticker price and carrying charge of the fuel purchase gives a total fuel cost of \$8,529/kgiHM. Dividing by the fuel burnup of 93 MWD/kgiHM gives a fuel cost of electricity of \$0.0104/kW-hr(e). Therefore, the fuel cost of the AHFTR is only 1.6 times the fuel cost of UOX electricity and is 73% of the fuel cost of the ABR. The reason for the cheaper

AHFTR fuel cost is the credit that the AHFTR receives for taking responsibility for the separated Am+Cm+Bk+Cf from the aqueous reprocessing company. Similar to the closed single-tier ABR case, the assumption is made that the cost of HLW disposal can be reduced if none of the SNF transuranic wastes, with the exception of small process losses, require geologic repository disposal.

Table 7-8. Fuel costs for the AHFTR tier of the closed double-tier AHFTR fuel cycle

	\$/MWD	Sticker Price (\$/kgHM)	Borrowing Time (Yr)	Carrying Charge (\$/kgHM)
Credit for UOX SNF	-\$6.00	-\$555.73	3.74	-\$207.84
Credit for ABR HLW	-\$13.70	-\$1,269.28	3.74	-\$474.71
UREX+3	\$17.83	\$1,651.35	3.74	\$617.60
Pyroprocessing	\$29.91	\$2,770.15	3.74	\$1,036.04
HLW Disposal-Aqueous	\$3.27	\$302.75	3.74	\$113.23
HLW Disposal-Pryo	\$2.74	\$253.93	2.86	\$72.62
AHFTR Fabrication*	\$2.59	\$239.86	2.86	\$68.60
AHFTR Fabrication**	\$24.67	\$2,285.37	2.86	\$653.62
NWPA Levee	\$8.16	\$755.87	2.86	\$216.18

*Aside: Cost of fuel fabrication corresponding to the HM taken from SNF (assuming a hot-cell facility for hot-fuel handling), **Aside: Cost of fuel fabrication corresponding to the HM taken from SFF (assuming a hot-cell facility for hot-fuel handling)

Also, the AHFTR has a smaller aqueous reprocessing cost than the ABR because the AHFTR draws less fuel from SNF for its external feed rate than the ABR (0.63 versus 1.85 in Figure 7-3, also see Table 3-14). The AHFTR requires less externally supplied make-up TRU from SNF because, it receives an additional mass stream from the pyroprocessor which would not be available if MAs were not diverted from the HLW and irradiated in targets.

The ABR in the closed double-tier case is being charged for the HLW disposal because it is not assuming responsibility for the Am+Cm+Bk+Cf wastes generated in the front end of its fuel cycle. The AHFTR receives a credit ($\$300/\text{kg} - \$275/\text{kg} = \$25/\text{kg}$) for taking these wastes. This credit is equal to the difference in the cost to dispose of the Am+Cm+Bk+Cf stream in the HLW waste ($\$300/\text{kgHM}$) and the disposal fee without Am+Cm+Bk+Cf ($\$275/\text{kgHM}$). This

credit combined with the UOX-SNF credit fully compensates for the cost of aqueous reprocessing.

The assumption that the HLW disposal fee can be reduced from \$300/kgHM to \$275/kgHM is not sufficient to reduce the AHFTR fuel cost to below the cost of the once-through fuel cycle. However, assuming that a new HLW disposal fee of \$225/kgHM can be achieved if all the MAs are eliminated from the HLW mass stream, the fuel cost of electricity for the AHFTR becomes equivalent to the fuel cost of UOX-LWRs.

Sensitivity Analysis

Though it is apparent that the HLW disposal fee can be arbitrarily adjusted to make, the AHFTR fuel costs comparable to UOX-LWR fuel costs, the overall closed two-tier fuel cycle at this stage in the analysis is not cost competitive to one-through. This is because the majority of the SFRs in the fast reactor fleet are ABRs with a non-competitive fuel cost. Therefore, a comparative analysis is needed to show how much fuel cycle unit costs need to change in order to make the overall closed two-tier fuel cycle cost competitive. First, the cost of uranium ore, conversion, enrichment and UOX fabrication will be adjusted to raise the once-through fuel cost to meet the ABR or AHFTR fuel cost. Next, the cost of aqueous reprocessing, pyroprocessing, HLW disposal and hot-fuel fabrication will be adjusted to lower the ABR and AHFTR fuel costs to the breakeven point with the once-through cost. Finally, a theoretical SFR utility operating a mix of ABRs and AHFTRs is evaluated to see what conditions need to apply in order to make the average cost of fuel to the utility equivalent to the once-through cost.

Breakeven Unit Costs for ABRs and AHFTRs

The breakeven fuel costs are calculated by holding all values of the above three base cases constant and evaluating the perturbation of each individual unit cost required to equate the overall fuel cost of electricity between the once-through and closed two-tier fuel cycle. This is

done by increasing the fuel cycle service costs of the once-through fuel cycle until the once-through option is as costly as the closed two-tier base case calculation. Conversely, the unit costs of reprocessing, HLW disposal and fuel fabrication can be reduced until the fuel costs of the closed two-tier option is as cheap as the once-through base case.

Table 7-9 shows the breakeven unit costs necessary to equate the ABR fuel costs to the UOX-LWR once-through fuel cycle or visa versa. The negative unit costs indicate that it is physically impossible to equate the fuel costs unless an external additional cash flow “fringe benefit” of revenue could be created by the given process in addition to the fuel cycle service provided by that process. Obviously, these cash flows do not exist in reality but are simply a numerical artifact of the unit cost perturbation. It is interesting to note that the cost of uranium would have to increase to \$143/lb of U_3O_8 in order to make fuel recycling in an ABR an attractive fuel cycle alternative to the once-through UOX-LWR fuel cycle. Coincidentally, the Uranium Exchange Consulting Company (UxC) quoted the price of uranium to be \$135/lb U_3O_8 in the summer of 2007. The UxC is an industry recognized uranium fuel cycle consulting company that continuously publishes the current market price for fuel cycle services including uranium ore, conversion and enrichment.

The breakeven unit costs necessary to equate the AHFTR fuel costs to the UOX-LWR once-through fuel cycle, or visa versa, is shown in Table 7-10. Remember, the AHFTR receives a credit that is equivalent to some fraction of the market HLW disposal costs which represents the money saved by the aqueous reprocessing company from not having to dispose Am+Cm+Bk+Cf transuranic waste. It is assumed that because pyroprocessing does not allow for removal of Am+Cm+Bk+Cf, the pyroprocessor HLW disposal cost is also equal to the reduced value of this cost. Therefore, the breakeven unit cost of the pyroprocessor’s HLW

disposal fee in Table 7-10 is equivalent to the reduced value of the HLW disposal fee extended to both aqueous reprocessor and pyroprocessor for not having to dispose of Am+Cm+Bk+Cf transuranic waste.

Table 7-9. Breakeven unit costs for equating the once-through fuel cost of electricity to that of the ABR in the closed two-tier fuel cycle

Fuel Service	Base Case Unit Cost	Breakeven Unit Cost	Unit
UOX-LWR Fuel Service Costs Increased/ABR Fuel Service Costs Held Constant			
Mined Uranium	\$20	\$143	\$/lb U ₃ O ₈
Conversion	\$11	\$242	\$/kgU as UF ₆
Separative Work	\$145	\$566	\$/kg-SWU
Fabrication UOX	\$250	\$2,727	\$/kgU Product
NWPA Levee	\$0.001	\$0.005	\$/kw-hr(e)
Interim Cask Storage	\$100	\$1,232	\$/kgHM Waste
ABR Fuel Service Costs Decreased/UOX LWR Fuel Service Costs Held Constant			
Aqueous Reprocessing	\$1,500	\$44	\$/kgHM Feed
Pyroprocessing	\$3,000	-\$4,822	\$/kgHM Feed
HLW Disposal (Pyro)*	\$275	-\$8,080	\$/kgHM Feed
HLW Disposal ABR (Aqueous)*	\$300	-\$1,156	\$/kgHM Feed
Fabrication - Cold Handling	\$1,500	-\$51,144	\$/kgHM Product
Fabrication -Hot Handling	\$2,500	-\$5,942	\$/kgHM Product

*Note: The aqueous process HLW disposal fee is higher than the pyroprocessing fee because in this scenario the ABR does not take responsibility for the Am+Cm+Bk+Cf forcing the reprocessing company to either dispose of it or pay for its incineration in an AHFTR.

Table 7-10. Breakeven unit costs for equating the once-through fuel cost of electricity to that of the AHFTR in the closed two-tier fuel cycle

Fuel Service	Base Case Unit Cost	Breakeven Unit Cost	Unit
UOX-LWR Fuel Service Costs Increased/AHFTR Fuel Service Costs Held Constant			
Mined Uranium	\$20	\$84.78	\$/lb U ₃ O ₈
Conversion	\$11	\$132.73	\$/kgU as UF ₆
Separative Work	\$145	\$366.66	\$/kg-SWU
Fabrication UOX	\$250	\$1,555.20	\$/kgU Product
NWPA Levee	\$0.001	\$0.012	\$/kw-hr(e)
Interim Cask Storage	\$100	\$1,265.49	\$/kgHM Waste
AHFTR Fuel Service Costs Decreased/UOX LWR Fuel Service Costs Held Constant			
Aqueous Reprocessing	\$1,500	-\$878.68	\$/kgHM Feed
Pyroprocessing	\$3,000	\$164.03	\$/kgHM Feed
HLW Disposal (Pyro)	\$275	\$227.53	\$/kgHM Feed
HLW Disposal ABR (Aqueous)	\$300	\$349.30	\$/kgHM Feed
Fabrication -Hot Handling	\$2,500	-\$147.84	\$/kgHM Product

Notice that this (Am+Cm+Bk+Cf free) (free) HLW disposal cost only needs to be less than one third of the currently estimated HLW disposal fee in order to make the AHFTR cost

competitive with the once-through UOX-LWR fuel cycle. Also it is noteworthy to point out that the cost of uranium ore required to make the once-through fuel costs as expensive as the AHFTR fuel costs is only \$85/lb U_3O_8 . The UxC quoted price of uranium ore was \$90/lb U_3O_8 in the December of 2007 at the time that this dissertation was being written.

It has been shown that the cost of uranium or the HLW disposal fee can be arbitrarily altered to show the cost competitiveness of either the ABR or the AHFTR independently. However, in reality the closed two-tier fuel cycle is intended to allow these two reactor types to operate in parallel. Therefore, it is necessary to determine the support ratio of AHFTRs needed to burn all of the Am+Cm+Bk+Cf produced by the aqueous reprocessing plant in support of both reactors.

The ABR requires the separation of 0.0352 kg SNF/MWD of SNF in order to produce the Np+Pu needed to satisfy the external feed demand of its driver fuel. In order to meet the Am+Cm+Bk+Cf external feed requirements of the targets, the AHFTR requires the separation of 0.1160 kgHM/MWD of SNF in addition to the SNF separation requirements of its driver fuel (0.0119 kg SNF/MWD). The ratio of the AHFTR processing demand on SNF to get the Am+Cm+Bk+Cf from ABRs over the rate that Am+Cm+Bk+Cf can be produced by the ABR reprocessing demand is effectively the support ratio of ABRs to AHFTRs in the fast reactor fleet. Hence, a support ratio (ABR per AHFTR $\equiv 0.1160/0.0352 = 3.3$) is required to burn, in AHFTRs, all of the Am+Cm+Bk+Cf separated at the aqueous reprocessing plant.

Using this support ratio, a utility is envisioned that operates a fleet of SFRs with one AHFTR for every 3.3 ABRs. In order to evaluate the cost competitiveness of the SFR utility, the average fuel cost between the ABRs and AHFTRs is evaluated, as opposed to evaluating for each

reactor type individually. The breakeven unit costs necessary to equate the utility's average fuel costs to the UOX-LWR once-through fuel cycle, or visa versa, is shown in Table 7-11.

Table 7-11. Breakeven unit costs for equating the once-through fuel cost of electricity to that of the average fuel cost of a combined fleet of ABRs and AHFTRs

Fuel Service	Base Case Unit Cost	Breakeven Unit Cost	Unit
UOX-LWR Fuel Service Costs Increased/Combined Fleet Fuel Service Costs Held Constant			
Mined Uranium	\$20	\$129	\$/lb U ₃ O ₈
Conversion	\$11	\$217	\$/kgU as UF ₆
Separative Work	\$145	\$519	\$/kg-SWU
Fabrication UOX	\$250	\$2,454	\$/kgU Product
NWPA Levee	\$0.001	\$0.006	\$/kw-hr(e)
Interim Cask Storage	\$100	\$1,236	\$/kgHM Waste
Combined Fleet Fuel Service Costs Decreased/UOX LWR Fuel Service Costs Held Constant			
Aqueous Reprocessing	\$1,500	-\$42	\$/kgHM Feed
Pyroprocessing	\$3,000	-\$3,247	\$/kgHM Feed
HLW Disposal (Pyro)	\$275	-\$69	\$/kgHM Feed
HLW Disposal ABR (Aqueous)	\$300	\$753	\$/kgHM Feed
Fabrication -Hot Handling	\$2,500	-\$3,985	\$/kgHM Product

It is apparent from Table 7-11 that the cost of uranium must reach \$130/lb U₃O₈ in order for the overall closed two-tier fuel cycle to reach cost competitiveness with the once-through UOX-LWR fuel cycle. It is also interesting to note that if the cost of uranium is only \$20/lb U₃O₈ then the HLW disposal credit will not be sufficient to achieve cost competitiveness. This is specified by the negative HLW disposal fee of a transuranic free HLW stream (i.e., equivalently the pyroprocessing HLW disposal fee). However if the cost of the once-through fuel cycle was slightly more expensive as a result of a higher uranium ore cost, then a HLW disposal credit might be found that could reduce the average SFR fuel cost to meet the higher once-through fuel cost.

Cost Sensitivities for a Combined ABR and AHFTR Fleet

In this section, a SFR utility is envisioned that operates a mix of ABRs and AHFTRs in order to burn the TRU generated by the UOX-LWR fleet. Based on the mass flows from Table 3-14, the support ratio (normalized per megawatt of installed reactor capacity) between ABRs, AHFTRs and LWRs is:

- 3.3 ABRs per AHFTR
- 0.6 SFRs per LWR

In order to make it more likely that the SFR fleet becomes cost competitive with the UOX-LWRs, the cost for the price of uranium is set to \$80/lb U_3O_8 as opposed to \$20/lb U_3O_8 . The higher uranium price increases the once-through UOX-LWR fuel cost of electricity to \$0.01/kW-hr(e). Next, a sensitivity analysis is conducted on the SFR utility where the unit cost of aqueous reprocessing and pyroprocessing is each individually varied from \$1,000/kgHM to \$3,000/kgHM. For each of these perturbations, the “transuranic-free” HLW disposal cost is adjusted until the average fuel cost to the SFR utility becomes equal to the \$0.01/kW-hr(e) fuel cost of the once-through UOX-LWR fuel cycle.

Figure 7-4 shows the ABR and AHFTR fuel costs for this breakeven scenario. Notice that the fuel costs for the ABR increase with increasing reprocessing cost. This trend is affected by the fact that the ABR is held accountable for MAs that it does not burn. Therefore, the ABR’s fuel cost does not receive the HLW disposal credit and must effectively reimburse the aqueous reprocessing company the full market price (\$300/kgHM) of transuranic HLW disposal. The fuel cost increases almost linearly because the aqueous reprocessing unit cost contribution to the total fuel cost is being linearly increased from \$1,000 to \$2,000.

The ABR and AHFTR fuel costs for a varying pyroprocessing costs are given in Figure 7-5. It is important to note that the ABR fuel cost is more sensitive to the cost of aqueous reprocessing than it is to pyroprocessing. This is because of the much higher SNF HM throughput to the aqueous reprocessing plant (0.0346 kgHM/MWD) than the pyroprocessor (0.00656 kgHM/MWD) (Figure 7-3). The higher throughput of the aqueous plant is due to the TRU content of SNF being so much less than that of SFF. Even though the cost of

pyroprocessing can be twice as high as aqueous reprocessing, the large aqueous plant throughput causes it to be much more sensitive to the cost of reprocessing.

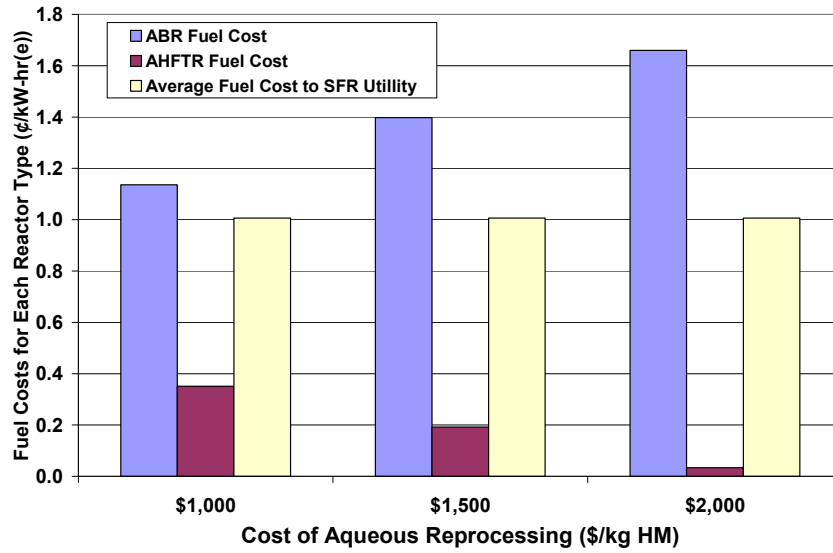


Figure 7-4. Fuel cycle costs for the ABR and AHFTR for varying costs of aqueous reprocessing adjusted by the HLW disposal credit for a breakeven average fuel cost

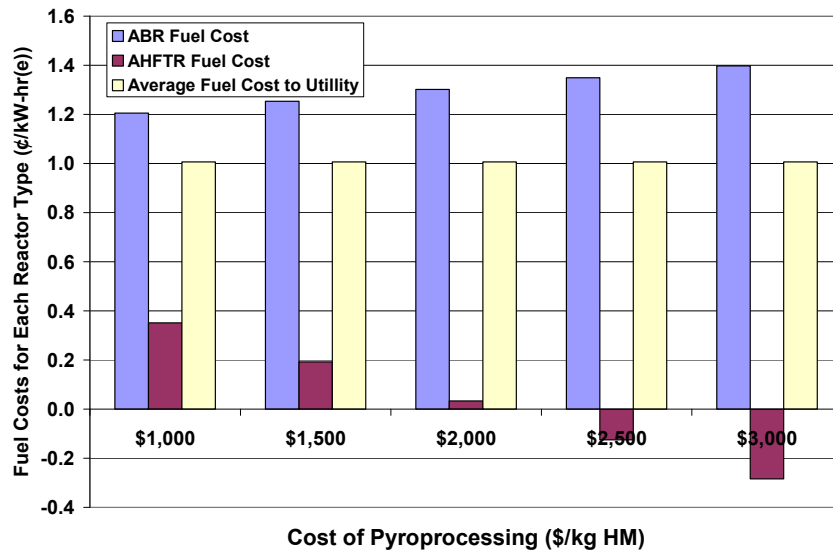


Figure 7-5. Fuel cycle costs for the ABR and AHFTR for varying costs of pyroprocessing adjusted by the HLW disposal credit for a breakeven fuel cost

The negative fuel cost for the AHFTR corresponds to a HLW disposal credit that becomes large enough to pay for all of the AHFTR fuel costs and eventually debits back to the SFR utility

some of the fuel expenditures paid on the ABR fuel. Figure 4-15 shows the impact of the perceived price versus cost of HLW disposal.

Note that if the actual cost of HLW disposal is not at all dependent on the presence of transuranic waste than it can not be varied as it is done in this study. This would be the case if deep geologic disposal is required for HLW even if $A_m+C_m+B_k+C_f$ are not present in the waste. However, if the $A_m+C_m+B_k+C_f$ is a large cost driver then its removal could greatly reduce the cost of HLW disposal. This may be the case if the cost of surface disposal of HLW is possible and this disposal is significantly cheaper than putting this waste in a deep geologic repository. If it is possible to have a HLW disposal fee so small that the closed fuel cycle is cheaper than the once-through fuel cycle, then the reprocessing company has the option to charge the most expensive market price for fuel services of the once-through competition. Therefore, the HLW disposal fee is used in Figure 7-5 to control the market expense or debit of AHFTR fuel in order to make the average fuel cost to the SFR utility equivalent to the once-through fuel cycle.

Figure 7-6 gives the transuranic-free HLW disposal fee as a function of the varying unit costs of reprocessing. These values are used to calculate the HLW disposal credit necessary to create the fuel costs of Figure 7-4 and Figure 7-5. The resulting HLW disposal credit is calculated in the same way as was done in Table 7-8. This credit is equal to the current market price (\$300/kgHM) minus the transuranic-free price from Figure 7-6.

The reason that the aqueous reprocessing cost in Figure 7-4 stops at \$2,000/kgHM is because the transuranic-free HLW disposal fee drops to zero below this value. Hence, the cost saving afforded by a reduced HLW disposal cost is insufficient to force the fuel cycle to become

cost competitive with the once-through fuel cycle if the aqueous reprocessing cost rises above \$2,000/kgHM.

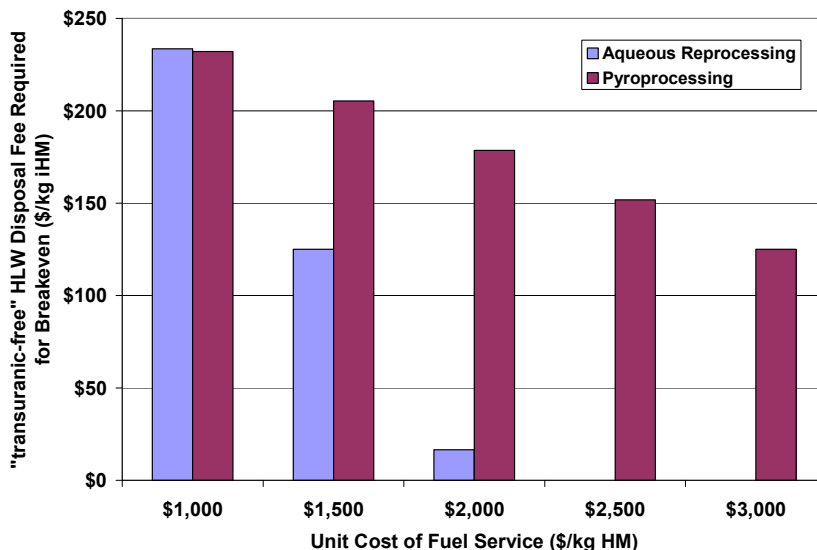


Figure 7-6. Transuranic-free HLW disposal fee adjusted until the fuel cost breakeven occurs for varying costs of reprocessing

It is apparent from Figure 7-5 and Figure 7-6 that even if the cost of pyroprocessing is as high as \$3,000/kgHM, the mixed-fleet fuel cycle can become cost competitive if the transuranic-free HLW disposal cost can be reduced to \$125/kgHM. Therefore, if the unit costs from Table 7-1, Table 7-4 and Table 7-6 are adopted, but with a \$80/lb U_3O_8 uranium ore price and a \$125/kgHM HLW disposal fee, then the SFR mixed-fleet utility will be cost competitive to the once-through fuel cycle.

Converting Neutrons into Dollars

If the mixed-fleet scenario from the previous section is considered with a \$125/kgHM HLW disposal fee and a \$80/lb U_3O_8 ore price with all other unit costs the same as in Table 7-1, Table 7-4 and Table 7-6, then the fuel costs to the ABR and AHFTR will be \$0.0140/kW-hr(e) and -\$0.0024/kW-hr(e), respectively. Combining these costs with the 3.3 ABR per AHFTR support ratio gives an average fuel cost to the mixed-fleet utility of \$0.0101/kW-hr(e). This

\$0.0101/kW-hr(e) value is the cost of the once-through LWR fuel cycle assuming \$80/lb U₃O₈. Therefore, for these assumptions in unit costs, the mixed-fleet fuel cost breaks even with that of the once-through fuel cycle.

It is interesting to note that if the ABR (CR=0.5) of the closed single-tier fuel cycle is allowed to pay this cheaper HLW disposal fee, its fuel cost is reduced to only \$0.0139/kW-hr(e). In fact, using the \$125/kgHM HLW disposal assumption with all the other unit costs of Table 7-1 and Table 7-4, the breakeven price of uranium would be approximately \$125/lb U₃O₈. As an aside, if one assumes the ABR (CR=0.75) design as opposed to the ABR (CR=0.5) design, the breakeven uranium price is \$105/lb U₃O₈. Therefore, there is a breakeven uranium price difference of at least \$25/lb U₃O₈ between the mixed-fleet fuel costs and the single-tier ABR fuel costs. The reason for the cost savings can be explained by a better neutron utilization afforded by incorporating the axial targets. Because of the MA in the targets becomes a source of plutonium in the AHFTR fuel cycle (Table 3-14), the overall mixed-fleet aqueous reprocessing requirements are actually less than both the ABR (CR=0.75) and ABR (CR=0.5) designs.

At face value, the HLW disposal credit that the AHFTR receives for taking ownership of the Am+Cm+Bk+Cf mass stream could be misinterpreted as a placeholder for redistributing the HLW disposal fee between the ABR and the AHFTR. This is actually not the case. The AHFTR considers the Am+Cm+Bk+Cf material in the fuel cycle as a commodity that is necessary for breeding plutonium. Hence, the AHFTR regards Am+Cm+Bk+Cf as a fuel and not a waste. Remembering back to Figure 7-3, the rate that HM is fed to both the ABR and AHFTR is exactly the same (1.04 gram iHM/MWD). This external feed is equivalently the rate that the external supply of mass is converted into fission energy. Remembering back to Table 3-15, 10% of this external mass stream (0.10 gram iHM/MWD), for the AHFTR, is Am+Cm+Bk+Cf. Also, the

Np+Pu supply is 0.15 gram iHM/MWD and the uranium supply is 0.78 gram iHM/MWD. On the other hand, the ABR (CR=0.5) does not receive any Am+Cm+Bk+Cf and has a Np+Pu supply of 0.45 gram iHM/MWD and a uranium supply of 0.59 gram iHM/MWD. Based on the fact that the AHFTR requires less Np+Pu feed than the ABR, it can be inferred that the aqueous reprocessing costs will be significantly less. The difference in the ABR and AHFTR fuel aqueous reprocessing cost can be seen by comparing Table 7-5 with Table 7-8.

So, the AHFTR derives 10% of its fission energy from the fission of Am+Cm+Bk+Cf, or its eventual transmutation into a fissile isotope that later undergo fission. The creation of fission energy through Am+Cm+Bk+Cf and uranium conversion reduces the AHFTR demand for externally supplied Np+Pu. Therefore, the AHFTR incurs less of an aqueous separations cost than the ABR (Table 7-5, Table 7-8). The aqueous reprocessing costs of the mixed-fleet and single-tier ABR scenarios are given in Table 7-12 for comparison purposes. Note that the external feed Np+Pu requirement of the AHFTR is less than for the ABR cores. Therefore, the aqueous reprocessing costs are less for the AHFTR than the ABRs. For completeness, the pyroprocessing costs are also given in Table 7-12.

Table 7-12. Inter-comparison of aqueous reprocessing costs for single-tier ABR scenarios and the double-tier combined ABR/AHFTR mixed-fleet

	Single-Tier		Double-Tier (Mixed-Fleet)	
	ABR (CR=0.5)	ABR (CR=0.75)	Np+Pu ABR	AHFTR
TRU External Feed (g iHM/MWD)	0.46	0.20	0.45	0.25
Aqueous Reprocessing Cost (\$/kgiHM)	\$6,821.38	\$3,037.21	\$7,086.50	\$1,651.35
Pyroprocessing Cost (\$/kgiHM)	\$2,633.36	\$3,630.82	\$2,637.87	\$2,770.15

The conversion of waste into fuel is made possible by the conservation of neutrons in the axial targets. This neutron conservation allows the ϵ CR to be high by creating plutonium fuel while allowing the ϵ CR to be closer to the ABR by destroying Am+Cm+Bk+Cf transuranics (Table 3-13). The ABR leaks excess neutrons out of the core in order to achieve a low ϵ CR. For

the ABR, the fCR and tCR is closer in value than the AHFTR because the plutonium economy of the fuel cycle is directly linked to the reactors neutron economy (i.e., leakage versus parasitic absorption in U-238). Unlike the ABR, the AHFTR uses excess neutrons to create fuel out of transuranic waste (i.e., Am+Cm+Bk+Cf). Hence, the fCR of the AHFTR is actually very near that of the ABR ($\text{CR}=0.75$) design which has a calculated fCR of 0.84 and a tCR value of 0.77. Yet the AHFTR's tCR is only 0.72. The difference in the tCR conversion ratios is created by the credit given to the creation of plutonium fuel from MAs (which are trans-uranium) instead of from uranium.

Because the AHFTR is consuming waste by converting it into fissile material, it provides a valuable service to the aqueous reprocessing company and indirectly to the ABR. This is the source of the HLW disposal credit. If all of the Am+Cm+Bk+Cf were evenly distributed throughout a fleet of ABRs with no AHFTR, this mass stream would eventually get converted into fission energy. However, more SNF would have to be separated at the aqueous reprocessing plant to provide plutonium to the ABR's, than if some of the plutonium was created by Am+Cm+Bk+Cf transmutation which is allowed by neutron recovery in axial targets. This is why the fuel costs are higher for a utility operating an ABR in a single-tier fuel cycle than the average fuel costs to a utility operating a mixed-fleet in a double-tier fuel cycle. In fact, the sensitivity analysis indicates that if a pyroprocessing cost of \$3,000/kgHM and a \$125/kgHM transuranic-free HLW disposal cost are possible, then the average fuel cost to the mixed-fleet SFR utility would be competitive with the cost of the once-through fuel cycle assuming the current-day uranium ore price of \$80/lb U_3O_8 .

CHAPTER 8 SUMMARY AND CONCLUSIONS

In the past several years there has been a renewed interest in sodium fast reactor (SFR) technology for the purpose of destroying transuranic waste (TRU) which is produced by light water reactors (LWR). The main driver for this decision comes from the fact that higher neutron energies allow all of the actinides, including the minor actinides (MA), to contribute to fission. Though MAs constitute only a tenth of one percent of all LWR spent nuclear fuel (SNF) mass, they are the most radiologically hazardous and constraining factor in the design of a geologic repository. The higher SFR neutron economy over thermal spectrum reactors makes possible a sustainable recycling strategy that can continuously irradiate the initial MA content of SNF, including all of their transmutation products. This sustainable burner strategy is the focus of the current Advanced Burner Reactor (ABR) designs intended to consume the TRU present in the SNF produced by LWRs.

A measure of TRU destruction is the SFR's conversion ratio (CR). The definition of the CR in recent years used for fuel cycle analysis has taken on the meaning of the net TRU produced divided by the net TRU destroyed by the reactor system. This definition is different from the traditional fissile definition (f CR) which is more based on the neutron balance between fissile produced divided by fissile destroyed. The slight difference between these two definitions is the fact that the transuranic (t CR) definition treats all TRU as if they were all of the same fissile quality. In reality this is not the case because most of the long-lived SNF MAs are not fissile by definition due to their neutron-to-proton pairing. Essentially, all even neutron numbered actinides exhibit a fission threshold, at about one MeV, due to the fact that additional kinetic energy is needed in order to overcome the critical energy for fission. The average neutron spectrum of a SFR exists in the energy range of this fission threshold. However, for

most real SFRs there is sufficient down-scattering to ensure that only a fraction of the neutrons in the core exist at energies high enough to induce fission in the MAs (Figure 8-1).

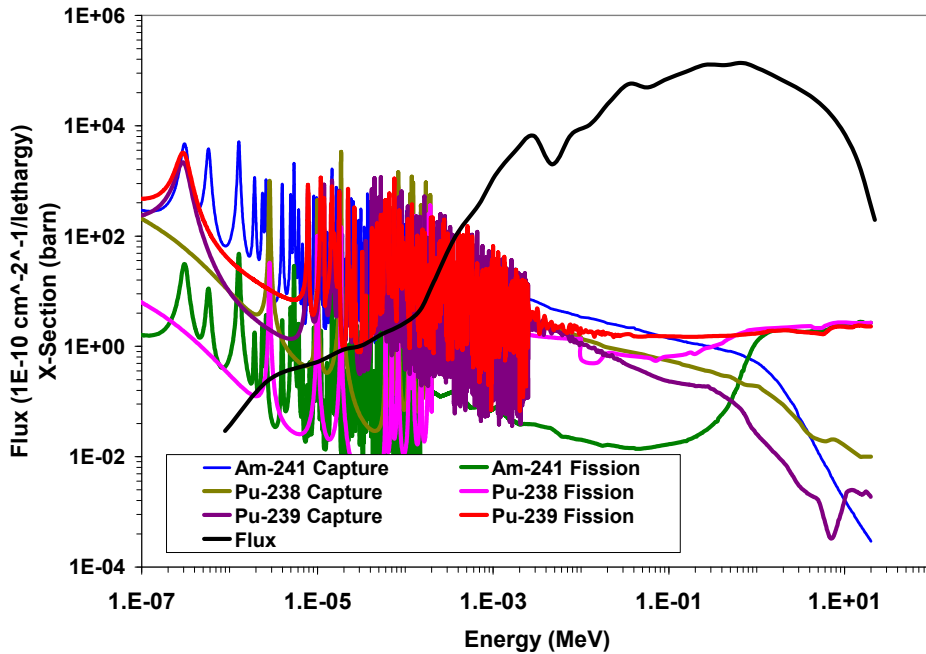


Figure 8-1. ENDF/B-VI cross section data for fission and neutron capture of Am-241, Pu-238 and Pu-239 plotted against the neutron spectrum of a metallic fueled sodium fast reactor

Nevertheless, transmutation of these MAs, in particular Am-241, leads to plutonium isotopes with significantly higher fission cross sections. Given that the capture cross section for Am-241 below its fission threshold is as high as the fission cross section of Pu-239, slight moderation of the SFR neutron flux can yield an energy spectrum conducive to Am-241 transmutation instead of Pu-239 fission. This fact is capitalized upon in this dissertation by adding an axial blanket to the ABR design that contains a combination of plutonium, americium and moderator which enhances neutron capture in Am-241. This hybrid ABR design is referred to in this dissertation as the Axial Heterogeneous Fast Transmutation Reactor (AHFTR). Since, the Am-241 neutron capture ultimately produces the plutonium isotope Pu-238, the axial target region becomes a source of plutonium in the fuel cycle similar to a uranium blanket in a Pu-239

breeder reactor. Pu-238 is itself an even neutron numbered actinide. However, its sub-threshold fission cross section is significantly greater than the initial Am-241 (Figure 8-1). This fact allows the AHFTR to have an k_{CR} value similar to that of an equivalent ABR design but with a k_{CR} value that is less.

Method of Reactor Design

Due to the large mean-free-path of fast neutrons compared to thermal neutrons, the effect of geometric buckling (i.e., neutron leakage) is a stronger contributor to the SFR's: k_{CR} , power distribution and coolant void response. To meet the criticality condition of a high leakage SFR core, the fissile concentration in the fuel is necessarily high. In order to decrease the k_{CR} , and hence increase TRU burning performance, the concentration of fertile uranium in the fuel must be decreased. The ABR and AHFTR both accomplish this by simultaneously increasing the TRU concentration while decreasing the U-238 concentration. This increase in the fissile inventory of the core necessitates that leakage be increased in order to meet the criticality requirement that the core's geometric and materials buckling be equated. In the AHFTR design, the radius of the core was increased by one row of fuel over that of the reference ABR design. The greater AHFTR core radius decreases the radial geometric buckling or curvature of the flux in the radial direction. This has the effect of decreasing the peak-to-average power ratio in the core which enables the AHFTR fuel to be irradiated more evenly than in the ABR (Figure 8-2). It also relaxes the need to smooth the radial power profile using higher enriched fuel in the outer region of the core.

Because of the reduced emphasis on higher enriched fuel, the AHFTR can draw upon the already existing experience established by past SFR's such as the Experimental Breeder Reactor's I and II (EBR-I and EBR-II). Thus, the fuel composition and assembly design of the

AHFTR closely matches that previously established by real reactors. Hence, with the exception of the target material, little fuels development work should be required to implement its design.

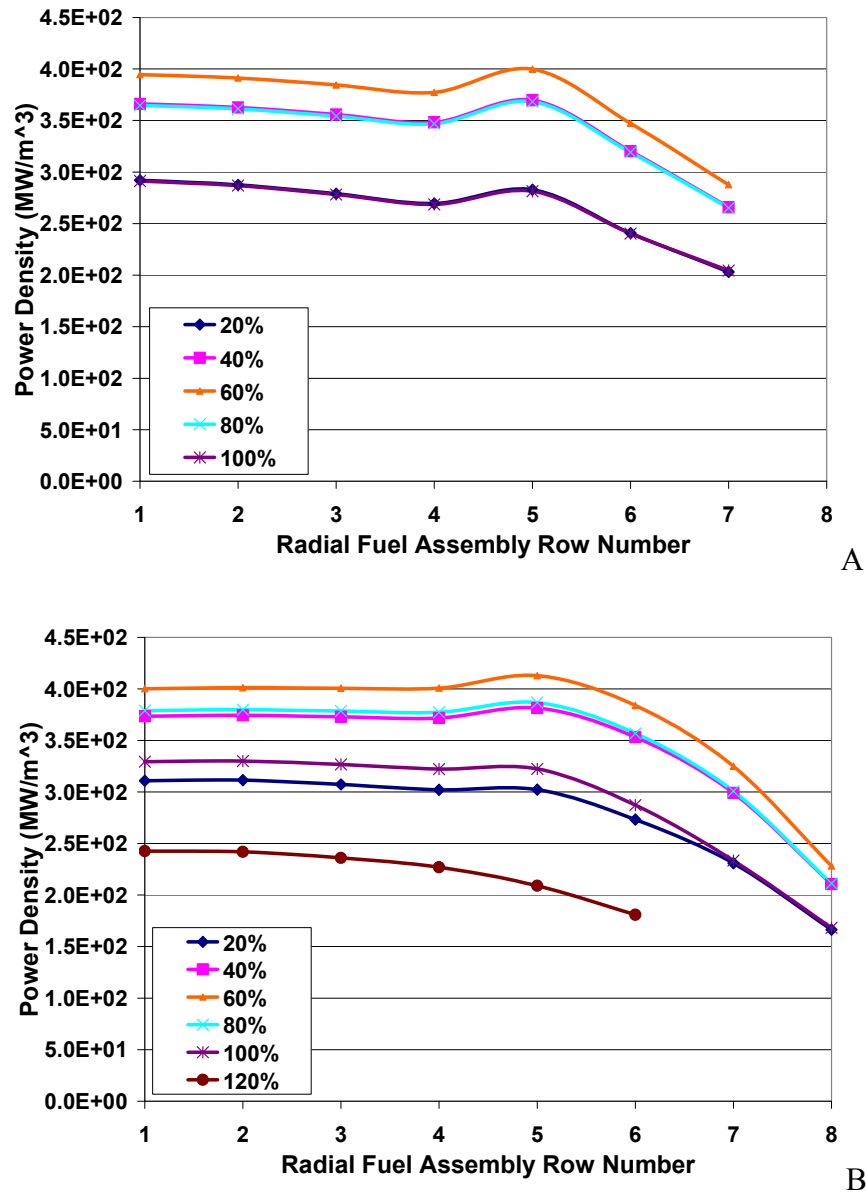


Figure 8-2. Radial power distribution for six axial slices through the core for the ABR (A) and AHFTR (B) (REBUS)

Because the AHFTR radial buckling was reduced, the geometric buckling in the axial direction had to be slightly increased. The resulting increase in axial leakage favors transmutation in the targets because more neutrons are lost from the active driver core and invested in neutron captures in the target region. In the axial target region, some of the fuel pins

contain blank rods of zirconium hydride moderator. These moderating rods shift the fast flux of the active core region to a more epithermal flux where the capture cross section of Am-241 is high compared to the Pu-239 cross section. This spectrum modulation causes the neutron mean-free-path to shorten while simultaneously increasing the importance of neutron capture in Am-241 relative to fission in Pu-239. Therefore, the leakage (and hence buckling) is reduced locally in the target region. This neutron trap effect enables enhanced utilization of neutrons in the AHFTR's fuel cycle. Note that the Pu-238 generated by the Am-241 is exposed to epithermal neutrons in the target spectrum and therefore has little fissile value. However when the bred Pu-238 is recycled and placed in the faster spectrum of the active core region, its fissile value becomes much higher. This spectrum shift, as a result of the fuel recycling process, is the distinguishing factor that gives the AHFTR an enhancement in ρ_{CR} without a corresponding increase in the ρ_{CR} .

Reactor Control and Safety Features

Some debate has existed in the transmutation community over whether or not Tc-99 can be effectively burned in a SFR. Tc-99 is a fission product with a concentration in SNF roughly equal to that of the MAs. Also, due to its long life and radiotoxicity, it is an isotope that must be considered in the long term design of a geologic repository. Tc-99 has approximately the same capture cross section of that of U-238 in the fast spectrum. However, the neutron capture cross section of Tc-99 is roughly three times less than that of Am-241. Therefore, moderated target studies by previous authors have shown that this isotope is fairly difficult to destroy in SFRs. Because the transmutation rate of Tc-99 is relatively small, in this dissertation it is used as the neutron poison in control rods for reactivity shim purposes only.

It was found that using the control assembly pattern used by the reference ABR design, Tc-99 could be used for shim and safety rods in the AHFTR. The effectiveness of Tc-99 as a

control rod poison lends itself to the relatively high atom concentration of Tc-99 atoms in the form of metallic technetium. The atomic density of metallic technetium is approximately three times higher than the B-10 concentration in 90% enriched boron carbide. Enriched boron carbide is a typical neutron absorber in many SFR designs due to the large unresolved cross section value of B-10. The neutron capture cross section of B-10 is approximately three and a half times that of Tc-99 in the fast neutron energy range. Therefore, Tc-99's reactivity shim worth in the SFR is almost but not quite as significant as enriched boron carbide.

As a side benefit, it was also found that the Tc-99 destruction rate in the shim rods during their withdrawal cycle from the AHFTR active core was approximately equal to the Tc-99 production rate in a typical pressurized water reactor. Therefore, though it may not be possible to "deep-burn" Tc-99 in dedicated targets as was proposed in previous transmutation studies, it may be feasible to modify the control rod design of SFRs (such as was done with the AHFTR) to have a net destruction benefit of technetium in the fuel cycle.

The AHFTR's void and Doppler coefficients were also calculated and compared to the ABR. Because special effort was taken to minimize the MA concentration in the driver fuel, the AHFTR's void and Doppler coefficients are comparable to the ABR design. The issue of a positive void coefficient resulting from spectrum hardening during a complete loss of sodium coolant was also addressed. This positive whole-core void worth also exists for the ABR and is typical of many SFR designs. In the past EBR-II experience, this positive void coefficient was countered by thermal expansion of the fuel. Fuel expansion decreases the density of the fuel and increases leakage. The net effect of these expansion feedbacks was an overall negative power coefficient. The AHFTR's radial and axial expansion coefficients were calculated to be negative and showed that the positive reactivity insertion of a whole core void event could be countered

by a reasonable amount of thermal expansion. The AHFTR Doppler coefficient is negative and comparable to the reference ABR case.

Code Validation

The majority of the fuel cycle calculations were performed using a suite of fast reactor analysis codes developed over the past three decades by Argonne National Laboratory: MC²-2, DIF3D and REBUS. Since these codes are adapted to fast reactor analysis, they make the assumption that the neutron spectrum and flux magnitude do not vary over large “same spectrum” regions of the core. Therefore, the cross section group constants generated by MC²-2 are done so using slowing down theory with a zero-dimensional critical buckling search. Core flux calculations are made by DIF3D using diffusion theory and homogenizing “smearing” fuel assemblies over radial and axial regions of the core in a hexagonal-z nodal discretization.

The accuracy of the moderated axial target transmutation analysis depends primarily on the change in the mean-free-path between the fast neutrons of the active core and the moderated neutrons of the target regions. Benchmark calculations were performed between DIF3D, and the variational transport code VARIANT which uses spherical harmonics, and the transport code MCNP which uses the Monte Carlo method. Good agreement was found between these three different codes for both the neutron spectrum and flux distributions of the AHFTR core. Further pin-lattice calculations, using MCNP, of the repeating moderator/target rod pattern showed that spatial self-shielding and shadowing effects in the target region were negligible. This acceptable result is due to the fact that only sufficient moderation was provided to shift the fast spectrum to epithermal energies below the one MeV fission threshold of the MAs. This softened fast spectrum is sufficient to achieve a moderate enhancement in the Am-241 transmutation rate without decreasing the neutron energies to the range of well resolved cross section resonances. Also, the epithermal neutron mean-free-path in the target region was sufficiently larger than the

fuel pin diameter and pitch dimensions. Thus, these target region neutrons do not have a high visibility to the local heterogeneities created by the moderating zirconium hydride pins.

Transmutation Target Fuel Design

The general philosophy of the AHFTR design is to demonstrate that a MA burner core could be constructed using existing or near term achievable technology. Therefore, the reactor design was tailored in such a way as to draw upon the existing fabrication and irradiation experience with metallic Pu/U/Zr fuels. Therefore, the composition of the AHFTR driver fuel was limited to approximately 20TRU/70U/10Zr which is almost identical to the ternary metal alloys tested at EBR-II. Also for feasibility purposes, the transmutation target's composition was based on recent irradiation testing of high MA content metal alloy fuels, which was performed at the Idaho National Laboratory's Advanced Test Reactor.

A set of fuel design criteria for the AHFTR was established to ensure that the heterogeneous core design does not produce peak power levels in the driver fuel and targets that could cause the fuel to fail. These design criteria were based on the experience with metal alloy SFR fuels gained by the operation of EBR-II and the Fast Flux Test Facility (FFTF).

First, all fuel assemblies in the core were restricted to a fast fluence limit of $4 \times 10^{23} \text{ cm}^{-2}$ ($E > 0.1 \text{ MeV}$) which is the operational limit, established at FFTF, for HT-9 fast reactor grade steel. HT-9 was used for cladding and structural components at both EBR-II and FFTF. Second, the gas plenum pressure in the fuel pins was not allowed to exceed that typical of EBR-II which is in the range of 30 atm to 50 atm. The gas plenum pressures calculated for the AHFTR were found to be within the operational experience of the EBR-II fuel pin data. In fact, the gas plenum length of the reference ABR design is sufficiently long to provide adequate space for the production of fission gasses and transmutation helium. Third, the temperature of the inner cladding wall was not allowed to exceed 650°C to prevent or minimize the possibility of fuel-to-

cladding chemical or eutectic interaction which is a unavoidable characteristic of metallic alloy fuel. Finally, all assemblies were limited to pellet centerline temperatures equal to or less than those of the homogeneous reference ABR which are also representative of EBR-II. Also, based on the EBR-II experience, the burnup of the AHFTR fuel was kept to within approximately 100 MWD/kg. It may be possible to increase this burnup limit as might be seen in some of the ABR designs. However, much of the EBR-II experience dictates that the likelihood of cladding failure became an issue at burnups higher than 100 MWD/kg due to swelling and mechanical and chemical interaction between cladding and the metal fuel. Because, it was desirable to establish the feasibility of a MA burner it was felt that a low probability of fuel failure was desirable. This is especially true when one considers the various volatility and radiological hazards of neptunium, americium, curium and californium which is present in non-trivial quantities in the AHFTR driver fuel and targets.

Fuel Processing and Repository Considerations

Much emphasis has been put on the importance of transmuted MAs, in particular Am-241, in this work. The impact of this transmutation on the radioactivity and the thermal heat production of the transmuted fuel have been addressed. It was determined that the driver fuel and transmutation targets both had specific neutron dose rates (per kg TRU) very similar to the reference ABR. This is an indication that the higher mass actinides created during the target irradiation, which are a source of spontaneous fission neutrons, can be burned effectively in the fast spectrum of the active core region. Though the AHFTR driver and target fuels exhibit higher gamma and heat emission rates than the ABR case, these rates do not exceed the worst case scenario for multi-recycling in an LWR. Also, these higher emission rates should be expected, considering the high throughput of americium and curium feedstock in the AHFTR recycling center.

The decay heat produced by fuel recycling process losses that might be seen by a geologic repository was also addressed. It was found that the increased concentration of Pu-238 and Cm-244 in the AHFTR fuel cycle caused a heat generation rate plateau in the repository after a few hundred years after actinide wastes were placed in the repository. This trend is different than exhibited by SNF because the higher Am-241 in this LWR waste causes the heat plateau to occur no sooner than 1000 years. Because the AHFTR heat plateau occurs earlier in the repository life, it can be argued that it is more likely that human institutions will be able to manage the repository performance during this peak heat time than if the repository were filled with SNF.

Fuel Cycle Economic Analysis

The economics of a mixed ABR and AHFTR fleet was considered. A SFR utility was envisioned that operates a mix of ABRs and AHFTRs in order to burn the TRU generated by the LWR fleet. In the mixed SFR fleet, the SNF neptunium and plutonium would be the feedstock for refueling the ABR's. Some of this neptunium and plutonium and all of the SNF americium, curium, berkelium and californium would be diverted to fuel the AHFTR. In this capacity, the AHFTR becomes a dedicated MA burner in the mix of reactors. Based on the mass balance between TRU production and destruction rates for each reactor, a support ratio of 3.3 MWth of ABRs per one MWth of AHFTRs was found. Also, 0.6 MWth of SFRs are needed per one MWth of LWRs.

This economics analysis shows that the conversion of americium into plutonium reduces the reprocessing demand for separating plutonium from SNF. This reduces the reprocessing costs to the reactor. Also because, the reactor consumes MAs and Tc-99, which are high level wastes (HLW), the reactor provides a valuable service to the SFR utility. The fact that the AHFTR saves fuel costs by transmuting waste atoms into fuel atoms is a direct example of how

the reactor attains an observably high fissile conversion ratio while at the same time being a transuranic burner.

A sensitivity analysis of fuel costs on reprocessing unit costs indicates that if the cost of HLW disposal can be reduced to \$125/kgHM due to the removal of MAs (and Tc-99), then the average fuel cost to the mixed-fleet SFR utility would be competitive with the cost of the once-through fuel cycle assuming the current-day uranium ore price of \$80/lb U₃O₈.

Concluding Remarks

It is recommended that if SFRs and LWRs are to exist in a symbiotic fuel relationship, then their waste management practices be balanced in such a way as to deliver the most amount of reactivity per neutron spectrum requirements. Sodium fast “breeder” reactors were envisioned at the beginning of the commercial nuclear industry because at that time it was commonly believed that uranium resources would become scarce. This was not the case and today LWRs use the fissile U-235 atom in enriched uranium to drive the chain reaction in those reactors. However, thermal spectrums as a general rule, with the exception of some thorium reactors, are deficient in the reactivity needed to sustainably bombard non-fissile material. This, in fact, is the nature of the breeder reactor. Breeder reactors possess the neutron balance between fissile production sources and sinks to continuously transmute non-fissile (i.e., fertile) isotopes into fissile isotopes. Due to their fission threshold nature and the fact that their transmutation leads to plutonium isotopes, MAs are by definition fertile. Therefore, investing neutrons into their transmutation into fissile material is the key element for extracting their maximum fissile worth. It is true that a high leakage core will reduce the net transuranic production. However, creating a high leakage core without a blanket (radial or axial) of fertile material will waste neutrons that could otherwise be used for transmutation. If a blanket of fertile MAs is used in place of uranium for

the purpose of breeding plutonium, then by definition a fissile breeder is created by enhancing transuranic minor actinide burning.

APPENDIX A REBUS INPUT DECK

Key components of the REBUS input deck used to model the final AHFTR design is given in this appendix.

```

REBUSINPUTAPPENDX.txt
#####REG
IONS MAPPED INTO REACTOR GEOMETRY#####
**CONTROL ASSEMBLY (1,0) **
30 CR01A 1 0 0 0.00000E+00 4.58640E+01
30 CR01B 1 0 0 4.58640E+01 9.17280E+01
30 CR01C 1 0 0 9.17280E+01 1.14660E+02
30 CR01D 1 0 0 1.14660E+02 1.28980E+02
30 CR01E 1 0 0 1.28980E+02 1.43300E+02
30 CR01F 1 0 0 1.43300E+02 1.57620E+02
30 CR01G 1 0 0 1.57620E+02 1.71940E+02
30 CR01H 1 0 0 1.71940E+02 1.86260E+02
30 CROHH 1 0 0 1.86260E+02 2.06260E+02
30 CR01I 1 0 0 2.06260E+02 2.33260E+02
30 CR01J 1 0 0 2.33260E+02 2.74295E+02
30 CR01K 1 0 0 2.74295E+02 3.97400E+02
**INNER CORE / IC01 / ROW 01 FUEL ASSEMBLIES**
30 IC01A 2 0 0 0.00000E+00 4.58640E+01
30 IC01B 2 0 0 4.58640E+01 9.17280E+01
30 IC01C 2 0 0 9.17280E+01 1.14660E+02
30 IC01D 2 0 0 1.14660E+02 1.28980E+02
30 IC01E 2 0 0 1.28980E+02 1.43300E+02
30 IC01F 2 0 0 1.43300E+02 1.57620E+02
30 IC01G 2 0 0 1.57620E+02 1.71940E+02
30 IC01H 2 0 0 1.71940E+02 1.86260E+02
30 TG01H 2 0 0 1.86260E+02 2.06260E+02
30 IC01I 2 0 0 2.06260E+02 2.33260E+02
30 IC01J 2 0 0 2.33260E+02 2.74295E+02
30 IC01K 2 0 0 2.74295E+02 3.97400E+02
**INNER CORE / IC02 / ROW 02 FUEL ASSEMBLIES**
30 IC02A 3 0 0 0.00000E+00 4.58640E+01
30 IC02B 3 0 0 4.58640E+01 9.17280E+01
30 IC02C 3 0 0 9.17280E+01 1.14660E+02
30 IC02D 3 0 0 1.14660E+02 1.28980E+02
30 IC02E 3 0 0 1.28980E+02 1.43300E+02
30 IC02F 3 0 0 1.43300E+02 1.57620E+02
30 IC02G 3 0 0 1.57620E+02 1.71940E+02
30 IC02H 3 0 0 1.71940E+02 1.86260E+02
30 TG02H 3 0 0 1.86260E+02 2.06260E+02
30 IC02I 3 0 0 2.06260E+02 2.33260E+02
30 IC02J 3 0 0 2.33260E+02 2.74295E+02
30 IC02K 3 0 0 2.74295E+02 3.97400E+02
**INNER CORE / IC03 / ROW 03 FUEL ASSEMBLIES**
30 IC03A 4 0 0 0.00000E+00 4.58640E+01
30 IC03B 4 0 0 4.58640E+01 9.17280E+01
30 IC03C 4 0 0 9.17280E+01 1.14660E+02
30 IC03D 4 0 0 1.14660E+02 1.28980E+02
30 IC03E 4 0 0 1.28980E+02 1.43300E+02
30 IC03F 4 0 0 1.43300E+02 1.57620E+02
30 IC03G 4 0 0 1.57620E+02 1.71940E+02
30 IC03H 4 0 0 1.71940E+02 1.86260E+02
30 TG03H 4 0 0 1.86260E+02 2.06260E+02
30 IC03I 4 0 0 2.06260E+02 2.33260E+02
30 IC03J 4 0 0 2.33260E+02 2.74295E+02
30 IC03K 4 0 0 2.74295E+02 3.97400E+02
**INNER CORE / IC04 / ROW 04 FUEL ASSEMBLIES**
30 IC04A 5 0 0 0.00000E+00 4.58640E+01
30 IC04B 5 0 0 4.58640E+01 9.17280E+01
30 IC04C 5 0 0 9.17280E+01 1.14660E+02
30 IC04D 5 0 0 1.14660E+02 1.28980E+02
30 IC04E 5 0 0 1.28980E+02 1.43300E+02
30 IC04F 5 0 0 1.43300E+02 1.57620E+02
30 IC04G 5 0 0 1.57620E+02 1.71940E+02
30 IC04H 5 0 0 1.71940E+02 1.86260E+02
Page 1

```

Figure A-1. REBUS A.NIP Type 30 Geometry Cards and A.BURN Type 11 In-Core Fuel Management Cards

```

REBUSINPUTAPPENDX.txt
30 CR01E 5 17 0 1.28980E+02 1.43300E+02
30 CR01F 5 17 0 1.43300E+02 1.57620E+02
30 CR01G 5 17 0 1.57620E+02 1.71940E+02
30 CR01H 5 17 0 1.71940E+02 1.86260E+02
30 CR0HH 5 17 0 1.86260E+02 2.06260E+02
30 CR01I 5 17 0 2.06260E+02 2.33260E+02
30 CR01J 5 17 0 2.33260E+02 2.74295E+02
30 CR01K 5 17 0 2.74295E+02 3.97400E+02
**CONTROL ASSEMBLY (5,19) **
30 CR01A 5 19 0 0.00000E+00 4.58640E+01
30 CR01B 5 19 0 4.58640E+01 9.17280E+01
30 CR01C 5 19 0 9.17280E+01 1.14660E+02
30 CR01D 5 19 0 1.14660E+02 1.28980E+02
30 CR01E 5 19 0 1.28980E+02 1.43300E+02
30 CR01F 5 19 0 1.43300E+02 1.57620E+02
30 CR01G 5 19 0 1.57620E+02 1.71940E+02
30 CR01H 5 19 0 1.71940E+02 1.86260E+02
30 CR0HH 5 19 0 1.86260E+02 2.06260E+02
30 CR01I 5 19 0 2.06260E+02 2.33260E+02
30 CR01J 5 19 0 2.33260E+02 2.74295E+02
30 CR01K 5 19 0 2.74295E+02 3.97400E+02
**CONTROL ASSEMBLY (5,21) **
30 CR01A 5 21 0 0.00000E+00 4.58640E+01
30 CR01B 5 21 0 4.58640E+01 9.17280E+01
30 CR01C 5 21 0 9.17280E+01 1.14660E+02
30 CR01D 5 21 0 1.14660E+02 1.28980E+02
30 CR01E 5 21 0 1.28980E+02 1.43300E+02
30 CR01F 5 21 0 1.43300E+02 1.57620E+02
30 CR01G 5 21 0 1.57620E+02 1.71940E+02
30 CR01H 5 21 0 1.71940E+02 1.86260E+02
30 CR0HH 5 21 0 1.86260E+02 2.06260E+02
30 CR01I 5 21 0 2.06260E+02 2.33260E+02
30 CR01J 5 21 0 2.33260E+02 2.74295E+02
30 CR01K 5 21 0 2.74295E+02 3.97400E+02
**CONTROL ASSEMBLY (5,23) **
30 CR01A 5 23 0 0.00000E+00 4.58640E+01
30 CR01B 5 23 0 4.58640E+01 9.17280E+01
30 CR01C 5 23 0 9.17280E+01 1.14660E+02
30 CR01D 5 23 0 1.14660E+02 1.28980E+02
30 CR01E 5 23 0 1.28980E+02 1.43300E+02
30 CR01F 5 23 0 1.43300E+02 1.57620E+02
30 CR01G 5 23 0 1.57620E+02 1.71940E+02
30 CR01H 5 23 0 1.71940E+02 1.86260E+02
30 CR0HH 5 23 0 1.86260E+02 2.06260E+02
30 CR01I 5 23 0 2.06260E+02 2.33260E+02
30 CR01J 5 23 0 2.33260E+02 2.74295E+02
30 CR01K 5 23 0 2.74295E+02 3.97400E+02

#####COM
POSITIONS MAPPED INTO REGIONS WITHIN REACTOR#####
****FUEL MANAGEMENT PATH - INNER CORE****
11 CPL01 0 1ICSC IC01D 2ICSC IC01D
11 CPL01 0 3ICSC IC01D 4ICSC IC01D
11 CPL01 0 5ICSC IC01D 6ICSC IC01D
11 CPL01 0 7MELTR
****FUEL MANAGEMENT PATH - INNER CORE****
11 CPL02 0 1ICSC IC01E 2ICSC IC01E
11 CPL02 0 3ICSC IC01E 4ICSC IC01E
11 CPL02 0 5ICSC IC01E 6ICSC IC01E
11 CPL02 0 7MELTR
****FUEL MANAGEMENT PATH - INNER CORE****
11 CPL03 0 1ICSC IC01F 2ICSC IC01F
11 CPL03 0 3ICSC IC01F 4ICSC IC01F

```

Figure A-1. Continued.

APPENDIX B PARAMETRIC DESIGN ANALYSIS

The full results of the parametric analysis performed in Chapter 3 are given in this appendix. The main parameters varied in this analysis were the core height and pin pitch-to-diameter ratio (Table 3-1 and Table 3-2). The reactor thermal power of the reactor core was held constant at 1000 MWth for all of these cases. The burnup in the first row of fuel at the core mid-plane was restricted to 18 at. %. These analyses gave an indication of the affects of core and fuel pin geometry on the: TRU enrichment, excess reactivity and cycle length. The down selections to the “tall” and “flat versions of the AHFTR in Chapter 3 were made based on the results of this parametric analysis.

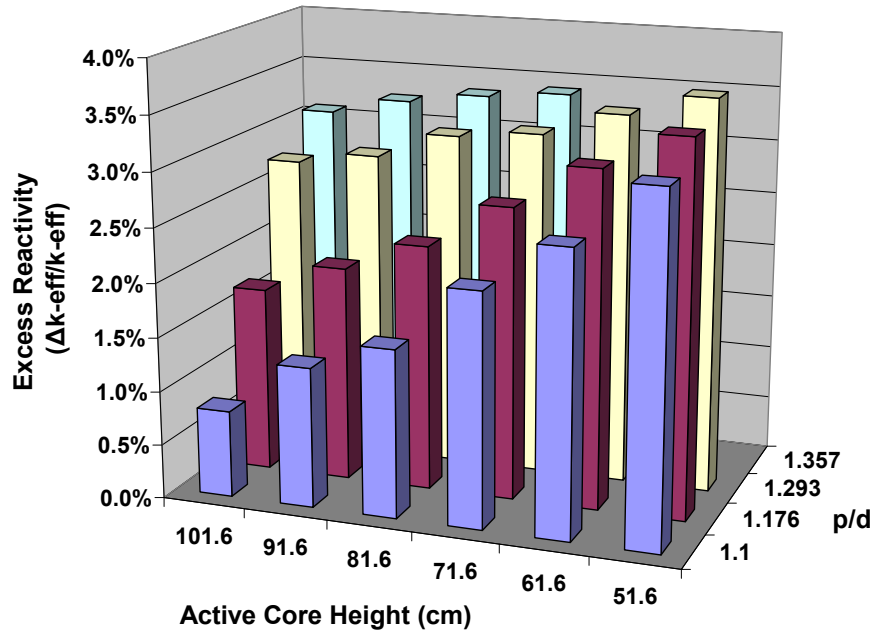


Figure B-1. Excess Reactivity of the core design in Figure 3-1 “tall” for varying core height and p/d (REBUS)

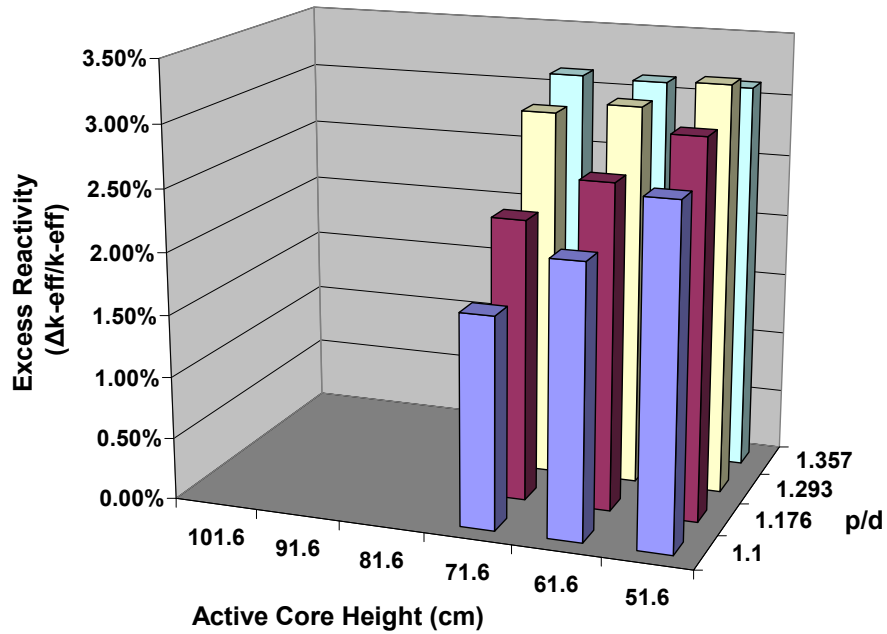


Figure B-2. Excess Reactivity of the core design in Figure 3-14 “flat” for varying core height and p/d (REBUS)

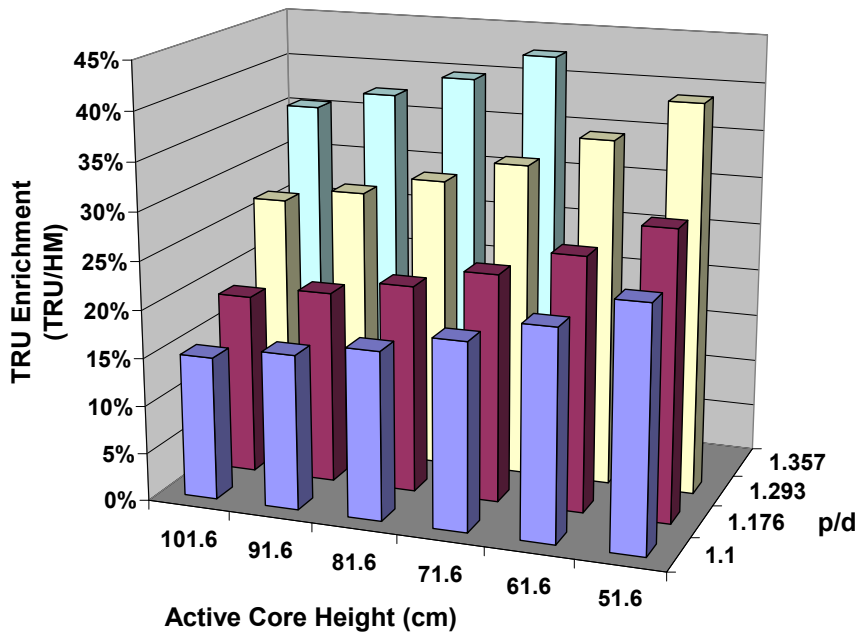


Figure B-3. TRU enrichment of the core given in Figure 3-1 “tall” for varying core height and p/d (REBUS)

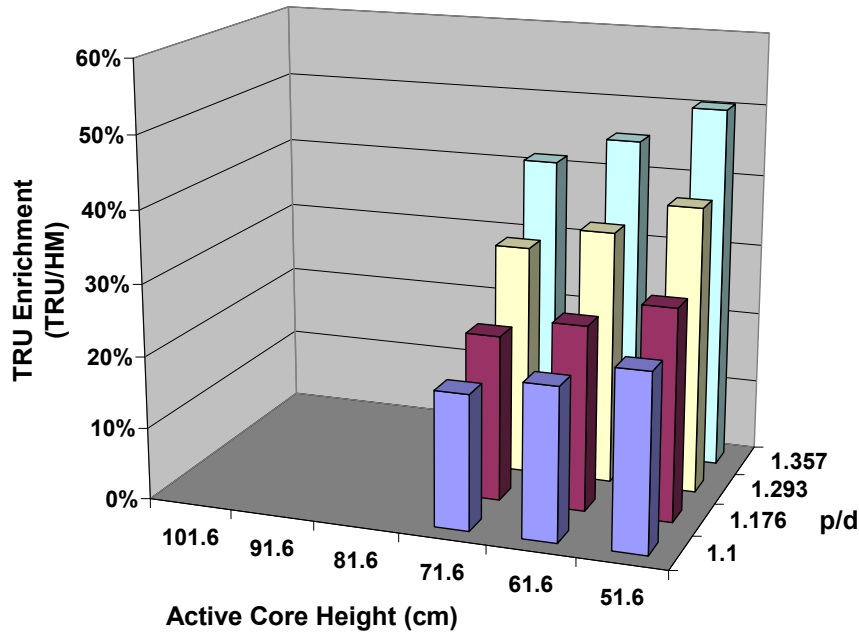


Figure B-4. TRU enrichment of the core design in Figure 3-14 “flat” for varying core height and p/d (REBUS)

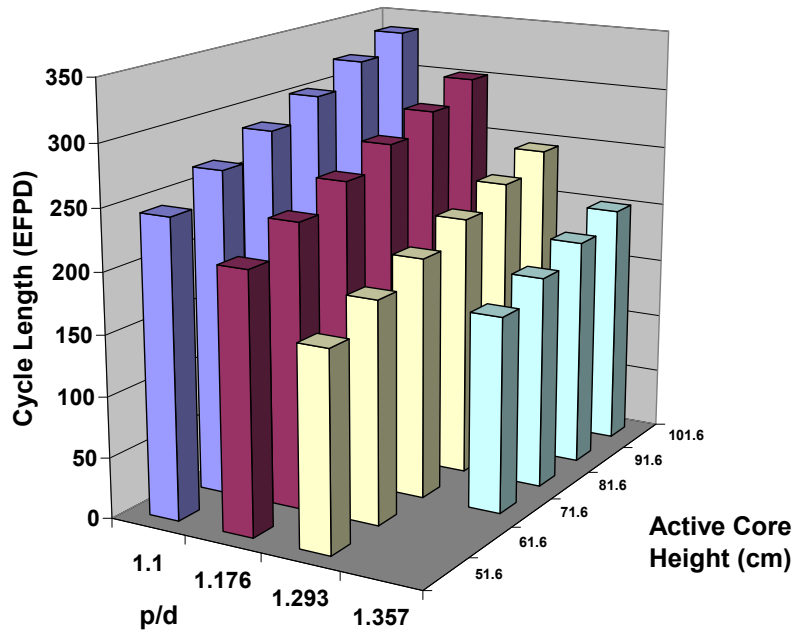


Figure B-5. Cycle length of the core given in Figure 3-1 “tall” for varying core height and p/d (REBUS)

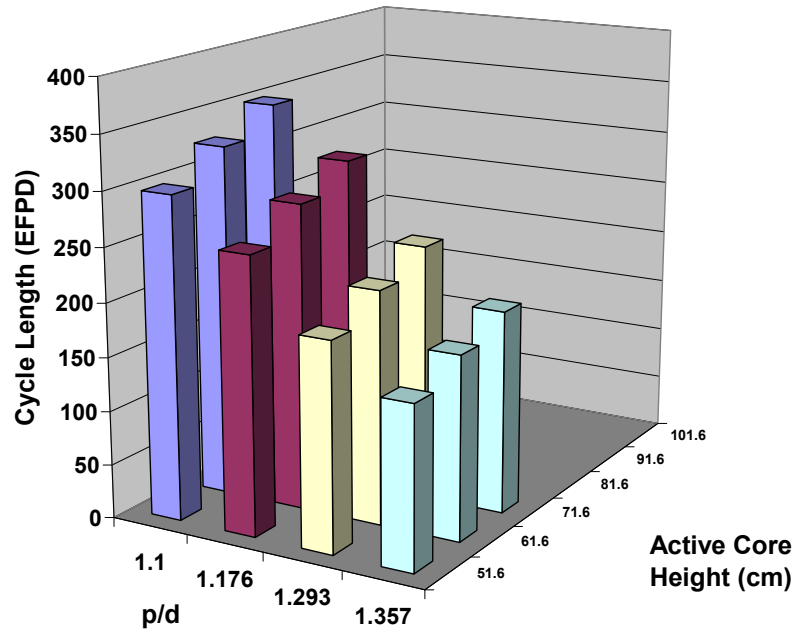


Figure B-6. Cycle length of the core design in Figure 3-14 “flat” for varying core height and p/d (REBUS)

LIST OF REFERENCES

1. US Department of Energy, "The History of Nuclear Energy," US Department of Energy, Office of Nuclear Energy, Science and Technology, DOE/NE-0088, Washington, DC.
2. E. BLAKE, "US Capacity Factors: A Small Gain to an Already Large Number," *Nuclear News*, 27-32, La Grange Park, Illinois, (May 2007).
3. R. COCHRAN and N. TSOULFANIDIS, *The Nuclear Fuel Cycle: Analysis and Management*, 2nd ed., American Nuclear Society, La Grange Park, Illinois, (1999).
4. "The Nuclear Waste Policy Act: As Ammended," US Department of Energy, Office of Civillian Radioactive Waste Management, Washington, DC, (2004).
5. "The Future Path for Advanced Spent Fuel Treatment and Transmutation Research," US Department of Energy, Office of Nuclear Energy, Science and Technology, Report to Congress on Advanced Fuel Cycle Initiative, Washington, DC, (2003).
6. "Nuclear Waste Fund Fee Adequacy: An Assessment," US Department of Energy, Office of Civillian Radioactive Waste Management, DOE/RW-0534, Washington, DC, (2001).
7. E. HOFFMAN, R. HILL, and M. WILLIAMSON, "Preliminary Core Design Studies for the Advanced Burner Reactor Over a Range of Conversion Ratios," ANL-AFCI-177, Argonne National Laboratory, Argonne, Illinois, (2006).
8. E. SHWAGERAUS, P. HEJZLAR, and M. KAZIMI, "A Combined Non-Fertile and UO₂ PWR Fuel Assembly for Actinide Waste Minimization," *Nuclear Technology*, **149**, 281-303 (2005).
9. W. CARMACK, R. FIELDING, P. MEDVEDEV, M. MEYER, M. TODOSOW, H. HAMILTON, J. NINO, S. PHILPOT, and J. TULENKO, "AECL/US INEERI-Development of Inert Matrix Fuels for Plutonium and Minor Actinide Management in Power Reactors-Fuel Requirements and Down Select Report," INL/EXT-05-00436, Idaho National Laboratory, Idaho Falls, Idaho, (2005).
10. V. BERTHOU, C. DEGUELDRE, and J. MAGILL, "Transmutation Characteristics in Thermal and Fast Neutron Spectra: Application to Americium," *Journal of Nuclear Materials*, **320**, 156-162 (2003).
11. F. MANN and R. SCHENTER, "Calculated Neutron Capture Cross Sections to the Americium Ground and Isomeric States," *Nuclear Science and Engineering*, **63**, 242-249 (1977).
12. "Yucca Mountain Science and Engineering Report, Rev. 1," US Department of Energy, Office of Civillian Radioactive Waste Management, DOE/RW-539-1, Washington, DC, (2002).
13. R. WIGELAND and T. BAUER, "Repository Benefits of AFCI Options", ANL-AFCI-129, Argonne National Laboratory, Argonne, Illinois, (2004).

14. K. WIRTZ, *Lectures on Fast Reactors*, American Nuclear Society, La Grange Park, Illinois, (1982)
15. H CHOI and T. DOWNAR, "A Liquid-Metal Reactor for Burning Minor Actinides of Spent Light Water Reactor Fuel - I," *Nuclear Science and Engineering*, **133**, 1-22 (1999).
16. A. STANCULESCU, J. GARNIER, J. ROUAULT, E. KIEFHABER, and R. SUNDERLAND, "Plutonium Burning and Minor Actinides Transmutation in a Fast Reactors: First Results Obtained within the Frame of the CAPRA Program," *Proc. International Nuclear Congress: Atoms for Energy*, Oct 2-6, 1994, Lyon, France, (1994).
17. A. VASILE, G. RIMPAULT, J. TOMMASI, C. DE SAINT JEAN, M. DELPECH, K. HESKETH, H. BEUAMONT, R. SUNDERLAND, T. NEWTON, P. SMITH, W. MASCHKE, D. HAAS, C. RAEDT, G. VAMBENEPE, and J. LEFEVRE, "Fast Reactors Fuel Cycle Core Physics Results from the CAPRA-CADRA Programme," *Proc. of Global01*, September 13-17, 2001, Paris, France, (2001).
18. E. GLUEKLER, "US. Advanced Liquid Metal Reactor (ALMR)," *Progress in Nuclear Energy*, **31**, No. 1-2, 43-61 (1997).
19. A. DUBBERLY, K. YOSHIDA, C. BOARDMAN, and T. WU, "Superprism Oxide and Metal Fuel Core Designs," *Proc. of ICONE8: International Conference on Nuclear Engineering*, April 2-6, 2000, Baltimore, Maryland, (2000).
20. E. MORRIS and M. SMITH, "Development of Low Conversion Ratio Fast Reactors for Transmutation," ANL-AAA-057, Argonne National Laboratory, Argonne, Illinois, (2002).
21. L. BUIRON, F. VARAINE, D. LORENZO, H. PALANCHER, and B. VALENTIN, "Minor Actinides Transmutation in SFR Depleted Uranium Radial Blanket, Neutronic and Thermal Hydraulic Evaluation," *Proc. of Global07*, September 9-13, 2007, Boise, Idaho, (2007).
22. K. FUJIMURA, T. SANDA, M. MAYUMI, S. MORO, M. SAITO, and H. SEKIMOTO, "Feasibility Study of Large Mox Fueled FBR Core Aimed At the Self-Consistent Nuclear Energy System," *Progress in Nuclear Energy*, **37**, No. 1-4, 177-185, (2000).
23. K. FUJIMURA, T. SANDA, M. YAMAWAKI, and K. KNASHI, "Enhancement of Transmutation Characteristics of the Minor Actinide Burning Fast Reactor Core Concept Using Hydride Fuel Targets and Its Introduction Scenario," *Journal of Nuclear Science and Technology*, **38**, No. 10, 879-886 (2001).
24. M. YAMAWAKI, H. SUWARNO, T. YAMAMATO, T. SANDA, K. FUJIMURA, and K. KAWASHIMA, "Concept of Hydride Fuel Target Subassemblies in a Fast Reactor Core for Effective Transmutation of MA," *Journal of Alloys and Compounds*, **271-273**, 530-533 (1998).

25. V. ELISEEV and E. POPLAVSKAYA, "Possibilities of Deep Burnup of Americium and Neptunium in the Core of a Fast Reactor," *Atomic Energy*, **96**, No. 3, 170-176 (2004).
26. M. ROME, A. HARISLUR, E. HERNIOU, A. ZAETTA, and J. TOMMASI, "Use of Fast Reactors to Burn Long-Life Actinides, Especially Am, Produced by Current Reactors," *Proc. of Physor96*, September 16-20, 1996, Mito, Japan, (1996).
27. M. ROME, A. HARISLUR, and E. HERNIOU, "Study of Once-Through Americium Matrices Strategy in Fast Reactors," *Proc. of ICONES5*, May 26-30, 1997, Nice, France, (1997).
28. T. SANDA, K. FUJIMURA, K. KOBAYASHI, K. KAWASHIMA, M. YAMAWAKI, and K. KONASHI, "Fast Reactor Core Concepts for Minor Actinide Transmutation Using Hydride Fuel Targets," *Journal of Nuclear Science and Technology*, **37**, No. 4, 335-343 (2000).
29. International Atomic Energy Agency, "Fast Reactor Database", Last Visited: March 1, 2008, <http://www.iaea.org/inis/nkm/nkm/aw/frdb/index.html>, (2008).
30. H. KURAIISHI, T. SAWADA, H. NINOKATA, and H. ENDO, "Inherent and Passive Safety Sodium-Cooled Fast Reactor Core Design with Minor Actinide and Fission Product Incineration," *Nuclear Science and Engineering*, **138**, 205-222 (2001).
31. K. ARIE, M. SUZUKI, M. KAWASHIMA, R. FUJITA, H. ENDO, A. TOUKURA, M. SAITO, and Y. FUJII-E, "Long-Lived Fission Product Burning Based on the Actinide Recycle Metal Fuel Core," *Progress in Nuclear Energy*, **32**, No. 3-4, 665-672 (1998).
32. Y. KIM, S. LEE, J. KIM, and W. PARK, "Feasibility of Using Burnable Poisons for Reduction of Coolant Void Reactivity in LMR for TRU Transmutation," *Proc. of Physor04*, April 25-29, 2004, Chicago, Illinois, (2004).
33. M. MESSAOUDI, and J. TOMMASI, "Fast Burner Reactor Devoted to Minor Actinide Incineration," *Nuclear Technology*, **137**, 84-96 (2002).
34. R. RICE, R. CURRAN, F. MCGINNIS, M. NOVICK, and F. THALGOTT, "EBR-I, Mark III-Design Report," ANL-5836, Idaho National Laboratory, Idaho Falls, Idaho, (1958).
35. L. KOCH, EBR-II: *Experimental Breeder Reactor*, ANL Internal Publication, Argonne National Laboratory, Argonne, Illinois, (2004).
36. Y. CHANG, R. HILL, E. FUJITA, D. WADE, Y. KUMAOKA, M. SUZUKI, M. KUWASHIMA, and H. NAKAGAWA, "Core Concepts for "Zero-Sodium-Void-Worth Core in Metal Fueled Fast Reactor," *Proc. of International Conference on Fast Reactors and Related Fuel Cycles*, Oct. 28 - Nov. 1, 1991, Kyoto, Japan, (1991).
37. G. VANDEGRIFT, M. REGALBUTO, S. AASE, A. BAKEL, T. BATTISTI, D. BOWERS, J. BYRNES, M. CLARK, J. EMERY, J. FALKENBERG, A. GELIS, C. PEREIRA, L. HAFENRICHTER, Y. TSAI, K. QUIGLEY and M. VANDER POL, "Designing and

Demonstration of the UREX+ Process Using Spent Nuclear Fuel,” *Proc. of ATATLANTE 2004: Advances for Future Nuclear Fuel Cycles*, June 21-24, 2004, Nimes, France, (2004).

38. R. FERRER, M. ASGARI, S. BAYS, and B. FORGET, “Computational Neutronics Methods and Transmutation Performance Analysis for Fast Reactors,” INL/EXT-07-12466, Idaho National Laboratory, Idaho, (2007).

39. S. PILLON, J. SOMERS, S. GRANDJEAN, and J. LACQUEMENT, “Aspects of Fabrication of Curium-Based Fuels and Targets,” *Journal of Nuclear Materials*, **320**, 36-43 (2003).

40. J. ACKERMAN, T. JOHNSON, and J. LAIDLER, “Waste Removal in Pyrochemical Fuel Processing for the Integral Fast Reactor,” *Proc. of The International Symposium on Actinides: Processing & Materials*, February 27-March 3, 1994, San Francisco, California, (1994).

41. H. HENRYSON II, B. TOPPEL, and C. STENBERG, “MC2-2: A Code to Calculate Fast Neutron Spectra and Multi-Group Cross-Sections,” ANL-8144, Argonne National Laboratory, Argonne, Illinois, (1976).

42. K. DERSTINE, DIF3D: “A Code to Solve One-, Two-, and Three-Dimensional Finite-Difference Diffusion Theory Problems,” ANL-82-64, Argonne National Laboratory, Argonne, Illinois, (1984).

43. B. TOPPEL, “A User’s Guide to the REBUS-3 Fuel Cycle Analysis Capability,” ANL-83-2, Argonne National Laboratory, Argonne, Illinois, (1983).

44. R. MCKNIGHT, J. STILLMAN, B. TOPPEL, and H. KHALIL, “Validation and Application of a Physics Database for Fast Reactor Fuel Cycle Analysis,” *Proc. of ANS: Topical Meeting on Advances in Reactor Physics*, April 11-15, 1994, Knoxville, Tennessee, (1994).

45. J. DUDERSTADT and L. HAMILTON, *Nuclear Reactor Analysis*, 1st ed., John Wiley & Sons, Inc., New York, (1976).

46. J. HOOVER, G. LEAF, D. MENELEY, and P. WALKER, “The Fuel Cycle Analysis System, REBUS Reactor Burnup System,” *Nuclear Science and Engineering*, **45**, 52-65 (1971).

47. D. HAMRIN, SCALE: “A Modular Code System for Performing Standard Computer Analysis for Licensing Evaluation,” ONRNL/TM-2005/39, Oak Ridge National Laboratory, Oak Ridge, Tennessee, (2006).

48. Los Alamos National Laboratory: X-5 Monte Carlo Team, “MCNP — A General Monte Carlo N-Particle Transport Code: Version 5,” LA-UR-03-1987, Los Alamos National Laboratory, Los Alamos, New Mexico, (2003).

49. D. POSTON and H. TRELLE, "MONTEBURNS 2.0: An Automated, Multi-Step Monte Carlo Burnup Code System," LA-UR-99-4999, Los Alamos National Laboratory, Los Alamos, New Mexico, (1999).
50. A. CROFF, "User's Manual for ORIGEN2 Computer Code," ORNL/TM-7175, Oak Ridge National Laboratory, Oak Ridge, Tennessee, (1980).
51. D. PELOWITZ (editor), "MCNPX User's Manual: Version 2.5.0," LA-CP-05-0369, Los Alamos National Laboratory, Los Alamos, New Mexico, (2005).
52. R. HILL, D. WADE, E. FUJITA, and H. KHALIL, "Physics Studies of Higher Actinide Consumption in an LMR," *Proc. of the International Conference on the Physics of Reactors*, April 23-27, 1990, Marseille, France, (1990).
53. M. SMITH, E. MORRIS, and R. HILL, "Physics and Safety Studies of a Low Conversion Ratio Sodium Cooled Fast Reactor," *Proc. of Global03*, November 16-20, 2003, New Orleans, Louisiana, (2003).
54. J. CAHALAN, M. SMITH, R. HILL, and F. DUNN, "Physics and Safety Studies of a Low Conversion Ratio Sodium Cooled Fast Reactor," *Proc. of Physor04*, April 25-29, 2004, Chicago, Illinois, (2004).
55. T. KIM and W. YANG, "A Metal Fuel Core Concept for 1000 MWt Advanced Burner Reactor (Interim Report)," ANL-AFCI-185, Argonne National Laboratory, Argonne, Illinois, (2007).
56. W. YANG, T. KIM, and C. GRANDY, "A Metal Fuel Core Concept for 1000 MWt Advanced Burner Reactor," *Proc. of Global07*, September 9-13, 2007, Boise, Idaho, (2007).
57. R. HOSTENY, "The ARC System Fuel Cycle Analysis Capability: REBUS-2," ANL-7721, Argonne National Laboratory, Argonne, Illinois, (1978).
58. "Advanced Fuel Cycle Initiative (AFCI) Comparison Report, FY 2006 Update," US Department of Energy, Office of Nuclear Energy, Science and Technology, Report to Congress on Advanced Fuel Cycle Initiative, Washington, DC, (2006).
59. K. MOORE and W. YOUNG, "Phase Studies of the Zr-H System at High Hydrogen Concentrations," *Journal of Nuclear Materials*, **27**, 316-324 (1968).
60. L. WALTERS, and J. KITTLE, "Development and Performance of Metal Fuel Elements for Fast Breeder Reactors," *Nuclear Technology*, **48**, 273-280 (1980).
61. L. WALTERS, and B. SEIDEL, "Performance of Metallic Fuels and Blankets in Liquid-Metal Fast Breeder Reactors," *Nuclear Technology*, **65**, 179-231 (1984).

62. A. WALTAR and A. REYNOLDS, *Fast Breeder Reactors*, Pergamon Press Inc., Maxwell House, Fairview Park, Elmsford, New York, (1981).
63. D. GELLES, "Microstructural Development in Reduced Activation Ferritic Alloys Irradiated to 200 dpa at 420C," *Journal of Nuclear Materials*, **212-215**, 714-719 (1994).
64. H. TSAI, A. COHEN, M. BILLONE, and L. NEIMARK, "Irradiation Performance of U-Pu-Zr Metal Fuels for Liquid Metal Cooled Reactors," *Proc. of ICONE3*, April 23-27, 1995, Kyoto, Japan, (1995).
65. R. MEULEKAMP and S. VAN DER MARCK, "Calculating the Effective Delayed Neutron Fraction with Monte Carlo," *Nuclear Science and Engineering*, **152**, 142-148 (2006).
66. W. YANG, Y. KIM, R. HILL, T. TAIWO, and H. KHALIL, "Long-Lived Fission Product Transmutation Studies," *Nuclear Science and Engineering*, **146**, 291-318 (2004).
67. R. HILL, D. WADE, J. LIAW, and E. FUJITA, "Physics Studies of Weapons Plutonium Disposition in the Integral Fast Reactor Closed Fuel Cycle," *Nuclear Science and Engineering*, **121**, 17-31 (1995).
68. RHODES, T. BAUER, G. STANFORD, J. REGIS, and C. DICKERMAN, "Fuel Motion in Overpower Tests of Metallic Integral Fast Reactor Fuel," *Nuclear Technology*, **98**, 91-99 (1992).
69. H. PLANCHON, R. SINGER, D. MOHR, and E. FELDMAN, "The Experimental Breeder Reactor II Inherent Shutdown and Heat Removal Tests - Results and Analysis," *Nuclear Engineering and Design*, **91**, 287-296 (1986).
70. G. GOLDEN, H. PLANCHON, J. SACKETT and R. SINGER, "Evolution of Thermal-Hydraulics Testing in EBR-II," *Nuclear Engineering and Design*, **101**, 3-12 (1987).
71. D. MOHR, L. CHANG, E. FELDMAN, P. BETTEN, and H. PLANCHON, "Loss-of-Primary-Flow-Without-Scram Tests: Pretest Predictions and Preliminary Results," *Nuclear Engineering and Design*, **101**, 45-46 (1987).
72. J. HERZOG, T. AOYAMA, H. TSAI, and E. DEAN, "A Transient Overpower Experiment in EBR-II," *Proc. of ARS94: International Meeting: Advanced Reactor Safety*, April 17-21, 1994, Pittsburgh, Pennsylvania, (1994).
73. H. OIGAWA, S. IJIMA, and M. BANDO, "Experiments and Analysis on Fuel Expansion and Bowing Reactivity Worth in Mock-up Cores of Metallic Fuel Fast Reactors at FCA," *Journal of Nuclear Science and Technology*, **36**, No. 10, 902-913 (1999).
74. OHMAE, A. MORINO, N. NAKAO, and S. HIRAO, "Channel Deformation Analysis for Fast Reactor Fuel Assemblies Undergoing Swelling and Thermal Bowing," *Nuclear Engineering and Design*, **23**, 309-320 (1972).

75. P. REINHALL, K. PARK, and R. ALBRECHT, "Analysis of Mechanical Bowing Phenomena of Fuel Assemblies in Passively Safe Advanced Liquid-Metal Reactors," *Nuclear Technology*, **83**, 197-204 (1988).
76. S. KAMAL and Y. ORECHWA, "Bowing of Core Assemblies in Advanced Liquid Metal Fast Reactors," *Proc. of Joint ASME/ANS Nuclear Power Conference*, July 20-23, 1986, Philadelphia, Pennsylvania, (1986).
77. "Preapplication Safety Evaluation Report for the Power Reactor Innovative Small Module (PRISM) Liquid-Metal Reactor - Final Report," Office of Nuclear Reactor Regulation, U.S. Nuclear Regulatory Commission, NUREG-1368, Rockville, Maryland (1994).
78. G. PALMIOTTI, E. LEWIS, and C. CARRICO, "VARIANT: VARIational Anisotropic Nodal Transport for Multidimensional Cartesian and Hexagonal Geometry Calculation," ANL-95/40, Argonne National Laboratory, Argonne, Illinois, (1995).
79. S. GLASSTONE and A. SESONSKE, *Nuclear Reactor Engineering*: 3rd Edition, Van Nostrand Reinhold Company, New York, New York, (1981).
80. Y. CHANG, P. FINCK and C. GRANDY, "Advanced Burner Test Reactor Preconceptual Design Report," ANL-ABR-1, Argonne National Laboratory, Argonne, Illinois, (2006).
81. K. KONASHI, B. TSUCHIYA, M. YAMAWAKI, K. FUJIMURA, and T. SANDA, "Development of Actinide-Hydride Target for Transmutation of Nuclear Waste," *Proc. of Global01*, September 13-17, 2001, Paris, France, (2001).
82. C. TILL, Y. CHANG, and W. HANNUM, "The Integral Fast Reactor - An Overview," *Progress in Nuclear Energy*, **31**, No. 1-2, 3-11 (1997).
83. D. WADE and R. HILL, "The Design Rationale of the IFR," *Progress in Nuclear Energy*, **31**, No 1-2, 13-42 (1997).
84. B. HILTION, D. PORTER, and S. HAYES, "AFC-1 Transmutation Fuels Post Irradiation Hot Cell Examination 4 to 8 at.% Final Report," INL/EXT-05-00785, Idaho National Laboratory, Idaho Falls, Idaho, (2006).
85. D. OLANDER, *Fundamental Aspects of Nuclear Fuel Elements*, National Technical Information Center, Office of Public Affairs Energy Research and Development Administration, Springfield, Virginia, TID-26711-P1, (1976).
86. G. HOFMAN, L. WALTERS, and T. BAUER, "Metallic Fast Reactor Fuels," *Progress in Nuclear Energy*, **31**, No. 1-2, 83-110 (1997).
87. K. EHRLICH, J. KONYS, and L. HEIKINHEIMO, "Materials for High Performance Light Water Reactors," *Journal of Nuclear Materials*, **327**, 140-147 (2004).

88. R. PAHL, C. LAHM, and S. HYES, "Performance of HT9 Clad Metallic Fuel at High Temperatures," *Journal of Nuclear Materials*, **204**, 141-147 (1993).
89. C. LAHM, J. KOENIG, P. BETTEN, J. BOTTCHER, W. LEHTO, and B. SEIDEL, "EBR-II Driver Fuel Qualification for Loss-of-Flow and Loss-of-Heat-Sink Tests without Scram," *Nuclear Engineering and Design*, **101**, 25-34 (1987).
90. TODREAS and M. KAZIMI, *Nuclear Systems: Vol. 1, Thermal Hydraulic Fundamentals*, Hemisphere, New York, (1990).
91. PETRI, and M. DAYANANDA, "Isothermal Diffusion in Uranium-Plutonium-Zirconium Alloys," *Journal of Nuclear Materials*, **240**, 131-143 (1997).
92. T. TAIWO, T. KIM, J. STILLLMAN, R. HILL, M. SALVATORES, and P. FINCK, "Assessment of a Heterogeneous PWR Assembly for Plutonium and Minor Actinide Recycle," *Nuclear Technology*, **155**, 34-54 (2006).
93. J. PLAMBECK, and J. EIDER, H. "Laitinen, Electrochemistry of the Lithium Hydride Cell," *Journal of the Electrochemical Society*, **113**, No. 9, 931-937 (1966).
94. T. NOHIRA and Y. ITA, "Electrochemical Hydrogen Absorbing Behavior of Pd and Pd-Li Alloys in a Molten LiCl-KCl-LiH System," *Journal of the Electrochemical Society*, **144**, No. 7, 2290-2295 (1997).
95. H. ITOZ and Y. HASEGAWA, "Electrode Behavior of Hydrogen Reduction in LiCl-KCl Melt: Voltammetric Analysis," *Journal of the Electrochemical Society*, **147**, No. 1, 285-295 (2000).
96. C. TRYBUS, J. SANECKI, and S. HENSLEE, "Casting of Metallic Fuel Containing Minor Actinide Additions," *Journal of Nuclear Materials*, **204**, 50-55 (1993).
97. B. HILTON, S. HAYES, D. PORTER, M. MEYER, J. KENNEDY, G. CHANG, D. UTTERBECK, and R. AMBROSEK, "Irradiation Performance of Fertile-Free Metallic Alloys for Actinide Transmutation," *IMF11: Workshop on the Research, Development and Implementation of Fissile-Free Nuclear Fuels*, October 10-12, 2006, Park City, Utah, (2006).
98. A. DUBBERLY, C. BOARDMAN, D. CARROLL, C. EHRMAN, and C. WALTER, "S-PRISM Fuel Cycle Study," *Proc. of ICAPP03*, May 4-7, 2003, Cordoba, Spain, (2003).
99. M. BUNN, S. FETTER, J. HOLDREN, and B. VAN DER ZWAAN, "The Economics of Reprocessing vs. Direct Disposal of Spent Nuclear Fuel," Harvard University/DE-FG26-99FT4028, Cambridge, Massachusetts, (2003).
100. E. BECKJORD, Executive Director, "The Future of Nuclear Power," Massachusetts Institute of Technology, Cambridge, Massachusetts, (2003).

101. L. KOCHETKOV, A. MALENKOV, V. POPLAVSKII, O. SARAIEV, K. SUKNEV, and A. KIRYUSHIN, "Achieving Competitiveness in Fast Reactors with Sodium Coolant," *Atomic Energy*, **83**, No. 6, 863-867 (1997).
102. M. KONOMURA and D M. ICHIMIYA, "Design Challenges for Sodium Cooled Fast Reactors," *Journal of Nuclear Materials*, **371**, 250-269 (2007).
103. Email Communication with Dr. Alistair Miller of Atomic Energy of Canada Limited, D2O Prices, millera@aecl.ca, (February 14, 2005).
104. R. SMITH, M. SHAY, S. SHORT, C. EHRMAN, and T. MYERS, "Estimated Cost of an ATW System," PNNL-13018, Pacific Northwest National Laboratory, Richland, Washington, (1999).
105. D. KIM, M. KAZIMI, M. DRISCOLL, and N. TODREAS, "The Economics of Transmutation Fuel Cycles, Core Physics and Engineering Aspects of Emerging Nuclear Energy Systems for Energy Generation and Transmutation," November 28 - December 1, 2000, Argonne, Illinois, (2000).
106. D. GROOM, Expert Group and Editorial Group Chairman "The Economics of the Nuclear Fuel Cycle," Nuclear Energy Agency: Organization for Economic Co-operation and Development, Paris, France, (1994).
107. League of Women Voters, *The Nuclear Waste Primer: A Handbook for Citizens*, 2nd ed., Lyons Press, New York, New York, (1986).
108. United States Enrichment Corporation, "2006 Annual Report: Investing in Nuclear's Future," <http://www.usec.com/>, Bethesda, Maryland, (2006).

BIOGRAPHICAL SKETCH

Samuel E. Bays was born the son of Gerald and Marva Bays in Topeka, Kansas on July 14, 1979. He was raised on a small family farm in the northeastern part of the state and graduated from Mission Valley High School in May 1997. He attended Kansas State University where he received his Bachelor of Science in Mechanical Engineering with an emphasis in Nuclear Engineering in May 2002. He later received a Master of Science degree in Nuclear Engineering at the University of Florida in August 2007. He now works in the reactor physics department at Idaho National Laboratory. His research interests include all aspects of reactor design, nuclear waste transmutation and hybrid nuclear energy systems.